



**ScuDo**  
Scuola di Dottorato – Doctoral School  
WHAT YOU ARE, TAKES YOU FAR



**西安交通大学**  
XIAN JIAOTONG UNIVERSITY

Doctoral Dissertation

Doctoral Program in Electronics Engineering (XXXIII<sup>rd</sup> cycle)

# **Uncertainty Quantification of Lines Excited by Transient Electromagnetic Disturbances Based on Stochastic Models**

A dissertation submitted to Politecnico di Torino and Xi'an  
Jiaotong University in partial fulfillment of the  
requirements for the degree of Doctor of Philosophy

**Ning Dong**

## **Supervisors**

Prof. Xie Yanzhao, Supervisor

Prof. Flavio G. Canavero Co-supervisor

Politecnico di Torino

Jan 13<sup>th</sup>, 2023



## ABSTRACT

The transient electromagnetic disturbance (TED), such as lightning electromagnetic pulse (LEMP), high altitude electromagnetic pulse (HEMP), and high power microwave (HPM) may couple into the power system through various conductors, such as power lines, communication cables, and other transmission line structures. The coupling responses may cause failure or even damage to the equipment connected with the lines. Existing studies have focused on the deterministic computational modeling of field-to-transmission line coupling under TED. However, the actual coupling response may vary in a wide range due to the inability to accurately obtain the parameters of TEDs, lines, and environments in the simulation; For TED events with low probability, deterministic simulation based on certain parameters cannot predict the possible variation and distribution of the responses, and it is hard to provide reasonable evaluations for the TED impact. To address the above problems, this dissertation takes HEMP as an example, stochastic models are developed for the generation and propagation of HEMP and field-to-transmission line coupling responses, respectively. The uncertainty quantification of the responses under HEMP is carried out by a proposed hierarchical stochastic model. Based on the uncertainty quantification results of the responses, a distribution-free vulnerability assessment method is proposed for the equipment connected with the transmission lines.

To study the impact of uncertainties in the source of HEMP and the environment, an accurate and efficient iterative self-consistent simulation scheme is developed for the simulation of HEMP generation and propagation. Since the full simulation of HEMP has no analytical expression, a physical-based stochastic surrogate model is derived from the simplified model of Compton electron motion. The proposed model can address the accuracy problem of constructing non-intrusive surrogate models, which is caused by the spatial distribution of the HEMP electric field amplitude and polarization angle is nonsmooth. The time-consuming can be reduced significantly from days to hours for the uncertainty quantification of the HEMP electric field on the ground.

In order to simulate the coupling responses, which may vary in a large range due to the uncertainty of TED, the field-to-lines coupling with nonlinear loads are modeled based on the analog behavior modeling, including a macromodel of transmission line with frequency-dependent characteristics and an equation-based dynamic nonlinear model of MOA. These two models can be easily combined together in the simulation. When the uncertainty variables are assumed as mutually independent variables, a stochastic models of transmission line coupling responses are intrusively constructed by expanding the telegraph equations through the polynomial chaos expansion method (PCE). When the inputs variables are no longer mutual independence. To address the problem of transferring arbitrary correlated multidimensional variables in the hierarchical stochastic models, we proposed a PCE method based on the kernel density estimation (KDE), that the orthogonal polynomial basic functions

can be constructed for the arbitrary correlated variables. The proposed KDE-PCE has the advantage of high efficiency and fast convergence speed. The coupling responses under uncertain HEMP environment can be quantified based on the proposed hierarchical stochastic model.

To evaluate the equipment connected with the transmission lines considering the uncertain coupling responses, a distribution-free vulnerability evaluation method is proposed, according to the framework of the quantification of margins and uncertainties (QMU) method. Since the effect tests usually result in few data, in order to overcome the effects caused by sampling variability and estimation errors, two non-parametric estimation/regression methods are proposed to estimate the quantiles and the tolerance bounds for the equipment strength. Without being constrained by the preset probability distribution, reasonable vulnerability assessment conclusions can be provided with certain confidence levels.

In this dissertation, the uncertainty quantification of the transmission line coupling responses under the TED has been systematically studied, the method proposed in the dissertation can be expended to carry out studies about the impact of other types of TEDs, and provide references for the protection design of the power system.

**KEY WORDS:** Transient electromagnetic disturbance; Uncertainty quantification; Stochastic model; Vulnerability assessment

**TYPE OF DISSERTATION:** Application Fundamental

# CONTENTS

|  |     |
|--|-----|
| ABSTRACT .....   | III |
| CONTENTS .....   | V   |
| SYMBOL ANNOTATION .....  | VII |
| 1 Introduction .....   | 1   |
| 1.1 Background and Significance.....   | 1   |
| 1.2 State of the art of the research .....   | 3   |
| 1.2.1 Study about computational modeling for generation and propagation of HEMP ...      | 3   |
| 1.2.2 Study about computational modeling for field-to-line coupling .....                | 5   |
| 1.2.3 Study about uncertainty quantification of the computational model .....            | 7   |
| 1.3 Major research content and organization of the dissertation.....                     | 10  |
| 2 Deterministic model and stochastic model for the TED .....                             | 12  |
| 2.1 Classical physical model for the generation and propagation of the HEMP.....         | 12  |
| 2.2 Efficient iterative and self-consistent simulation scheme of the HEMP .....          | 17  |
| 2.2.1 Iterative algorithm for HEMP with consideration of self-consistent effect .....    | 17  |
| 2.2.2 Stability and convergence analysis of the iterative simulation .....               | 21  |
| 2.2.3 Validation of the numerical simulation of the HEMP .....                           | 22  |
| 2.3 Physical-based stochastic surrogate model for the HEMP distribution on the ground    | 26  |
| 2.3.1 Surrogate model based on the simplified dipole and quadrupole .....                | 27  |
| 2.3.2 Physical-based stochastic surrogate model based on SVM.....                        | 30  |
| 2.3.3 Uncertainty Quantification of HEMP based on the stochastic surrogate model ...     | 33  |
| 2.4 Concluding remarks .....   | 35  |
| 3 Deterministic model and stochastic model for field-to-line coupling.....               | 36  |
| 3.1 Classical physical model for TLs excited by external fields.....                     | 36  |
| 3.2 Macromodel for field coupling to lines with nonlinear loads .....                    | 42  |
| 3.2.1 Frequency-domain macromodel of field-to-line coupling .....                        | 42  |
| 3.2.2 Time-domain macromodel for field-to-line coupling with nonlinear load.....         | 45  |
| 3.2.3 Validation of the field-to-line coupling macromodel .....                          | 53  |
| 3.3 Stochastic model of field-to-line coupling based on polynomial chaos expansion ..... | 56  |
| 3.3.1 Stochastic model with uncertainties of lines .....                                 | 57  |
| 3.3.2 Stochastic model with uncertainties of fields.....                                 | 60  |
| 3.4 Concluding remarks .....   | 64  |
| 4 Hierarchical stochastic model for TED-to-line coupling responses.....                  | 65  |
| 4.1 Polynomial chaos expansion method with arbitrary and correlated multivariate .....   | 65  |
| 4.1.1 PDF estimation of multivariate based on MCMC-KDE .....                             | 67  |
| 4.1.2 Generation of correlated multivariate orthonormal polynomials .....                | 71  |
| 4.1.3 Coefficient calculation with arbitrary distribution correlated multivariate.....   | 74  |
| 4.1.4 Uncertainty quantification with KDE-PCE.....                                       | 76  |
| 4.2 Uncertainty quantification of TED and coupling response based on the hierarchical    |     |

|   |     |
|---|-----|
| stochastic model .....  | 77  |
| 4.2.1 Uncertainty quantification of the HEMP waveform .....                           | 77  |
| 4.2.2 Uncertainty quantification of the HEMP-to-line coupling responses .....         | 82  |
| 4.2.3 Uncertainty quantification of line coupling response with nonlinear load .....  | 85  |
| Concluding remarks .....  | 86  |
| 5 Vulnerability assessment based on quantification of margins and uncertainties ..... | 88  |
| 5.1 Distribution-free quantification of margins and uncertainties .....               | 88  |
| 5.1.1 Basic concept and procedure of uncertainty quantification for margins.....      | 88  |
| 5.1.2 QMU metric based on quantiles and tolerance bounds.....                         | 90  |
| 5.2 Uncertainty quantification for equipment strength based on experiment .....       | 93  |
| 5.2.1 Equivalence between PCI experiment and field-to-line coupling.....              | 93  |
| 5.2.2 Nonparametric estimation method based on order statistics .....                 | 100 |
| 5.2.3 Nonparametric regression method based on MaxEnt-Bagging.....                    | 104 |
| 5.2.4 Validation of the distribution-free QMU method .....                            | 109 |
| 5.3 Evaluation of equipment vulnerability based on the distribution-free QMU method   | 110 |
| 5.4 Concluding remarks .....  | 113 |
| 6 Conclusions and perspectives.....   | 114 |
| 6.1 Conclusions .....   | 114 |
| 6.2 Future work .....   | 115 |
| Acknowledgments.....  | 117 |
| References .....  | 118 |
| Achievements .....  | 130 |
| Declarations  |     |

## SYMBOL ANNOTATION

|   |   |
|---|---|
| $\mathbf{B}_e$  | The geomagnetic field vector  |
| $c$   | The velocity of light   |
| CF  | The QMU metric  |
| $d$   | The distance  |
| $D_{\text{RMS}}$                                      | The root-mean-square deviation  |
| $e$   | The charge of the electron  |
| $\mathbf{e}_r, \mathbf{e}_\theta, \mathbf{e}_\varphi$ | The unit vector in directions $\varphi, \theta, r$  |
| $\mathbf{e}_x, \mathbf{e}_y, \mathbf{e}_z$            | The unit vector in directions $x, y, z$   |
| $e(\xi)$  | The monic polynomial of multivariate (when the symbol appears with a subscript, the subscript indicates the number of the polynomial) |
| $E(X)$  | The expectation of variable or event $X$  |
| $E_\gamma$  | The energy of prompt gamma photon   |
| $E_e$   | The invariant mass of the electron  |
| $\mathbf{E}, \mathbf{B}$                              | The matrix of electric field and magnetic field vector  |
| $\mathbf{E}_t, \mathbf{E}_r$                          | The matrix of transverse and component of the electric field in the spherical coordinate system                                       |
| $\mathbf{E}_v, \mathbf{E}_h$                          | The vertical and horizontal components of the electric field vector   |
| $\mathbf{E}^{\text{inc}}, \mathbf{H}^{\text{inc}}$    | Incident fields vector  |
| $\mathbf{E}^{\text{ref}}, \mathbf{H}^{\text{ref}}$    | Reflected fields vector reflected by the ground   |
| $E_{\text{max}}$                                      | The peak value of the electric field  |
| $E_\varphi, E_\theta, E_r$                            | $\varphi, \theta, r$ components of the electric field   |
| $E_x, E_y, E_z$                                       | $x, y, z$ components of the electric field  |
| $E_v, E_h$  | The amplitude of the vertical and horizontal components of the electric field   |
| $f_c$   | The temporal profile of the prompt gamma rays   |
| $F_\chi(x)$   | The probability that the threshold $\chi$ is less than $x$  |
| $F_X^{(C)}, F_X^{(D)}$                                | The cumulated probability density of the stress and strength of the equipment   |
| $H(X)$  | The information entropy of variable or event $X$ .  |
| $H_x, H_y, H_z$                                       | $x, y, z$ components of the electric field at distance $n\Delta r$ and time $j\Delta t$ in the Cartesian coordinate system            |
| $\mathbf{J}$  | The Compton current vector  |

|                                |   |
|--------------------------------|---|
| $J_\varphi, J_\theta, J_r$     | $\varphi, \theta, r$ components of Compton current  |
| $k_1$                          | The attachment coefficient between electron and molecular                                       |
| $k_2$                          | The electron-positive ion recombination coefficient   |
| $k_3$                          | The ion-ion recombination coefficient   |
| $k_E, \alpha_E, \beta_E$       | Time coefficient in the analytic description of HEMP  |
| $K(\cdot)$                     | The kernel function   |
| $l$                            | The length of the transmission line.  |
| $l_{CP}$                       | The length of the pulse injection coupler   |
| $m_e$                          | The mass of the electron  |
| $M, U$                         | The margin between stress and strength and its uncertainty                                      |
| $n_{se}, n_+$                  | The density of secondary electrons and positive ion   |
| $p(x), \tilde{p}(x)$           | The probability density distribution and the estimation of the probability density distribution |
| $P(X)$                         | The probability of variable or event $X$  |
| $Q$                            | QMU metric: QMU calculator  |
| $Q_{1-p}, Q_p$                 | The lower and upper $p$ quantile  |
| $Q_{1-p,\gamma}, Q_{p,\gamma}$ | The tolerance bound for lower and upper $p$ quantile  |
| $r_0$                          | The classical radius of the electron  |
| $R_E$                          | The radius of the Earth   |
| $R_v, R_h$                     | Reflection coefficients for vertical and horizontal fields                                      |
| $R$                            | The failure probability   |
| $S$                            | The generation rate of the secondary electrons  |
| $s_i, s_i^T$                   | Sobol's first sensitivity indices and total sensitivity indices                                 |
| $t$                            | Time  |
| $T_{\gamma,w}$                 | The full width at half maximum of the prompt gamma rays   |
| $T_r, T_{FWHM}$                | The 10%-90% rise time and the full width at half maximum of HEMP                                |
| TR                             | QMU metric: tolerance ratio   |
| $U_e$                          | The swarm characteristic energy of the secondary electrons                                      |
| $\mathbf{v}_p$                 | The velocity of Compton electron  |
| $\mathbf{v}_s$                 | The velocity of the secondary electrons   |
| $\nu_m$                        | The momentum exchange collision frequency of the secondary electrons                            |
| $\nu_w$                        | The energy exchange collision frequency of the secondary electrons                              |



|                                  |  |
|----------------------------------|--|
| $\mathbf{V}, \mathbf{I}$         | The matrix of total voltages and current vectors along the transmission lines  |
| $\mathbf{V}_s, \mathbf{I}_s$     | The matrix of distributed voltage and current source vectors along the transmission lines caused by the incident field   |
| $\mathbf{w}, \tilde{\mathbf{w}}$ | The matrix of weights calculated by the probability density distribution and its estimation  |
| $W_i$                            | The weight of Compton electrons  |
| $x, \mathbf{x}$                  | Sample of univariate $\xi$ (or vector of multivariate $\xi$ ), (when the symbol appears with superscript and subscript, the subscript indicates the number of the variable, and the superscript refers to the source of the variable(s)) |
| $\mathbf{Z}, \mathbf{Y}$         | The per-unit-length impedance and admittance matrices of transmission lines  |
| $\mathbf{Z}_C, \mathbf{Y}_C$     | The characteristic impedance and admittance matrix   |
| $\alpha, \psi, \phi$             | The polarization angle, elevation angle, and azimuth angle of the electromagnetic fields incident to ground  |
| $\delta$                         | The angle between the observation point and geomagnetic South  |
| $\epsilon_0, \epsilon_r$         | The dielectric of vacuum and relative dielectric constant  |
| $\eta$                           | The obliquity factor for the multiple scattering effect of Compton electrons   |
| $\theta_b$                       | The geomagnetic inclination  |
| $\mu_0, \mu_r$                   | The permeability of vacuum and relative permeability   |
| $\mu_e$                          | The mobility of the secondary electrons  |
| $\mu_{i,j}^{\xi}$                | The central moment of the $i$ -th and the $j$ -th monic polynomial of variable(s) $\xi$  |
| $\xi, \xi$                       | Single uncertainty variable and vector of multiple variables (when the symbol appears with superscript and subscript, the subscript indicates the number of the variable, and the superscript refers to the source of the variable(s))   |
| $\phi_C, \theta_C$               | The scattering angle of Compton scattering gamma photon and Compton scattering electron  |
| $\phi(\xi), \psi(\xi)$           | The univariate basis functions and the multivariate basis functions for polynomial chaos expression (when the symbol appears with superscript and subscript, the subscript indicates the number of the basis function)                   |
| $\phi_{a_i^m}(\xi_i)$            | The $a$ -th univariate basis function for the $i$ -th variable in the $m$ -th multivariate basis functions   |
| $\sigma_g$                       | The conductivity of the ground   |
| $\sigma_{KN}$                    | The Compton scattering cross-section   |

|                        |   |
|------------------------|---|
| $\tau$                 | Time in the retarded time system  |
| $\Phi$                 | The chain parameter matrix  |
| $\Phi_{TL}, \Phi_{CP}$ | The chain parameter matrix of transmission lines, pulse injection coupler system    |
| $\Phi_{FC}, \Phi_{ST}$ | The chain parameter matrix of the magnetic core and stray parameters of the coupler |

# 1 Introduction

## 1.1 Background and Significance

Transient electromagnetic disturbances (TEDs), such as high altitude electromagnetic pulse (HEMP), lightning electromagnetic pulse (LEMP), power system switcher switching, geomagnetic disturbance (GMD), and high power microwaves (HPM) are potential threats to modern power grids and other infrastructure<sup>[1]-[6]</sup>. TEDs have the common feature that electromagnetic energy builds up quickly to a high level, therefore, they may couple to transmission line (TL) structures, such as long-distance transmission power lines and distribution power lines, communication cables in the power systems, power lines, and communication cables in the substations connected with the secondary equipment. Although most of the equipment is settled in metal cabinets, which can shield direct electromagnetic field radiation impact, the potential coupling paths are widely distributed and inevitably exposed to the transient electromagnetic field. TEDs may arouse induced voltages and currents along the lines and inject them to the equipment. Electrical and electronic equipment in the modern power system is increasingly intelligent and susceptible to the impact of external transient electromagnetic interference. The coupling responses may cause serious effects or even damage to the conductors and electronics and electrical equipment connected to the lines<sup>[7]-[13]</sup>. It is important to pay more attention to the response of the TLs injected into the equipment port caused by TED.

Most of the abovementioned TEDs have the common features of very fast rise time, wide spectrum coverage, high amplitude of field density, and wide geometrical coverage and may cause significant coupling responses. For instance, transient electromagnetic fields generated around by the lightning strike usually have coverage with a radius of kilometers<sup>[14]</sup>. Under the excitation of LEMP, there may be induced voltage of tens or even hundreds of kilovolts on the overhead power lines, which may cause flashover and even damage to electric equipment connected with the power lines such as insulators, power transformers, and electric reactors. Lightning may also couple into the lines and cables in the substation, and cause failure or even damage to the terminated secondary electronic equipment such as the supervisory control and data acquisition (SCADA) system, and instrumentation and control (I&C) system. HEMP generated by the high altitude burst usually has geometrical coverage with a radius of thousands of kilometers. The early-time HEMP has a rise time of less than tens of nanoseconds and an electric field amplitude of tens of kilovolts per meter. The medium-time HEMP has a similar frequency spectrum to LEMP. In the experiment in the 1960s, it was found that HEMP can couple into overhead power lines, and the induced voltages and currents may result in a series of faults in the power systems, such as flashover and breakdown of insulators on the line and short-circuit faults, reduction of the insulation of the transformer or even damage<sup>[15]</sup>. There is a significant effect on the secondary equipment as well. Within the wide radiation range of HEMP, a large number of abovementioned faults may occur in a short time, which

will cause a stability crisis for the power system, and eventually lead to a large-scale cascade failure of the power system. In summary, TED may directly affect the normal distribution of electricity, cause irreversible damage to the power system, and may have a long recovery period.

Most of the TEDs are high-impact events with low probabilities for the power systems. Although the occurrence frequency is usually low, once it happened, it may cause serious impacts on the power system. In order to predict and defend the risk reasonably, in addition to accurate simulation of the coupling responses in the power system excited by the TED, it is also necessary to quantify the potential coupling responses based on the probability study with the consideration of the uncertainty in the parameters of TED, lines, and environment. The probability research of lightning and LEMP is relatively mature. By conventional measurement, lightning towers measurement, and rocket-triggered lightning experiment, etc., the lightning activities in specific areas are collected. The probability distribution of lightning current amplitude, and ground lightning density are summarized<sup>[196]-[199]</sup>. Existing studies agree that the probability of lightning current amplitude follows a certain statistical distribution law. Several empirical formulas of the probability of lightning current amplitude were recommended in standards<sup>[16][17]</sup>. The impact of the LEMP can be quantified according to the probability distribution of lightning, such as the lightning-induced voltage flashover rate<sup>[18][19]</sup>. And the statistical results can be used to guide the design of protection in the power system, such as the arrangement of overhead ground wire and lightning arrester.

Different from LEMP, HEMP is a kind of TED that rarely happens, but its illumination range is larger and the threat level is higher than that of lightning. The existing lightning protection facilities (lightning arresters) have been proved to have higher residual voltage and worse protection performance under nanosecond impulse<sup>[145][146]</sup>, and they may be insufficient to completely prevent the induced overvoltage of HEMP. To evaluate a local system to TED, a common method is to define a "bounding case" to represent the worst case of the TED. The conservative bounding electrometric environment can qualitatively identify the threat to the lines and electrical and electronic systems. However, the conservative assessment may cause the overestimation of the potential effects for wide-area distributed systems and leads to unnecessary over-protection. A stochastic simulation framework based on Monte Carlo (MC) method was proposed to analyze the induced coupling on the lines and port of equipment when the power system is excited by HEMP<sup>[24]</sup>.

In addition, the geometrical coverage radius of the HEMP may be larger than several kilometers, and the HEMP has a specific distribution pattern known as "smile face". The distribution of the power system may cover a large area as well, the lines and equipment in the system may face different HEMP environment. If the spatial properties of the HEMP are ignored, it may provide unrealistic estimates for the coupling responses<sup>[20]-[21]</sup>. Therefore, the spatial variation inherent in HEMP should be investigated, including the details of the waveform of the electromagnetic field, incident angles, and polarization angles of incidence<sup>[22]</sup>.

In general, the study of TED's impact on the power systems needs a probability-based study to balance the high impact and low probability and obtain reasonable evaluation results

for system evaluation and defense. Most of the existing probability studies are based on the classical MC method. The efficiency of MC limits the development of relative research. This dissertation will consider the potential uncertainties in the processes of TED coupling to the lines in the power systems, with the idea of uncertainty quantification, stochastic models are established for the generation of HEMP and field-to-line coupling respectively. A hierarchical stochastic model is established to obtain relatively comprehensive uncertainty quantification of the coupling responses excited by HEMP. Valuable statistical information on the coupling responses will be provided for the vulnerability of the equipment in the power system. The uncertainty quantification of the response based on the stochastic model has the potential to be extended to the study of other TED.

## 1.2 State of the art of the research

The uncertainty quantification of the responses on the TLs under the TED is a systematic study, including the deterministic modeling of the TED, the deterministic modeling of field-to-line coupling, and the corresponding stochastic models. The physical-based deterministic model with high confidence is fundamental. The stochastic model is for uncertainty quantification.

### 1.2.1 Study about computational modeling for generation and propagation of HEMP

The generation and propagation of early-time high-altitude electromagnetic pulse (EMP) have been widely studied and concluded to be a self-consistent physical process including photons, electrons, and electromagnetic (EM) fields<sup>[32]-[38]</sup>. The simulation depends on the modeling of the high-energy Compton electrons produced by prompt gamma rays and the modeling of the low-energy secondary electrons produced by Compton electrons. Fast-moving Compton recoil electrons constitute Compton current and become the source current of the HEMP. Secondary electrons act to attenuate the generation and propagation of HEMP. Meanwhile, Compton electrons and secondary electrons are affected by the produced electromagnetic fields.

The physical basic of the numerical simulation of HEMP was proposed by Karzas and Latter<sup>[25]-[31]</sup>. A non-self-consistent simulation method based on high-frequency approximation (HFA) is well-developed and efficient. The simulation of electromagnetic fields is simplified to a set of ordinary differential equations based on Maxwell curl equation. The HFA is well-used in follow-up studies. The main defect of their model is that the calculation of current and electromagnetic fields is not self-consistent, and the influence of EM fields on electron motion is ignored in the simulation. Considering the self-consistent effect may complicate the HEMP simulation. It was not considered worth the time penalty in the early days. The non-self-consistent method will overestimate the amplitude of HEMP.

With the development of computing technology, the self-consistent effect is appreciated once computer codes are available. Several HEMP codes that include the self-consistent effect have been developed, such as the Compton high-altitude pulse code (CHAP) developed by

Longmire and Longley<sup>[40]</sup>, the code based on an extension model of the original Karzas-Latter-Longmire model for high-altitude electromagnetic pulse (EXEMP) developed by Leuthäuser<sup>[41]</sup>, and the code for calculation of high-altitude electromagnetic pulse (CHEMP) developed by Brau<sup>[39]</sup>, et al. In the self-consistent simulation of HEMP, it is necessary to calculate not only the equations of EM fields but also the motion equation of the electron as well as the influence of the electromagnetic fields on the electron motion. Therefore, the self-consistent algorithms are much more complex.

In the following period, there were many studies about the simulation of HEMP, most of them are based on the HFA and focused on detailed simulation of gamma photon model, Compton electron motion model, secondary electron and conductivity model<sup>[114]-[122]</sup>.

Recently, an integral algorithm based on the Jefimenko equation is also used to solve HEMP in the simplified case<sup>[43]-[45]</sup>. The three-dimensional effect can be considered to simulate HEMP in the integral algorithm. The results show that not only the current on the line of sight determines the EM fields, but also the current source in the space around the line of sight contributes to the electromagnetic pulse. The integral algorithm can be used to study the influence of scattering gamma as well. However, the integration method is only a simple integration of the current that has been calculated, it is a non-self-consistent method.

Particle-in-cell (PIC) method was introduced for the simulation of HEMP as well, such as the unitedly developed PIC code (UNIPIC) and EMPulse<sup>[130]-[132]</sup>. The PIC simulation requires large-scale computing resources<sup>[132]</sup>. It can achieve an accurate self-consistent solution in the source region but have difficulty in providing the radiation field outside the source region in a limited time<sup>[130]</sup>. Compared with the non-self-consistent methods, the self-consistent calculation methods are more complex and less efficient.

With further investigation of the physical mechanism of HEMP, the simulation model becomes more and more detailed and complex. The difficulty in the simulation of a HEMP environment is that there are many parameters with uncertain values in the simulation model.

The research and analysis of waveform characteristics and standards are very important for the follow-up research of the induced response on conductors. The “Bell Laboratories” waveform is widely used for civil HEMP assessments. The waveform represents an envelope of field shapes under various calculations<sup>[46]</sup>. Longmire and Leuthäuser provided nominal results of the HEMP with variable parameters of prompt gamma yield, to specify more relieved threat levels than the worst case<sup>[40][41]</sup>. Radasky has analyzed numerous calculations performed by Longmire. He fitted a waveform with a maximal bounding case of the results. This new curve represents a less severe environment than the Bell Laboratories waveform, which is considered to be more reasonable. The proposed waveform has been adopted as the IEC HEMP radiated environment<sup>[189]</sup>. Giri reviewed the evolution of the HEMP waveform standard in the report and discussed various definition standards and their applications<sup>[47][48]</sup>.

The HEMP radiated field has a specific spatial distribution pattern. The amplitude, pulse width, and angles of the EM fields may vary greatly in a wide area. To quantify the response in widely distributed objects such as power systems, the HEMP results with spatial variation should be used induced instead of a standard HEMP waveform. The smile diagram given in

IEC 61000-2-9 describes the amplitude distribution<sup>[187]</sup>. However, it is verified by research that the smile diagram would exaggerate the potential effects when the prompt gamma yield is low, and that the amplitude does not decay to approximately 50% of the peak field at the horizon as given in the standard<sup>[23]</sup>. Two alternate HEMP environment descriptions have been developed: one arising from a simple radiating dipole moment model<sup>[49]</sup>, and the other resulting from curve-fitting of CHAP results<sup>[40]</sup>. Both the two alternate models consider spatial variation without the influence of uncertainty parameters of HEMP.

According to the specific spatial distribution of the HEMP, the amplitude, pulse width, and angles of the EM fields may vary greatly in a wide area. The spatial distributed of HEMP has been widely reported, and several studies have taken it into account in the impact analysis of local systems<sup>[20]-[24]</sup>. The power system is placed in a large area, and the lines and equipment in the system may face different HEMP environments. If the spatial properties of the HEMP are ignored, it may provide unrealistic estimates for the coupling responses. Therefore, the spatial variation inherent in HEMP should be investigated, including the details of the waveform of the electromagnetic field, incident angles, and polarization angles of incidence<sup>[22]</sup>. However, the studies so far do not include any attempt to quantify power system performance in HEMP environments.

In a recent report [23], five benchmark HEMP scenarios were used to study the probability behavior of the coupling responses in the power system. Only two variables of the HEMP (yield and height of burst) were considered. The consideration of uncertain factors that may cause variation in HEMP is poor. In addition, the report mentioned that the usage of the smile diagram in the IEC standard 61000-2-9 would exaggerate the potential effects of the power system, that the amplitude did not decay to approximately 50% of the peak field at the horizon, as given in the standard.

In general, the self-consistent simulation of HEMP is complex, many parameters in the simulation are difficult to be determined, which may have potential impacts on the results of HEMP. Meanwhile, most of the studies on the spatial distribution of HEMP are qualitative studies, which is difficult to be used for the uncertainty quantification of coupling response on TLs in the power system.

### 1.2.2 Study about computational modeling for field-to-line coupling

The purpose of simulation and investigation of HEMP is for reasonable assessment and scientific protection of transient response. As a significant coupling path of signal and energy, the TL plays an important role in the field of power systems excited by TED. The problem of induced response on overhead and buried TLs have been well-developed for decades. There is a large number of reports on the coupling between electromagnetic fields and TLs.

To solve the voltages and currents induced by external fields on conducting wires, exact solutions can be solved by using full-wave numerical methods based on Maxwell's equations, such as the Finite Difference Time Domain method (FDTD) or Method of Moments (MoM<sup>[59]</sup>). However, due to the significant difference between the length of a typical TL and the size of the element for simulation, the full-wave methods require long computing times and huge memory.

TL theory has been proposed to cope with the interaction between incident electromagnetic fields and long-distance lines, when the length of the lines is much greater than the wavelength of the EM signals, and the wavelength is much greater than the cross-section of TLs. The antenna mode current is ignored at the terminal of the TLs, the transmission mode current and voltage can represent the transient response. Taylor derived the telegraph equation with a distributed source for the TLs excited by an electromagnetic field, where the distributed voltage and current sources are generated by the incident electric field<sup>[50]</sup>. Agrawal treated the field-to-line coupling as an electromagnetic scattering problem, introduced the concept of scattering voltage concept, and derived the time-domain telegraph equation in a form different from the Taylor telegraph equation with only distributed voltage sources<sup>[51]</sup>. Different models were also proposed by Vance, and Rachidi, Chowdhuri-Gross<sup>[52][53][54]</sup>. Several researchers discussed and compared these different models<sup>[55][56][57]</sup>. It was concluded that the Taylor, Agrawal, and Rachidi models are equivalent and can provide the same results. The distributed sources in the Chowdhuri-Gross model and Vance model are incomplete, the Chowdhuri-Gross model lacks the source term generated by the incident magnetic field compared with the Taylor model, Vance model lacks the lumped voltage source term at the terminal compared with the Agrawal model. Ianoz has verified the TL model by experiment, that numerical results obtained by the TL model can predict the induced response on TLs with good agreement<sup>[55][58]</sup>. It is worth noting that the results are adaptable, even when the TLs used in the experiment did not satisfy strictly the assumption, that the cross-section of TLs should be much less than the minimum wavelength.

Many studies modified the TL model to bring it closer to the real situation. Guerrieri, Rachidi, and Sunde investigate the influence of frequency-dependent imperfect ground<sup>[60][53][61]</sup>, Li investigates the influence of sag on the overhead TLs<sup>[63]</sup>, Nucci investigates the influence of corona<sup>[64]</sup>. For the transient response at the terminal of the TLs, imperfect ground and corona will enhance the induced current, and the sag will decrease the induced current.

The TL method has high efficiency in solving the transient response. Although the assumption of  $h \ll \lambda$  may be too strict to be satisfied, the results are accurate as long as most of the spectrum of the electrical signal in the frequency domain is low than  $c/2(h + \delta_\infty)$ , where  $\delta_\infty = 2/\sigma_g(\epsilon_g/\mu_0)^{1/2}$  is determined by the electronic parameter of imperfect ground<sup>[65]</sup>. Considering the uncertainty of the model parameters, the further promotion of the accuracy of results is not the goal of this dissertation, it is more significant to reveal the essential mechanism and influence rules of the incident field coupling, and to quantify the uncertainty of induced response and obtain its statistical characteristics with the reasonable TL models.

Frequency domain methods including frequency-domain BLT (Baum, Liu, Tesche) equation<sup>[69]</sup>, chain parameter matrix<sup>[82]</sup>, frequency-domain distributed analytical representation and iterative technique (DARIT)<sup>[68]</sup>, time-domain methods including time domain BLT equation, finite-difference time-domain (FDTD) method<sup>[66]</sup>, delay extraction-based passive compact macromodeling algorithm (DEPACT)<sup>[66]</sup>, macromodels combine with commercial circuit software<sup>[74]</sup>, et al are proposed to solve the field-to-line coupling. The



terminal loads of the TLs in the power system are complex, including nonlinear devices, such as transient voltage surge suppressors including metal-oxide surge arrester (MOA) along the power lines and transient voltage suppressors in secondary systems, which is important and should be considered in the simulation of coupling response of TED.

To calculate the coupling responses on nonlinear terminal loads, time-domain methods are necessary. Developing efficient macromodels for TLs is a popular strategy with the advantages: (1) in the analysis of TLs with complex loads integrated in the commercial circuit solvers, (2) in the statistical analysis of TLs with uncertain variables<sup>[66]-[75]</sup>. In this dissertation, the macromodel is adopted as an appropriate and valid tool to study the deterministic responses of TLs with terminal linear or nonlinear equipment excited by TED.

### 1.2.3 Study about uncertainty quantification of the computational model

Uncertainty quantification of computational modeling is the process of determining the effect of input uncertainties on the output of interest. The uncertainty can be divided into two kinds<sup>[78][79]</sup>.

The aleatory uncertainties, or objective uncertainties, data uncertainties, irreducible uncertainties, and per-measurement uncertainties, are usually introduced in the processing of data, such as the measurement to obtain the data or the estimation from data, etc. The equipment failure probability obtained by experiment is usually with aleatory uncertainties. When the data is sufficient, the failure probability is usually presented by the inherent probability distribution of the threshold. When the data size is small, the sampling variability and estimation errors are negligible, probability distribution and tolerance bounds with certain confidence levels can be used to describe the probability distribution of the threshold.

The epistemic uncertainties, or model uncertainties, reducible uncertainties, and parameter uncertainties, are caused by the unknown or unsure variables in the model. There may be many different groups of parameters to interpret the variables, but it is hard to tell which is the best one or the correct one. The uncertainties in the TED-to-line coupling responses are epistemic uncertainties, which are caused by the uncertain parameters in computational modeling. If all the parameters are known without uncertainties, the responses can be determined by the deterministic models. It is assumed that there are no aleatory uncertainties in the theoretical study part. Therefore, the uncertainties of responses are quantified by uncertainty quantification of the computational modeling with uncertain variables. The statistical results are of great interest to the researcher, such as the first and second statistical moment (mean value and variation interval), as well as the range and distribution of output quantities, such as the probability density distribution (PDF) and cumulative probability density distribution (CDF). Although few studies are focusing on the uncertainty quantification of TED-to-line coupling, studies for uncertainty quantification in other fields can be used for reference.

MC is one of the most traditional statistical methods and is widely used in the uncertainty quantification of HEMP and TL problems. MC is a non-intrusive uncertainty quantification method with a low convergence speed of  $1/N$ .  $N$  refers to the number of samples. Accuracy statistical results usually require a large number of samples. In 2002, Ianoz first introduced the

MC into the probability analysis of field-couple-to-line, taking the azimuth angle, polarization angle, and elevation angle of the incident field as random variables<sup>[83]</sup>. The probability distributions of the induced voltage and current amplitude were included in the IEC standard<sup>[187]</sup>. Subsequently, MC was commonly applied to the probability studies of the induced response on conductors excited by HEMP in important systematic research of the department of energy and electric power research institute. A stochastic simulation framework is proposed to analyze the failure mode when the power system is excited by HEMP<sup>[24]</sup>. MC method was utilized to generate HEMP sources from the IEC standard, according to the observer on the surface of the earth relative to the blast. The coupled voltage on the power lines was calculated in each Monte Carlo replication, which has been already proved to be unreasonable<sup>[23]</sup>.

The stochastic reduce order method (SROM) is an optimized MC method. In 2017, Fei introduced the SROM into the uncertainty analysis of field-couple-to-line, the samples obtained by MC are optimized by the subset of samples with minimum Euclidean distance sampling<sup>[85][86]</sup>. The probability density distribution of the original problem is represented by using the probability results of the optimal subset. However, for the nonlinear problem with large variance and poor smoothness, it has low convergence speed.

Recently, instead of considering directly the random output of a deterministic model, the stochastic model is proposed, in order to consider the resultant random process of interest<sup>[87]</sup>. Which embeds the stochastic properties into the equations governing the physical process. The efficiency may be greatly improved when using the stochastic model to study the uncertainty properties, since it is no need for the large number of full computations.

The polynomial chaos expansion method (PCE) has developed rapidly to build the stochastic model with a linear combination of orthogonal polynomials. PCE has been applied in the uncertainty quantification of TLs problem<sup>[88]-[100]</sup>. PCE has a small error and high computational efficiency for uncertainty quantification with few variables. When there are many uncertain parameters of both TLs and radiation fields that need to be considered at the same time, PCE faces the problem of “dimensional curse”. The number of polynomial chaotic expansion terms with multiple parameters and the number of configuration points required to calculate polynomial parameters increase sharply with the increase of parameter dimension.

In order to solve the dimensional curse in uncertainty quantification with complex physical processes and numerous variables, there are three kinds of approaches.

The first way is to optimize the high-dimensional PCE. Larbi introduced the least square regression method to replace the projection method, and the PCE can be regressed directly from a small number of data<sup>[98]</sup>. Zhang introduced the tensor recovery method based on quadrature integration. The high-dimensional complete tensor used for integration is obtained through tensor recovery from a very small set of data<sup>[102][103]</sup>. And other complementary strategies to realize the sparsity of the PCE in high dimensions are proposed, such as the norm hyperbolic truncation method, least angle regression, orthogonal matching pursuit, etc<sup>[178]</sup>.

The second way is to construct the nonparametric surrogate models by the non-intrusive uncertainty quantification method. Artificial neural network, Gaussian response surface

method, and support vector machine (SVM) are widely-used nonparametric surrogate model methods. Trincherò introduced SVM to the uncertainty quantification of multiconductor TLs<sup>[104]</sup>.

Table 1-1 Comparison of state-of-the-art stochastic model methods

| Method                           |                             | Advantages                        | Disadvantages                                      | Scope of problem                  |
|----------------------------------|-----------------------------|-----------------------------------|--|-----------------------------------|
| Spare PCE                        | Intrusive/<br>Non-intrusive | High efficiency                   | Process of sparsity may require repeated solution  | High-dimensional variables        |
| Stochastic collection (SC)       | Non-intrusive               | High efficiency                   | Slow convergence for high dimensional variables    | High-dimensional variables        |
| Tensor recovery PCE              | Non-intrusive               | Very few samples are needed       | Difficult to execute, poor robustness              | High-dimensional variables        |
| Gaussian response surface method | Non-intrusive               | High efficiency                   | may lead to over fitting                           | High-dimensional variables.       |
| Support vector machine (SVM)     | Non-intrusive               | High efficiency, high convergence | Difficult to deal with unsmooth objection function | problem with no analytic solution |
| Hierarchical stochastic model    | Intrusive/<br>Non-intrusive | Less variables for each model     | Difficult to deal with arbitrary related variables | High-dimensional variables        |

The third way is to split the physical problems and therefore simplify the mathematical problem of uncertainty quantification. A hierarchical stochastic model can be built if the physical problem can be divided into several independent simulations<sup>[170][171]</sup>. The outputs of the former stage simulation with uncertainties are used as inputs for the next stage simulation, component-level (lower-level) uncertainty parameters are represented by equipment-level (higher-level) uncertainties with a decrease in the number of parameters. However, the parameters that are transferred between the multi-stage uncertainty quantification models are usually correlated. The uncertainty quantification with correlated inputs is so far not fully addressed by PCE. One possible solution to the problem is to change the correlate variables into independent variables by using orthogonal transformation or expansion, but cannot eliminate the high-order or nonlinear correlations for the variables<sup>[87][172]</sup>. Rosenblatt transform and Nataf’s transform are useful to transfer the correlated variables into independent Gaussian variables, but require the conditional PDF, which is hard to obtain<sup>[173][174]</sup>. The copula and vine copula method is recently developed to transfer the correlated multivariates into independent ones by expressing the joint probability distributions in terms of their marginal distributions and copulas (or vines) from data. But this method is so far limited to variables following parametric distribution<sup>[175][176]</sup>. In addition, when the inputs are high-dimensional variables, or when many parametric families of pair copulas are considered for the vine construction, this approach may become computationally prohibitive.

In general, the uncertainty quantification of coupling responses caused by TED, including the uncertainty of the TED and lines, is a problem with complex physical processes and numerous variables. The studies based on MC are low efficiency, and the time-consuming of the MC method limits further investigation. Different stochastic models should be established for deterministic computational models with and without analytical expression.

### 1.3 Major research content and organization of the dissertation

The major research content of this dissertation is to study the uncertainty quantification of the coupling responses on the TLs under transient electromagnetic disturbances. The main research work includes the deterministic and stochastic models of the field and TLs excited by fields, a hierarchical framework linking them together considering the arbitrary distribution correlated uncertainty variables that are transferred between different stochastic models, vulnerability assessment method of equipment connected with lines based on the statistical results of the coupling responses and experiment data with uncertainty. The organization of the dissertation is shown in Figure 1-1.

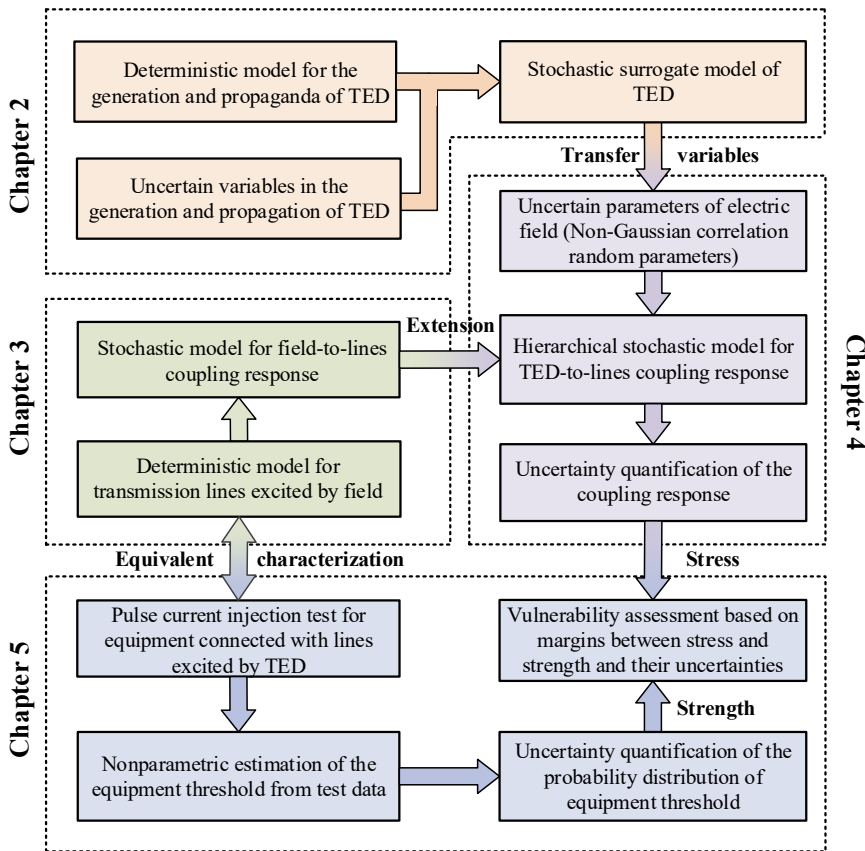


Figure 1-1 Major research content of this dissertation

In Chapter 2, the HEMP is studied as an example kind of TED. The deterministic model and stochastic model of EMP are developed. The deterministic model of the generation and propagation of HEMP and the stochastic model for the spatial distribution of HEMP on the ground is established. An iterative self-consistent simulation scheme is proposed based on the classical physical model, including the scattering of gamma photons and electrons, the behavior of electrons, and electromagnetic fields. The proposed iterative simulation scheme can provide efficient deterministic numerical results for HEMP in a wide area. The physical-based stochastic surrogate model is proposed based on a simplified dipole and quadrupole model and can describe the spatial distribution characteristics and stochastic characteristics of the HEMP incident to the ground surface. The physical-based stochastic model is fitted by the results obtained by the deterministic simulation.

In Chapter 3, the deterministic model and stochastic model for the TLs excited by external fields are presented. The macromodel of lines with nonlinear load excited by the external field is represented based on the analogy behavior modeling, to provide the deterministic solution respectively. The dynamic nonlinear model is established to correct the behavior of MOA connected with lines, when the amplitude and rise time of the induced current vary in a large range. Stochastic models for the TLs excited by external fields are established based on the PCE, for the situation with random lines, the situation with random fields, and the situation with uncertainty for both fields, lines, and ground. The coefficient of the stochastic models is solved by the deterministic macromodel.

In Chapter 4, to combine the stochastic model of HEMP and the stochastic model of field-to-line coupling, a hierarchical stochastic model is proposed. To solve the problem of transferring arbitrary distribution correlated multidimensional variables in the hierarchical stochastic models, such as the uncertainty quantification of field-to-line coupling using the statistical results of the HEMP as the inputs, the proposed hierarchical stochastic model is based on the Kernel distribution estimation method (KDE), which can accurately estimate the joint probability distribution and construct orthogonal polynomial basic functions for the arbitrary correlated variables. The hierarchical stochastic models have the advantage of high efficiency and fast convergence speed, which is suitable for the uncertainty quantification of the problem that can be divided into several independent physical processes. The statistical results of the uncertainty quantification can be used for the vulnerability assessment of the equipment connected with the lines.

In Chapter 5, a distribution-free quantification of margins method (QMU) is proposed for the equipment vulnerability assessment based on the uncertainty quantification of the coupling responses on the TLs, which can be regarded as stress for the equipment under TED with epistemic uncertainties. The strength of the equipment is obtained by the pulse current injection (PCI) test, which is derived to be equivalent to the coupling responses caused by the TED by adjustment of the parameter of the experiment platform. Two nonparametric estimation methods are proposed for effect data and binary state data, respectively, to estimate the unknown inherent probability distribution of equipment strength and the aleatory uncertainty introduced by the sampling variability and estimation errors from small samples from the test. Since both the stress and strength with uncertainties are rarely from typical distribution, the proposed QMU method based on a proposed quantile-based metric does not rely on the preset distribution type, it can provide reasonable evaluations with confidence levels.

The last chapter presents the summary and future works.

## 2 Deterministic model and stochastic model for the TED

The parameters and the time-domain waveform of the incident field are of great importance for the coupling response simulation, the potential distribution of the incident field parameters should be quantified. Taking HEMP as an example TED, the spatial distribution of HEMP is no uniform and may vary in a wide range affected by the position, height, yield of the source and geomagnetic field, air density and other environmental parameters. In order to study the reasonable variation and potential distribution of HEMP with the consideration of uncertain factors in the complex physical process, the efficient deterministic model for the generation and propagation of the HEMP and the stochastic model for the HEMP on the ground with spatial characteristic are developed in this chapter.

### 2.1 Classical physical model for the generation and propagation of the HEMP

The generation and propagation of high-altitude electromagnetic pulse have been widely studied and concluded to be a self-consistent process between electrons and the electromagnetic (EM) fields<sup>[32]-[37]</sup>. The simulation depends on the modeling of the high-energy Compton electrons produced by prompt gamma rays and the modeling of the low-energy secondary electrons produced by Compton electrons. Compton electrons are deflected in the geomagnetic field and generate electromagnetic radiation. Secondary electrons attenuate the generation and propagation of HEMP. Meanwhile, Compton electrons and secondary electrons are affected by the produced electromagnetic (EM) fields. The self-consistent effect mainly refers to the interactions between the Compton electrons and the EM fields. It should be noted that the secondary electron is also related to the EM fields in a different way<sup>[123]</sup>. The physical mechanism of generation and propagation of HEMP is shown in Figure 2-1.

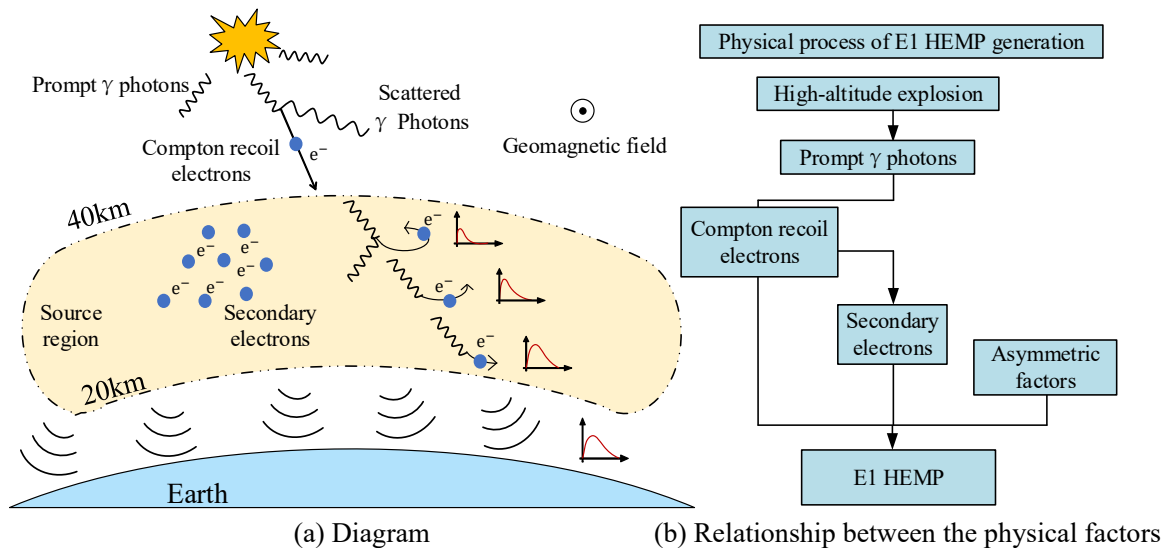


Figure 2-1 Physical mechanism of generation and propagation of early-time HEMP

The full computational HEMP model has been developed for several decades including the simulation of the Compton electrons and the secondary electrons and the solution of the EM fields. Here is a brief overview.

1) Compton current made up of Compton electrons

Compton electrons, also called primary electrons, are produced continuously by prompt gamma rays. The Compton current is obtained by integrating electrons

$$\mathbf{J}(t, r) = \sum_W -eW_i \int_{t-t_{\text{life}}}^t f_c(t'-r'/c) \mathbf{v}_p(t-t') / \eta(t-t') dt' \quad (2-1)$$

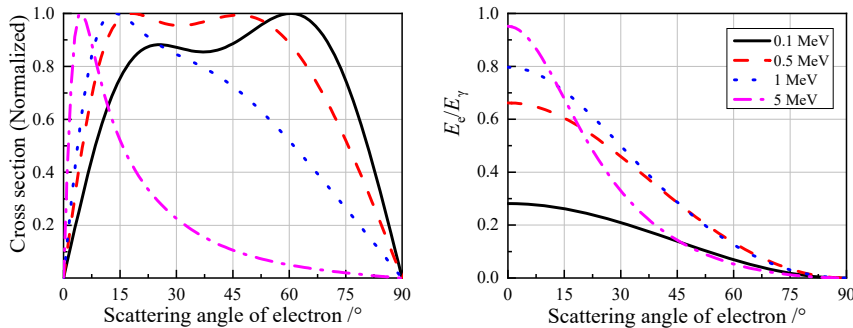
where  $f_c$  — temporal profile of the prompt gamma rays;  $\mathbf{v}_p(t-t')$  — velocity of the Compton electrons generated at distance  $r'$  and time  $t'$ ;  $\eta$  — obliquity factor;  $t_{\text{life}}$  — time before the average velocity of the Compton electrons decrease to zero;  $W_i$  — the weights of the Compton electrons with velocity  $\mathbf{v}_p$ , which are determined by the Compton scattering. The weights of the Compton electrons are calculated by the differential of the Compton cross-section along the scattering angle of recoil electrons, which is derived from Klein-Nishina formula:

$$d\sigma_{\text{KN}} = \frac{2\pi r_0^2}{2} \left( \frac{1}{1+\alpha_c(1-\cos\phi_c)} \right)^2 \left( \frac{1}{1+\alpha_c(1-\cos\phi_c)} + \alpha_c(1-\cos\phi_c) - 1 + \cos^2\phi_c \right) \sin\phi_c d\phi_c \quad (2-2)$$

where,  $\alpha_c = E_\gamma / (m_0 c^2)$ ;  $r_0$  — classical radius of the electron;  $\phi_c$  — the scattering angle of scattering gamma photon, which can be transferred to the scattering angle of the Compton electron  $\theta_c$ :

$$\cot\theta_c = (1 + \alpha_c) \tan(\phi_c / 2) \quad (2-3)$$

The probability distribution of the scattering Compton electron angle and relevant electron energy are obtained by the differential forms of the K-N formula and shown in Figure 2-2. The total energy of scattering photon and scattering electrons is equal to the energy of the incident photon. When the scattering photon energy is larger than the Compton scattering threshold, the Compton scattering photon energy may produce scattering electrons continually until the energy is less than 0.1 MeV.



(a) Cross section of scattering angle of electron      (b) Energy versus scattering angle of electron

Figure 2-2 Scattering angle and energy of scattering electrons angle

The initial velocity of scattering electrons is obtained from the gamma photon:

$$v_p = c\sqrt{1 - (m_e c^2 / (E_e + m_e c^2))^2} \quad (2-4)$$

where  $m_e$ — electron mass;  $E_e$  — invariant mass of the electron.

The retarded time  $\tau = t - r/c$  system is introduced to solve this problem. An auxiliary parameter  $\tau' = t - t'$  is used to make the equation more concise, yielding

$$\mathbf{J}(\tau) = \sum_W -eW_i \int_0^{t_{ife}} f(\tau - \tau' + (r - r')/c) \mathbf{v}_p(\tau') / \eta(\tau') d\tau' \quad (2-5)$$

Compton electron velocity is calculated via the momentum equation<sup>[37]</sup>

$$m_e \gamma \frac{d\mathbf{v}_p}{d\tau} = -e\mathbf{E} - e\mathbf{v}_p \times (\mathbf{B}_e + \mathbf{B}) - g_E(W) \frac{\mathbf{v}_p}{|\mathbf{v}_p|} \quad (2-6)$$

where  $\mathbf{E}$ ,  $\mathbf{B}$  — generated electromagnetic fields;  $\mathbf{B}_e$  — geomagnetic field;  $\gamma = \sqrt{1 - (v_0/c)^2}$  — relative factor;  $W$  — the kinetic energy of the electron;  $g_E(W)$  — the energy loss when the electron moving through air and is given by Bethe's formula<sup>[36]</sup>. The obliquity factor  $\eta$  represents the multiple scattering effects of Compton electrons from the interactions with air<sup>[115][116]</sup>.

$$\frac{d\eta}{d\tau} = f_E(W) \mathbf{v}_p + e(\eta^2 - 1) \frac{\mathbf{E} \cdot \mathbf{v}_p}{m_e v_p^2} \quad (2-7)$$

where  $f_E(W)$  and  $g_E(W)$  are given by the underlying collisional process. The second term arises due to the component of the electric field parallel to the momentum of the particle.

As electrons fly at a high speed, they are deflected due to the effects of the geomagnetic field  $\mathbf{B}_e$  and generated magnetic field. If Equation (2-6) only considers the static geomagnetic field, it is called a non-self-consistent simulation. Otherwise, it is a self-consistent simulation.

## 2) Air conductivity affected by secondary electrons

Compton electrons give birth to lots of low-energy secondary electrons during the collisional process. The nonequilibrium electron swarm model has been proposed to model the secondary electrons<sup>[116]-[122]</sup>. The density  $n_{se}$ , velocity  $\mathbf{v}_s$ , and swarm characteristic energy  $U_e$  of the secondary electrons are described by a set of differential equations with respect to the electric field. It implicitly accounts for the time evolution of the conduction electron energy distribution.

$$\begin{aligned} \frac{dn_{se}}{d\tau} &= S - k_1(U_e)n_{se} - k_2(U_e)n_+n_{se} \\ \frac{dn_+}{d\tau} &= k_1(U_e)n_{se} - k_3(U_e)(n_+ - n_{se})n_{se} \\ m_e \frac{d\mathbf{v}_s}{d\tau} &= -e\mathbf{E} - v_m(U_e)\mathbf{v}_s - \mathbf{v}_s \frac{S}{n_{se}} \\ \frac{dU_e}{d\tau} &= -\frac{2}{3} \frac{e}{m_e} \mathbf{v}_s \cdot \mathbf{E} - \left( \frac{2}{3} v_w(U_e) - \frac{S}{n_{se}} \right) \cdot (U_e(t) - U_{e0}) \end{aligned} \quad (2-8)$$



where  $n_{se}, n_+$  — the number density of the secondary electrons and positive ions;  $\nu_m$  — the momentum exchange collision frequency;  $\nu_w$  — the energy exchange collision frequency;  $U_e$  — the swarm characteristic energy;  $k_1 \sim k_3$  — the attachment and recombination coefficients.  $S$  — the generation rate of the secondary electrons and is determined by the kinetic energy loss of Compton electrons, as

$$S(\tau) = \sum_W -eW_i \int_0^{t_{life}} W_i f_C(\tau - \tau' + \frac{r-r'}{c}) g_E(W) d\tau' \quad (2-9)$$

The time for the secondary electrons to reach equilibrium decreases with the increase of air pressure. When the air pressure is high enough, the time before equilibrium is short compared with the rise time of HEMP. When simulating the HEMP downward to the ground, the source region of interest is about tens of kilometers in height, where the time to equilibrium is short enough to be ignored and the equilibrium assumption is acceptable. The equilibrium model is a widely adopted simplified model for the secondary electrons<sup>[123]-[125]</sup>. The coefficients dependent on  $U_e$  in (2-8) are approximated as constants. The air conductivity in the equilibrium model is calculated as:

$$\sigma = e (n_{se} \mu_e(\mathbf{E}) + (n_+ + n_-) \mu_i(\mathbf{E})) \quad (2-10)$$

where  $\mu_e$  — the electrons mobility of secondary electrons;  $\mu_i$  — the ion mobility.

In the simulation of early-time HEMP, the ionic conductivity component can generally be ignored, which will only dominate very late-time conductivity considering the attachment and recombination of the electron<sup>[35]</sup>. Electron mobility  $\mu_e$  was fitted as a function of the local electric field<sup>[126][127]</sup>. When the electric field is small, the mobility can be approximated as constants. With the increase of the electric field, the mobility of the secondary electrons decreases.

### 3) EM Fields based on HFA

The international system of units (MKS) is applied here. All equations of Compton current, air conductivity, and electromagnetic fields are solved in the spherical coordinate system, and the origin point is set as the explosion point. For consistency of the investigation of the electrons, the simulation of EM field is carried out in the retarded time system with the change of the calculator:

$$\frac{\partial}{\partial t} \rightarrow \frac{\partial}{\partial \tau}, \nabla \rightarrow \nabla - \frac{1}{c} \cdot \frac{\partial}{\partial \tau} \quad (2-11)$$

Maxwell's curl equations in the retarded time system is changed as:

$$\begin{aligned} -\nabla^2 \mathbf{E} + \frac{1}{c\epsilon_0} (\nabla \cdot \mathbf{J}) \mathbf{e}_r + \frac{1}{\epsilon_0} \nabla \rho_0 + \frac{\partial}{\partial \tau} \left[ \frac{2}{c} \frac{1}{r} \frac{\partial}{\partial r} (\mathbf{rE}) + \mu_0 (\mathbf{J} - \mathbf{J}_0 \mathbf{e}_r) \right] &= 0 \\ -\nabla^2 \mathbf{B} + \mu_0 \nabla \times \mathbf{J} + \frac{\partial}{\partial \tau} \left[ \frac{2}{c} \frac{1}{r} \frac{\partial}{\partial r} (\mathbf{rB}) \right] + \frac{\mu_0}{c} \frac{\partial}{\partial \tau} (\mathbf{J}_\phi \mathbf{e}_\theta - \mathbf{J}_\theta \mathbf{e}_\phi) &= 0 \end{aligned} \quad (2-12)$$

The equations of three components of the electric field are written as:

$$\begin{aligned}
-(\nabla^2 \mathbf{E})_\theta + \frac{1}{\varepsilon_0} (\nabla \rho_0)_\theta + \frac{\partial}{\partial \tau} \left[ \frac{2}{c} \frac{1}{r} \frac{\partial}{\partial r} (\mathbf{rE}_\theta) + \mu_0 \mathbf{J}_\theta \right] &= 0 \\
-(\nabla^2 \mathbf{E})_\varphi + \frac{1}{\varepsilon_0} (\nabla \rho_0)_\varphi + \frac{\partial}{\partial \tau} \left[ \frac{2}{c} \frac{1}{r} \frac{\partial}{\partial r} (\mathbf{rE}_\varphi) + \mu_0 \mathbf{J}_\varphi \right] &= 0 \\
-(\nabla^2 \mathbf{E})_r + \frac{1}{c\varepsilon_0} (\nabla \cdot \mathbf{J})_r + \frac{1}{\varepsilon_0} (\nabla \rho_0)_r + \frac{\partial}{\partial \tau} \left[ \frac{2}{c} \frac{1}{r} \frac{\partial}{\partial r} (\mathbf{rE}_r) \right] &= 0
\end{aligned} \tag{2-13}$$

Based on the HFA, which assumed that the signal changes with time is much more greater than it changes with space,  $\partial \mathbf{J} / \partial r \ll \partial \mathbf{J} / \partial \tau$ , a group of classical functions that describes the EM fields is obtained

$$\begin{aligned}
\frac{\partial \mathbf{rE}_\theta}{\partial r} &= -\frac{c\mu_0}{2} \mathbf{rJ}_\theta - \frac{c\mu_0}{2} \sigma \mathbf{rE}_\theta, & \frac{\partial \mathbf{rE}_\varphi}{\partial r} &= -\frac{c\mu_0}{2} \mathbf{rJ}_\varphi - \frac{c\mu_0}{2} \sigma \mathbf{rE}_\varphi \\
\frac{\partial \mathbf{E}_r}{\partial \tau} &= -c^2 \mu_0 \mathbf{J}_r - c^2 \mu_0 \sigma \mathbf{E}_r
\end{aligned} \tag{2-14}$$

The electric field and the Compton current are divided into transverse and radial components. The transverse electric field component is integrated along with the radial distance while the radial component is integrated along time. The magnetic field equations can be obtained as well:

$$\begin{aligned}
\frac{\partial \mathbf{rB}_\theta}{\partial r} &= -\frac{1}{c} \frac{\partial \mathbf{rE}_\varphi}{\partial r}, & \frac{\partial \mathbf{rB}_\varphi}{\partial r} &= \frac{1}{c} \frac{\partial \mathbf{rE}_\theta}{\partial r} \\
\frac{\partial \mathbf{B}_r}{\partial \tau} &= 0
\end{aligned} \tag{2-15}$$

The EM fields are generated by Compton current and attenuated by air conductivity. The limitation of the secondary electrons to the generated fields is called the saturation effect.

#### 4) Self-consistent relationship between parameters

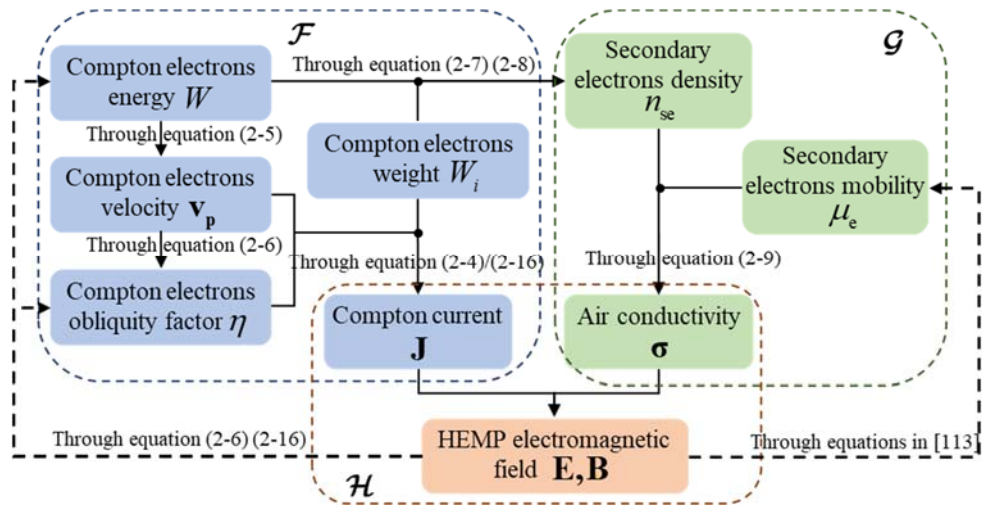


Figure 2-3 Relationship between physical parameters (The equation before and after the slash are used in the case with and without the consideration of self-consistency, respectively.)

The EM fields are generated by the Compton current and affect the Compton electrons

in turn. They remove energy from the Compton electrons. The EM fields occur not only in the electron momentum Equation (2-6) but also in the differential equation (2-7) of the obliquity factor.

The interaction between the secondary electrons and the electric field is simulated in a different way from the self-consistent effect. The build-up of air conductivity limits the growth of the fields. And the density and mobility of the secondary electrons are affected by the electric field.

Key physical parameters and their interaction relationship in the HEMP simulation model are illustrated in Figure 2-3. In addition, when the self-consistent effect represented by the arrow with dashed lines is ignored, it degenerates into a non-self-consistent HEMP simulation.

## 2.2 Efficient iterative and self-consistent simulation scheme of the HEMP

The classical photon-electron-electromagnetic fields model processes with self-consistent effect between electrons and electromagnetic fields is introduced in Section 2.1. An iterative full computation scheme is proposed in this section for the numerical simulation of the HEMP incident to the ground in a large area.

### 2.2.1 Iterative algorithm for HEMP with consideration of self-consistent effect

Consideration of the self-consistent effect may complicate the HEMP simulation, therefore it was not considered worth the time penalty in the early days. With the development of computing technology, the self-consistent effect is appreciated once computer codes were available. EXEMP is a self-consistent developed by Leuthäuser, which achieved the self-consistent simulation without iteration method. The Compton current and air conductivity were calculated using the EM fields of neighbor spatial finite elements. EM fields at distance  $r$  were calculated based on Equation (2-13) and Equation (2-15), which were then considered as the external fields for the motion of electrons at distance  $r + \Delta r$ . The computation procedure of the physical parameters is shown in Figure 2-3.

The spatial step should be sufficiently small to ensure the accuracy of self-consistency simulation, which increases the computation time. Reference [34] claimed that, when the simulation was executed considering the self-consistent effect, there was a significant increase in the CPU time compared to the non-self-consistency cases.

To overcome the disadvantage of time-consuming of self-consistency simulation, we applied an iterative scheme to simulate HEMP with the consideration of self-consistency. In this method, first, the electrons and the EM fields were solved separately, assuming the Compton electrons were not affected by the generated EM fields. Then, the missing coupling self-consistent interactions were corrected by the iterative process. The decoupled iteration method reduces the time complexity of the simulation and does not require small spatial steps compared to EXEMP method. Moreover, parallelization of the code can further improve efficiency.

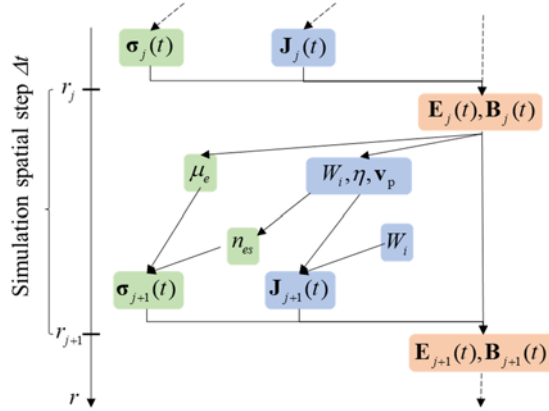


Figure 2-4 Flow chart of the computation order of the HEMP physical parameters with the consideration of self-consistency in the EXEMP method

The Compton electrons were calculated as “test particles” at first, which means the EM fields produced by the electrons were ignored during electron simulations. A non-self-consistent form of Equation (2-6) was utilized, in which only the geomagnetic field was considered.

It should be noted that, when self-consistency was taken into consideration, the force EM fields exerted on the Compton electrons varied with both time and position. The Compton electrons generated at different times face different time-domain waveforms of EM fields. Therefore, the velocity of electrons generated at different moments should be simulated differently.

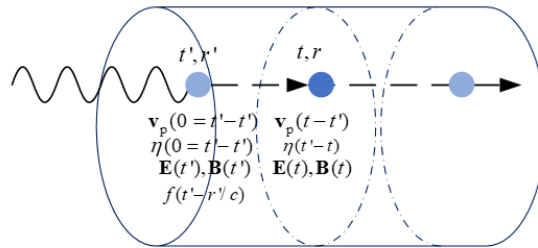


Figure 2-5 Schematic diagram of Compton recoil electrons

An auxiliary variable  $u$  was thus introduced to describe the generation moment of electrons, described as

$$u = \tau - \tau' + (r - r') / c \quad (2-16)$$

The momentum equation in a retarded time system was rewritten as

$$m_e \gamma \frac{d\mathbf{v}_p(\tau')}{d\tau} = -e\mathbf{E}(u + \tau' - (r - r') / c) - e\mathbf{v}_p(\tau') \times (\mathbf{B}_e + \mathbf{B}(u + \tau' - (r - r') / c)) - g(W) \frac{\mathbf{v}_p}{|\mathbf{v}_p|} \quad (2-17)$$

where

$$(r - r') / c = \int_0^{\tau'} v_{pr}(\tau'') d\tau''$$

Therefore, the integral equation in Equation (2-5) is altered as

$$\mathbf{J}(\tau) = \sum_w -eW_i \int_0^\tau f(u) \frac{\mathbf{v}_p(\tau')}{\eta(\tau')} \frac{du}{1 - v_{p,r}(\tau')/c} \quad (2-18)$$

where  $v_{p,r}$  — the radial component velocity of the Compton electrons. The Compton currents with the consideration of the EM fields can be simulated, and the equation has nothing to do with the spatial variation of the electromagnetic fields.

The simulation for the Compton current was cast in a compact operator as

$$\mathbf{J} = \mathcal{F}(\mathbf{E}, \mathbf{B}) \quad (2-19)$$

where operator  $\mathcal{F}$  represents the above algebraic operations in Equation (2-18) for each spatial finite element in the calculation area. The Compton current vectors in the time domain were obtained with the local EM fields as inputs.

As analyzed in Section 2.1, the secondary electrons were simulated as a consequence of Compton electrons. The density of the secondary electrons was simulated from the dynamic process including generation and vanishing. When the interaction between EM fields and electrons was taken into consideration in the later iterations, the equilibrium model was used to simulate the air conductivity. The calculation of air conductivity was cast in a compact operator  $\mathcal{G}$ .

The differential equation of electric field in Equation (2-14) was solved based on the finite-difference expression along the radial direction for the transverse component  $\mathbf{E}_t$  and along the time direction for the radial component  $\mathbf{E}_r$ , as

$$E_\phi(j+1, n) = \frac{(4 - c\mu_0\Delta r\sigma(j+1/2, n) - 2\Delta r/r_{j+1/2})E_\phi(j, n) - 4c\mu_0\Delta rJ_\phi(j+1/2, n)}{4 + c\mu_0\Delta r\sigma(j+1/2, n) + 2\Delta r/r_{j+1/2}} \quad (2-20)$$

$$E_\theta(j+1, n) = \frac{(4 - c\mu_0\Delta r\sigma(j+1/2, n) - 2\Delta r/r_{j+1/2})E_\theta(j, n) - 4c\mu_0\Delta rJ_\theta(j+1/2, n)}{4 + c\mu_0\Delta r\sigma(j+1/2, n) + 2\Delta r/r_{j+1/2}}$$

$$E_r(j, n+1) = \frac{2 - \Delta tc^2\mu_0\sigma(j, n+1/2)}{2 + \Delta tc^2\mu_0\sigma(j, n+1/2)} E_r(j, n) - \frac{2\Delta tc^2\mu_0}{2 + \Delta tc^2\mu_0\sigma(j, n+1/2)} J_r(j, n+1/2) \quad (2-21)$$

where  $n$  and  $j$  refer to time and distance indices, respectively. It was the same for the solution of the magnetic field. The solution of the EM fields differential Equation (2-14) and (2-15) was cast in a compact operator  $\mathcal{H}$ .

Collecting these functions, we may predict the HEMP with the following equation system

$$\begin{cases} \mathbf{J} = \mathcal{F}(\mathbf{E}, \mathbf{B}) \\ \boldsymbol{\sigma} = \mathcal{G}(\mathbf{J}, \mathbf{E}) \\ \mathbf{E}, \mathbf{B} = \mathcal{H}(\mathbf{J}, \boldsymbol{\sigma}) \end{cases} \quad (2-22)$$

It should be noted that the equation system only showed the relationship between the given variables and did not mean that only the variables in the bracket were required in the HEMP simulation.

The solution of this system was supposed to satisfy all three functions at the same time. Such that the self-consistent HEMP solver could be achieved by the iterative scheme. A fixed-

point iterative scheme was built to solve the HEMP equation system. The evaluation of the Compton current, air conductivity, and EM fields were carried out sequentially, as

$$\begin{cases} \mathbf{J}^{(k)} = \mathcal{F}(\mathbf{E}^{(k)}, \mathbf{B}^{(k)}) \\ \boldsymbol{\sigma}^{(k)} = \mathcal{G}(\mathbf{J}^{(k)}, \mathbf{E}^{(k)}) \\ \mathbf{E}^{(k+1)}, \mathbf{B}^{(k+1)} = \mathcal{H}(\mathbf{J}^{(k)}, \boldsymbol{\sigma}^{(k)}) \end{cases}, k = 1, 2, \dots, K \quad (2-23)$$

with  $k$  referring to the iteration times. The iterative scheme carried out a sequence of calculations until the results converged to the correct solution.

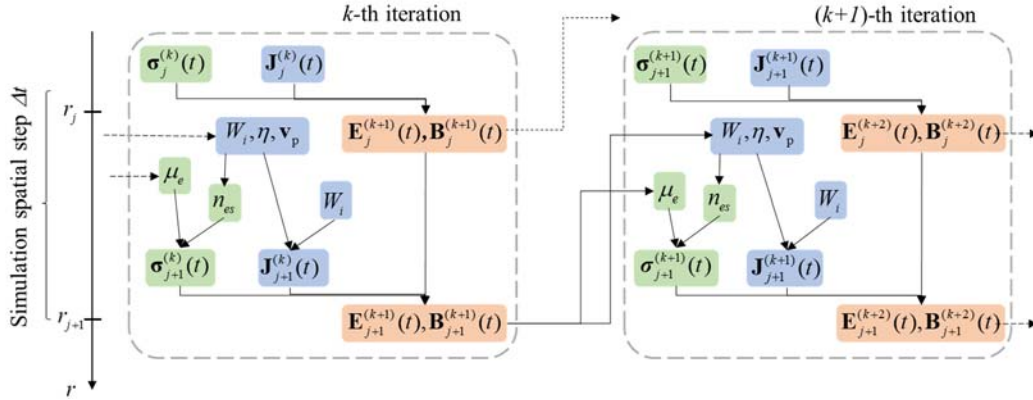


Figure 2-6 Flow chart of the computation order of the HEMP physical parameters with the consideration of self-consistency in the proposed iteration scheme

The major steps of the iterative scheme are listed as follows:

- (a) In the first iteration, self-consistency was ignored. With only the geomagnetic field considered, the initial condition was given as

$$\mathbf{E}^{(1)} = \mathbf{0}, \mathbf{B}^{(1)} = \mathbf{B}_e \quad (2-24)$$

The initial density and velocity of Compton electrons and weight  $W_i$  in (2-5) were determined by the Compton scattering process between prompt gamma photons and air. The results of Compton current  $\mathbf{J}^{(1)}$  and air conductivity  $\boldsymbol{\sigma}^{(1)}$  in the time domain at each spatial step were simulated.

- (b) The EM fields  $\mathbf{E}^{(2)}$  and  $\mathbf{B}^{(2)}$  were solved by applying non-self-consistent Compton current  $\mathbf{J}^{(1)}$  and air conductivity  $\boldsymbol{\sigma}^{(1)}$ .
- (c) The iterations were continued to correct the missing interactions between electrons and EM fields. The results of the EM fields were taken into the new simulation loop as the independent fields exerted on the electrons.

The Compton current  $\mathbf{J}^{(k)}$  and air conductivity  $\boldsymbol{\sigma}^{(k)}$  were simulated. The newly generated EM fields affected both electron velocities and obliquity factors. However, the weight and initial state of Compton electrons had nothing to do with the EM fields, which was consistent with the result in the first iteration. The density of secondary electrons  $n_{es}$  was determined by kinetic energy loss and needed to be updated.

- (d) The EM fields  $\mathbf{E}^{(k+1)}$  and  $\mathbf{B}^{(k+1)}$  were solved by applying the Compton current  $\mathbf{J}^{(k)}$  and

air conductivity  $\sigma^{(k)}$ .

- (e) After the second iteration loop, the error of the EM fields was calculated for the whole simulation region between two iterations. Steps 3) and 4) were repeated until the error of the EM fields was less than a given error.

The numerical results of  $\mathbf{J}^{(k)}$ ,  $\sigma^{(k)}$ ,  $\mathbf{E}^{(k+1)}$  and  $\mathbf{B}^{(k+1)}$  of the last iteration were considered as an expected solution of the coupled equations in (2-23), and it can be regarded as a self-consistent solution for HEMP.

The computation order of the HEMP physical parameters in the iterative scheme is shown in Figure 2-6. Compared to the graphical depiction for EXEMP, the simulation of electrons between spatial finite elements was decoupled. And thanks to (2-18), the term of the field in the equation of Compton current, which is originally a function of space and time, is converted into a time-dependent variation only. The simulation of the Compton current and air conductivity can be executed independently for each spatial finite element. In addition, the parallelizable code can further improve the efficiency of the proposed iterative scheme.

### 2.2.2 Stability and convergence analysis of the iterative simulation

To achieve stability and convergence while solving partial differential equations of HEMP by the method of finite difference, the discretization of space and time should be constrained by the Courant-Friedrichs-Lewy (CFL) stability condition. The size of the time step should be less than or equal to that required for the EM wave passing through one spatial step. However, due to the application of retarded-time coordinate system, the spatial step could be enlarged and achieve stable results as well. Since the iterative scheme has no specific requirement for small spatial steps, its efficiency advantages will be realized.

Convergence analysis of the iterative algorithm was divided into two parts: the convergence of the Compton current and the convergence of air conductivity. The EM fields converged naturally as a result.

The convergence of Compton current was given qualitatively. The generated EM fields removed energy from the Compton electrons, weakened the electron velocity, and reduced the Compton current. In later iterations, when the Compton current decreased, the EM fields decreased and the weakening effect of the EM fields on electron motion also decreased, which increased the Compton current in turn. The reverse was also the same. The Compton current tended to be balanced during iterations, as the changes of EM fields and current were mutually restricted.

Air conductivity was also affected by the electric field, but there were different rules. Its convergence was shown quantitatively. For any radial Compton current, (2-10) was substituted into the second and third equation in (2-23), such that the difference of the radial electric fields between two iterations was obtained as

$$E_r^{(k+1)}(r, n) - E_r^{(k)}(r, n) = E_r^{(k+1)}(r, n-1) - E_r^{(k)}(r, n-1) - \Delta\tau c^2 \mu_0 e n_{es} (\mu(E_r^{(k)}(r, n)) \cdot E_r^{(k)}(r, n) - \mu(E_r^{(k-1)}(r, n)) \cdot E_r^{(k-1)}(r, n)) \quad (2-25)$$

Let  $\phi(x) = \mu_e(x)x$ , there is always  $\phi' < 2N_0/N$ , according to the numerical results in

Reference [116].  $N$  and  $N_0$  refer to the atmospheric density and standard atmospheric density. The inequality was obtained when  $n=1$ , which means  $t=\Delta t$ ,

$$|E_r^{(k+1)}(r,1) - E_r^{(k)}(r,1)| \leq \Delta\tau c^2 \mu_0 e n_{se} \phi'_{\max} \cdot |E_r^{(2)}(r,1) - E_r^{(1)}(r,1)| \quad (2-26)$$

By recursion, inequality was obtained as

$$E_r^{(k+1)}(r,n) - E_r^{(k)}(r,n) \leq L^{k-1} \cdot |E_r^{(2)}(r,m) - E_r^{(1)}(r,m)| \quad (2-27)$$

where

$$L = 4\Delta\tau c^2 \mu_0 e N_{\max}, \quad N_{\max} = \max(n_{se}(\tau, r) \cdot N_0 / N)$$

$$|E_r^{(2)}(r,m) - E_r^{(1)}(r,m)| = \max\{|E_r^{(2)}(r,1) - E_r^{(1)}(r,1)|, \dots, |E_r^{(2)}(r,n) - E_r^{(1)}(r,n)|\}$$

The density of secondary electrons  $n_{es}$  is affected by air density, prompt gamma yield, and many other factors. During the numerical simulation, there is  $N_{\max} < 10^{17}$  for the prompt gamma yield up to 3 kt. When  $\Delta\tau < 10^{-10}$  and  $L < 1$ , the convergence of the electric field in the iteration is guaranteed. When the value of  $N_{\max}(N_0/N)$  is larger than  $10^{17}$ , the convergence of the iterations can be ensured by reducing the size of the time step. The relationship between the transverse electric field and air conductivity can be proven in the same way.

Therefore, substituting (2-10) into both ends of the inequality, it was concluded that

$$\sigma^{(k+1)}(r,n) - \sigma^{(k)}(r,n) < L^{k-1} \cdot \max\{|\sigma^{(2)}(r,n) - \sigma^{(1)}(r,n)|\} \quad (2-28)$$

The convergence of air conductivity within the iteration was thus proven.

When the current and conductivity converged through iterations, the EM fields of HEMP converged as a consequence.

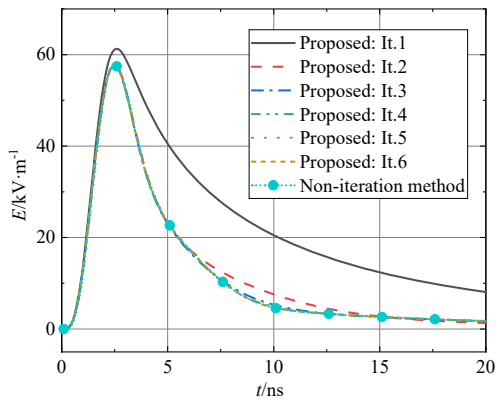
### 2.2.3 Validation of the numerical simulation of the HEMP

In the first case, the HEMP generated by a high-altitude nuclear explosion was simulated, with the burst at 100 km. The total prompt gamma yield was 3 kt, with the monoenergetic prompt gamma ray of 1.6 MeV. The value of the geomagnetic field was simplified as being uniform in space and was set to 50  $\mu\text{T}$ . The atmospheric density was described by the exponential model. The value of this case was determined with reference to previous studies<sup>[46][47]</sup>.

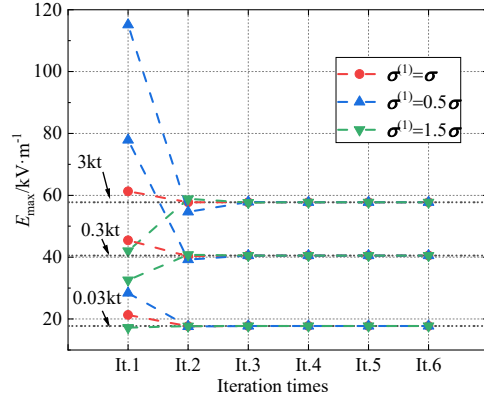
We simulated the time-domain waveforms of the total electric field on the ground, the Compton current, and the air conductivity in the source region with the consideration of self-consistency by the proposed iterative scheme and the EXEMP method. The numerical results of the electric field time-domain waveform on the earth's surface are shown in Figure 2-7 (a). The numerical results of the Compton current and air conductivity in the source region are shown in Figure 2-8.

After six iterations, the proposed iterative method is well convergent for different conditions and has good agreement with the conventional non-iteration method. The first iteration can be seen as the non-self-consistent simulation, while the results in the sixth iteration can be seen as well-solved self-consistent results.



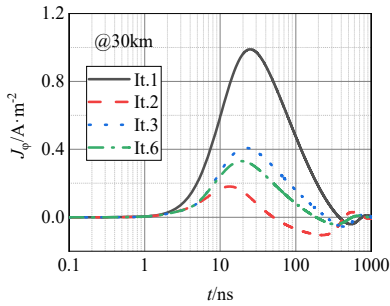


(a) Time-domain waveform

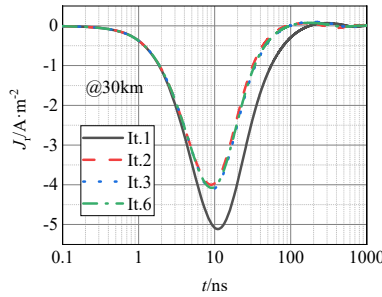


(b) Electric field amplitude in iterations with different initial conditions

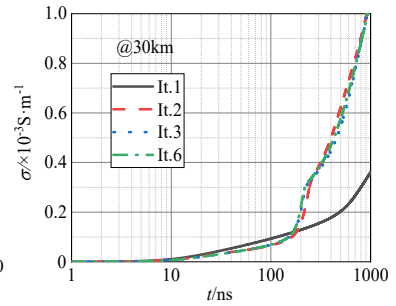
Figure 2-7 Numerical results of the electric field incident to the ground simulated by the proposed iterative scheme



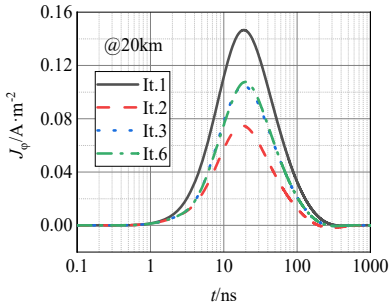
(a) Transverse Compton current at 30 km.



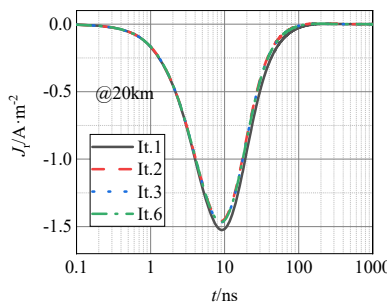
(b) Radial Compton current at 30 km.



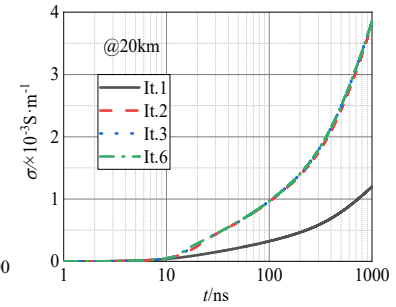
(c) Air conductivity at 30 km



(d) Transverse Compton current at 20 km



(e) Radial Compton current at 20 km



(f) Air conductivity at 20 km

Figure 2-8 Numerical results of transverse Compton current and air conductivity simulated by the proposed iterative scheme

Ignoring the self-consistent effect in simulations may lead to higher amplitude and longer duration of the electric field. Moreover, the self-consistent effect has more impact on the wave tail, since the effect of the self-consistent field on electrons accumulates over time.

We found that the peak of the electric field occurred earlier than that of the Compton current, because the fields were saturated with the existence of secondary electrons. The saturation effect also showed a nonlinear relationship between current and fields. When the self-consistent effect was taken into consideration, even the amplitude of transverse Compton current decreased by 58% and 35% at the height of 30 km and 20 km, and the amplitude of

the electric field on the ground changed by less than 7%.

To accelerate the convergence of the iterative scheme, we used a successive overrelaxation (SOR) method in the Compton current simulation. The Compton current in the  $(k+1)$ -th iteration was simulated based on SOR, as

$$\mathbf{J}^{k+1} = (1 - \omega)\mathbf{J}^k + \omega\mathcal{F}(\mathbf{E}^{k+1}, \mathbf{B}^{k+1}) \quad (2-29)$$

where  $\omega$  is the SOR relaxation factor. An appropriate value of the relaxation factor can help accelerate the convergence of the results.

Through the qualitative analysis of the abovementioned equations, the influence of the EM fields and current on each other was found to be a negative feedback process. When the current increased, the generated HEMP became stronger. Meanwhile, the stronger the EM fields were, the greater the inhibition on the movement of Compton electrons was, which reduced the Compton current. Conversely, when the current decreased, it led to decreased EM fields, which also reduced the effect of the EM fields on the current.

We can obtain the same conclusion from the numerical results shown in Figure 2-8. The Compton current in the second iteration had the smallest amplitude because of the large negative impact of the generated EM fields and lack of self-consistency limitation. In the third iteration, the current became small, and the restriction of the EM fields on the current became weak. As a result, the EM fields of the third iteration became large again.

We can conclude from (2-29) that when the value of  $\omega$  is between 0 and 1, the change of current caused by the EM fields is artificially weakened. This is consistent with the negative feedback process of the Compton current within the iterative scheme.

To check the influence of the relaxation factor, the integral absolute error (IAE) is by integrating the absolute error between the electric fields over time and space

$$\varepsilon = \sum_{r=1}^R \sum_{n=1}^N \frac{E^{k+1}(r, n) - E_{r,n}^\infty(r, n)}{E_{r,n}^\infty(r, n)} \quad (E_{r,n}^\infty \neq 0) \quad (2-30)$$

where  $\varepsilon$  represents the error between the numerical results of each iteration and the expected results.  $E^\infty$  is the result of the electric field obtained by the last time iteration, which is regarded as the expected results.

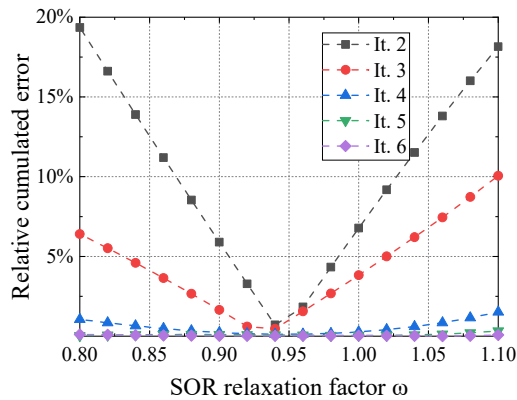


Figure 2-9 Relative cumulated error of the numerical results versus different values of relaxation factor

The integral absolute error was investigated for different values of the SOR relaxation

factor. With SOR optimization and an appropriate relaxation factor, the convergence occurred faster and required fewer iterations. When the value of  $\omega$  was around 0.94, convergence sped up and the relative cumulated error after 3rd iteration was less than 1%.

Table 2-1 shows the execution time of the case in Section 0, simulated by the different methods. The proposed iterative simulation code was developed in Matlab on a LINUX-based parallel platform. The parallel code used up to 56 processors. Since there is no open-source simulation code, the conventional non-iteration method is reproduced by Matlab according to reference [38]. The reproduced code run on the same LINUX-based platform. Since the calculation of fields and electrons are decoupled in the proposed method, the communication cost is low. The result suggested that the computational efficiency of the proposed iterative scheme was greatly improved by increasing the number of processors for the Compton current simulation.

Table 2-1 Computation time of different codes for the same case with and without the consideration of self-consistency

| Method               | Computation time /min             |                           |     |     |    |
|----------------------|-----------------------------------|---------------------------|-----|-----|----|
|                      | Conventional non-iteration method | Proposed iterative scheme | 1   | 20  | 56 |
| Number of processors | 1                                 | 1                         | 20  | 56  |    |
| Non-self-consistent  | 1.7                               | 1.7                       | 1.1 | 1.0 |    |
| Self-consistent      | 193.0                             | 88.9                      | 5.9 | 3.2 |    |

The improvement of the parallel simulation can be quantified by defining the "speed-up" as the ratio between the computation time when the processor number was one  $t_1$  and actual:

$$S = t_1 / t_N \tag{2-31}$$

where  $t_N$  refers to the computation time with  $i$  processors. Figure 2-10 shows that, with the number of processors increased, the speed-up had an upper limit because of communication and non-parallelizable parts, which mainly refer to the simulation of the EM fields.

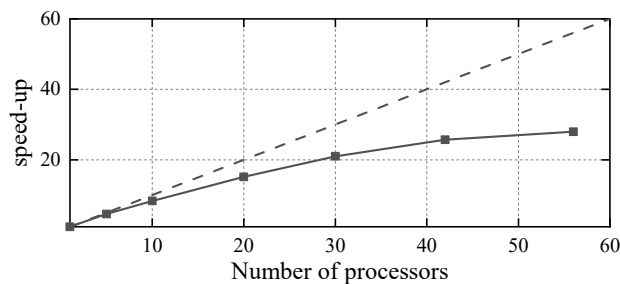


Figure 2-10 Speed-up of the proposed iteration scheme by the parallel computation code versus number of processors.

For both methods, the calculation time increased when considering self-consistency. Compared with the non-iterative EXEMP method, the computational efficiency can be improved up to 60 times with an error of less than 1% by the proposed iterative scheme.

Figure 2-11 shows the distribution of the electric field within the whole geometrical

coverage area on the earth surface, when the geomagnetic inclination is  $60^\circ$ . The origin point in the figures is the projection of the burst on the ground, which is called the ground zero point (GZ). The distribution pattern of the electric field amplitude is matched with the smile diagram recommended in IEC 61000-2-9<sup>[187]</sup>.

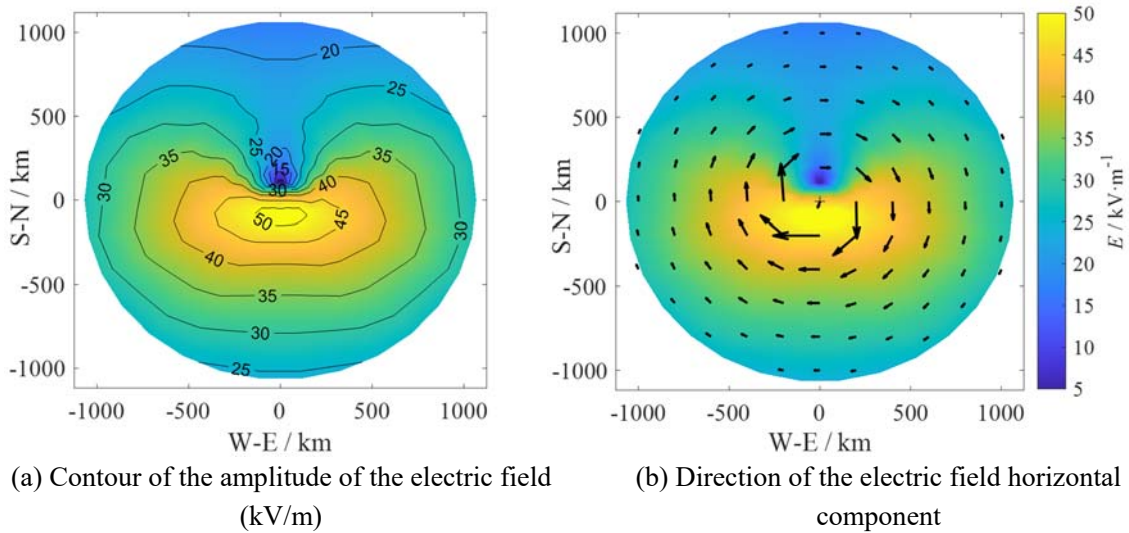


Figure 2-11 (a) The electric field incident to the ground (Parameters: prompt gamma yield 3 kt, geomagnetic inclination  $60^\circ$ , height of burst 100 km.)

### 2.3 Physical-based stochastic surrogate model for the HEMP distribution on the ground

EMP is the result of a self-consistent processes, including air ionization by photons and electrons, the behavior of the electrons, and interaction between current and electromagnetic fields. Uncertainties are introduced into HEMP calculation inevitably because of the existence of uncertain factors.

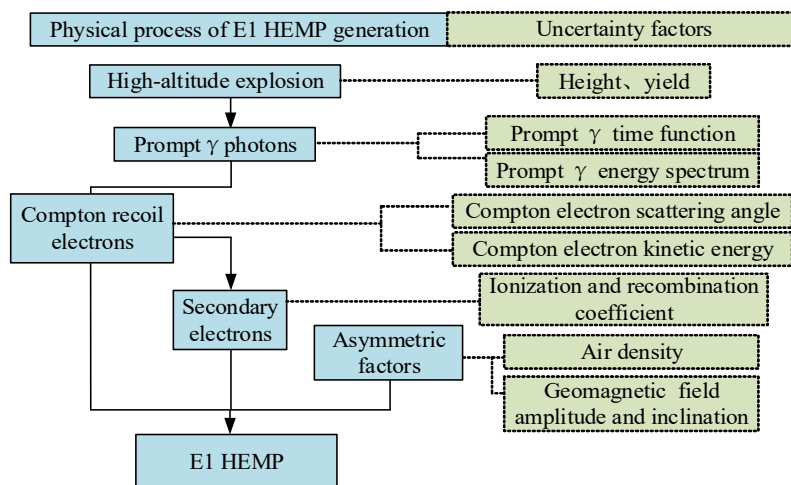


Figure 2-12 Uncertain factors in the generation of HEMP

The full simulation of HEMP includes the Compton scattering of prompt gamma photons and electrons, the behavior of electrons, and the propagation of electromagnetic fields.

Uncertainty quantification of the HEMP may lead to numerous repeats of the full simulation, and may be unaffordable and time-consuming. Even though the proposed iterative scheme can improve the simulation efficiency greatly, it is still expensive for uncertainty quantification. In order to study the uncertainty of the HEMP considering the previous-mentioned uncertain factors, a surrogate model is needed. Since the HEMP calculation cannot be expressed by analytical expressions, meanwhile the spatial distribution of the HEMP electric field amplitude and polarization angle is non-smooth, and the construction of non-intrusive surrogate models is difficult. Therefore, a physical-based stochastic surrogate model is proposed to describe the spatial distribution characteristics and stochastic characteristics of the HEMP incident to the ground surface.

### 2.3.1 Surrogate model based on the simplified dipole and quadrupole

In order to conveniently express the electric field distribution near the ground, a coordinate system is established with the GZ as the coordinate origin, as shown in Figure 2-13.

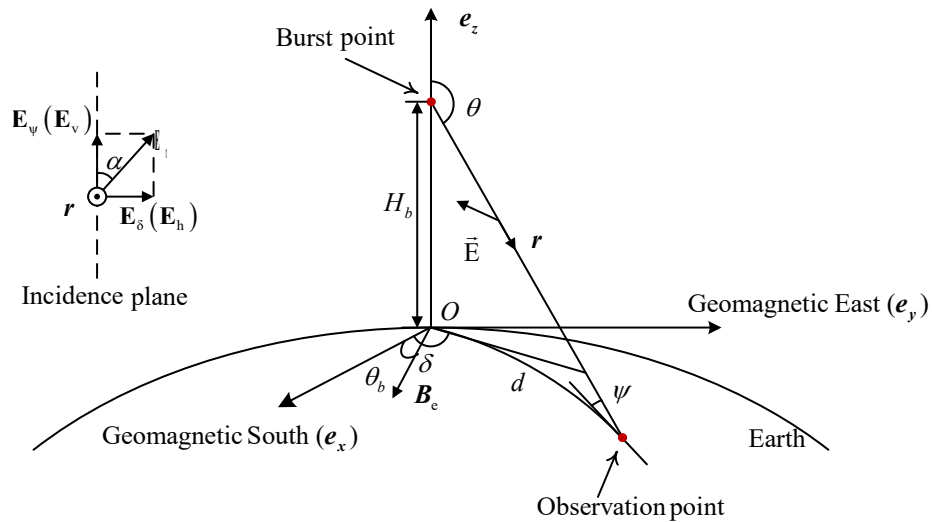


Figure 2-13 Definition of the elevation angle  $\psi$ , the direction angle  $\delta$ , polarization angle  $\alpha$ , and geomagnetic inclination  $\theta_b$  of the electric field

Looking back into the generation mechanism of HEMP, the EM fields are generated mainly by the deflection of Compton electrons in the geomagnetic field. The electric fields on the ground are mainly transverse, the amplitude of the fields is mainly dependent on the behavior of the transverse component of the Compton electron in the source region. Assuming the Compton current source is limited in the source region and the variation of Compton current with height is negligible in the source region. There is no new electric field that will be generated below the source region. Then the electric field reaches the ground in the form of a plane wave. The electric fields on the ground can be expressed by the approximation of the first term in (2-14)

$$\mathbf{E}_t \approx -\frac{c\mu_0}{2} \mathbf{J}_t \frac{1}{r_g} \approx \frac{c\mu_0}{2} e \frac{N}{r_g} \mathbf{v}_p \quad (2-32)$$

where  $\mathbf{J}_t$  — the transverse Compton current in the source region.  $r_g$  — the distance in the line

of sight from the source region to the observation point on the ground.

Compton electrons have the initial forward velocity gained from the prompt gamma photon. Once the electrons move forward along the radial direction, they are deflected by the geomagnetic field and have a transverse velocity component perpendicular to the geomagnetic field. When velocity is calculated in a short time,

$$\mathbf{v}'_p \approx -\frac{e}{m_e} \mathbf{v}_0 \times \mathbf{B}_e \Delta t = -\frac{e}{m_e} \Delta t v_0 (\mathbf{e}_r \times \mathbf{B}_e) \quad (2-33)$$

where  $\mathbf{e}_r$  — the unit vectors of the radial direction (from the detonation point to the observer point), as shown in the coordinate system shown in Figure 2-13. The geomagnetic North and East direction are the positive direction of the X and Y axis, respectively. For calculation purposes, a new spherical coordinate system with the origin at the gamma source is established.

The geomagnetic field vector can be extended into the form of absolute value  $|\mathbf{B}_e|$  and unit vector  $\mathbf{b}$ .  $\mathbf{b}$  in the spherical coordinate system can be transferred by the rotational transformation matrix:

$$[b_r \quad b_\theta \quad b_\delta]^T = \underbrace{\begin{pmatrix} \sin \theta \cos \delta & \sin \theta \sin \delta & \cos \theta \\ \cos \theta \cos \delta & \cos \theta \sin \delta & -\sin \theta \\ -\sin \delta & \cos \delta & 0 \end{pmatrix}}_{\mathbf{R}} [b_x \quad 0 \quad b_z]^T \quad (2-34)$$

where  $\mathbf{R}$  — the rotational transformation matrix.  $\mathbf{R}$  is a unit orthogonal matrix, there is  $\mathbf{R}^T = \mathbf{R}^{-1}$ .  $\mathbf{R}^T$  can be used as the inversion rotational transformation matrix for the vectors from the spherical coordinate to the Cartesian coordinate system.

The fields generated by the Compton electron with  $\mathbf{v}'_p$  are in the same direction as  $\mathbf{v}'_p$  and perpendicular to the geomagnetic field and radial direction. In fact,  $\mathbf{v}'_p$  is comparable with the initial velocity  $\mathbf{v}_0$ . As a consequence,  $\mathbf{v}'_p$  causes a second-turned velocity component  $\mathbf{v}''_{p,t}$

$$\mathbf{v}''_p = -\frac{e}{m_e} \mathbf{v}'_p \times \mathbf{B}_e \Delta t = -\left(\frac{e}{m_e} \Delta t\right)^2 v_0 ((\mathbf{e}_r \times \mathbf{B}_e) \times \mathbf{B}_e) \quad (2-35)$$

The second-turned velocity is not completely perpendicular to the radial direction. Part of  $\mathbf{v}''_{p,t}$  is parallel to the radial direction, which only causes local radial electric fields and is ignored here. Part of  $\mathbf{v}''_{p,t}$  is perpendicular to the radial direction and contributes to the electric fields on the ground.

$$\mathbf{v}''_{p,t} = -\left(\frac{e}{m_e} \Delta t\right)^2 v_0 [\mathbf{e}_r \times ((\mathbf{r} \times \mathbf{B}_e) \times \mathbf{B}_e) \times \mathbf{e}_r] \quad (2-36)$$

The second-turned  $\mathbf{v}''_{p,t}$  will produce a new vertical component, but each new component will be smaller by a factor of  $(\Delta t e / m_e)^2 |\mathbf{B}_e|$ . To balance the rationality and efficiency of the simplified model, we stop at the second-order approximation here.

The electric fields caused by the electrons with the velocity of  $\mathbf{v}'_p$  is usually called the magnetic dipole term of the field. Because the spatial variation of  $\mathbf{v}'_p$  is only determined by

the geomagnetic field. The electric field caused by the electrons with the velocity of  $\mathbf{v}_{p,t}''$  is usually called an electric quadrupole term. The transverse component of the HEMP can be approximated by the sum of these two fields

$$\mathbf{E}_t \propto \frac{c\mu_0}{2} e \frac{N}{r_g} (\mathbf{v}'_p + \mathbf{v}''_{p,t}) \quad (2-37)$$

Substitute (2-36) into (2-37), an approximated closed-form of electric fields is obtained only considering the existence of Compton current and can be used as a surrogate model to estimate the amplitude of the electric field with respect to  $\mathbf{r}$  and  $\mathbf{b}$ .

$$\begin{aligned} \mathbf{E}_t &\propto D |\mathbf{B}_e| (\mathbf{e}_r \times \mathbf{b}) + \left( D |\mathbf{B}_e| \frac{e}{m} \Delta t \right) |\mathbf{B}_e| (\mathbf{e}_r \times ((\mathbf{e}_r \times \mathbf{b}) \times \mathbf{b}) \times \mathbf{e}_r) \\ &= D |\mathbf{B}_e| \sin(\theta_{r,B}) + D |\mathbf{B}_e|^2 \frac{e}{m} \Delta t \sin(\theta_{r,B}) \cos(\theta_{r,B}) \\ D &= \frac{c\mu_0}{2} \frac{e}{m_e} \frac{N}{r_g} \Delta t, \quad \theta_{r,B} = \langle \mathbf{e}_r, \mathbf{b} \rangle \end{aligned} \quad (2-38)$$

where  $D$  is a variable related to distance from the source. The relative relationship between the electric field at the same distance from the GZ can be approximated analytically.

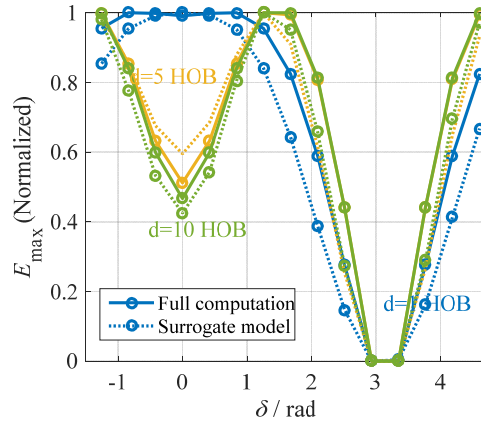


Figure 2-14 Estimated amplitude of the fields with the change of direction at different distances from GZ, obtained by surrogate model and full computation

Figure 2-14 shows the variation of the estimated amplitude of the fields at different directions and different distances from GZ, when  $\Delta t=2$  ns. The amplitude is normalized and compared with the full simulation results. It can describe the key characteristics of spatial distribution for HEMP on the ground.

The electric fields are not strictly east-west symmetry. The direction of the electron velocity of the dipole term is east-west symmetric. Therefore, the electric fields contributed by the dipole term have opposite directions and equal amplitude. The direction of the electric quadrupole is not centrosymmetric. In the west of GZ, the horizontal component of the resulting electric field cancels part of the electric field by the dipole term, in the east, the horizontal component of the resulting electric field enhances the electric field by the dipole term. Therefore, the total field will be slightly higher on the east side than on the west side.

$D$  is a function of distance and has no analytical expression, it should be fitted by the deterministic results with different distances from GZ.

The surrogate model based on the dipole and quadrupole can be used to describe part of the spatial distribution characteristic of the HEMP incident on the ground. For sure, the results are subject to error, ignoring the effect of air drag, secondary scattering of the Compton electrons, the effect of the secondary electron, and the effect of self-consistency.

### 2.3.2 Physical-based stochastic surrogate model based on SVM

According to the previous discussion, the electric field may be affected by numerous variables. In order to study the uncertainty of HEMP with spatial distribution characteristics under various uncertainties, as well as correct the error of the simplified surrogate mode,  $D$  is no longer a function of distance. The transverse component of the electric field (2-38) can be divided into two-term,

$$\begin{aligned}\mathbf{E}_t &= E_\theta(\xi)\mathbf{e}_\theta + E_\delta(\xi)\mathbf{e}_\delta \\ E_\theta(\xi) &= -F'(\xi)|\mathbf{B}_e|b_\delta + G'(\xi)|\mathbf{B}_e|^2 b_\theta b_r \\ E_\delta(\xi) &= F'(\xi)|\mathbf{B}_e|b_\theta + G'(\xi)|\mathbf{B}_e|^2 b_\delta b_r\end{aligned}\quad (2-39)$$

where  $E_\theta$  — the vertical polarization component;  $E_\delta$  — the horizontal polarization component according to the polarization. In fact,  $E_\delta$  and  $E_\phi$  are equivalent to  $E_\theta$  and  $E_\phi$  in the spherical coordinate system with the explosion point as the origin point.  $\xi$  is a vector collecting the independent variables with uncertainties.  $F'(\xi)$  and  $G'(\xi)$  are the coefficient of dipole term and quadrupole term. They are functions of a series of uncertain variables, such as the prompt gamma yield, the height of the burst height, the prompt gamma time function, and the geomagnetic field. They also vary with the relative distance and direction from GZ.

$$\begin{aligned}F'(\xi) &= F(d, \delta, H_b, Y, f_\gamma, B_e, \theta_e, \dots) \\ G'(\xi) &= G(d, \delta, H_b, Y, f_\gamma, B_e, \theta_e, \dots)\end{aligned}\quad (2-40)$$

The electric field polarization angle is calculated by the two transverse components

$$\alpha(\xi) = \text{atan}(E_\delta(\xi) / E_\theta(\xi)) \quad (2-41)$$

The elevation angle of the electric field incident to the ground surface is the function of relative distance from GZ, and can be calculated as

$$\psi(\xi) = \cos\left(\frac{R_E + H_b}{R_E} \sin\left(\frac{R_E \pi - d}{2R_E + H_b}\right)\right) \quad (2-42)$$

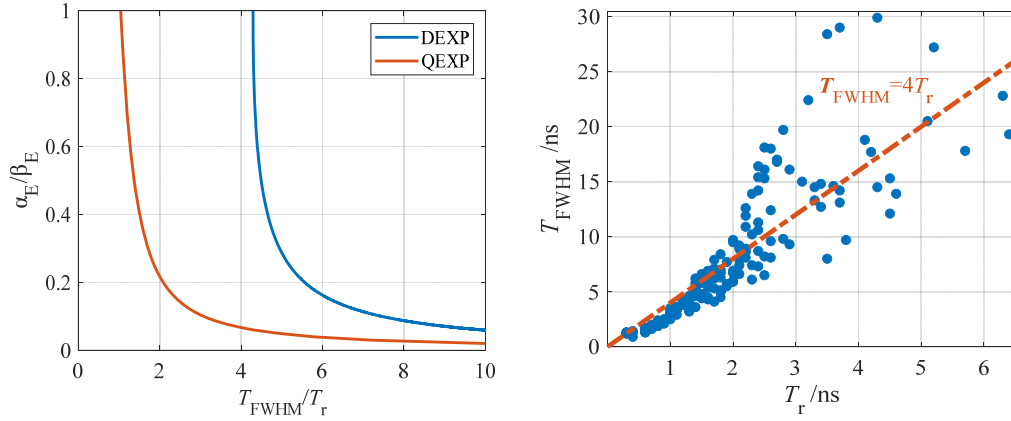
To combine the obtained EM field results with field-to-line coupling simulation, and to quantify the uncertainty of both fields and conductors, it is best to use an analytical description for the time domain amplitude of the EM fields with closed-form frequency domain expression.

There are three widely-used descriptions for the transient signal with fast rise and wide frequency band, as shown in Table 2-2.



Table 2-2 Typical descriptions for the transient signal with fast rise and wide frequency band

| Descriptions | Time-domain expression   | Frequency-domain expression  |
|--------------|--|--|
| DEXP [128]   | $E(t) = kE_0 [e^{-\beta_E t} - e^{-\alpha_E t}] u(t)$            | $E(\omega) = kE_0 \left( \frac{1}{j\omega + \beta_E} - \frac{1}{j\omega + \alpha_E} \right)$   |
| QEXP [129]   | $E(t) = \frac{E_0 k}{e^{-\alpha_E(t-t_0)} + e^{\beta_E(t-t_0)}}$ | $E(\omega) = \frac{E_0 k}{\alpha_E + \beta_E} \operatorname{csc} \left[ \frac{\pi}{\alpha_E + \beta_E} (j\omega + \alpha_E) \right] e^{j\omega t_0}$ |
| PEXP [156]   | $E(t) = kE_0 (1 - e^{-\alpha_E t})^p e^{-\beta_E t} u(t)$        | $E(\omega) = k_E E_0 \sum_{n=0}^p \left[ \frac{(-1)^n p!}{n!(p-n)!} \frac{1}{n\alpha + \beta_E + j\omega} \right]$                                   |



(a) Relationship between the time coefficients and the ratio of  $T_{FWHM}$  and  $T_r$  of DEXP and QEXP (b) Relationship between  $T_{FWHM}$  versus  $T_r$  of the HEMP waveform

Figure 2-15 The ratio of  $T_{FWHM}$  and  $T_r$  for actual HEMP waveform and analytical expression, respectively

DEXP is the simplest form for HEMP waveform, but it introduces an unexpected increase in the high frequency in the frequency domain because the waveform is forced to zero at the initial time. It also has difficulty fitting the waveform when the ratio of  $T_{FWHM}$  and  $T_r$  is less than 4, as shown in Figure 2-15 (a). However, it is common for the HEMP waveform that the ratio of  $T_{FWHM}$  and  $T_r$  is less than 4, as shown in Figure 2-15 (b). The quotient of double exponential (QEXP), and the p-power of double exponential (PEXP) have common behavior in both the time domain and frequency domain. The PEXP has a complex analytical solution in the frequency domain. Therefore, the QEXP is the best closed-form expression to describe the HEMP waveform.  $\alpha_E$  and  $\beta_E$  are calculated from  $T_{FWHM}$  and  $T_r$ .  $k_E$  is the normalization coefficient of the amplitude and is a function of  $\alpha_E$  and  $\beta_E$ .

Therefore, a time-domain surrogate model for the electric field with the consideration of uncertain variables can be obtained

$$E_t(t, \xi) = E_0(\xi) \frac{k_E}{e^{-\alpha_E(\xi)(t-t_0)} + e^{\beta_E(\xi)(t-t_0)}} \quad (2-43)$$

$$E_0(\xi) = |\mathbf{B}_e| \sqrt{\left( (F'(\xi))^2 + (G'(\xi) |\mathbf{B}_e| b_r)^2 \right) (b_\delta^2 + b_\theta^2)}$$

There are four independent stochastic functions to be solved in the surrogate model,  $F(\xi)$  and  $G(\xi)$  are solved by the amplitude of the vertical polarization and horizontal polarization

components,  $\alpha_E(\xi)$  and  $\beta_E(\xi)$  are fitted by the time domain waveform of the total field. Support vector machine (SVM) is used to fit the four stochastic functions, which is a non-parametric approach to construct surrogate functions for problems with high dimensional variables.

Taking  $F'(\xi)$  as an example, it can be expressed as a non-parametric multivariate function

$$F'(\xi) \approx f_{SVM}(\xi) = \sum_{i=1}^L a_i K(\xi_i, \xi) + b \quad (2-44)$$

where  $K(x_i, x)$  is the kernel function. Several common kernel function is shown in Table 2-3.

Table 2-3 Commonly used kernel function in SVM

| Kernel function                      | $K(\mathbf{x}_i, \mathbf{x})$                        |
|--------------------------------------|--|
| Linear                               | $\mathbf{x}_i^T \mathbf{x}$                          |
| p-order polynomial                   | $(1 + \mathbf{x}_i^T \mathbf{x})^q$                  |
| Gaussian radial basis function (RBF) | $\exp(-\ \mathbf{x}_i - \mathbf{x}\ ^2 / 2\sigma^2)$ |
| Sigmoid                              | $\tanh(c\mathbf{x}_i^T \mathbf{x} + z)$              |

When solving the coefficient  $a_i$  and  $b$  by the least-squares method (LS-SVM), the amount of the coefficient is independent of the number of uncertain variables and is determined by the number of samples. Therefore, SVM has good performance in high-dimensional problems with a small sample set<sup>[193]</sup>. The LS-SVM is achieved by the MATLAB toolbox LS-SVMLab<sup>[194]</sup>.

For comparison, another surrogate model is constructed directly based on the SVM fitting

$$E'_i(t, \xi) = F''_{SVM}(\xi) \quad (2-45)$$

$F''_{SVM}(\xi)$  is fitted by the HEMP amplitude sampling from multivariate  $\xi$  based on SVM fitting.

To validate and compare the performance of these surrogate models, consider a case with 5 uncertain parameters. The RBF is chosen as the kernel function for both SVM-only surrogate model and the physical-based SVM surrogate model.

The distance  $d$  from the GZ and direction angle  $\delta$  are also variables, since the spatial distribution characteristics of the electric field within the whole illustration range are considered.

Figure 2-16 shows the CDF of electric field amplitude obtained from different methods. Both the physical-based stochastic surrogate model and the SVM-only stochastic model are trained with 200 training samples. The performance of surrogate models with different sizes of training samples is compared in Table 2-4.

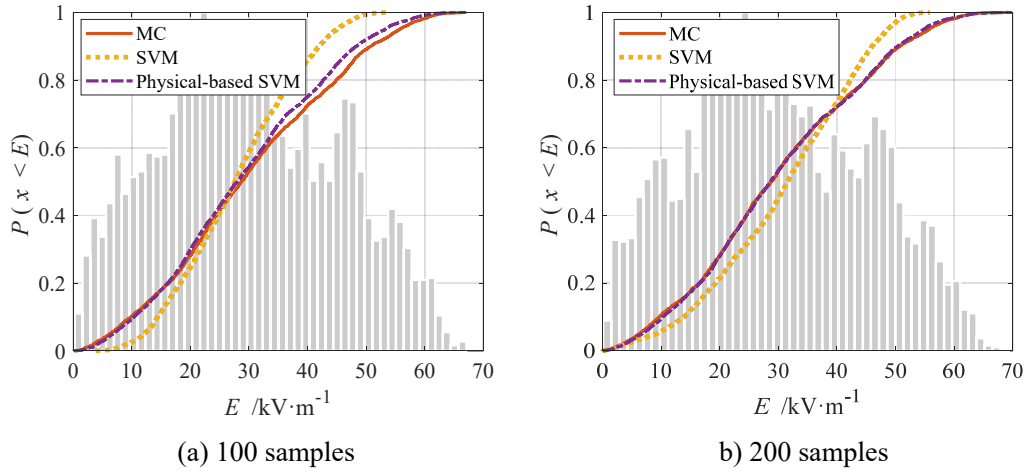


Figure 2-16 CDF of electric field amplitude with different number of samples

The physical-based stochastic surrogate model performs better than the stochastic model constructed by only SVM with fast convergence and high accuracy. This is because the non-intrusive stochastic models have a common disadvantage in dealing with non-smooth object functions. The spatial distribution of the HEMP is non-smooth according to the deterministic results. The root-mean-square deviation  $D_{RMS}$  indicates the distance between the CDF of the results between the stochastic model and the MC method. The physical-based stochastic surrogate model can greatly improve the performance of the non-intrusive stochastic model, by providing an analytic expression based on the simplified model, because the simplified model of Compton electron can describe the specific distribution pattern of the HEMP. The improvement is significant when the amount of samples is small.

Table 2-4 Comparison of time consumption and accuracy of MC, physical-based SVM and SVM-only

|           | MC       | Physical-based SVM |         |          | SVM     |         |          |
|-----------|----------|--------------------|---------|----------|---------|---------|----------|
| Samples   | 2000     | 100                | 200     | 1000     | 100     | 200     | 1000     |
| $D_{RMS}$ | \        | 0.029              | 0.020   | 0.012    | 0.180   | 0.125   | 0.039    |
| Time      | 48h18min | 2h19min            | 4h40min | 24h11min | 2h18min | 4h40min | 24h11min |

It shows that the uncertainty quantification based on the stochastic surrogate models reduces the time-consuming of tens of hours than the conventional MC method. The time-consuming of the surrogate models is mainly determined by the full simulation of the training samples, the construction of the surrogate models is less than one minute.

### 2.3.3 Uncertainty Quantification of HEMP based on the stochastic surrogate model

The uncertainty of potential HEMP for the power system is quantified by using the proposed physical-based SVM surrogate model

Frequentist probability distribution is the preferred method to characterize the uncertainty of variables, that is, the probability of events is expressed by the possible frequency. However, for the variables with epistemic uncertainty, there is rarely a frequentist probability, the

subjective probability is utilized as a credible alternative. The uniform distribution can be assumed for the variable without a special probability feature, as long as the range is meaningful. The inclination and amplitude of the geomagnetic field are used as dependent variables of latitude and longitude.

Figure 2-17 shows the probability distributions of the amplitude  $E_{\max}$ , the rise time  $T_r$ , the pulse width  $T_{\text{FWHM}}$  of the HEMP waveform, the polarization angle, and the elevation angle of the field incident to the earth surface. These are parameters we are concerned about in the simulation of coupling response. It should be noted that these quantities are dependent variables of uncertainty influence factors of the HEMP field. The variables are not independent of each other. The results in Figure 2-17 show that there is a strong correlation between parameters, and the relationship between parameters has a large uncertainty range as well.

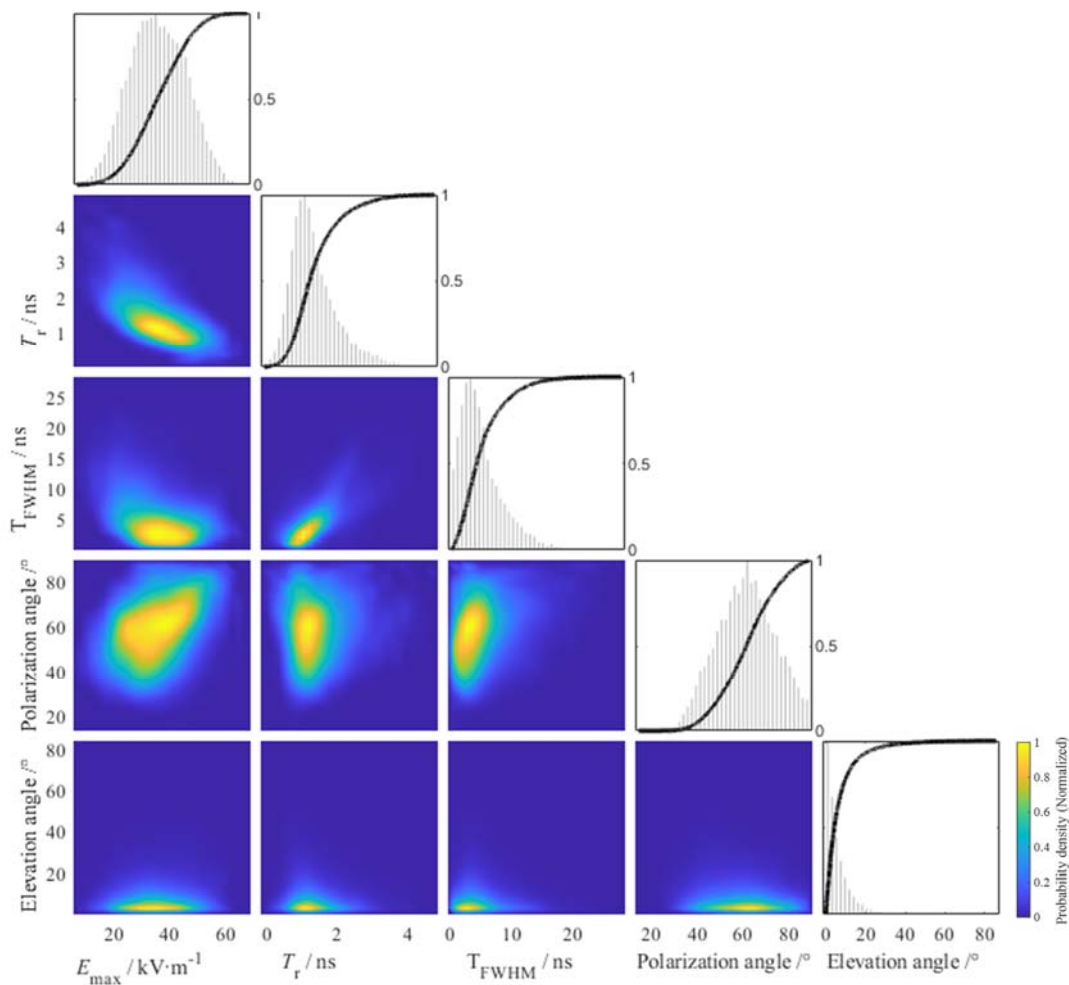


Figure 2-17 The joint and marginal distributions of the amplitude, the rise time, the FWHM, the polarization angle, the elevation angle, and the direction angle obtained by the stochastic surrogate model of the HEMP. The color represents the normalized joint probability density.

The first two graphs in the first column in Figure 2-17 show a strong inverse relationship between the amplitude and the rise time of the HEMP waveform. This is consistent with the previous quantitative analysis. The increase in amplitude is often the result of the increase of Compton current, which leads to an increase in the build-up level of the secondary electrons.

The high-pass filtering effect of the air plasma becomes obvious and causes a fast time-domain waveform. This is important for the study of coupling responses on the TLs.

The graphs in the third row show that horizontal polarization is the dominant component when the electric field is large. There is almost no completely vertical polarization electric field. Since the most severe coupling case is the grazing incidence with vertical polarization, the coupling responses on the lines may be overestimated if the distribution of polarization is ignored.

## 2.4 Concluding remarks

In order to quantify the potential distribution of the field parameters used in the study of field-to-line coupling responses, a full computation model and a physical-based stochastic surrogate model of HEMP are developed in this section.

(1) The self-consistent process of the generation and propagation of HEMP is simulated by the proposed iterative self-consistent algorithm, which can greatly improve the computation efficiency with similar accuracy, the computation efficiency can be improved up to 60 times compared with the conventional self-consistent method. In the simulation of HEMP with prompt gamma yield ranging from tens tons to several kilotons, for both prompt gamma ray of monoenergetic and energy spectrum, the self-consistent effect plays a non-negligible role and led to different reductions (up to 20%) in the amplitude of the electric field.

(2) The amplitude of the HEMP increases with the increase of the gamma yield and gradually saturates because of the self-consistent effect and saturate effect. The geomagnetic inclination affects the spatial distribution of the HEMP amplitude and polarization angle. With the geomagnetic inclination increase, the horizontal component of the electric field is increasingly dominant.

(3) A physical-based stochastic surrogate model of HEMP incident to the ground is proposed based on the simplified model, to address the problem of difficulty in constructing non-intrusive surrogate models, since the HEMP calculation cannot be expressed by analytical expressions and the spatial distribution of the HEMP electric field amplitude and polarization angle are non-smooth. Compare to the conventional Monte Carlo method, it requires fewer full simulations, reducing the time-consuming from days to hours.

(4) From the uncertainty quantification of the HEMP, some conclusions are as follows: there is an upper limit for the electric field amplitude caused by the self-consistent effect and saturation effect; the increase in the amplitude is often accompanied by a decrease in the pulse width; the horizontal polarization is the dominant component when the electric field is large. The uncertainty quantification of key parameters of HEMP such as amplitude, rise time, and polarization angle is carried out and will be used in subsequent uncertainty quantification of field-to-line coupling.

### 3 Deterministic model and stochastic model for field-to-line coupling

In this chapter, the deterministic model and stochastic model for the lines excited by external fields are presented. In order to simulate the potential coupling responses of lines with nonlinear loads (such as MOA), when the coupling responses may vary in a large range due to the uncertainty of incident field, the macromodels of field-to-lines coupling are established by equating the transmission line distribution characteristics to the behaviors at ports, which can deal with the frequency-dependent characteristics as well as the nonlinear load of the lines. An equation-based dynamic nonlinear model is proposed to represent the MOA response when the rise time of the induced current may vary in a wide range. The deterministic model of field-to-lines coupling responses has analytic expression, therefore, the stochastic models of the coupling responses on the line are intrusively constructed by expanding the telegraph equations through the polynomial chaos expansion method. It can be used for the uncertainty quantification of coupling response, when the uncertain parameters coming from lines and incident fields are mutually independent.

#### 3.1 Classical physical model for TLs excited by external fields

Lines and wires in the power systems, including elevated TLs, communication lines, etc., are typical coupling paths for electric fields in power systems. These overhead lines can be abstracted as multiconductor above the ground, as shown in Figure 3-1. When the TLs are excited by the external electromagnetic field, the induced voltages and currents along the lines can be described by the telegraph equipment.

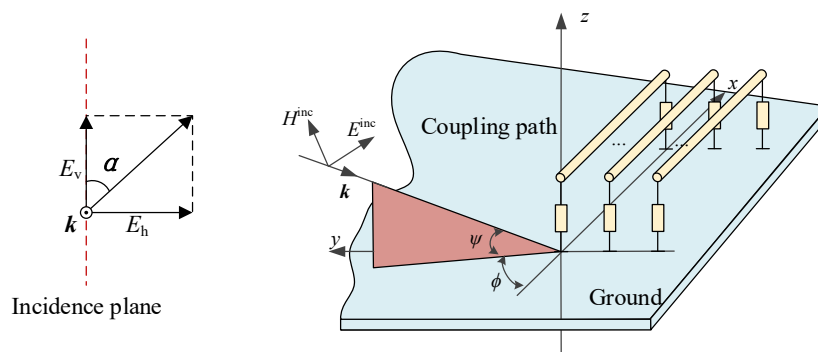


Figure 3-1 The diagram of TLs excited by the external field

Taylor model, Agrawal model, and Rachidi model are three well-known models that describe the TLs excited by the fields<sup>[133]-[135]</sup>. The usage of different variables of TL and field components in the model leads to different forms of the formula, as shown in Table 3-1.

Table 3-1 Comparison of three models of field coupling to two-conductor TL

|               | Telegraph equation   | boundary conditions   | Variable   | field components     |
|---------------|--|---|--|----------------------|
| Taylor model  | $\begin{cases} \frac{dV(x)}{dx} + ZI(x) = V'_{s1}(x) \\ \frac{dI(x)}{dx} + YV(x) = I'_{s1}(x) \end{cases}$   | $\begin{cases} V(0) = -Z_1 I(0) \\ V(L) = Z_2 I(L) \end{cases}$   | Total voltage and current $V, I$                 | $E_z, E_x^{ex}, H_y$ |
| Agrawal model | $\begin{cases} \frac{dV^{sca}(x)}{dx} + ZI(x) = V_{s2}(x) \\ \frac{dI(x)}{dx} + YV^{sca}(x) = 0 \end{cases}$ | $\begin{cases} V^{sca}(0) = -Z_1 I(0) - V_{s21} \\ V^{sca}(L) = Z_2 I(L) - V_{s22} \end{cases}$                 | Scattering current $V^{sca}$ , total voltage $I$ | $E_x, E_z$           |
| Rachidi model | $\begin{cases} \frac{dV(x)}{dx} + Z' I^{sca}(x) = 0 \\ \frac{dI^{sca}(x)}{dx} + YV(x) = I_s(x) \end{cases}$  | $\begin{cases} I^{sca}(0) = -\frac{V(0)}{Z_1} - I_{s31} \\ I^{sca}(L) = \frac{V(L)}{Z_2} - I_{s32} \end{cases}$ | Scattering current $I^{sca}$ , total voltage $V$ | $E_x, H_x, H_y$      |

Despite the different forms, the three models can provide equivalent simulations for the TL. The advantage of the Agrawal model and Rachidi model is that the formulas have a simple form with only one source term caused by the incident field. The advantage of the Taylor model is that the total currents and voltages on the TLs are solved directly. In this dissertation, the Taylor model is utilized to develop the macromodel. The equations can be easily transferred into the form of two-ports and can be combined with the solution of load terminals directly.

Consider a group of  $N$  multiconductors, including  $N-1$  overhead transmission line and lossy ground. The geometric arrangement is shown in Figure 3-1. The  $i$ -th conductor is located at a height of  $h_i$  above the ground. The telegraph equation considering the field-to-line coupling based on the Taylor model for these MTL in the Laplace domain is

$$\begin{aligned} \frac{d}{dx} \mathbf{V}(x, \omega) + \mathbf{Z}(\omega) \mathbf{I}(x, \omega) &= \mathbf{V}_s(x, \omega) \\ \frac{d}{dx} \mathbf{I}(x, \omega) + \mathbf{Y}(\omega) \mathbf{V}(x, \omega) &= \mathbf{I}_s(x, \omega) \end{aligned} \quad (3-1)$$

where  $\mathbf{V}, \mathbf{I}$  — the total voltages and current along the conductors;  $\mathbf{V}_s, \mathbf{I}_s$  — the distributed voltage and current source caused by the external field;  $\mathbf{Z}, \mathbf{Y}$  — the per-unit-length impedance and admittance matrices of conductors.  $\mathbf{V}, \mathbf{I}, \mathbf{V}_s, \mathbf{I}_s$  are vectors of  $N \times 1$  order.  $\mathbf{Z}, \mathbf{Y}$  are vectors of  $N \times N$  order.

The voltage source is made up of two parts, one is the excitation magnetic field flux between the wire and the ground, and the other part is the horizontal components of the electric field on the ground. The current source of the telegraph equation is determined by the vertical components of the electric field located at the height of the conductors.

$$\begin{aligned} \mathbf{V}_s(x) &= -j\omega\mu_0 \left( \int_0^{h_i} H_y(x, y_i, z) dz \right) + (E_x(x, y_i, 0)) \\ \mathbf{I}_s(x) &= -\mathbf{Y} \left( \int_0^{h_i} E_z(x, y_i, z) dz \right) \end{aligned} \quad (3-2)$$

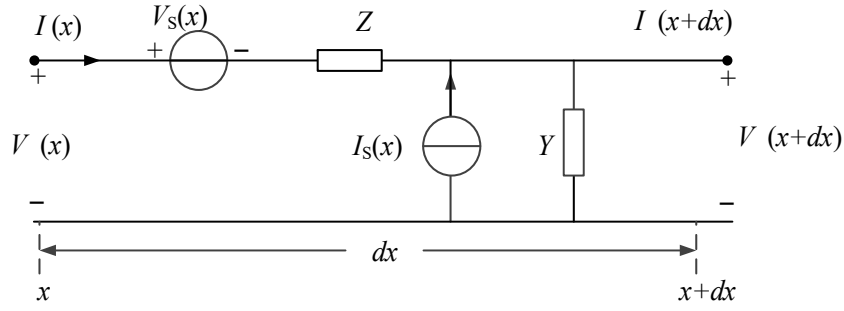


Figure 3-2 The per-unit-length equivalent circuit with incident field based on Taylor

The per-unit-length (p.u.l.) impedance and admittance of the MTL are calculated by the inductance  $\mathbf{L}$ , capacitance  $\mathbf{C}$ , frequency-dependent conductor internal impedance  $\mathbf{Z}_w(s)$ , frequency-dependent ground admittance, and conductance  $\mathbf{Z}_g(s)$ ,  $\mathbf{Y}_g(s)$ .

$$\begin{aligned} \mathbf{Z}(\omega) &= \mathbf{Z}_w(\omega) + \mathbf{Z}_g(\omega) + j\omega\mathbf{L} \\ \mathbf{Y}(\omega) &= j\omega\mathbf{C}\mathbf{Y}_g(\omega) / (j\omega\mathbf{C} + \mathbf{Y}_g(\omega)) \end{aligned} \quad (3-3)$$

The inductance matrix  $\mathbf{L}$  includes the self-inductance of conductors and mutual inductance between conductors:

$$\begin{cases} L_{ii} = \frac{\mu_0}{2\pi} \ln \frac{2h_i}{r_i} \\ L_{ij} = \frac{\mu_0}{2\pi} \ln \left( 1 + \frac{4h_i h_j}{d_{ij}^2} \right) \end{cases} \quad (3-4)$$

where  $r_i$ ,  $h_i$  — the radius and height of each conductor,  $d_{ij}$  — the distance between conductor  $i$  and conductor  $j$ .

The capacitance matrix can be calculated from the inductance matrix:

$$\mathbf{C} = \mu_0 \varepsilon_0 \mathbf{L}^{-1} \quad (3-5)$$

The frequency-dependent ground impedance and conductance  $\mathbf{Z}_g(\omega)$ ,  $\mathbf{Y}_g(\omega)$  are caused by the lossy ground. When the frequency of the signal is high, the displacement currents in the soil should be taken into consideration in the calculation of transmission line parameters. The logarithmic approximation proposed by Sunde is widely used for the ground impedance for the single line<sup>[61]</sup> and has been extended to the mutual ground impedance<sup>[62]</sup>:

$$\begin{cases} Z_{g,ii} = \frac{j\omega\mu_0}{2\pi} \ln \frac{1 + \gamma_g h_i}{\gamma_g h_i} \\ Z_{g,ij} = \frac{j\omega\mu_0}{4\pi} \ln \frac{[1 + \gamma_g (\frac{h_i + h_j}{2})]^2 + \gamma_g (\frac{d_{ij}}{2})^2}{\gamma_g (\frac{h_i + h_j}{2})^2 + \gamma_g (\frac{d_{ij}}{2})^2} \end{cases} \quad (3-6)$$

where,  $\gamma_g = \sqrt{j\omega\mu_0(\sigma_g + j\omega\varepsilon_r)}$  is the propagation constant,  $\sigma_g$  and  $\varepsilon_r$  are conductivity and relative dielectric of the ground.

The ground conductance matrix  $\mathbf{Y}_g(\omega)$  is calculated by the ground impedance  $\mathbf{Z}_g(\omega)$



$$\mathbf{Y}_g = \gamma_g^2 \mathbf{Z}_g^{-1} \quad (3-7)$$

The boundary conditions determined by the loads at both ends are

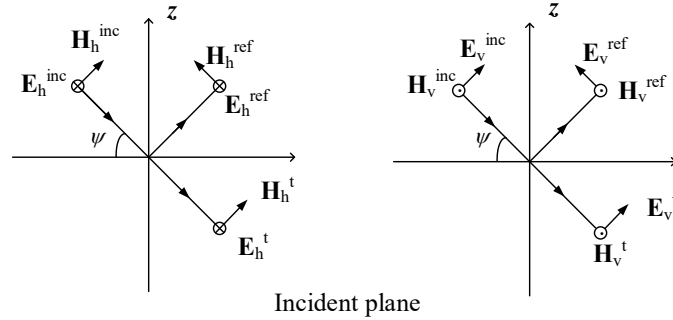
$$\begin{aligned} \mathbf{V}(0, \omega) &= \mathbf{V}_s + \mathbf{Z}_s \mathbf{I}(0, \omega) \\ \mathbf{V}(l, \omega) &= \mathbf{V}_L + \mathbf{Z}_L \mathbf{I}(l, \omega) \end{aligned} \quad (3-8)$$

The distributed source term  $\mathbf{V}_s(x)$  and  $\mathbf{I}_s(x)$  are calculated by electromagnetic fields made up of the incident fields  $\mathbf{E}^{\text{inc}}$ ,  $\mathbf{B}^{\text{inc}}$  and the reflected fields  $\mathbf{E}^{\text{ref}}$ ,  $\mathbf{B}^{\text{ref}}$  reflected by the ground.

The incident wave can be expressed as

$$\begin{aligned} \mathbf{E}^{\text{inc}} &= E_0(\omega) [(\cos \alpha \sin \psi \cos \phi + \sin \alpha \sin \phi) \mathbf{e}_x + \\ &\quad (-\cos \alpha \sin \psi \sin \phi + \sin \alpha \cos \phi) \mathbf{e}_y + \cos \alpha \cos \psi \mathbf{e}_z] e^{-jkx \cos \psi \cos \phi} e^{jky \cos \psi \sin \phi} e^{jkz \sin \psi} \\ \mathbf{H}^{\text{inc}} &= E_0(\omega) / Z_0 [(\sin \alpha \sin \psi \cos \phi - \cos \alpha \sin \phi) \mathbf{e}_x + \\ &\quad (-\sin \alpha \sin \psi \sin \phi - \cos \alpha \cos \phi) \mathbf{e}_y + \sin \alpha \cos \psi \mathbf{e}_z] e^{-jkx \cos \psi \cos \phi} e^{jky \cos \psi \sin \phi} e^{jkz \sin \psi} \end{aligned} \quad (3-9)$$

Electromagnetic waves will be reflected and transmitted at the ground surface. The results of reflection and transmission are determined by the polarization of the incident EM waves. The EM field is divided into a horizontal polarization component and a vertical polarization component according to the polarization direction of the electric field, as shown in Figure 3-3.



(a) Horizontal polarization EM fields      (b) Vertical polarization EM fields

Figure 3-3 Schematic diagram of the reflection and transmission of electromagnetic waves at the ground surface

Therefore, the total electromagnetic fields can be expressed as

$$\begin{aligned} \mathbf{E}^{\text{total}} &= \mathbf{E}_{x,v}^{\text{inc}} - R_v \mathbf{E}_{x,v}^{\text{inc}} + \mathbf{E}_{y,v}^{\text{inc}} - R_v \mathbf{E}_{y,v}^{\text{inc}} + \mathbf{E}_{z,v}^{\text{inc}} + R_v \mathbf{E}_{z,v}^{\text{inc}} \\ &= \mathbf{E}_{x,h}^{\text{inc}} + R_h \mathbf{E}_{x,h}^{\text{inc}} + \mathbf{E}_{y,h}^{\text{inc}} + R_h \mathbf{E}_{y,h}^{\text{inc}} \\ \mathbf{H}^{\text{total}} &= \mathbf{H}_{x,v}^{\text{inc}} + R_v \mathbf{H}_{x,v}^{\text{inc}} + \mathbf{H}_{y,v}^{\text{inc}} + R_v \mathbf{H}_{y,v}^{\text{inc}} \\ &= \mathbf{H}_{x,h}^{\text{inc}} - R_h \mathbf{H}_{x,h}^{\text{inc}} + \mathbf{H}_{y,h}^{\text{inc}} - R_h \mathbf{H}_{y,h}^{\text{inc}} + \mathbf{H}_{z,v}^{\text{inc}} + R_v \mathbf{H}_{z,v}^{\text{inc}} \end{aligned} \quad (3-10)$$

where  $R_v$  and  $R_h$  — the Fresnel reflection coefficients of the vertical and horizontal polarization components.

$$\begin{aligned}
R_v &= \frac{\varepsilon_r \left(1 + \frac{\sigma_g}{j\omega\varepsilon_r\varepsilon_0}\right) \sin\psi - \sqrt{\varepsilon_r \left(1 + \frac{\sigma_g}{j\omega\varepsilon_r\varepsilon_0}\right) - \cos^2\psi}}{\varepsilon_r \left(1 + \frac{\sigma_g}{j\omega\varepsilon_0}\right) \sin\psi + \sqrt{\varepsilon_r \left(1 + \frac{\sigma_g}{j\omega\varepsilon_r\varepsilon_0}\right) - \cos^2\psi}} \\
R_h &= \frac{\sin\psi - \sqrt{\varepsilon_r \left(1 + \frac{\sigma_g}{j\omega\varepsilon_r\varepsilon_0}\right) - \cos^2\psi}}{\sin\psi + \sqrt{\varepsilon_r \left(1 + \frac{\sigma_g}{j\omega\varepsilon_r\varepsilon_0}\right) - \cos^2\psi}} \\
k &= \omega\sqrt{\varepsilon_0\mu_0}
\end{aligned} \tag{3-11}$$

The reflected field can be obtained as:

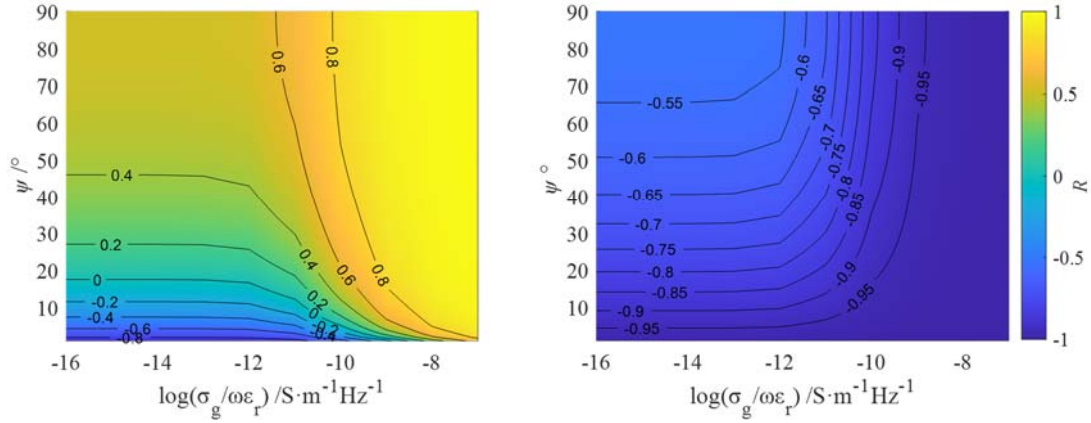
$$\begin{aligned}
\mathbf{E}^{\text{ref}} &= E_0(\omega)[(-R_v \cos\alpha \sin\psi \cos\phi + R_h \sin\alpha \sin\phi)\mathbf{e}_x + \\
&\quad (+R_v \cos\alpha \sin\psi \sin\phi + R_h \sin\alpha \cos\phi)\mathbf{e}_y + R_v \cos\alpha \cos\psi \mathbf{e}_z] e^{-jkx \cos\psi \cos\phi} e^{jky \cos\psi \sin\phi} e^{-jkz \sin\psi} \\
\mathbf{H}^{\text{ref}} &= E_0(\omega)/Z_0[(-R_h \sin\alpha \sin\psi \cos\phi - R_v \cos\alpha \sin\phi)\mathbf{e}_x + \\
&\quad (R_h \sin\alpha \sin\psi \sin\phi - R_v \cos\alpha \cos\phi)\mathbf{e}_y + R_h \sin\alpha \cos\psi \mathbf{e}_z] e^{-jkx \cos\psi \cos\phi} e^{jky \cos\psi \sin\phi} e^{-jkz \sin\psi}
\end{aligned} \tag{3-12}$$

Reflection coefficients  $R_v$  and  $R_h$  vary with elevation angles, signal frequency, material permittivity, and conductivity. For the ideal conductor, there is no tangential electric field and no normal magnetic field on the surface, therefore  $R_v = 1$  and  $R_h = -1$ . Common values of conductivity and relative permittivity of several common materials for the earth's surface are shown in Table 3-2. The reflected field should be discussed separately according to the vertical and horizontal polarization of the electric field.

Table 3-2 Conductivity and relative permittivity of several common materials of the earth's surface

|   | Dry soil   | Wet soil      | Sandy ground | Sea water |
|---|------------|---------------|--------------|-----------|
| Conductivity $\sigma_g/\text{S}\cdot\text{m}^{-1}$  | 0.001~0.01 | 0.01~0.03     | <0.001       | 4         |
| Dielectric constant $\varepsilon_r$                 | 3~5        | 4-40          | 6-8          | 81        |
| $\sigma_g/\varepsilon_r/\text{S}\cdot\text{m}^{-1}$ | 0.002~0.3  | 0.0004~0.0075 | <0.00016     | 0.04      |

When the elevation angle is small, part of the vertical polarization component field that is perpendicular to the ground is opposite to the incident field. When the elevation angle is small, it enhances the incident field. In contrast, the part of the vertical polarization component that is horizontal to the ground enhances the incident field at a small elevation angle, and with the increase of the incident elevation angle, it will decrease the incident field. The horizontal polarization component of the electric field is always parallel to the ground, and the reflection field always attenuates the incident field, but the effect is getting weaker.



(a)  $R_v$  for vertically polarized field

(b)  $R_h$  for horizontally polarized field

Figure 3-4 Influence of the elevation angle, signal frequency, and permittivity, and conductivity on the reflection coefficients

When the incident field is a plane wave with angles shown in Figure 3-1, there is

$$\begin{aligned}
 E_z(x, y_i, z) &= E_0 \cos \alpha \cos \psi \left( e^{jkz \sin \psi} + R_v e^{-jkz \sin \psi} \right) e^{-jkx \cos \psi \cos \phi} e^{jky \cos \psi \sin \phi} \\
 E_x(x, y_i, 0) &= E_0 \left[ \cos \alpha \sin \psi \cos \phi (1 - R_v) + \sin \alpha \sin \phi (1 + R_h) \right] e^{-jkx \cos \psi \cos \phi} e^{jky \cos \psi \sin \phi} \\
 H_y(x, y_i, z) &= -\frac{E_0}{377} \left[ \sin \alpha \sin \psi \sin \phi \left( e^{jkz \sin \psi} - R_h e^{-jkz \sin \psi} \right) \right. \\
 &\quad \left. + \cos \alpha \cos \phi \left( e^{jkz \sin \psi} + R_v e^{-jkz \sin \psi} \right) \right] e^{-jkx \cos \psi \cos \phi} e^{jky \cos \psi \sin \phi}
 \end{aligned} \tag{3-13}$$

Therefore, the distribution voltage and current source for each transmission line in the Taylor model are expressed as

$$\begin{aligned}
 \mathbf{V}_s(x) &= -j\omega\mu_0 \left( \int_0^h -\frac{E_0}{377} \left[ \sin \alpha \sin \psi \sin \phi \left( e^{jkz \sin \psi} - R_h e^{-jkz \sin \psi} \right) \right. \right. \\
 &\quad \left. \left. + \cos \alpha \cos \phi \left( e^{jkz \sin \psi} + R_v e^{-jkz \sin \psi} \right) \right] dz \right) e^{-jkx \cos \psi \cos \phi} e^{jky \cos \psi \sin \phi} \\
 &\quad + E_0 \left[ \cos \alpha \sin \psi \cos \phi (1 - R_v) + \sin \alpha \sin \phi (1 + R_h) \right] e^{-jkx \cos \psi \cos \phi} e^{jky \cos \psi \sin \phi} \\
 &= e^{-jkx \cos \psi \cos \phi} e^{jky \cos \psi \sin \phi} \left( \frac{\omega\mu_0 E_0}{377k \sin \psi} \left[ \sin \alpha \sin \psi \sin \phi \left( (e^{jkh \sin \psi} - 1) + R_h (e^{-jkh \sin \psi} - 1) \right) \right. \right. \\
 &\quad \left. \left. + \cos \alpha \cos \phi \left( (e^{jkh \sin \psi} - 1) - R_v (e^{-jkh \sin \psi} - 1) \right) \right] \right. \\
 &\quad \left. + E_0 \left[ \cos \alpha \sin \psi \cos \phi (1 - R_v) + \sin \alpha \sin \phi (1 + R_h) \right] \right)
 \end{aligned} \tag{3-14}$$

$$\begin{aligned}
 \mathbf{I}_s(x) &= -\mathbf{Y} \left( \int_0^h E_0 \cos \alpha \cos \psi \left( e^{jkz \sin \psi} + R_v e^{-jkz \sin \psi} \right) dz \right) e^{-jkx \cos \psi \cos \phi} e^{jky \cos \psi \sin \phi} \\
 &= e^{-jkx \cos \psi \cos \phi} e^{jky \cos \psi \sin \phi} \frac{-\mathbf{Y} E_0}{jk \sin \psi} \cos \alpha \cos \psi \left( (e^{jkh \sin \psi} - 1) - R_v (e^{-jkh \sin \psi} - 1) \right)
 \end{aligned} \tag{3-15}$$

According to the assumptions of transmission lines, that the size of cross-section  $h$  is smaller than the wavelength, the source term caused by the incident field can be approximated as:

$$\begin{aligned}
 \mathbf{I}_s(x) &= -\mathbf{Y} \left( \int_0^h E_0 \cos \alpha \cos \psi \left( e^{jkz \sin \psi} + R_v e^{-jkz \sin \psi} \right) dz \right) e^{-jkx \cos \psi \cos \phi} e^{jky \cos \psi \sin \phi} \\
 &= e^{-jkx \cos \psi \cos \phi} \underbrace{e^{jky \cos \psi \sin \phi} - \mathbf{Y} E_0 h \cos \alpha \cos \psi (1 + R_v)}_{\mathbf{B}}
 \end{aligned} \tag{3-16}$$

$$\begin{aligned}
\mathbf{V}_s(x) &= -j\omega\mu_0 \left( \int_0^h -\frac{E_0}{377} \begin{bmatrix} \sin\alpha \sin\psi \sin\phi (e^{jkz \sin\psi} - R_h e^{-jkz \sin\psi}) \\ + \cos\alpha \cos\phi (e^{jkz \sin\psi} + R_v e^{-jkz \sin\psi}) \end{bmatrix} dz \right) e^{-jkx \cos\psi \cos\phi} e^{jky \cos\psi \sin\phi} \\
&\quad + E_0 \left[ \cos\alpha \sin\psi \cos\phi (1 - R_v) + \sin\alpha \sin\phi (1 + R_h) \right] e^{-jkx \cos\psi \cos\phi} e^{jky \cos\psi \sin\phi} \\
&= e^{-jkx \cos\psi \cos\phi} e^{jky \cos\psi \sin\phi} E_0 \underbrace{\begin{bmatrix} \omega\mu_0 h \begin{bmatrix} \sin\alpha \sin\psi \sin\phi (1 - R_h) \\ + \cos\alpha \cos\phi (1 + R_v) \end{bmatrix} \\ + [\cos\alpha \sin\psi \cos\phi (1 - R_v) + \sin\alpha \sin\phi (1 + R_h)] \end{bmatrix}}_A
\end{aligned} \tag{3-17}$$

## 3.2 Macromodel for field coupling to lines with nonlinear loads

### 3.2.1 Frequency-domain macromodel of field-to-line coupling

Equations in (3-1) can be expressed in the matrix-exponential form, and the solution can be obtained by making an analogy of the state-variable equations<sup>[136]</sup>

$$\begin{bmatrix} \mathbf{V}(l, \omega) \\ \mathbf{I}(l, \omega) \end{bmatrix} = \mathbf{\Phi}(l) \begin{bmatrix} \mathbf{V}(0, \omega) \\ \mathbf{I}(0, \omega) \end{bmatrix} + \begin{bmatrix} \mathbf{V}_{FT}(l, \omega) \\ \mathbf{I}_{FT}(l, \omega) \end{bmatrix} \tag{3-18}$$

where

$$\begin{bmatrix} \mathbf{V}_{FT}(l, \omega) \\ \mathbf{I}_{FT}(l, \omega) \end{bmatrix} = \int_0^l \mathbf{\Phi}(l-x) \begin{bmatrix} \mathbf{V}_s(x, \omega) \\ \mathbf{I}_s(x, \omega) \end{bmatrix} dx \tag{3-19}$$

The chain parameter matrix  $\mathbf{\Phi}(x)$  is calculated as

$$\mathbf{\Phi}(x) = e^{\begin{bmatrix} 0 & -Z \\ -Y & 0 \end{bmatrix} x} = \begin{bmatrix} \mathbf{\Phi}_{11}(x) & \mathbf{\Phi}_{12}(x) \\ \mathbf{\Phi}_{21}(x) & \mathbf{\Phi}_{22}(x) \end{bmatrix} \tag{3-20}$$

$$\begin{aligned}
\mathbf{\Phi}_{11}(x) &= \frac{1}{2} \left( e^{\sqrt{ZY}x} + e^{-\sqrt{ZY}x} \right) & \mathbf{\Phi}_{12}(x) &= -\frac{1}{2} \left( e^{\sqrt{ZY}x} - e^{-\sqrt{ZY}x} \right) \mathbf{Z}_C \\
\mathbf{\Phi}_{21}(x) &= -\frac{1}{2} \mathbf{Y}_C \left( e^{\sqrt{ZY}x} - e^{-\sqrt{ZY}x} \right) & \mathbf{\Phi}_{22}(x) &= \frac{1}{2} \mathbf{Z}_C^{-1} \left( e^{\sqrt{ZY}x} + e^{-\sqrt{ZY}x} \right) \mathbf{Z}_C
\end{aligned} \tag{3-21}$$

The characteristic impedance and admittance matrix are calculated by the TL parameters:

$$\mathbf{Z}_C = \mathbf{Z} \mathbf{T}_V^{-1} \boldsymbol{\gamma}^{-1} \mathbf{T}_V, \quad \mathbf{Y}_C = \mathbf{Z}^{-1} \mathbf{T}_V \boldsymbol{\gamma} \mathbf{T}_V^{-1}, \quad \boldsymbol{\gamma}^2 = \mathbf{T}_V^{-1} \mathbf{Z} \mathbf{Y} \mathbf{T}_V = \text{diag}\{\gamma_1^2, \dots, \gamma_n^2\} \tag{3-22}$$

where  $\mathbf{T}_V$  are  $N \times N$  nonsingular complex matrices used to diagonalizable the voltage and current matrix.

For the two-conductor system made up of a single line and the ground, the chain parameter matrix degenerates to

$$\begin{aligned}
\mathbf{\Phi}_{11}(x) &= \frac{e^{\gamma x} + e^{-\gamma x}}{2} & \mathbf{\Phi}_{12}(x) &= -\mathbf{Z}_C \frac{e^{\gamma x} - e^{-\gamma x}}{2} \\
\mathbf{\Phi}_{21}(x) &= -\frac{e^{\gamma x} - e^{-\gamma x}}{2} \cdot \mathbf{Z}_C^{-1} & \mathbf{\Phi}_{22}(x) &= \frac{e^{\gamma x} + e^{-\gamma x}}{2}
\end{aligned} \tag{3-23}$$

where  $\boldsymbol{\gamma}^2 = \mathbf{Z} \mathbf{Y}$ .

With the numerical results of the chain parameter matrix, the forcing function caused by the incident field is calculated analytically:

$$\begin{aligned} \mathbf{T}_V^{-1} \mathbf{V}_{FT}(l) &= \int_0^l \begin{pmatrix} \frac{e^{\sqrt{ZY}(l-x)} + e^{-\sqrt{ZY}(l-x)}}{2} e^{-jkx \cos \psi \cos \phi} \mathbf{A} \\ -\mathbf{Z}_C \frac{e^{\sqrt{ZY}(l-x)} - e^{-\sqrt{ZY}(l-x)}}{2} e^{-jkx \cos \psi \cos \phi} \mathbf{B} \end{pmatrix} dx \\ &= \frac{1}{2} \mathbf{A} \left( \frac{e^{-jkl \cos \psi \cos \phi} - e^{-\sqrt{ZY}l}}{-\sqrt{ZY} - jk \cos \psi \cos \phi} + \frac{e^{-jkl \cos \psi \cos \phi} - e^{-\sqrt{ZY}l}}{\sqrt{ZY} - jk \cos \psi \cos \phi} \right) \\ &\quad - \frac{1}{2} \mathbf{Z}_C \mathbf{B} \left( \frac{e^{-jkl \cos \psi \cos \phi} - e^{-\sqrt{ZY}l}}{-\sqrt{ZY} - jk \cos \psi \cos \phi} - \frac{e^{-jkl \cos \psi \cos \phi} - e^{-\sqrt{ZY}l}}{\sqrt{ZY} - jk \cos \psi \cos \phi} \right) \end{aligned} \quad (3-24)$$

$$\begin{aligned} \mathbf{T}_I^{-1} \mathbf{I}_{FT}(l) &= \int_0^l \begin{pmatrix} -\mathbf{Y}_C \frac{e^{\sqrt{ZY}(l-x)} - e^{-\sqrt{ZY}(l-x)}}{2} e^{-jkx \cos \psi \cos \phi} \mathbf{T}_V^{-1} \mathbf{A} \\ + \frac{e^{\sqrt{ZY}(l-x)} + e^{-\sqrt{ZY}(l-x)}}{2} e^{-jkx \cos \psi \cos \phi} \mathbf{A} \end{pmatrix} dx \\ &= -\frac{1}{2} \mathbf{Y}_C \mathbf{A} \left( \frac{e^{-jkl \cos \psi \cos \phi} - e^{-\sqrt{ZY}l}}{-\sqrt{ZY} - jk \cos \psi \cos \phi} - \frac{e^{-jkl \cos \psi \cos \phi} - e^{-\sqrt{ZY}l}}{\sqrt{ZY} - jk \cos \psi \cos \phi} \right) \\ &\quad + \frac{1}{2} \mathbf{B} \left( \frac{e^{-jkl \cos \psi \cos \phi} - e^{-\sqrt{ZY}l}}{-\sqrt{ZY} - jk \cos \psi \cos \phi} + \frac{e^{-jkl \cos \psi \cos \phi} - e^{-\sqrt{ZY}l}}{\sqrt{ZY} - jk \cos \psi \cos \phi} \right) \end{aligned} \quad (3-25)$$

Equation (3-25) can be simplified as:

$$\begin{bmatrix} \mathbf{V}_{FT}(l) \\ \mathbf{I}_{FT}(l) \end{bmatrix} = (-\Phi(l) + e^{-jkl \cos \psi \cos \phi}) \underbrace{\begin{bmatrix} -jk \cos \psi \cos \phi \mathbf{1} & \sqrt{ZY} \mathbf{Z}_C \\ \sqrt{ZY} / \mathbf{Z}_C & -jk \cos \psi \cos \phi \mathbf{1} \end{bmatrix}^{-1}}_{\mathbf{F}} \begin{bmatrix} \mathbf{A} \\ \mathbf{B} \end{bmatrix} \quad (3-26)$$

Equation (3-18) can be written as:

$$\begin{bmatrix} \mathbf{V}(l, \omega) \\ \mathbf{I}(l, \omega) \end{bmatrix} = \Phi(l) \left( \begin{bmatrix} \mathbf{V}(0, \omega) \\ \mathbf{I}(0, \omega) \end{bmatrix} + \begin{bmatrix} \mathbf{V}_{F1} \\ \mathbf{I}_{F1} \end{bmatrix} \right) + \begin{bmatrix} \mathbf{V}_{F2} \\ \mathbf{I}_{F2} \end{bmatrix} \quad (3-27)$$

where the forcing functions are split into two parts:

$$\begin{bmatrix} \mathbf{V}_{F1} \\ \mathbf{I}_{F1} \end{bmatrix} = -\mathbf{F} \begin{bmatrix} \mathbf{A} \\ \mathbf{B} \end{bmatrix}, \quad \begin{bmatrix} \mathbf{V}_{F2} \\ \mathbf{I}_{F2} \end{bmatrix} = e^{-jkl \cos \psi \cos \phi} \mathbf{F} \begin{bmatrix} \mathbf{A} \\ \mathbf{B} \end{bmatrix} = -e^{-jkl \cos \psi \cos \phi} \begin{bmatrix} \mathbf{V}_{F1} \\ \mathbf{I}_{F1} \end{bmatrix} \quad (3-28)$$

When only the induced responses on terminal loads of the TL are concerned, the simulation can be transferred into the simulation of a two-port (or  $N$ -port,  $N$  is the number of conductors) macromodel, as shown in Figure 3-5.

The difference between the two parts of forcing functions in (2-33) is a delay operation in the time domain. The time delay equals the difference between the time when the incident field reaches two ends of the TLs. Therefore, when a line with a length of  $l=l_1+l_2$  is divided into two connected sections, the macromodel for two sections is:

$$\begin{aligned}
\begin{bmatrix} \mathbf{V}(l_1, \omega) \\ \mathbf{I}(l_1, \omega) \end{bmatrix} &= \Phi(l_1) \left( \begin{bmatrix} \mathbf{V}(0, s) \\ \mathbf{I}(0, s) \end{bmatrix} - \mathbf{F} \begin{bmatrix} \mathbf{A} \\ \mathbf{B} \end{bmatrix} \right) + e^{-jkl_1 \cos \psi \cos \phi} \mathbf{F} \begin{bmatrix} \mathbf{A} \\ \mathbf{B} \end{bmatrix} \\
\begin{bmatrix} \mathbf{V}(l_2, \omega) \\ \mathbf{I}(l_2, \omega) \end{bmatrix} &= \Phi(l_2) \left( \begin{bmatrix} \Phi(l_1) \left( \begin{bmatrix} \mathbf{V}(0, s) \\ \mathbf{I}(0, s) \end{bmatrix} - \mathbf{F} \begin{bmatrix} \mathbf{A} \\ \mathbf{B} \end{bmatrix} \right) \\ + e^{-jkl_1 \cos \psi \cos \phi} \mathbf{F} \begin{bmatrix} \mathbf{A} \\ \mathbf{B} \end{bmatrix} - \mathbf{F} \begin{bmatrix} \mathbf{A} e^{-jkl_1 \cos \psi \cos \phi} \\ \mathbf{B} e^{-jkl_1 \cos \psi \cos \phi} \end{bmatrix} \right) + e^{-jkl_2 \cos \psi \cos \phi} \mathbf{F} \begin{bmatrix} \mathbf{A} e^{-jkl_1 \cos \psi \cos \phi} \\ \mathbf{B} e^{-jkl_1 \cos \psi \cos \phi} \end{bmatrix} \\
&= \Phi(l) \left( \begin{bmatrix} \mathbf{V}(0, \omega) \\ \mathbf{I}(0, \omega) \end{bmatrix} - \mathbf{F} \begin{bmatrix} \mathbf{A} \\ \mathbf{B} \end{bmatrix} \right) + e^{-jkl \cos \psi \cos \phi} \mathbf{F} \begin{bmatrix} \mathbf{A} \\ \mathbf{B} \end{bmatrix}
\end{aligned} \tag{3-29}$$

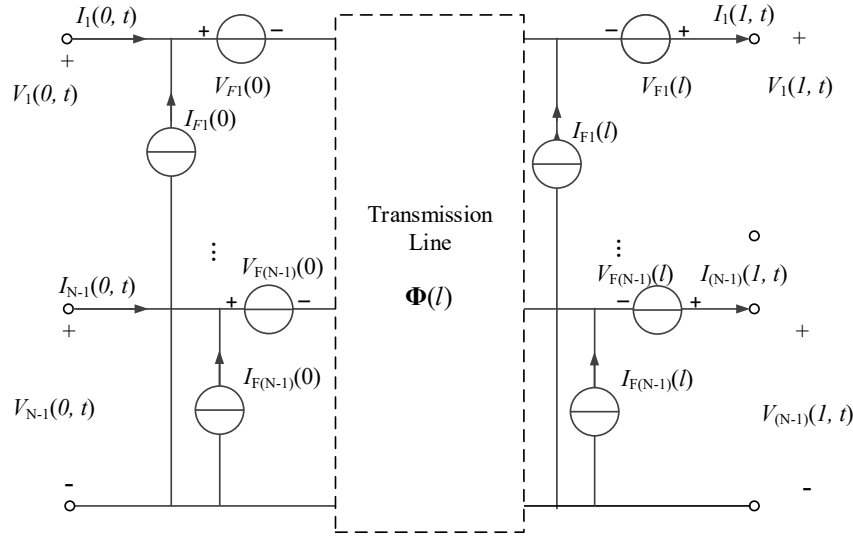


Figure 3-5 Macromodel with N-port for the N-1 TLs above the ground excited by external field

The macromodel has the advantage that if there is a load connected in the middle of the TL, a virtual breakpoint can be set and simulate the TL as two separate sections.

Add and subtract equations in (3-27) respectively, the following formulations can be obtained

$$\begin{aligned}
\mathbf{V}(0, \omega) - \mathbf{Z}_C(\omega) \mathbf{I}(0, \omega) &= \mathbf{H}(s) [\mathbf{V}(l, \omega) - \mathbf{Z}_C(\omega) \mathbf{I}(l, \omega)] + \mathbf{E}_1(\omega) \\
\mathbf{V}(l, \omega) + \mathbf{Z}_C(\omega) \mathbf{I}(l, \omega) &= \mathbf{H}(s) [\mathbf{V}(0, \omega) + \mathbf{Z}_C(\omega) \mathbf{I}(0, \omega)] + \mathbf{E}_2(\omega)
\end{aligned} \tag{3-30}$$

where

$$\mathbf{H}(\omega) = \mathbf{e}^{-\sqrt{\mathbf{ZY}l}} \tag{3-31}$$

The forcing function is expressed by  $\mathbf{E}_1(\omega)$  and  $\mathbf{E}_2(\omega)$

$$\begin{aligned}
\mathbf{E}_1(\omega) &= -\mathbf{H}(\omega) (\mathbf{V}_{F2} - \mathbf{Z}_C \mathbf{I}_{F2}) - (\mathbf{V}_{F1} - \mathbf{Z}_C \mathbf{I}_{F1}) \\
\mathbf{E}_2(\omega) &= \mathbf{H}(\omega) (\mathbf{V}_{F1} + \mathbf{Z}_C \mathbf{I}_{F1}) + (\mathbf{V}_{F2} + \mathbf{Z}_C \mathbf{I}_{F2})
\end{aligned} \tag{3-32}$$

When the load at both end of the conductors are linear systems, the closed-form of induced current can be obtained according to Equation (3-18) and boundary conditions in Equation (3-8)

$$\mathbf{I}(0) = \frac{\mathbf{E}_1(\omega)}{\Phi_{11}\mathbf{Z}_S + \mathbf{Z}_L\Phi_{22} - \Phi_{12} - \mathbf{Z}_L\Phi_{21}\mathbf{Z}_S} \quad (3-33)$$

$$\mathbf{I}(l) = \mathbf{I}_{FT}(l) + (\Phi_{22} - \Phi_{21}\mathbf{Z}_S)\mathbf{I}(0)$$

### 3.2.2 Time-domain macromodel for field-to-line coupling with nonlinear load

There are a large number of nonlinear devices in power systems, such as kinds of transient voltage surge suppressors, such as the MOAs along the power lines. Since they are important overvoltage protection devices and may limit the coupling responses excited by the field, it is necessary to consider their influence in the simulation.

For the simulation of the line connected with nonlinear elements, a time-domain macromodel of MTLs excited by the external fields is developed in this section.

Transfer (3-30) from the Laplace domain to the time domain:

$$\begin{aligned} \widehat{\mathbf{V}}(0,t) - \widehat{\mathbf{Z}}_C(t) * \widehat{\mathbf{I}}(0,t) &= \widehat{\mathbf{H}}(t) * [\widehat{\mathbf{V}}(l,t) - \widehat{\mathbf{Z}}_C(t) * \widehat{\mathbf{I}}(l,t)] + \widehat{\mathbf{E}}_1(t) \\ \widehat{\mathbf{V}}(l,t) + \widehat{\mathbf{Z}}_C(t) * \widehat{\mathbf{I}}(l,t) &= \widehat{\mathbf{H}}(t) * [\widehat{\mathbf{V}}(0,t) + \widehat{\mathbf{Z}}_C(t) * \widehat{\mathbf{I}}(0,t)] + \widehat{\mathbf{E}}_2(t) \end{aligned} \quad (3-34)$$

‘\*’ represents the convolution in the time domain,  $\mathbf{Z}_C(t)$ ,  $\mathbf{H}(t)$ ,  $\mathbf{E}_1(t)$ ,  $\mathbf{E}_2(t)$  can be transferred from the numerical results in the frequency domain. The boundary conditions determined by the loads at both ends are:

$$\begin{aligned} \widehat{\mathbf{V}}(0,t) &= \widehat{\mathbf{V}}_S + \widehat{\mathbf{Z}}_S\widehat{\mathbf{I}}(0,t) \\ \widehat{\mathbf{V}}(l,t) &= \widehat{\mathbf{V}}_L + \widehat{\mathbf{Z}}_L\widehat{\mathbf{I}}(l,t) \end{aligned} \quad (3-35)$$

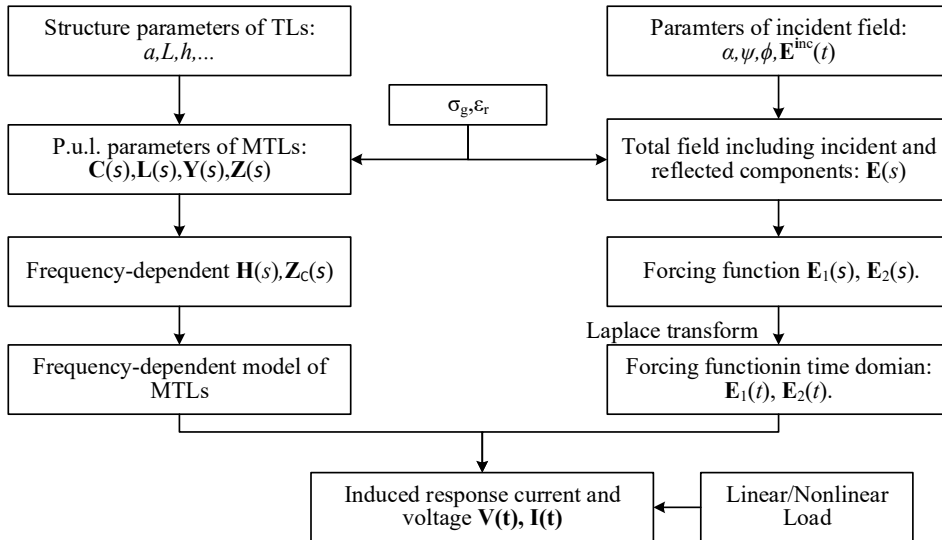


Figure 3-6 Comparison of far-end induced current by frequency-domain and time-domain macromodel

To solve the nonlinear load, Equation (3-34) can be implemented as a two-port network by using custom frequency-dependent components in time-domain circuit solver software such as the analog behavioral modeling controlled source in Spice, and the frequency-dependent (phase) model in PSCAD<sup>[74][75]</sup>. Here we achieved the macromodel in Spice

The procedure of constructing a time-domain macromodel for the TL excited by the

external fields is shown in Figure 3-6.

MOAs are widely-used transient voltage surge suppressors connected with TLs in power systems, they are the most significant nonlinear devices as well. The typical piecewise behavior of MOA nonlinear characteristics is represented in Figure 3-7<sup>[143]</sup>. It is divided into three regions according to the current density through the MOA. The voltage-current characteristic is approximately linear and exhibits capacitive behavior in region I, the leakage region, where the MOA is subjected to the power system operating voltage<sup>[138]-[140]</sup>. The MOA's electrical behavior is resistive in region II, the breakdown region. The resistance decreases and voltage is maintained near a clamping level in an extensive range of currents ranging from milliamperes to about  $10^3$  A/cm<sup>2</sup><sup>[140][141]</sup>.

In region III, the high current region, the decreasing rate in resistance of MOA reduces, where it is excited by lightning and many other kinds of overvoltage with peak current above kiloamperes.

The piecewise behavior of the nonlinear resistor can be defined by a 4-parameter logistic function referring to<sup>[142]</sup>, showing that the resistance changes slightly in regions I and III, and decreases rapidly in region II.

$$R = \frac{R_I}{(1 + (u/c)^d)} + \frac{R_{III}}{(u/b)^a} \quad (3-36)$$

where  $R_I$  — the leakage resistance at the low current region;  $R_{III}$  — the leakage resistance at the low current region and equivalent resistance in region III. They can be calculated from the residual voltage and current at MOA's clamping voltage  $c$ , and nominal residual voltage  $b$  at nominal discharge current, respectively. Parameters  $d$  and  $a$  are calculated by the current and voltage where the MOA works in region II and region III. The values of  $d$  and  $a$  are derived by the manufacturer's data for switching surges and typical lightning surges, as

$$\begin{aligned} d &= \log(R_I I_{\text{switching}} / V_{\text{switching}}) / \log(V_{\text{switching}} / c) \\ a &= \log(R_{III} I_{\text{lightning}} / V_{\text{lightning}}) / \log(V_{\text{lightning}} / b) \end{aligned} \quad (3-37)$$

The voltage-current behavior can be represented as:

$$i = \frac{u}{R_I / (1 + (u/c)^d) + R_{III} / (u/b)^a} \quad (3-38)$$

where  $i$  and  $u$  — the current and voltage of the nonlinear element  $R$  in the proposed model. It should be noticed that, for steep impulses,  $i$  and  $u$  do not represent the actual current and voltage through and across the MOA because of the existence of inductor  $L$  and capacitor  $C$ .

In fact, when MOA works in region III and part of region II, a dynamic nonlinear characteristic is observed as shown in Figure 3-7. The residual voltage across the MOA increases as the front time of the impulse current becomes faster<sup>[144]-[148]</sup>. The residual voltage under 1- $\mu$ s front-time impulse current is about 6%-10% higher than that under standard lightning surge (8/20  $\mu$ s)<sup>[144]</sup>; the residual voltage under very fast transient (VFT) overvoltage with nanosecond-level front time is 50%-60% higher<sup>[145]</sup>.



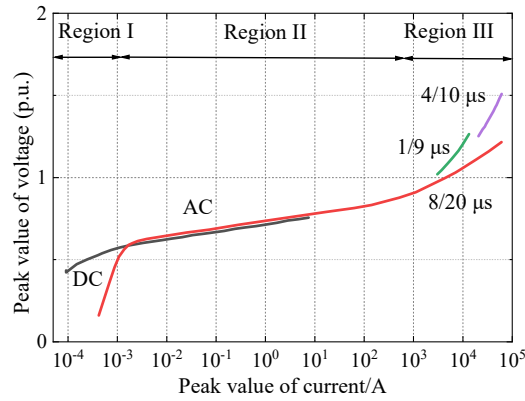


Figure 3-7. Typical voltage-current characteristics of MOA<sup>[143]</sup>

The existing nonlinear model of MOA has less consideration of the dynamic characteristics under impulse with nanosecond-level rise time. This may lead to the wrong conclusion that MOAs can limit the induced current and voltage and provide protection under various uncertainties of incident fields and lines.

A test platform was built to study the dynamic nonlinearity characteristics of MOA, as shown in Figure 3-8.

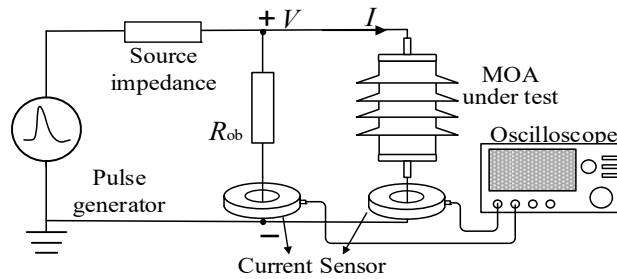


Figure 3-8 Schematic diagram of the experimental setup of a 10-kV MOA

The pulse generator is a multi-stage Marx circuit. The front time and pulse width of the output signal are controlled by the inductance and capacitance of the Marx circuit. Combined with the source impedance, it can be regarded as a pulse current source, which can generate impulses with nanosecond-level front time from 20 ns to 400 ns and impulses with microsecond-level front time from 1 μs to 30 μs. A low-inductance resistor  $R_{ob} = 300 \Omega$  was connected in parallel with the MOA under test, the voltage on the MOA could be obtained from the current through the resistor  $R_{ob}$ , to avoid the effect of the limited bandwidth of the capacitive voltage divider. The current sensors used in the experiment are Pearson 8590C with a bandwidth of 150 MHz. The oscilloscope used in the experiment is Tektronix DPO3054 with a bandwidth of 500 MHz.

Two types of MOA with different nominal voltages were tested. Their specifications are shown in Table 3-3. Their voltage-current characteristics obtained by the experiment are shown in Figure 3-9. The voltage is normalized to the residual voltage at nominal discharge current  $I=5 \text{ kA}$  with standard 8/20 μs lightning impulse. For both MOAs, the peak voltage increase when the front time becomes faster.

Table 3-3 Specifications of MOAs

| Parameters                                 | Voltage / kV |              |
|--|--------------|--------------|
|  | YH5WZ-17/45  | YH5WZ-5/13.5 |
| Nominal voltage                            | 17           | 5            |
| Reference Voltage at DC 1mA                | 24           | 7.5          |
| Residual voltage at 5 kA lightning impulse | 45           | 13.5         |
| Residual voltage at switching impulse      | 38.3         | 11.5         |
| Residual voltage at steep current          | 51.5         | 15.5         |

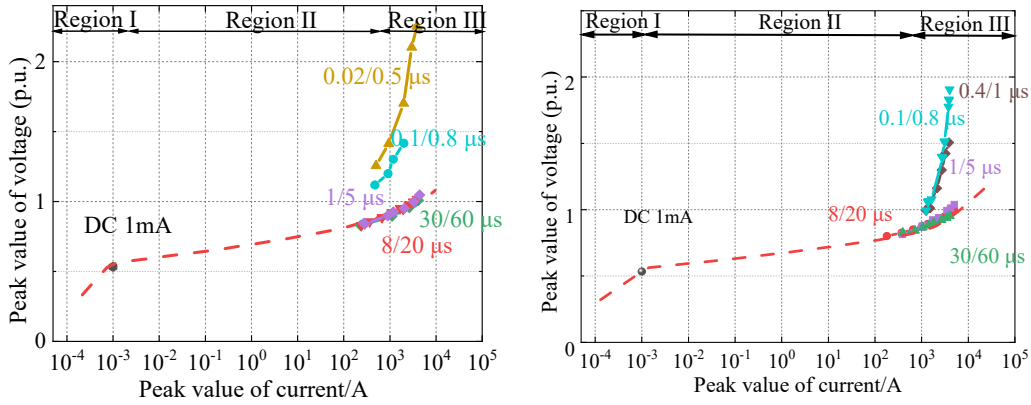


Figure 3-9. Voltage-current characteristics of MOAs. The symbol line shows the measurement results. The symbol dash lines are fitted from manufacturer's data by using Equation (3-38).

According to previous references and laboratory tests, the dynamic characteristic occurs mainly when MOA operates in region III and part of region II. In this region, being the current and voltage large, the nonlinear resistor modeled by Equation (3-38) can be approximated as

$$i \approx \frac{b}{R_{III}} \left( \frac{u}{b} \right)^{a+1} \quad (3-39)$$

Equation (3-39) is consistent with the form of the widely used power function of nonlinear resistance models<sup>[147]</sup>.

To represent the dynamic characteristic of MOA, that the residual voltage increases as the front time of the impulse current become faster, an improved equation is proposed to describe the dynamic nonlinear resistance in region III

$$i \approx \frac{b}{R_{III}} \left( \frac{u}{k(f_i)^{a/a+1} \cdot b} \right)^{a+1} \quad (3-40)$$

where  $k(f_i)$  — the frequency-dependent multiplication factor, which increases monotonically with the frequency of the current signal. As the rise time becomes faster, the higher the frequency domain of the current impulse is, the larger  $k$  is, and the residual voltage increases.

The multiplication factor  $k(f_i)$  can be represented by some discrete values from tests with different impulses, such as fast surges of 1/9 μs, and VFT of 100 ns, 20ns, etc. For each kind of impulse, the frequency is calculated by the front time; the voltage across the MOA under

nominal discharge current can be obtained from measured results, previous studies, or manufacturer's data; the value of the multiplication factor is calculated by the ratio of the voltage at the moment of current peak to the nominal residual voltage. This is because the voltage peak across the MOA is contributed by both the nonlinear resistance and the inductance, the overshoot contributed by inductance is large when the front time of the current impulse is fast. At the moment of current peak, the derivative of current with respect to time equals zero, the influence of inductance can be ignored, and the values of voltage and current can be seen as determined by the nonlinear resistance in the model.

Table 3-4 Multiplication factor table of a YH5WZ-17/45 MOA

| f(Hz)    | 0    | 3E4 | 6E4  | 2E5  | 2E6 | 1E7  |
|----------|------|-----|------|------|-----|------|
| $k(f_i)$ | 0.99 | 1   | 1.01 | 1.05 | 1.3 | 1.45 |

Therefore, the complete dynamic nonlinear resistance  $R$  can be described by the equation

$$i = \frac{u}{R_I / (1 + (u / c)^d) + R_{III} / (u / (k(f_i) \cdot b))^a} \quad (3-41)$$

The MOA model resistance defined by this equation is regarded as a dynamic model. In contrast, the model with a nonlinear resistance  $R$  described by Equation (3-38) can be regarded as a static equation-based model.

Based on the measured results, a multiplication factor table for the dynamic characteristic of the YH5WZ-17/45 MOA is provided in Table 3-4. It should be noticed that the values may vary for other MOAs from different manufacturers. It is recommended to use the optimization algorithm to achieve better parameters for the model, such as the genetic algorithm and harmony search method<sup>[154][155]</sup>.

The proposed model has piecewise nonlinear characteristics and frequency-dependent characteristics simultaneously. To solve this mixed frequency/time domain element, a new circuit element is defined based on the analog behavioral modeling (ABM) feature of Spice. Spice simulators can serve as a programming language and solve general mathematical problems by transforming them into electric circuits with controlled sources<sup>[153]</sup>.



(a) Proposed circuit model for MOA (b) Proposed dynamic nonlinear resistance defined by (3-41)

Figure 3-10 Proposed MOA model

When applying the static equation-based resistor  $R$ , a voltage-controlled current source  $G_R$  is defined by (3-38). When applying the dynamic equation-based resistor described by Equation (3-41), the newly defined equation-based resistor is constructed by two controlled sources  $G_{R1}$  and  $G_{R2}$  connected in series, as shown in Figure 3-10 (b).  $R_1$  and  $R_2$  are two large resistances of  $10^{15} \Omega$  to avoid the non-convergence and instability of the solution. In fact, the

currents through  $R_1$  and  $R_2$  are small so they can be ignored. Therefore, the behavior of the newly defined element is represented by

$$u = u_1 + u_2, i \approx i_1 \approx i_2$$

where  $u_1$ ,  $u_2$  and  $i_1$ ,  $i_2$  are voltage and current across controlled sources  $G_{R1}$  and  $G_{R2}$ , respectively.

The controlling equations of  $G_{R1}$  and  $G_{R2}$  are as

$$\begin{cases} k(f_i)^a \cdot i_1 = i_1', & i_1' = \frac{u_1}{R_{III} / (u / b)^a} \\ i_2 = \frac{u_2}{R_I / (1 + (u / c)^d)} \end{cases} \quad (3-42)$$

$G_{R1}$  is a frequency response table voltage-controlled current sources, defined by the first two equations in (3-42). The frequency response table is aiming to realize the multiplication factor  $k(f_i)$ . The auxiliary variable  $i_1'$  is introduced to ensure that the multiplication factor is directly multiplied by the current as it relates to the frequency of the current.  $G_{R2}$  is an expression-based voltage-controlled current source represented by the last equation in (3-42). The Spice netlist defining the improved dynamic equation-based resistor is attached.

**Spice netlist** for the equation-based Resistor with Dynamic Nonlinear Characteristic

---

```
.SUBCKT NonlinearR 1 2
G1 1 3 FREQ {V(1,3) / (R_III*((b) / abs(V(1,2))) ** a)} = MAG
+ (0, k(0)-a, 0)
+ ...
+ (f, k(f)-a, 0)
RG1 1 2 1E15
G2 3 2 VALUE={V(3,2) / (R_I / (1 + (abs(V(1,2))/c) ** d))}
RG2 2 3 1E15
.ENDS NonlinearR
```

---

The performance of the proposed model was investigated for two MOAs with different nominal voltages. The simulation was performed in Spice. The influence of the current amplitude and frequency on the model were compared with the measured result based on the test platform in Fig. 2.

Fig. 6 shows the responses of a YH5WZ-17/45 MOA under different impulses with peak values around 1 kA and 4 kA. The static model refers to the conventional static model with the resistor defined by (1). The dynamic model refers to the proposed model with a dynamic nonlinear resistor defined by (5). The capacitance and inductance in two models are the same.

For the impulse with 30- $\mu$ s front time, there is almost no difference between the two models. The improvement of the dynamic model becomes significant as the pulse front time becomes faster, especially when the current is large. For the surges with 20-ns front time, the proposed model greatly improves the predicted waveform at the early 500 ns.

The voltage-current curves of the YH5WZ-17/45 MOA are drawn in Figure 3-12. For the impulses with front time of 1, 8, and 30  $\mu$ s, both models are in good agreement with the

experiment. Measured results show that there is still a nonlinear relationship between the voltage and current under VFT, even though the nonlinearity is weaker than that under the lightning surges. The variation of the peak voltage under VFT simulated by the static model is relatively linear, which is mainly contributed by inductance in the MOA model. It implied that the dynamic nonlinear characteristics of the MOA can be hardly described by only modifying the value of the inductance in the MOA model. By comparison, the dynamic model shows good agreement with the measured results.

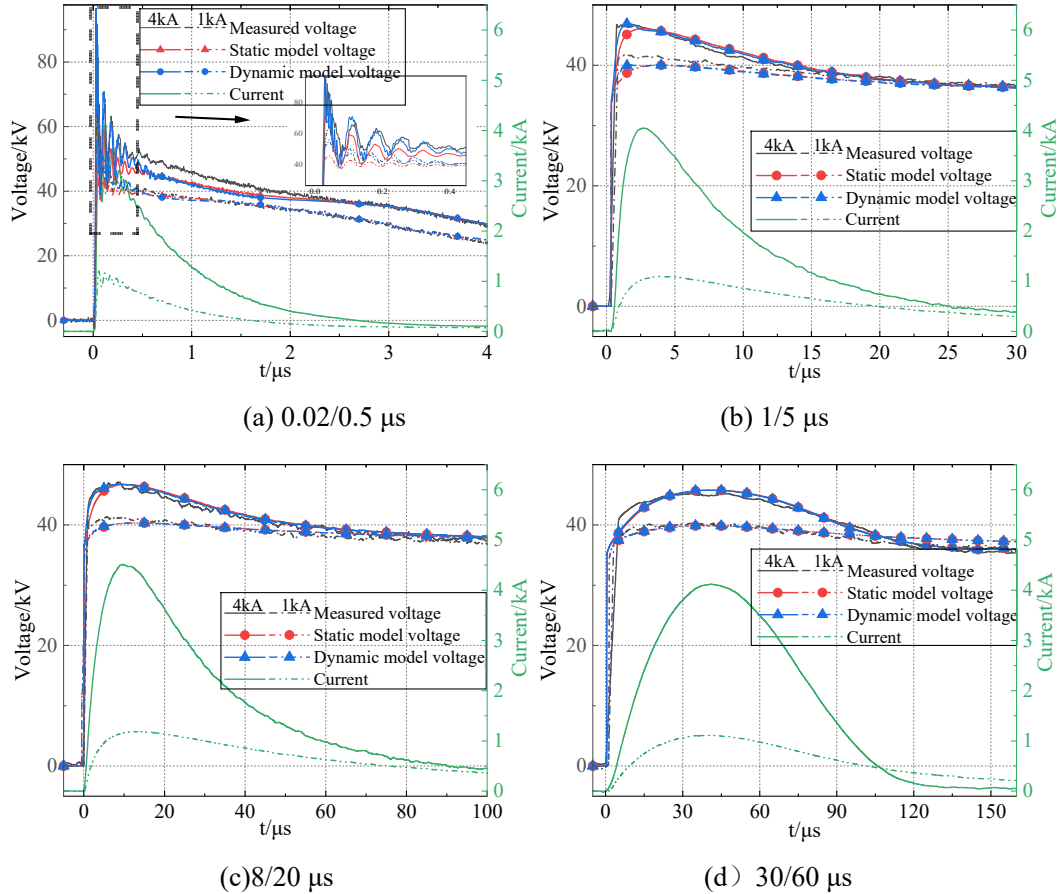


Figure 3-11. Responses of a YH5WZ-17/45 MOA under different current impulses obtained by measurement and simulation

To quantitatively evaluate the performance of different models, the percentage error of the peak voltage and absorbed energy of the MOA were used[141]

$$P_e = \left| \frac{(P_s - P_m)}{P_m} \right| \cdot 100\%$$

$$E_e = \left| \frac{\left( \int_0^t V_s(t) I_m(t) dt - \int_0^t V_m(t) I_m(t) dt \right)}{\int_0^t V_m(t) I_m(t) dt} \right| \cdot 100\% \quad (3-43)$$

where  $V$ ,  $I$ , and  $P$  are the voltage, current, and peak voltage of the MOA. s and m in the subscript represent that the quantity are obtained by simulation and measurement, respectively.

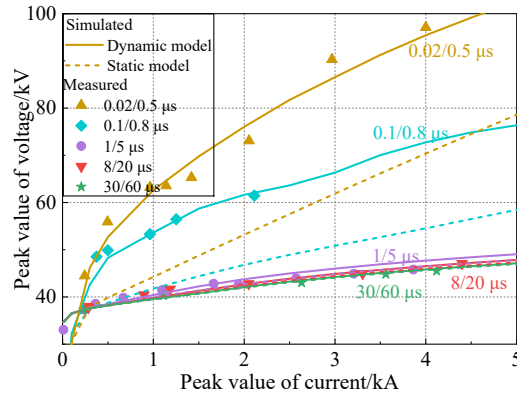


Figure 3-12. Voltage-current characteristics of a YH5WZ-17/45 MOA obtained by simulation and measurement

The coefficient of determination  $R^2$  was defined to evaluate the performance of the models in the wide range of amplitude and frequency:

$$R^2 = 1 - \left( \sum (P_s - P_m)^2 \right) / \left( \sum (P_m - \bar{P}_m)^2 \right) \quad (3-44)$$

where  $N$  refers to the total number of tests for each sample.  $\bar{P}_m$  is the mean value of the peak voltage.

Table 3-5 Errors in the Peak Voltage, Absorbed Energy and the Coefficient of Determination  $R^2$  in a wide range of amplitude and frequency

| Analysis Parameters |         | $P_e / \%$    |               |                  |               | $E_e / \%$    |               |                  |               | $1-R^2$ |
|---------------------|---------|---------------|---------------|------------------|---------------|---------------|---------------|------------------|---------------|---------|
| Sample              | Model   | 30/60 $\mu s$ |               | 0.02/0.5 $\mu s$ |               | 30/60 $\mu s$ |               | 0.02/0.5 $\mu s$ |               | /       |
|                     |         | $\approx 1kA$ | $\approx 4kA$ | $\approx 1kA$    | $\approx 4kA$ | $\approx 1kA$ | $\approx 4kA$ | $\approx 1kA$    | $\approx 4kA$ |         |
| YH5WZ-17/45         | Dynamic | 0.91          | 2.10          | 0.67             | 1.61          | 1.25          | 0.54          | 1.54             | 5.3           | 0.03    |
|                     | Static  | 0.46          | 3.03          | 25.5             | 27.9          | 1.52          | 0.55          | 2.58             | 9.05          | 1.53    |
| YH5WZ-5/13.5        | Dynamic | 0.09          | 0.15          | 0.34             | 3.81          | 1.22          | 0.51          | 0.20             | 3.81          | 0.04    |
|                     | Static  | 0.09          | 0.23          | 20.6             | 22.8          | 1.22          | 0.51          | 1.74             | 5.02          | 1.31    |

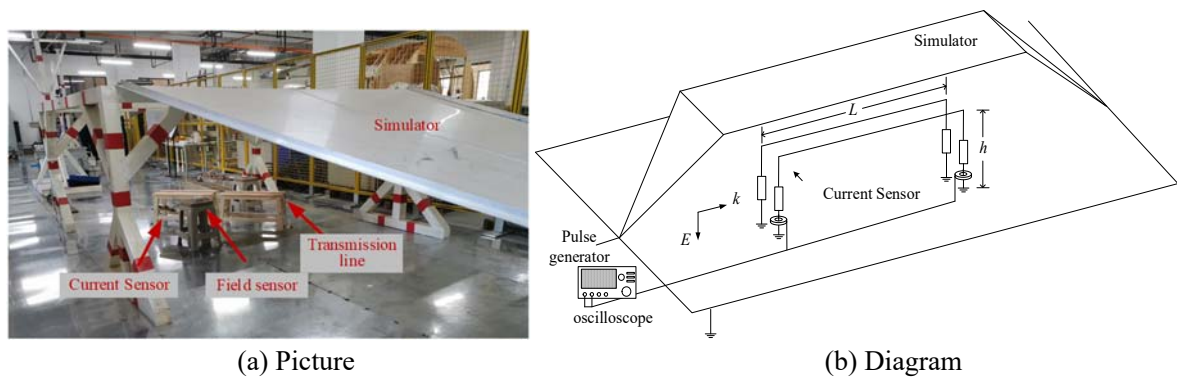
Table 3-4 shows the errors between the simulation and measurement under the fastest and the slowest pulses we used in tests. The proposed dynamic model improves the prediction for both the peak voltage and absorbed energy of the MOA, the errors are less than 6%. The prediction for peak voltage across the MOA under VFT is improved significantly from more than 20% to less than 4%. The decrease of  $1-R^2$  indicates that the proposed model provides better simulation than the static model for the peak value in a wide range of amplitude and frequency.

Both the macromodel of transmission lines excited by the external field and the dynamic nonlinear load of MOA are derived based on equations and are implemented in Spice. Therefore, they can be easily combined together to simulate the transmission lines with nonlinear loads.

### 3.2.3 Validation of the field-to-line coupling macromodel

#### 1) Case 1: Validation by comparison with the experiment

To validate the established frequency-domain and time-domain macromodel for TLs excited by fields. A field-to-line coupling experiment platform is established as shown in Figure 3-13. An overhead line is settled in an electromagnetic pulse simulator. The type of the line is JGG-10kV, the diameter of the multistrand stranded tinned copper conductor is 1.5 mm, and the thickness of the silicone rubber insulation coating is 3.6 mm. The dielectric coating causes an increase in the p.u.l. The capacitance of the TL, which is corrected by the finite element method<sup>[82]</sup>. The line under test is 1.6 m-long and lying at a height of 0.42 m. The loads at both ends are  $110 \Omega$  non-inductance resistors.



(a) Picture (b) Diagram  
Figure 3-13 The field-to-line coupling experiment platform

The incident field waveform generated by the simulator is a double exponential (DEXP) waveform with a rise time of 5 ns and pulse width of 40 ns. The field is total vertically polarized with an elevation angle of zero. The ground is made of aluminum and can be regarded as perfect ground. The actual time domain waveform of the electric field is measured and shown in Figure 3-14.

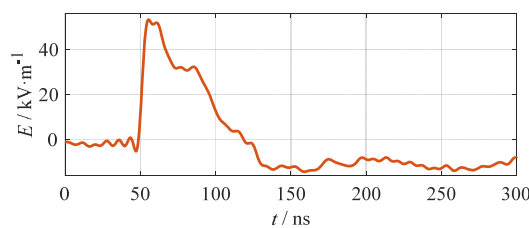
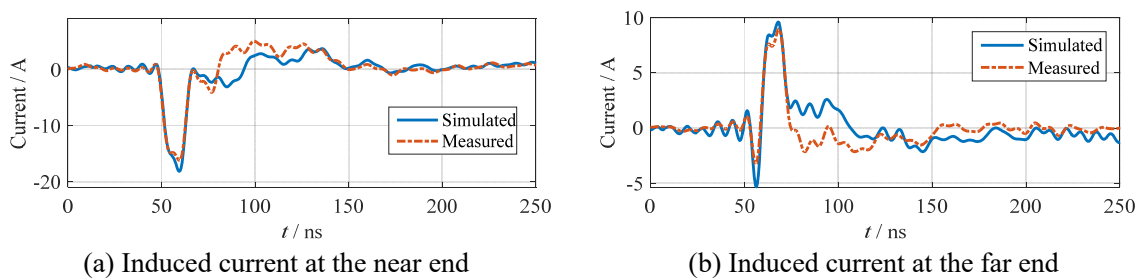


Figure 3-14 Time domain waveform of the electric field in the simulator



(a) Induced current at the near end (b) Induced current at the far end  
Figure 3-15 Induced current on the TL (The simulation result is obtained by frequency domain macromodel. Parameters for incident field:  $\phi=0^\circ$ .)

The currents at both loads are measured by the current sensor Pearson 8585C with a band

wide up to 200 MHz. The oscilloscope used in the experiment is Tektronix DPO3054 with a bandwidth of 500 MHz. The positive direction of current is defined as the direction flowing to the ground.

The simulation results are obtained by the frequency model and its inverse Fourier transform. The induced currents at both ends are shown in Figure 3-15. The simulation and measured results are in good agreement.

2) Case 2: Field-to-line coupling responses with nonlinear load

For the MOA connected to the lines in the power system, parts of the MOAs are settled at the terminal of TLs and connected in parallel with the equipment under protection. Parts of the MOAs are settled along the TLs, especially in the low-voltage level power system. Combining the nonlinear model with the simulation of field-to-line coupling, single lines with nonlinear load at different positions excited by the external field are simulated.

Figure 3-16 shows the simulation for an elevated power line with a MOA connected in parallel with the terminal load. With the decrease of the incident field azimuth angle, the amplitude of the coupling response increases, and the rise time becomes faster. The simulation with the conventional static MOA provides residual voltage with similar peak values under different incident fields. In contrast, the simulation with the proposed dynamic MOA model can represent the variation of the voltage on the MOA when the rise times of the coupling response is different.

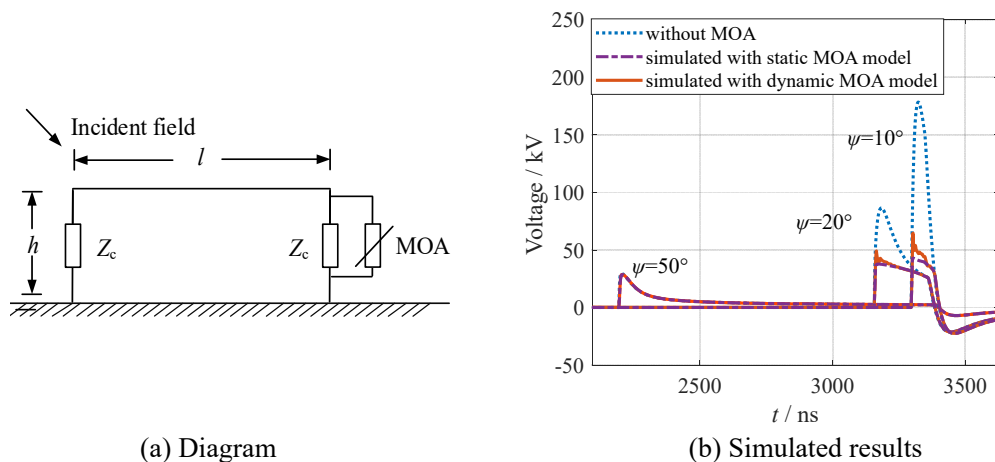


Figure 3-16 The field-to-line coupling responses with and without MOA. Parameters:  $l=1000$  m,  $h=1$  m,  $\varphi=0^\circ$ ,  $\alpha=20^\circ$ ,  $\psi=50^\circ, 20^\circ, 10^\circ$ .

In order to simulate the influence of the MOA settled along the line, virtual endpoints are set for the TLs, where MOA is connected with the lines. The line in Figure 3-17 (a) are simulated as two connected segments by the macromodel.

The results in Figure 3-17 (b) show that, when the MOA is close to the terminal equipment, it can limit the induced voltage for the terminal load. When the distance between MOA and terminal equipment increases, the MOA cannot provide efficient protection for the terminal load. When the distance is greater than an effective coupling length (ECL), although the induced voltage can be greatly reduced at the position of the MOA, large coupling responses are generated on the line behind the MOA. Therefore, the MOA at a distance from



the terminal of the line cannot reduce the amplitude of induced voltage on the terminal load, it can only reduce the pulse width slightly.

The ECL can be calculated as<sup>[137]</sup>

$$l_{ECL} \approx T_r \frac{v}{1 - v/c \cos \phi \cos \psi} \quad (3-45)$$

where  $v$  — the velocity of the coupling responses propagating along the lines;  $T_r$  — the rise time of the incident field.

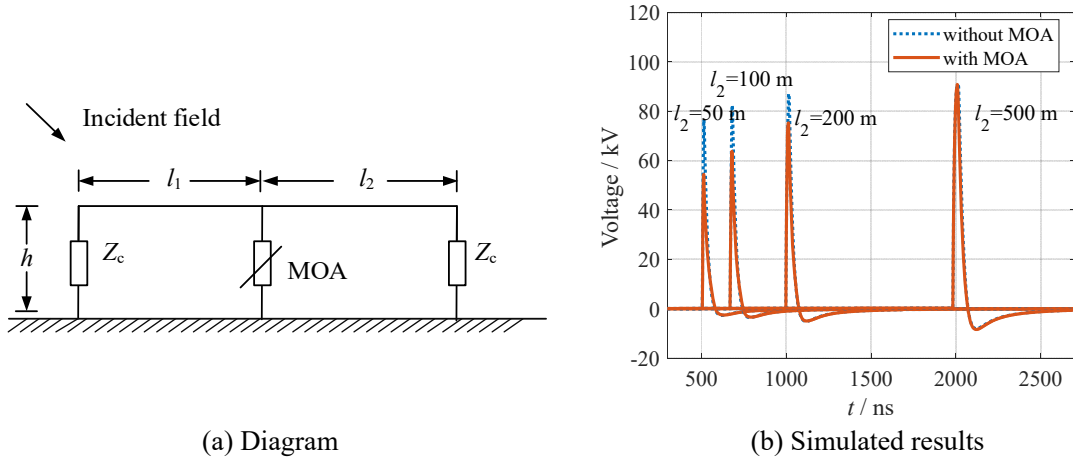


Figure 3-17 The field-to-line coupling responses with and without MOA. Parameters:  $\phi=0^\circ$ ,  $\alpha=20^\circ$ ,  $\psi=30^\circ$ ,  $h=1$  m,  $l_1=100$  m,  $l_2=50, 100, 200, 500$  m.

When the length is larger than ECL, the amplitude of coupling responses will not increase very much, as shown in Figure 3-18. The polarization of the incident field does not affect the ECL. The increase in the rise time of the incident field signal will lead to a longer ECL and higher amplitude of the induced responses.

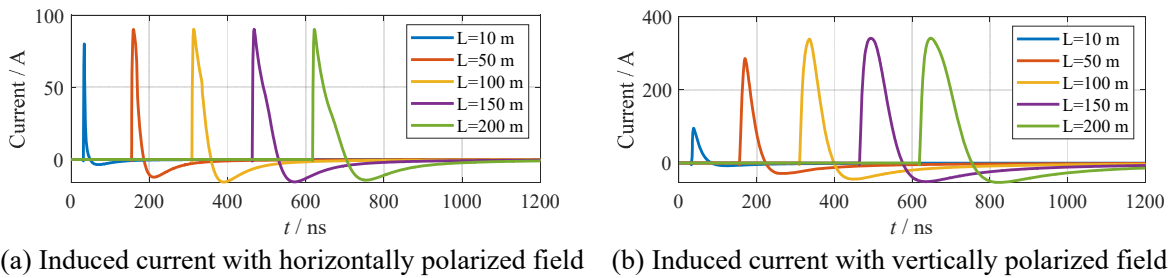


Figure 3-18 Influence of the length of the line on the induced current (Parameters:  $h=1$  m,  $\psi=10^\circ$ ,  $\phi=20^\circ$ . (a)  $\alpha=90^\circ$ . (b)  $\alpha=0^\circ$ .)

The saturation of the FWHM of the coupling response occurs at a longer length than the saturation of amplitude, as shown in Figure 3-18 (b). Other ECL of the line can be defined to estimate the severe case of FWHM of the coupling responses:

$$l_{ECL2} \approx T_{FWHM} \frac{v}{1 - v/c \cos \phi \cos \psi} \quad (3-46)$$

where  $T_{FWHM}$  refers to the full width at half maxima of the incident field.

The length of power lines in the power system is usually several kilometers. The ECL

can be used to estimate the critical length of the lines and simplify the simulation of TLs in complex networks with nonlinear loads.

### 3.3 Stochastic model of field-to-line coupling based on polynomial chaos expansion

Due to quantitative analysis based on the deterministic model, many influence variables may have great impacts on the coupling response, such as the height, radius of the lines, waveform, polarization angles, and incident angles of the field. The intrusive PCE method is the preferred choice for uncertainty quantification of problems with analytic forms. Meanwhile, the intrusive PCE has the convenience of combining with the macromodel of the objective function and is solved by simulation software<sup>[157]-[159]</sup>.

The central concept is to construct a surrogate model instead of the original objective function. The surrogate model is constructed by projecting the objective function on a set of orthogonal polynomial basis functions  $\{\psi_k\}_{k \in \mathbb{N}_0}$ , and then using the set of  $d$ -order truncated orthogonal polynomials to approximate the stochastic problem

$$y(\xi) = c_0 \psi_0(\xi) + \sum_{m=1, \dots, d} c_m \psi_m(\xi) + R_n(\xi). \quad (3-47)$$

where  $\xi$  — the vector collecting the independent and normalized variables. The polynomial basis functions for multivariate are the product of the polynomial basis functions of univariate:

$$\psi_m(\xi_1, \xi_2, \dots, \xi_n) = \prod_{i=1}^n \phi_{a_i^m}(\xi_i). \quad (3-48)$$

where  $\phi_{a_i^m}$  with subscript  $a_i^m$  represents the univariate basis functions for the  $i$ -th variable in the  $m$ -th multivariate basis functions.

The basic functions are mutually orthogonal according to the definition of polynomial orthogonality

$$\langle \phi_k(\xi), \phi_n(\xi) \rangle = \int_{\Omega} \phi_k(\xi) \phi_n(\xi) p(\xi) d\xi = \|\phi_k\|^2 \delta_{k,n} \quad (3-49)$$

$$\langle \psi_{k_1}(\xi), \psi_{k_2}(\xi) \rangle = \int_{\Omega} \psi_{k_1}(\xi) \psi_{k_2}(\xi) p(\xi) d\xi = \delta_{k_1, k_2} \prod_{i=1}^n \|\phi_{k_{1a}^i}\|^2 \quad (3-50)$$

where  $\|\cdot\|^2$  denotes the Euclidean 2-norm.  $\delta_{mn}$  is the Kronecker operator

$$\delta_{mn} = \begin{cases} 1, & m = n \\ 0, & m \neq n \end{cases}. \quad (3-51)$$

When the parameters are from normal distributions  $N(0,1)$ , the univariate basis functions are called Hermite polynomials<sup>[168][89]</sup>:

$$\begin{aligned} \phi_1 &= 1, & \phi_2 &= \xi, & \phi_3 &= \xi^2 - 1 \\ \phi_4 &= \xi^3 - 3\xi, & \phi_5 &= \xi^4 - 6\xi^2 + 3 \\ \phi_6 &= \xi^5 - 10\xi^3 + 15\xi \end{aligned} \quad (3-52)$$

There is an analytical solution for the inner product of each univariate basis function:

$$\|\phi_k\|^2 = k! \quad (3-53)$$

When the basic functions are orthogonal and complete basic functions, the truncation error term  $R_n(\xi)$  is orthogonal to the subspace consisting of  $d$ -order polynomials  $\{\psi_k\}_{k=1,\dots,d}$ . It is always the most optimal truncated, which means that the truncation error is monotonically decreasing with the truncation order.

One of the eases of the PCE is that the first two order moment quantities of the PCE are statistical results themselves. The value of the expectation of the uncertainty output  $y(\xi)$  equals the 0-order term. The variance of  $y(\xi)$  equals the sum of squares of the expansion coefficients with weight. Thus, the analysis quantities of the output variables can be performed directly by using the surrogate model.

### 3.3.1 Stochastic model with uncertainties of lines

When considering the parameters of the lines excited by the incident field, such as the radius and height of the lines, assuming the parameters are from normal distributions, the p.u.l. parameters of the TLs and the total voltage and current along the lines can be decomposed by using the multivariate Hermite polynomials PCE.

$$\begin{aligned} \mathbf{V}(x, \omega, \xi^{(L)}) &= \sum_m^p c_m^{(V)}(x, \omega) \psi_m(\xi^{(L)}) \\ \mathbf{I}(x, \omega, \xi^{(L)}) &= \sum_m^p c_m^{(I)}(x, \omega) \psi_m(\xi^{(L)}) \end{aligned} \quad (3-54)$$

$$\mathbf{Z}(x, \omega, \xi^{(L)}) = \sum_m^p c_m^{(Z)} \psi_m(\xi^{(L)}), \quad \mathbf{Y}(x, \omega, \xi^{(L)}) = \sum_m^p c_m^{(Y)} \psi_m(\xi^{(L)}) \quad (3-55)$$

Equations in (3-54) can be regarded as the stochastic model of the transmission line with uncertainties excited by the incident field. The stochastic characteristics caused by the uncertain variables are represented by the combination of  $\psi_m(\xi^{(L)})$ . The coefficients  $c_m^{(V)}$ ,  $c_m^{(I)}$  are undefined and need to be solved. The coefficient  $c_m^{(Z)}$ ,  $c_m^{(Y)}$  in (3-55) can be solved from the Galerkin projection of (3-3).

$$\begin{aligned} c_m^{(Z)} &= \int_{\Omega} \psi_m(\xi) \mathbf{Z}(\xi) p(\xi) d\xi / \langle \psi_m(\xi), \psi_m(\xi) \rangle \\ c_m^{(Y)} &= \int_{\Omega} \psi_m(\xi) \mathbf{Y}(\xi) p(\xi) d\xi / \langle \psi_m(\xi), \psi_m(\xi) \rangle \end{aligned} \quad (3-56)$$

Substitute the PCE of voltage and current and the p.u.l. parameters into (3-1),

$$\begin{aligned} \frac{d}{dx} \sum_m^p c_m^{(V)}(\omega) \psi_m(\xi^{(L)}) + \left( \sum_m^p c_m^{(Z)} \psi_m(\xi^{(L)}) \right) \left( \sum_m^p c_m^{(I)}(\omega) \psi_m(\xi^{(L)}) \right) &= \mathbf{V}_s(x, \omega) \\ \frac{d}{dx} \sum_m^p c_m^{(I)}(\omega) \psi_m(\xi^{(L)}) + \left( \sum_m^p c_m^{(Y)} \psi_m(\xi^{(L)}) \right) \left( \sum_m^p c_m^{(V)}(\omega) \psi_m(\xi^{(L)}) \right) &= \left( \sum_m^p c_m^{(Y)} \psi_m(\xi^{(L)}) \right) \mathbf{I}'_s(x, \omega) \end{aligned} \quad (3-57)$$

Do the inner product of the equation and basic functions  $\psi_m$ ,

$$\begin{aligned} \frac{d}{dx} c_m^{(V)}(\omega) + \sum_{k_1}^p c_{k_1}^{(I)} \left( \sum_{k_2}^p c_k^{(Z)}(\omega) \alpha_{mk_1k_2} \right) &= \delta_{1,m} \mathbf{V}_s(x, \omega) \\ \frac{d}{dx} c_m^{(I)}(\omega) + \sum_{k_1}^p c_{k_1}^{(V)} \left( \sum_{k_2}^p c_k^{(Y)}(\omega) \alpha_{mk_1k_2} \right) &= c_m^{(Y)} \mathbf{I}'_s(x, \omega) \end{aligned} \quad (3-58)$$

A new set of equations can be obtained:

$$\begin{aligned} \frac{d}{dx} \begin{bmatrix} c_1^{(V)}(x, \omega) \\ \dots \\ c_p^{(V)}(x, \omega) \end{bmatrix} + \underbrace{\begin{bmatrix} Z'_{1,1} & \dots & Z'_{1,p} \\ \dots & Z'_{m,k_1} & \dots \\ Z'_{p,1} & \dots & Z'_{p,p} \end{bmatrix}}_{\mathbf{Z}'} \begin{bmatrix} c_1^{(I)}(x, \omega) \\ \dots \\ c_p^{(I)}(x, \omega) \end{bmatrix} &= \begin{bmatrix} \mathbf{V}_s(x, \omega) \\ \mathbf{0} \\ 0 \end{bmatrix} \\ \frac{d}{dx} \begin{bmatrix} c_1^{(I)}(x, \omega) \\ \dots \\ c_p^{(I)}(x, \omega) \end{bmatrix} + \underbrace{\begin{bmatrix} Y'_{1,1} & \dots & Y'_{1,p} \\ \dots & Y'_{m,k_1} & \dots \\ Y'_{p,1} & \dots & Y'_{p,p} \end{bmatrix}}_{\mathbf{Y}'} \begin{bmatrix} c_1^{(V)}(x, \omega) \\ \dots \\ c_p^{(V)}(x, \omega) \end{bmatrix} &= \begin{bmatrix} Y'_{1,1} & \dots & Y'_{1,p} \\ \dots & Y'_{m,k_1} & \dots \\ Y'_{p,1} & \dots & Y'_{p,p} \end{bmatrix} \begin{bmatrix} \mathbf{I}'_s(x, \omega) \\ \mathbf{0} \\ 0 \end{bmatrix} \end{aligned} \quad (3-59)$$

The distributed sources caused by the incident field only appear in the first row of the function group. The elements in  $\mathbf{Z}'$ ,  $\mathbf{Y}'$  are calculated as follows:

$$Z'_{m,k_1} = \sum_{k_2}^p c_k^{(Z)}(s) \alpha_{m,k_1,k_2}, \quad Y'_{m,k_1} = \sum_{k_2}^p c_k^{(Y)}(s) \alpha_{m,k_1,k_2} \quad (3-60)$$

$$\alpha_{m,k_1,k_2} = \frac{\langle \psi_m(\xi^{(L)}), \psi_{k_1}(\xi^{(L)}) \psi_{k_2}(\xi^{(L)}) \rangle}{\langle \psi_m(\xi^{(L)}), \psi_m(\xi^{(L)}) \rangle} \quad (3-61)$$

New matrices  $\mathbf{Z}'$ ,  $\mathbf{Y}'$  construct telegraph equations for a group of augmented TLs excited with distributed source only on the first line.  $c_m^{(V)}, c_m^{(I)}$  which is the voltage and current of each line in the augmented transmission lines system. (3-59) can be solved as a deterministic question. Since we are concerned about the voltage and current at the terminals of the lines, the unknown coefficients  $c_m^{(V)}(0, \omega), c_m^{(I)}(0, \omega), c_m^{(V)}(l, \omega), c_m^{(I)}(l, \omega)$  in the stochastic model (3-59) can be solved by using the frequency-domain macromodel of the augmented TL system. Equation (3-59) can also be converted into the time domain by Laplace transform and solved by the time-domain macromodel as well.

However, the variation of the line parameters may have impacts on the distributed source  $\mathbf{V}_s$  and  $\mathbf{I}_s$  caused by the incident fields. For example, when the height of the line changes, the total magnetic flux passing through the cross-section of the transmission lines changes. The height of the lines is a significant variable in the distributed sources as well, as shown in (3-17). The distributed source should be decomposed by PCE as well.

$$\begin{aligned} \mathbf{V}_s(x, \omega) &= \sum_m^p c_m^{(VS)}(\omega) \psi_m(\xi^{(L)}) \\ \mathbf{I}'_s(x, \omega) &= \sum_m^p c_m^{(VS)}(\omega) \psi_m(\xi^{(L)}) \end{aligned} \quad (3-62)$$

Thus, the Equation (3-59) is rewritten as:

$$\begin{aligned} \frac{d}{dx} \begin{bmatrix} c_1^{(V)}(x, \omega) \\ \dots \\ c_p^{(V)}(x, \omega) \end{bmatrix} + \mathbf{Z}' \begin{bmatrix} c_1^{(I)}(x, \omega) \\ \dots \\ c_p^{(I)}(x, \omega) \end{bmatrix} &= \begin{bmatrix} c_1^{(VS)} \\ \dots \\ c_m^{(VS)} \end{bmatrix} \\ \frac{d}{dx} \begin{bmatrix} c_1^{(I)}(x, \omega) \\ \dots \\ c_p^{(I)}(x, \omega) \end{bmatrix} + \mathbf{Y}' \begin{bmatrix} c_1^{(V)}(x, \omega) \\ \dots \\ c_p^{(V)}(x, \omega) \end{bmatrix} &= \mathbf{Y}' \begin{bmatrix} c_1^{(IS)} \\ \dots \\ c_m^{(IS)} \end{bmatrix} \end{aligned} \quad (3-63)$$

To validate the stochastic model of TLs excited by field, a 100 m-long overhead line on the lossy ground excited by a field with the Bell HEMP waveform is studied<sup>[45]</sup>. Loads at both ends of the lines are 100  $\Omega$ . The diameter of the lines is 10 mm. The height of the line is a random variable from Gaussian distribution  $N(10,2)$  (m), and can be decomposed by the Hermite polynomials PCE:

$$h = \sum_m^p c_m^{(h)} \phi_m(\xi) \quad (3-64)$$

$\mathbf{Z}'$ ,  $\mathbf{Y}'$  are calculated by (3-60).  $\mathbf{V}_s$ ,  $\mathbf{I}_s$  are calculated as follows:

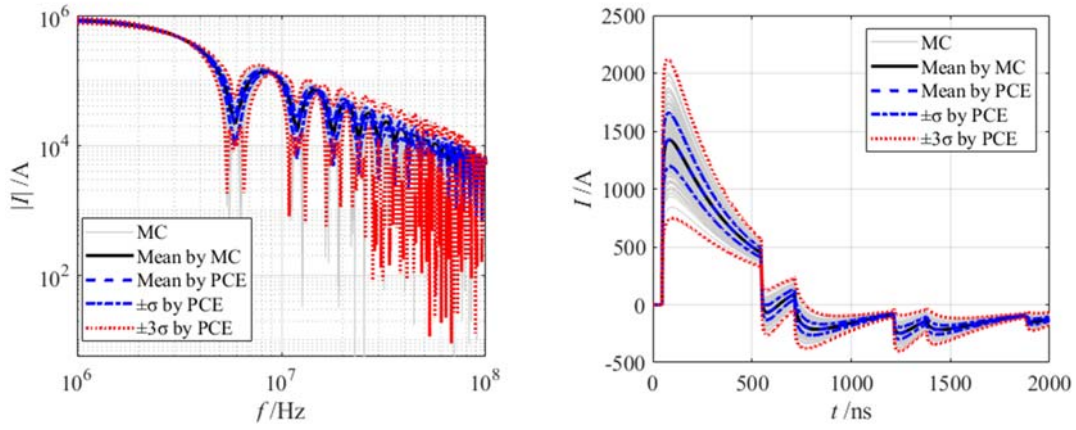
$$\begin{aligned} c_1^{(VS)} &= e^{-jkx \cos \psi \cos \phi} e^{jky \cos \psi \sin \phi} E_0 \left( \begin{bmatrix} \left[ \cos \alpha \sin \psi \cos \phi (1 - R_v) + \sin \alpha \sin \phi (1 + R_h) \right] \\ + \omega \mu_0 c_1^{(h)} \begin{bmatrix} \sin \alpha \sin \psi \sin \phi (1 - R_h) \\ + \cos \alpha \cos \phi (1 + R_v) \end{bmatrix} \end{bmatrix} \right) \\ c_2^{(VS)} &= e^{-jkx \cos \psi \cos \phi} e^{jky \cos \psi \sin \phi} E_0 \omega \mu_0 c_2^{(h)} \begin{bmatrix} \sin \alpha \sin \psi \sin \phi (1 - R_h) \\ + \cos \alpha \cos \phi (1 + R_v) \end{bmatrix} \\ \dots & \\ c_m^{(VS)} &= e^{-jkx \cos \psi \cos \phi} e^{jky \cos \psi \sin \phi} E_0 \omega \mu_0 c_m^{(h)} \begin{bmatrix} \sin \alpha \sin \psi \sin \phi (1 - R_h) \\ + \cos \alpha \cos \phi (1 + R_v) \end{bmatrix} \end{aligned} \quad (3-65)$$

$$c_m^{(IS)} = e^{-jkx \cos \psi \cos \phi} e^{jky \cos \psi \sin \phi} E_0 c_2^{(h)} \cos \alpha \cos \psi (1 + R_v) \quad (3-66)$$

Figure 3-19 shows the results obtained by 100 times MC and 3-order PCE simulation by solving (3-63) in the frequency domain and time domain. Mean current can be calculated directly by the first term of PCE. The variance can be calculated by the sum of the coefficient except for the first terms:

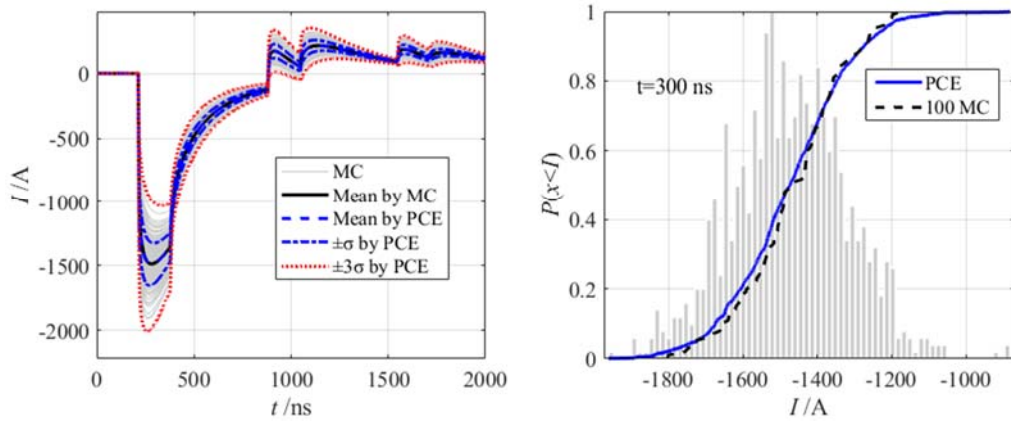
$$E(I) = c_1^{(I)}, \quad \text{Var}(I) = \sum_m^P (c_m^{(I)})^2. \quad (3-67)$$

Both frequency domain and time domain stochastic models show good predictions of the mean and variance of coupling responses, even though there are reflections caused by the mismatching at the terminals. The built-up of augmented TLs system with frequency-dependent p.u.l. parameters cost 30.1 s, the simulation of the augmented TLs system in frequency domain caused 57.8 s. 100 times MC simulation of TL with uncertain height in frequency domain caused 104 min 42 s. The stochastic model brought a  $71 \times$  speed-up.



(a) Induced current in the frequency domain (b) Induced current in the time domain  
 Figure 3-19 Expectation and variance interval of the near-end induced current in frequency domain and time domain results

The PCE calculated by the augmented TLs can be used to repeatedly calculate the probability distribution of current at any time (or frequency). Figure 3-20 shows the results for the far-end induced current. 3-order current. The CDF calculated from a 3-order augmented TLs system is in good agreement with 1000 times MC simulation.



(a) Induced current in the time domain (b) CDF of the induced current at 300 ns  
 Figure 3-20 Expectation and variance interval and probability distribution of the far-end induced current in time domain results

### 3.3.2 Stochastic model with uncertainties of fields

When the uncertainties of the incident field parameters are considered, such as the incident angle, electric field waveform, etc. Hermite polynomials PCE is used to decompose the distributed current source in the telegraph equation caused by the incident field:

$$\begin{aligned}
 \mathbf{V}_s(x, \omega, \xi^{(F)}) &= \sum_m^p c_m^{(F1)}(x, \omega) \psi_m(\xi^{(F)}) \\
 \mathbf{I}_s(x, \omega, \xi^{(F)}) &= \mathbf{Y} \sum_m^p c_m^{(F2)}(x, \omega) \psi_m(\xi^{(F)})
 \end{aligned}
 \tag{3-68}$$

The forcing function caused by the incident field is calculated as

$$\begin{aligned} \mathbf{V}_{\text{FT}}(l, \omega, \xi^{(\text{F})}) &= \sum_m^p c_m^{(\text{F3})}(\omega) \psi_m(\xi^{(\text{F})}) \\ \mathbf{I}_{\text{FT}}(l, \omega, \xi^{(\text{F})}) &= \sum_m^p c_m^{(\text{F4})}(\omega) \psi_m(\xi^{(\text{F})}) \end{aligned} \quad (3-69)$$

where

$$\begin{bmatrix} c_m^{(\text{F3})} \\ c_m^{(\text{F4})} \end{bmatrix} = \begin{bmatrix} \int_0^l [\Phi_{11}(l-x)(c_m^{(\text{F1})}(x, s)) + \Phi_{12}(l-x)(c_m^{(\text{F2})}(x, s))] dx \\ \int_0^l [\Phi_{21}(l-x)(c_m^{(\text{F1})}(x, s)) + \Phi_{22}(l-x)\mathbf{Y}(c_m^{(\text{F2})}(x, s))] dx \end{bmatrix} \quad (3-70)$$

For simplification, take a single conductor as an example, the induced current at both ends of the TL can be written as

$$\begin{aligned} \mathbf{I}(0, \omega, \xi^{(\text{F})}) &= \sum_m^p c_m^{(\text{F5})}(\omega) \psi_m(\xi^{(\text{F})}) \\ \mathbf{I}(l, \omega, \xi^{(\text{F})}) &= \sum_m^p c_m^{(\text{F6})}(\omega) \psi_m(\xi^{(\text{F})}) \end{aligned} \quad (3-71)$$

where

$$\begin{aligned} c_m^{(\text{F5})}(\omega) &= \frac{c_a^{(\text{F3})}(\omega) - \mathbf{Z}_L c_a^{(\text{F4})}(\omega)}{\frac{e^{\gamma l} + e^{-\gamma l}}{2}(\mathbf{Z}_S + \mathbf{Z}_L) + \frac{e^{\gamma l} - e^{-\gamma l}}{2}(\mathbf{Z}_C + \frac{\mathbf{Z}_S \mathbf{Z}_L}{\mathbf{Z}_C})} \\ c_m^{(\text{F6})}(\omega) &= \frac{c_a^{(\text{F3})}(\omega) + \mathbf{Z}_S c_a^{(\text{F4})}(\omega)}{\frac{e^{\gamma l} + e^{-\gamma l}}{2}(\mathbf{Z}_S + \mathbf{Z}_L) + \frac{e^{\gamma l} - e^{-\gamma l}}{2}(\mathbf{Z}_C + \frac{\mathbf{Z}_S \mathbf{Z}_L}{\mathbf{Z}_C})} \end{aligned} \quad (3-72)$$

Equation (3-71) can be regarded as the stochastic model for the TL excited by incident fields. For the TL terminating under a linear load, there are always two groups of coefficients that need to be solved.  $c_m^{(\text{F1})}, c_m^{(\text{F2})}$  can be solved by decomposing (3-16) and (3-17). Otherwise,  $c_m^{(\text{F5})}, c_m^{(\text{F6})}$  can be solved by decomposing (3-33) directly.

When coefficients  $c_m^{(\text{F5})}, c_m^{(\text{F6})}$  are decomposed directly, the target functions used for Galerkin projection become complex. The non-invasive method can be used to build the stochastic model, such as the stochastic collection method (SC). For the time domain form of (3-71) transferred by Laplace transform

$$\begin{aligned} \mathbf{I}(0, t, \xi^{(\text{F})}) &= \sum_m^p c_m^{(\text{F5})}(t) \psi_m(\xi^{(\text{F})}) \\ \mathbf{I}(l, t, \xi^{(\text{F})}) &= \sum_m^p c_m^{(\text{F6})}(t) \psi_m(\xi^{(\text{F})}) \end{aligned} \quad (3-73)$$

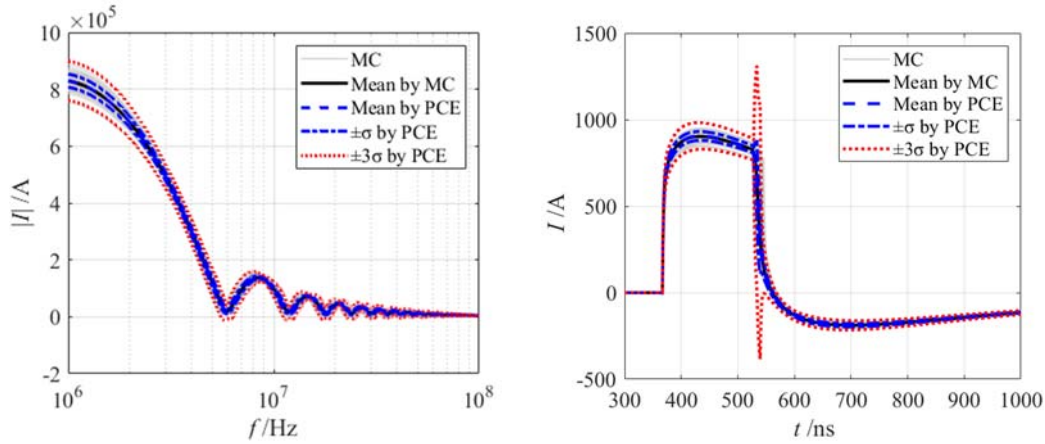
The far-end induced current can be expressed as

$$\underbrace{\begin{bmatrix} \mathbf{I}(l, t, \xi_1^{(F)}) \\ \mathbf{I}(l, t, \xi_2^{(F)}) \\ \vdots \\ \mathbf{I}(l, t, \xi_Q^{(F)}) \end{bmatrix}}_{\mathbf{Y}(t)} = \underbrace{\begin{bmatrix} 1 & \psi_2(\xi_1^{(F)}) & \cdots & \psi_P(\xi_1^{(F)}) \\ 1 & \psi_2(\xi_Q^{(F)}) & & \psi_P(\xi_Q^{(F)}) \\ \vdots & & \ddots & \vdots \\ 1 & \psi_2(\xi_Q^{(F)}) & \cdots & \psi_P(\xi_Q^{(F)}) \end{bmatrix}}_{\Phi} \underbrace{\begin{bmatrix} c_1^{(F6)}(t) \\ c_2^{(F6)}(t) \\ \vdots \\ c_P^{(F6)}(t) \end{bmatrix}}_{\mathbf{C}(t)} \quad (3-74)$$

where  $\mathbf{I}(l, t, \xi_p^{(F)})$  is the numerical result for some variables samples.  $c_2^{(F6)}$  can be solved by

$$\mathbf{C}(t) = \Phi^{-1} \mathbf{Y}(t) \quad (3-75)$$

To validate the stochastic model of TLs excited by the field with uncertainties, a 100 m-long overhead line excited by HEMP is studied. The diameter and height of the line are 10 mm and 10 m, respectively. Loads at both ends are matched. The incident field is with the Bell HEMP waveform<sup>[45]</sup>. The azimuth angle, polarization angles, and elevation angles are random variables from Gaussian distribution  $N(\pi/4, \pi/4)$ . Figure 3-21 shows the results obtained by 100 times MC and PCE simulation by SC method with 3-order Gaussian quadrature nodes in the frequency domain and time domain. When the variation interval of the variables is small, the frequency-domain stochastic model can well demonstrate the mean and uncertainty interval of the induced current. Gibbs phenomenon occurs in the results in the time domain at the abrupt change point in the waveform.

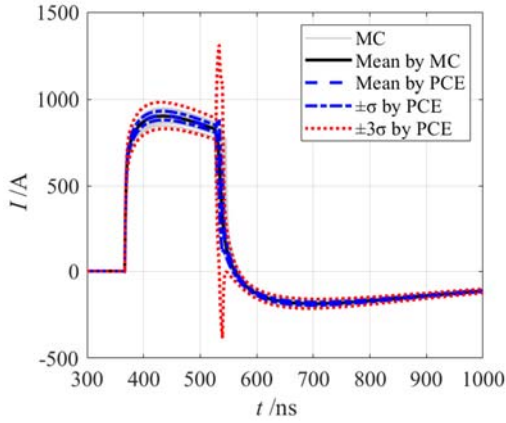


(a) Induced current simulated by the frequency-domain stochastic model      (b) Induced current simulated by the time-domain stochastic model

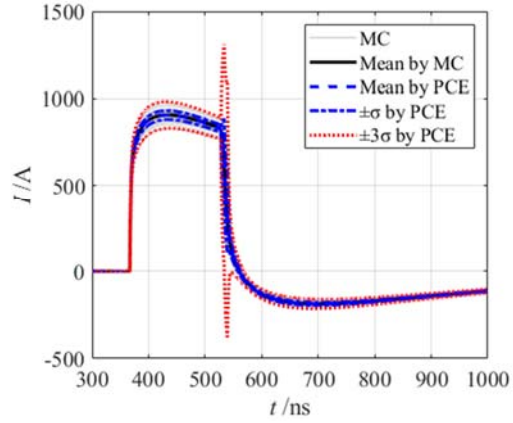
Figure 3-21 Expectation and variance interval of far-end induced current obtained by frequency-domain stochastic model and time-domain stochastic model

Figure 3-22 shows the results obtained by the inverse Fourier transform of different orders frequency-domain stochastic model. Gibbs phenomenon will not affect the accuracy of frequency-domain results, but when the frequency results are transferred into the time domain, equivalent to the time-domain stochastic model results, there is a similar Gibbs phenomenon as well. The increase in the order has a slight improvement for the Gibbs phenomenon.





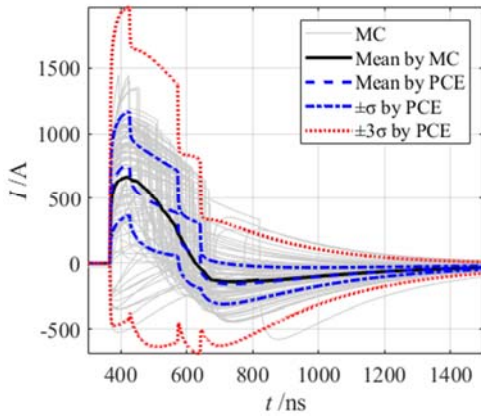
(a) Induced current simulated by a 3-order frequency-domain stochastic model



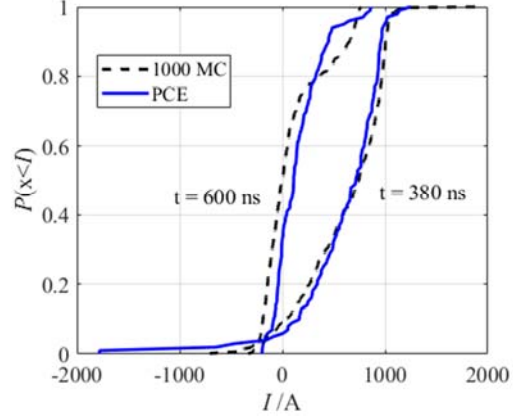
(b) Induced current simulated by a 9-order frequency-domain stochastic model

Figure 3-22 Expectation and variance interval of far-end induced current obtained by the inverse Fourier transform of 3-order and 9-order frequency-domain stochastic model

When the value of angles varies in a large interval, such as  $\phi \sim N(\pi/4, \pi/4)$ , Figure 3-23 shows the significant Gibbs phenomenon in the time domain results.



(a) Induced current in time-domain



(b) CDF of induced current at 380 and 600 ns

Figure 3-23 Expectation and variance interval and probability distribution of far-end induced current obtained by the inverse Fourier transform of 9-order frequency-domain stochastic model

The stochastic current in the time domain can no longer be obtained by the repeated calculation of currents on the augmented TLs. Thus we can study the uncertainty of induced current by the stochastic model of the induced current amplitude, which will be introduced in detail in Chapter 4.

$$\|\mathbf{I}_{eq}(\xi)\|_{\infty} = \sum_a^p c_a^{(A)}(\omega) \psi_a(\xi). \quad (3-76)$$

When the parameters of lines and incident field are both uncertain and mutually independent, a stochastic model can be constructed first only for the lines with uncertainty parameters, and the stochastic model can be re-used for the simulation with different sampled parameters of the incident field. The results can be filled in (3-74) to construct a stochastic model, which accounts for both uncertainties from lines and fields.

### 3.4 Concluding remarks

(1) An equation-based dynamic nonlinear model for the MOA was proposed and realized in Spice. It can be used to simulate the responses on the lines when the amplitude and rise time of the coupling responses vary in a wide range. Two different types of MOA used in the power distribution systems were tested for validation. The proposed model was validated from measured results, the error of simulated peak voltage and absorbed energy is less than 6%. Once the model is established for a certain MOA, it is capable to predict the responses of the MOA under different surges with front time ranging from 20 ns to 30  $\mu$ s.

(2) When the rise time of the incident field waveform decreases, on the one hand, the rise time of the induced response will decrease, the nonlinearity of the MOAs declines, and the residual voltage across the MOA increases; on the other hand, the ECL of the lines will decrease, and the protection range of the MOA declines. When the distance between the MOAs and the protection equipment is greater than ECL, the distant MOAs can be ignored to simplify the simulation.

(3) The stochastic models for TLs were established based on the intrusive PCE method and solved in the form of macromodel. When the augmented TLs are constructed for the telegraph equation with uncertain parameters, the change of distributed sources should be decomposed by PCE simultaneously. Compared with the conventional MC method, the proposed stochastic model can speed up the uncertainty quantification of the coupling responses by tens of times.

## 4 Hierarchical stochastic model for TED-to-line coupling responses

To investigate the uncertainty of coupling responses on the TLs excited by TED, the problem is divided into a two-stage hierarchical uncertainty quantification problem, including the uncertainty quantification of the field by the stochastic model in Chapter 2, and the uncertainty quantification of the TLs coupling responses by the stochastic model in Chapter 3.

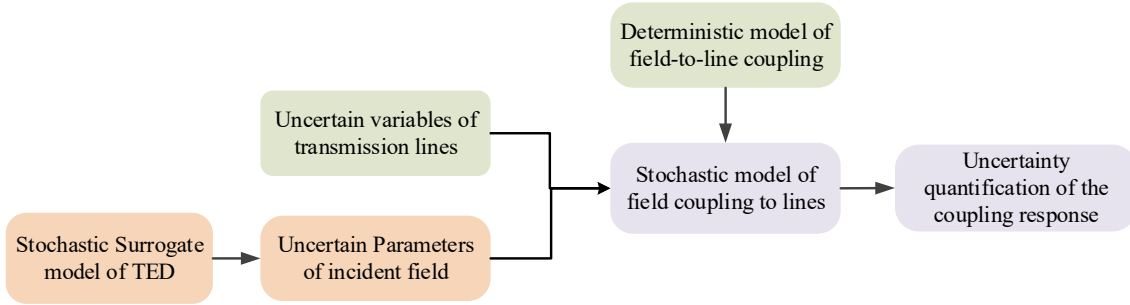


Figure 4-1 Diagram of the hierarchical stochastic modeling for the uncertainty quantification of the field coupling to lines

Further study about uncertainty quantification of the coupling responses on the TL based on the hierarchical framework is needed. The transfer of physical parameters from the first stage to the second stage brings new problems. When the results of the former stage uncertainty quantification process propagate into the second stage uncertainty quantification as input variables, these variables are rarely from the classical probability distribution, sometimes the variables are no longer mutually independent. Two key issues still need to be addressed. (1) The first issue is to appropriately describe the random and correlated multi-dimensional parameters obtained from the first stage and inputted into the second stage. (2) The second issue is to establish a distribution-free and correlated uncertainty quantification method and use it to study the uncertainty of the TL with random fields.

In this chapter, we propose a polynomial chaos method for the non-Gaussian and correlated multivariate based on the Kernel distribution estimation method (KDE), named KDE-PCE, to construct the rest part of the hierarchical stochastic modeling for TL coupling responses under incident fields.

### 4.1 Polynomial chaos expansion method with arbitrary and correlated multivariate

In Chapter 3, we have built the stochastic model for TLs excited by field by using the Hermite polynomials as the basis functions, assuming the random variables obey Gaussian distribution. In order to use Hermite polynomials for random variables from other distributions, the variables should be transformed into new variables from Gaussian distribution by Gaussian anamorphosis or normal score transformation, and the computational efficiency and convergence speed are reduced. Askey-Scheme provides several classical basis functions for univariate following certain distributions<sup>[167]</sup>.

Table 4-1 Wiener-Askey scheme table for generalized polynomial chaos basis functions and correspondence random variables<sup>[168]</sup>.

| Random variables     |   | Support       | PC basic function | Normalization coefficient $\ \phi_m\ ^2$  |
|----------------------|---|---------------|-------------------|---|
| Type                 | PDF   |               |                   |   |
| Gauss Distribution   | $(2\pi)^{-1/2} e^{-x^2/2}$                          | $\mathbb{R}$  | Hermite           | $k!$  |
| Beta Distribution    | $\frac{(1-x)^\alpha (1+x)^\beta}{B(\alpha, \beta)}$ | $[-1, 1]$     | Jacobi            | $\frac{2^{\alpha+\beta+1} \Gamma(k+\alpha+1) \Gamma(k+\beta+1)}{k! (2k+\alpha+\beta+1) \Gamma(k+\alpha+\beta+1)}$ |
| Gamma Distribution   | $x^\alpha e^{-x} / \Gamma(\alpha+1)$                | $[0, \infty)$ | Laguerre          | $\frac{\Gamma(k+\alpha+1)}{k!}$   |
| Uniform Distribution | $1/2$   | $[-1, 1]$     | Legendre          | $\frac{2}{2k+1}$  |

The arbitrary PCE (a-PCE) generalizes chaos expansion techniques can deal with variables with arbitrary probability distributions, as long as they are mutually independent<sup>[169]</sup>. Piecewise cubic interpolation and piecewise rational quadratic interpolation are proposed to construct closed-form density functions and determine the special forms of generalized polynomial-chaos basis functions<sup>[68]</sup>.

For questions with multiple independent uncertain variables, a multidimensional orthogonal basis needs to be constructed. Since the joint probability distribution function of multiple independent random variables is isomorphic to the tensor product of the marginal distribution, the multivariate basis functions consist of the product of univariate orthogonal basic function according to each variable marginal distribution.

When the variables are correlated, the problem is completely different. It is no longer reasonable to use the product of univariate orthogonal basic function. The PCE can be transformed into the form of independent variables by converting the variables by inference to the marginal distribution and their copula<sup>[177]</sup>. Rosenblatt transform and Nataf's transform are useful to transfer the correlated variables into independent Gaussian variables, but require the conditional PDF, which is hard to be obtained<sup>[173][174]</sup>. The copula and vine-copula method is recently developed to express the joint probability distributions in terms of their marginal distributions and copulas (or vines) from data. However, this method is so far limited to low-dimensional (typically bivariate) problems<sup>[175][176]</sup>. When the inputs are high-dimensional variables, or when many parametric families of pair copulas are considered for the vine construction, this approach may become computationally prohibitive<sup>[176]</sup>. Another disadvantage is that it changes the relationship between the input variables and the objective function, which may lead to an unexpectedly high degree and slow convergence speed, just like the transformation-based univariate PCE. It is necessary to construct new multivariate Hilbert variable spaces and a completely new multivariate polynomial basis starting from the definition of polynomial orthogonality.

The multilevel field-to-line coupling uncertainty quantification faces three difficulties at the same time: (1) there are multiple input variables; (2) the variables are following distributions that are hard to be described by classical probability distribution; (3) some of the variables are correlated, which make the description of the joint probability distribution even harder.

Therefore, we proposed a PCE method for non-Gaussian and correlated variables based on the kernel distribution estimation method (KDE), named KDE-PCE, which has the following advantages: (i) KDE is a numerically dependent method. When the data samples are sufficient, The proposed method can describe the independent and correlated variables of arbitrary distribution. The input uncertain variables that needed to be estimated are obtained from the previous uncertainty quantification. So that the data samples are sufficient. (ii) The performance of KDE is almost independent of the choice of the kernel as long as the bandwidth is appropriate. When solving the PCE coefficients by Galerkin projection, the use of a uniform kernel or some special kernel can guarantee or even help the objective function to be integrated analytically. (iii) The expressions of KDE are simple and can be considered as a very little computational burden. Since the variable probability distribution is needed in the process of constructing polynomials, calculating the coefficients using numerical integration (numerical integration is more commonly used to solve the coefficients due to a large number of variables), and analyzing the probability distribution of the output using PCE, it only takes one-time computational cost. (iv) The use of a multi-variable polynomial basis constructed based on KDE is consistent with the original probability distribution of the input variables, which guarantees the optimal convergence speed of PCE and helps to reduce the polynomial terms.

The construction of the proposed KDE-PCE is divided into three main steps: first, estimate the joint probability distribution of variables. Second, find the distribution-free orthogonal polynomial basis functions or the correlated variables. Third, calculate the coefficients of each basic function term. The three steps are introduced below.

#### 4.1.1 PDF estimation of multivariate based on MCMC-KDE

The approximation of the probability distribution of the variables is necessary, and the PDF is significant during constructing polynomials, calculating the coefficients using numerical integration, and analyzing the probability distribution of the output using PCE. For density estimation of individual variables, there are common methods including variable estimation methods, such as the Bayesian method, and nonparametric estimation methods, such as asymptotic probability Extraction<sup>[160][160]</sup>, piecewise Cubic Interpolation<sup>[162][163]</sup>, and piecewise rational quadratic interpolation<sup>[164][165]</sup>. For correlated variables, the Gaussian mixture method and kernel density estimation are two common methods. The Gaussian mixture model is suitable for data that can be determined to be generated from a Gaussian model, or approximation Gaussian distribution. However, the objective uncertainty variables, obtained as outputs of a previous uncertainty quantification process, obviously do not have the characteristics of a Gaussian distribution. Thus, data-driven KDE is used to estimate the probability distribution and the correlated relationship of the variables.

KDE also known as Parzen window estimation, is a completely data-driven estimation method. Assume that  $x_1, \dots, x_n$  are the sample of random variables  $x$  and the probability density function of the variables is  $f(x)$ , then the general kernel density estimation can be expressed as

$$p(x) \approx \tilde{p}(x) = \frac{1}{Nh} \sum_{i=1}^N K\left(\frac{x-x_i}{h}\right) \quad (4-1)$$

where  $h$  is the bandwidth, and  $N$  is the amount of data. When  $N \rightarrow \infty$ , the estimated  $\tilde{p}(x)$  converges to real probability  $p(x)$ .  $K(\cdot)$  is the kernel function. The shape and value domain of the kernel function control shape of the PDF. Commonly used kernel functions include Uniform kernel, triangular kernel, and Gaussian kernel, as shown in Table 4-2.

Table 4-2 Commonly used kernel function in KDE

| Kernel function | $K(u)$                       |
|-----------------|------------------------------|
| Uniform         | $(1/2)I( u  \leq 1)$         |
| Triangle        | $(1- u )I(u \leq 1)$         |
| Epanechnikov    | $(3/4)(1-u^2)I(u \leq 1)$    |
| Gaussian        | $(2\pi)^{-1/2} \exp(-u^2/2)$ |

It has been widely recognized that the performance of a kernel density estimator is primarily determined by the choice of bandwidth. By contrast, it is little affected by the choice of kernel function<sup>[180]-[182]</sup>. Therefore, a uniform kernel or Gaussian kernel can guarantee or even help the objective function to be integrated analytically, which is one of the advantages of the KDE-PCE.

When the bandwidth  $h$  is small, the kernel density estimation curve  $\tilde{p}$  is curved and smooth, showing the multi-peaked characteristic that the original probability density function  $p$  does not have. When the bandwidth  $h$  is large, the kernel density estimation curve  $\tilde{p}$  is smooth, but it will cover more details. Therefore, it is very important and necessary to choose the appropriate values for bandwidth.

The kernel estimation of the joint probability density for multivariate is expressed as

$$\tilde{p}_{\mathbf{H}}(\xi) = \frac{1}{N} \sum_{i=1}^N K_{\mathbf{H}}(\xi - \mathbf{x}_i) = \frac{1}{N} \sum_{i=1}^N \frac{1}{|\mathbf{H}|^{1/2}} K[\mathbf{H}^{-1/2}(\xi - \mathbf{x}_i)] \quad (4-2)$$

where  $K$  can be multidimensional Gaussian distribution or other multidimensional kernel function with the following forms

$$\int_{\mathbf{R}^d} K(\xi) d\xi = 1, \int_{\mathbf{R}^d} \xi K(\xi) d\xi = 0, \int_{\mathbf{R}^d} \xi \xi^T K(\xi) d\xi = \mathbf{I}_d$$

The performance of multivariate KDE, just the same as univariate KDEs, hardly depends on the shape of the kernel function. The problem is how to determine the optimal bandwidth matrix. The kernel density estimation results vary greatly under different bandwidths  $\mathbf{H}$ , which is usually restricted to a symmetric positive diagonal matrix.

$$\mathbf{H} = \text{diag}[h_1^2, h_2^2, \dots, h_d^2] \quad (4-3)$$

Thus, the joint probability density function can be expressed as

$$\tilde{p}_H(\xi) = \frac{1}{N} \sum_{i=1}^N \frac{1}{h_1 h_2 \dots h_d} K\left(\frac{\xi_1 - x_{i,1}}{h_1}, \dots, \frac{\xi_d - x_{i,d}}{h_d}\right), K(\xi) = K(\xi_1) K(\xi_2) \dots K(\xi_d) \quad (4-4)$$

The most widely used optimal diagonal bandwidth, named the “normal reference rule”<sup>[181]</sup>, can be approximated as:

$$h_i = \sigma_i \left\{ \frac{4}{(d+2)n} \right\}^{1/(d+4)} \quad (4-5)$$

where  $\sigma_i$  is the standard deviation of the  $i$ -th variable. However, for high-dimensional non-Gaussian random samples, the normal reference rule provides a convenient but inaccurate estimation for the bandwidth, especially for high-dimensional variables. It often leads to too narrow bandwidth and very unsmooth or even incoherent density estimation results.

Here, the Markov chain Monte Carlo (MCMC) algorithm is utilized to estimate the optimal bandwidth matrix for multivariate KDE based on the Gibbs sampling method. The procedure of the MCMC-KDE is shown in Figure 4-2. One of the advantages is that it won't increase the difficulty as the dimension of data increases when using MCMC-KDE. With a Gaussian distribution assumption of the prior density of bandwidths, the posterior of the elements in bandwidth  $\mathbf{H}$  is calculated by the Bayesian theorem with cross-validation (CV) samples  $\{\hat{\mathbf{x}}_i, i=1, \dots, N_{CV}\}$ .

$$\pi(\mathbf{H} | \lambda, \{\hat{\mathbf{x}}_i\}) = L(\{\hat{\mathbf{x}}_i\} | \mathbf{H}) \pi(\mathbf{H} | \lambda) \quad (4-6)$$

For convenience, the assumption of prior density, the sample ranges of all dimensions are scaled to the same level  $[0,1]$ . The Scott approximation is chosen as the means, and the  $\lambda$  is the standard deviation with values of 1. The prior density is

$$\pi(\mathbf{H} | \lambda) = \prod_{i=1}^d (1/\sqrt{2\pi}\lambda) \exp\left(-\frac{(h_i - \sigma_i)^2}{2\lambda^2}\right) \quad (4-7)$$

The likelihood function of the bandwidth matrix is calculated as:

$$L(\{\hat{\mathbf{x}}_i\} | \mathbf{H}) = \prod_{i=1}^{N_{CV}} p_H(\hat{\mathbf{x}}_i) = \prod_{i=1}^{N_{CV}} \left[ \frac{1}{N} \sum_{j=1}^N \frac{1}{h_1 h_2 \dots h_d} K\left(\frac{\hat{x}_i - x_{j,1}}{h_1}, \dots, \frac{\hat{x}_i - x_{j,d}}{h_d}\right) \right] \quad (4-8)$$

The posterior  $\mathbf{H}$  is simulated by using the multidimensional sequential axis switching Gibbs sampling method. The procedure is shown in Figure 4-2. The probable values of the posterior distribution for each variable made up the best combination of matrix  $\mathbf{H}$ .

The proposed method is compared with conventional estimation methods. The joint distribution of the three correlated variables is estimated as an example,  $\xi_1 \sim N(0,1)$ ,  $\xi_2 \sim \text{Beta}(1,3)$ ,  $\xi_3 \sim \text{Weibull}(1,3)$ , the copula between every two variables are Gaussian dependencies, the distribution of the variables is shown in Figure 4-3.

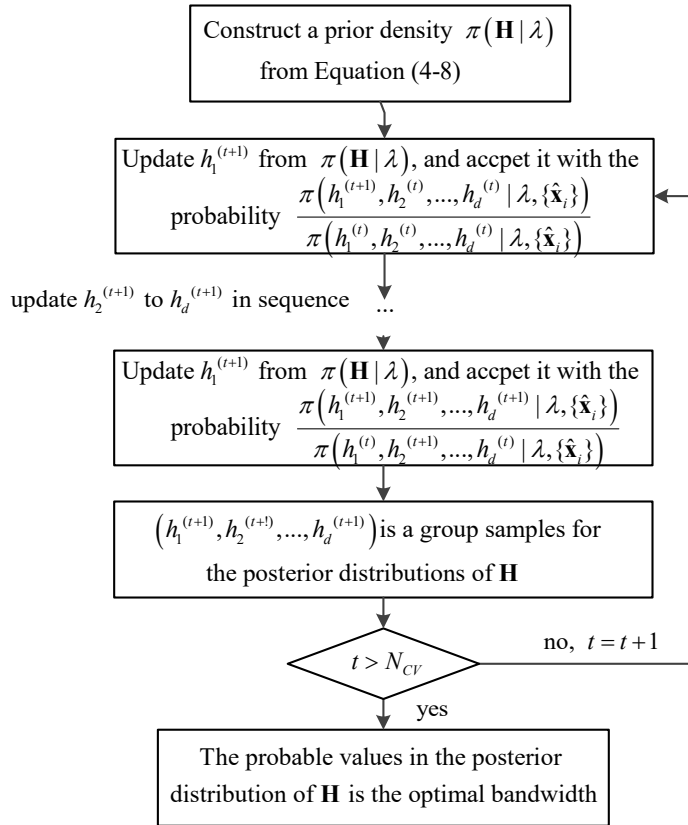


Figure 4-2 Flow chart of the bandwidths estimation in the MCMC-KDE based on the Gibbs sampling method

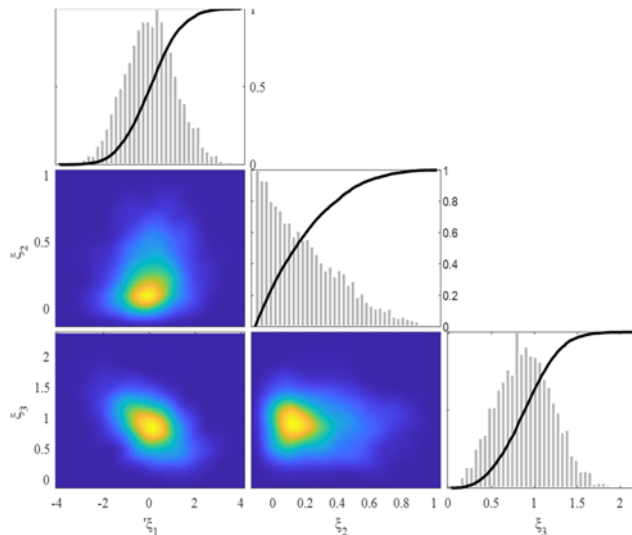


Figure 4-3 The joint and marginal distributions of three correlated variables

The diagonal bandwidth matrix  $\mathbf{H}$  given by the “normal reference rule” equals  $\text{diag}[0.007, 0.019, 0.013]$ , which is too narrow to construct the 3-dimensional joint distribution. The estimated marginal distributions are shown in Figure 4-5 (b). While  $\mathbf{H}=\text{diag}[0.072, 0.045, 0.081]$  is given by MCMC-KDE, as shown in Figure 4-4. The performance of different estimation methods is evaluated by the quantile-quantile plot (Q-Q plot) and root-mean-square deviation  $D_{\text{RMS}}$  in Figure 4-5:



$$D_{\text{RMS}} = \frac{\sqrt{\frac{1}{s} \sum_{i=1}^s (\overline{CDF}_i - CDF_i)^2}}{\frac{1}{s} \sum_{i=1}^s CDF_i} \quad (4-9)$$

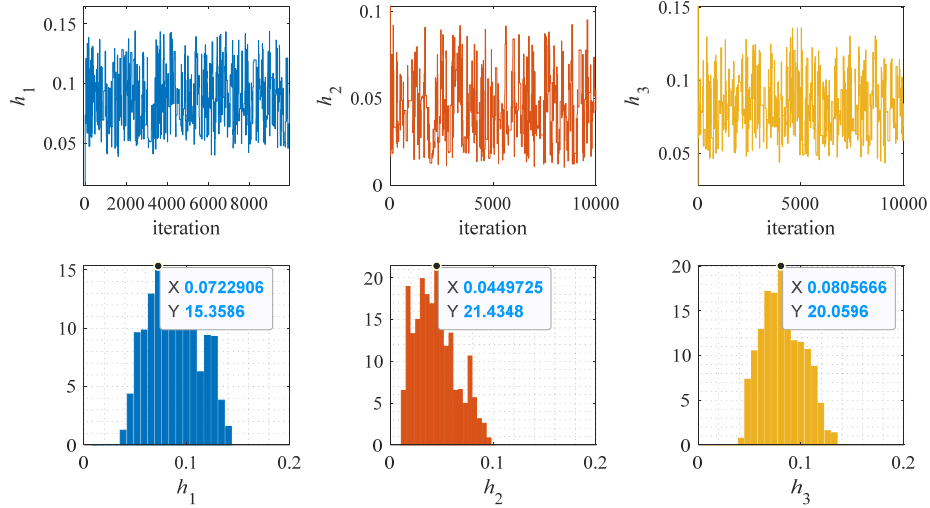


Figure 4-4 Bandwidth selection for multivariate kernel density estimation using MCMC, starting from the prior given by the normal reference rule

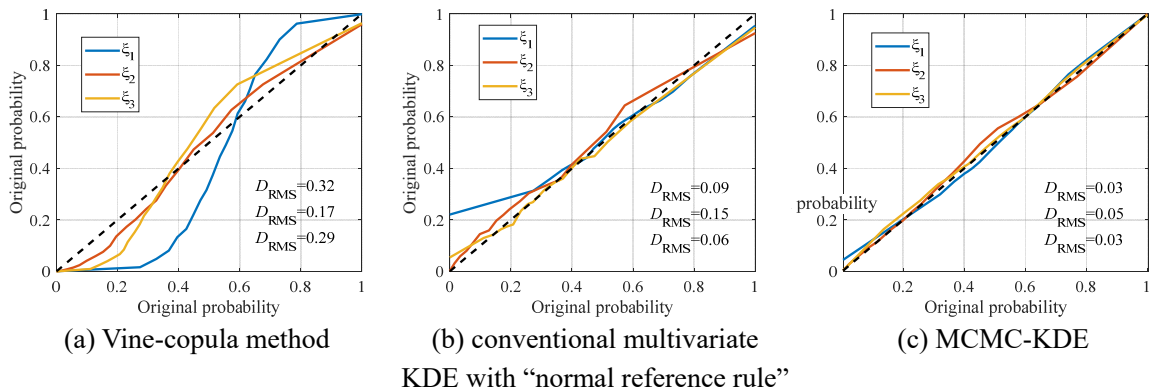


Figure 4-5 Q-Q plot of the original CDF and estimated CDF by using different methods

The KDE estimation shows a better description of the probability distribution of correlated multivariate, KDE based on MCMC can further improve the performance. The correctness and accuracy estimation of the arbitrary distribution correlated multivariate PDF is significant for the development of hierarchical stochastic models.

#### 4.1.2 Generation of correlated multivariate orthonormal polynomials

The basic polynomial functions are strongly related to the probability distribution of the variables, the appropriate basic functions can improve the convergence speed of PCE and helps to reduce the order of the polynomial expansion. For the variable from the nonparametric PDF obtained by the KDE, the basis in Table 4-1 can be no longer used. New basis polynomials for arbitrary distribution variables are needed.

When there is an arbitrary distribution variable, or when the multiple variables are

mutually independent, the basic functions can be constructed separately, and the orthogonal polynomial basis for the variable is generated by the origin moment method<sup>[179]</sup>.

When the random variables are correlated multivariate, the influence of the interaction between variables must be taken into consideration, otherwise, the basic functions are not mutually orthogonal. The Gram-Schmidt algorithm is used to construct a general orthogonal polynomial basis starting from the definition of polynomial orthogonality

$$\int_{\Omega} \phi_m(\xi) \phi_n(\xi) p(\xi) d\xi = \delta_{mn} \quad (4-10)$$

The polynomial basis functions are constructed from a sum of the multivariable monic polynomials,  $\{e_j(\xi) = 1, \xi_1, \xi_2, \xi_1^2, \xi_2^2, \xi_1 \xi_2, \dots\}_{j=0}^P$ . The monic polynomials are obtained from the total-order expansion of multivariable and reordered by the order of each monic polynomial. The number of terms for  $n$  correlated variables up to  $dm$ -order is as

$$P = \frac{(n + dm)!}{n! dm!} - 1$$

The polynomial basis functions  $\{\phi_k^{cor}\}_{k=1, \dots, P}$  are unique depending on the order of monic polynomials and follow recurrence relation,

$$\begin{aligned} \phi_1(\xi) &= 1 \\ \phi_k(\xi) &= e_j(\xi) - \sum_{k=0}^{j-1} \frac{\langle e_j(\xi), \phi_k(\xi) \rangle}{\langle \phi_k(\xi), \phi_k(\xi) \rangle} \phi_k(\xi) \end{aligned} \quad (4-11)$$

The  $m$ -th polynomial basis  $\phi_m(\xi)$  for the correlated multivariate group  $\xi$  is

$$\phi_m(\xi) = e_m(\xi) + \alpha_{m-1}^m \cdot e_{m-1}(\xi) \cdots + \alpha_1^m e_1(\xi) \cdot \xi + \alpha_0^m \quad (4-12)$$

where the coefficients  $\alpha_k^m$  for the  $m$ -order polynomial basis are calculated by the inverse of the central moment matrix

$$\begin{bmatrix} \alpha_0^m \\ \alpha_1^m \\ \vdots \\ \alpha_{m-1}^m \\ 1 \end{bmatrix} = \begin{bmatrix} \mu_{0,0}^{\xi} & \mu_{0,1}^{\xi} & \dots & \mu_{0,m}^{\xi} \\ \mu_{1,0}^{\xi} & \mu_{1,1}^{\xi} & & \mu_{1,m}^{\xi} \\ \vdots & \vdots & \ddots & \vdots \\ \mu_{m-1,0}^{\xi} & \mu_{m-1,1}^{\xi} & \dots & \mu_{m-1,m}^{\xi} \\ 0 & 0 & \dots & 1 \end{bmatrix}^{-1} \begin{bmatrix} 0 \\ 0 \\ \vdots \\ 0 \\ 1 \end{bmatrix} \quad (4-13)$$

What is different here, the central moment is calculated using the expectation of the product of two monic polynomials, instead of the powers of the variables.

$$\mu_{i,j}^{\xi} = \int_{\Xi} e_i(\xi) e_j(\xi) p(\xi) d\xi, \quad i, j = 0, 1, \dots, N \quad (4-14)$$

In this hierarchical uncertainty quantification framework, the variables are obtained from the results of the former stage of uncertainty quantification. With the PDF estimated by the KDE, the central moment in (4-15) can be calculated by Monto-Carlo integral

$$\mu_{i,j}^{\xi} = E(e_i(\xi)e_j(\xi)) \approx \frac{\sum_i^N e_i(\mathbf{x}_i)e_j(\mathbf{x}_i)p(\mathbf{x}_i)}{\sum_i^N \tilde{p}(\mathbf{x}_i)} \quad (4-15)$$

where  $\{\mathbf{x}_i, i=1, \dots, N\}$  are random samples in the definition space of  $\xi$  from the uniform distribution.  $\tilde{p}(\mathbf{x}_i)$  is the PDF of  $\mathbf{x}_i$  estimated by MCMC-KDE. Fortunately, all of the central moment can be solved by the same group of samples, which reduce the simulation cost significantly while monic polynomials  $e_j(\xi)$  are closed-form expressions and can be calculated conveniently.

When there are both independent variables and correlated variables, the polynomial construction follows the following steps:

Step 1: Determine the physically independent variables. Calculate the Pearson correlation coefficient between every two variables and identify variables that can be considered independent.

Step 2: Build the independent polynomial chaos basis for the independent variables  $\{\phi_k^{\text{ind}}\}_{k=1, \dots, Q_1}$ .

Step 3: Construct the correlated multivariate polynomial basis  $\{\phi_k^{\text{cor}}\}_{k=1, \dots, Q_2}$  from a certain sum of the multivariate monic polynomials for the correlated multivariate.

Step 4: Construct the total multivariate basis functions from the tensor product of independent polynomial basis and correlated polynomial basis

$$\psi_m(\xi_1, \xi_2, \dots, \xi_n) = \prod_{i=1}^n \phi_{a_i}^m(\xi_i) \quad (4-16)$$

where  $m$  refers to the number of the multivariate basic function,  $a_i^m$  refers to the number as well as the order univariate basic function for  $\xi_i$  in the  $m$ -th multivariate basic function.

The  $q$ -norm hyperbolic truncation method is used to limit the number of high-order terms with many interacting variables. The term is discarded when the  $q$ -norm of the basic function orders is large than the truncated order  $d$  of the polynomial expansion:

$$\|m\|_q > d, \quad \|m\|_q = \left( \sum_{i=1}^M (a_i^m)^q \right)^{1/q} \quad (4-17)$$

Table 4-3 Multivariate basis functions obtained by tensor product and hyperbolic truncation

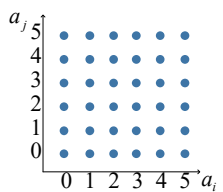
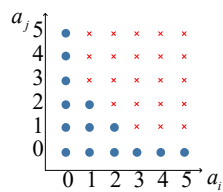
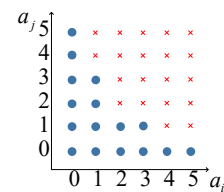
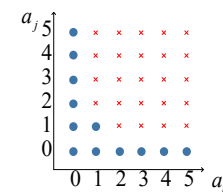
|                 | Tensor product  | $q$ -norm hyperbolic truncation  |   |  |
|-----------------|---|--|---|--|
| Number of terms |  | <br>$q = 3/4$ | <br>$q = 1/2$ | <br>$q = 1/4$ |

Table 4-3 shows the multivariate basis functions generated by the tensor product become

sparse by the hyperbolic truncation method.

### 4.1.3 Coefficient calculation with arbitrary distribution correlated multivariate

The core of constructing the PCE is to solve the coefficient  $c_m$  for each basis term in Equation (4-1) .

For the objective function that can be integrated analytically, the Galerkin projection method is the optimal way to ensure that the truncated polynomial has the minimum error

$$c_m = \|\psi_m\|^{-2} \int \psi_m(\xi) \cdot y(\xi) p(\xi) d\xi, \quad \|\psi_m\|^2 = \int \psi_m(\xi) \cdot \psi_m(\xi) p(\xi) d\xi \quad (4-18)$$

Numerical integration is widely used as an alternative to analytical integration, such as the Monte Carlo integration, the Gauss quadrature, and the Clenshaw-Curtis quadrature integration<sup>[183][184]</sup>. According to the properties of the polynomial and the quadrature principles, summation at quadrature nodes makes sure the accuracy of quadrature integration. For the quadrature nodes  $\{\mathbf{x}_g\}_{\text{Gauss}}$ , the coefficient can be solved by a series of summations

$$c_m = \int \psi_m(\xi) \cdot y(\xi) p(\xi) d\xi / \|\psi_m\|^2 \approx \sum_{k=1}^N \psi_m(\mathbf{x}_k) w_k / \|\psi_m\|^2 \quad (4-19)$$

The functions

$$\begin{bmatrix} c_0 \\ c_1 \|\psi_1\|^2 \\ \vdots \\ c_Q \|\psi_Q\|^2 \end{bmatrix} = \begin{bmatrix} 1 & 1 & \cdots & 1 \\ \psi_1(\mathbf{x}_1) & \psi_1(\mathbf{x}_2) & & \psi_1(\mathbf{x}_N) \\ \vdots & & \ddots & \vdots \\ \psi_Q(\mathbf{x}_1) & \psi_Q(\mathbf{x}_2) & \cdots & \psi_Q(\mathbf{x}_N) \end{bmatrix} \begin{bmatrix} y(\mathbf{x}_1) p(\mathbf{x}_1) \\ y(\mathbf{x}_2) p(\mathbf{x}_2) \\ \vdots \\ y(\mathbf{x}_N) p(\mathbf{x}_N) \end{bmatrix} \quad (4-20)$$

can be written as

$$\mathbf{C} = \Phi(\mathbf{x})[\mathbf{Y} \cdot \mathbf{w}] / \|\Phi^2\| \quad (4-21)$$

where  $p(\mathbf{x}_N)$  in matrix  $\mathbf{w}$  is the joint probability density for variable  $\mathbf{x}_N$ .

According to quadrature rules, for the integration of univariate functions with single variables,  $G$  Gauss nodes can provide accurate solutions for  $(2G-1)$ -order univariate integration.  $G$  Clenshaw-Curtis quadrature nodes can provide accurate solutions for  $(G+1)$ -order univariate integration. As for the multivariate situations, it remains an open problem to determine the required minimum number of quadrature nodes<sup>[185]</sup>. The state-of-the-art method is to solve a nonlinear least-square optimization problem

$$\min_{\bar{\epsilon}, \mathbf{w} \geq 0} \|\Phi(\mathbf{x})\hat{\mathbf{w}} - \mathbf{e}_1\|_2^2, \quad \mathbf{e}_1 = [1 \quad \dots \quad 0]^T \quad (4-22)$$

It is obvious that, when  $\tilde{\mathbf{w}}$  is calculated by the joint probability density  $\tilde{p}(\mathbf{x}_k)$  of the nodes  $\{\mathbf{x}_k\}$  estimated by the MCMC-KDE, the one-time calculation will not increase the calculation component burden. The random sample set satisfying KDE distribution is a natural group of solutions for the optimization problems. Therefore, we develop a new optimal

algorithm to generate optimal Gauss quadrature nodes for the PCE basis.

From the collection of multi-dimensional samples  $\{\mathbf{x}_1, \dots, \mathbf{x}_M\}$  from  $\tilde{p}(\xi)$ , which can be the same collection used to construct the PCE basis functions, several subsets of  $G$  samples  $\{\tilde{\mathbf{x}}_1, \dots, \tilde{\mathbf{x}}_G\}$  are randomly regenerated. For each subset, the other samples from the collection are divided into  $G$  multi-dimensional Voronoi regions  $\Gamma_i$  centered at  $\tilde{\mathbf{x}}_i$  according to their Euclidean distance. For each sample  $\mathbf{x}_i$  in the subset, there is a distance summation

$$d^{(i)} = \sum_{j \in \Gamma_i} \|\mathbf{x}_j - \tilde{\mathbf{x}}_i\|^2, \{\mathbf{x}_j \in \Gamma_k, \|\mathbf{x}_j - \tilde{\mathbf{x}}_i\| \leq \|\mathbf{x}_j - \tilde{\mathbf{x}}_k\|, k = 1, \dots, G\} \quad (4-23)$$

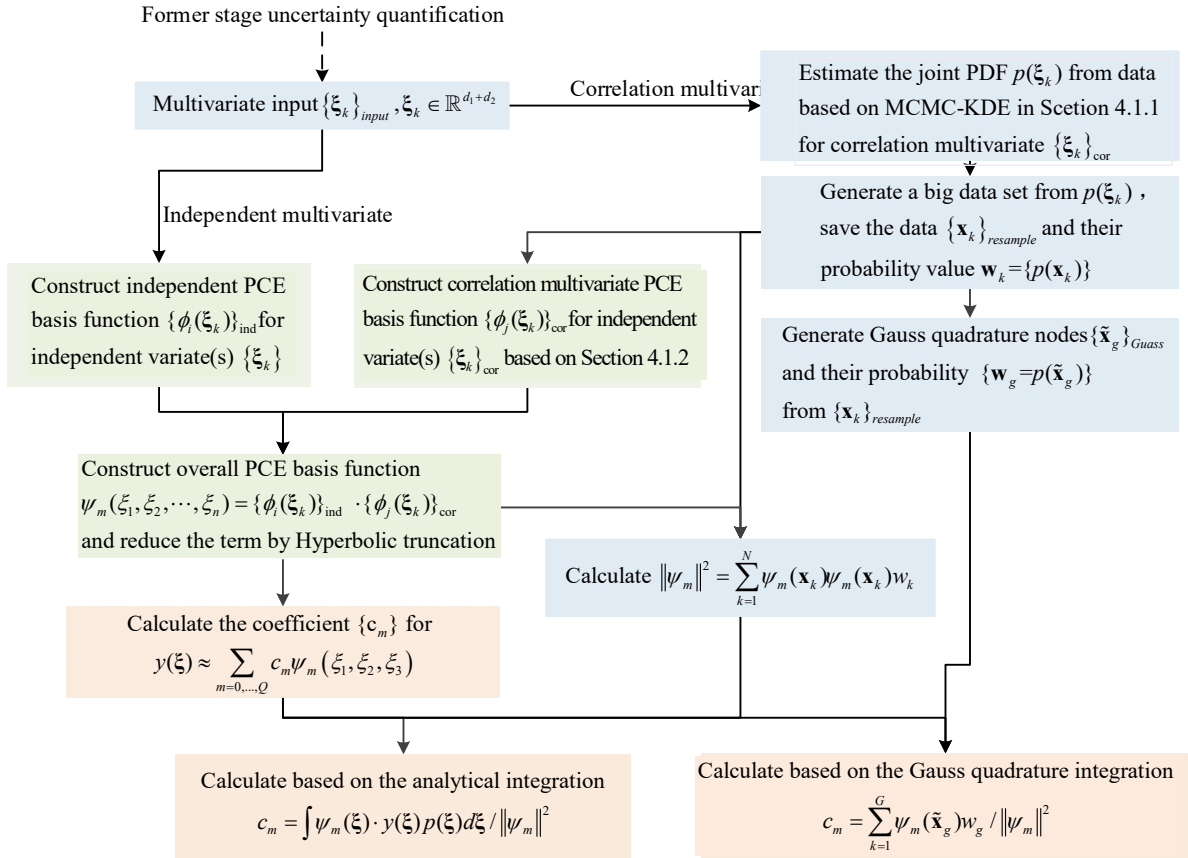


Figure 4-6 Procedure of the proposed KDE-PCE with both multivariates and multivariates

The optimal subset is chosen with the subset with the lowest overall distance

$$d = \sum_{k=1}^m d^{(k)} \quad (4-24)$$

This optimal subset is the most widely separated to represent the sample collections, as well as guarantee the approximation solution of Equation (4-21).

The least-square method (LS) is widely used to solve the coefficients of PCE as well. Since the PCE can be written in the following form

$$\Phi(\mathbf{x})^T \mathbf{C} = \mathbf{Y} \quad (4-25)$$

By solving the least-square optimization problem

$$\max \frac{\partial}{\partial \mathbf{C}} \|\Phi(\mathbf{x})^T \mathbf{C} - \mathbf{Y}\|^2$$

the polynomial coefficient can be obtained, and the coefficient is calculated as

$$\mathbf{C} = (\Phi(\mathbf{x})\Phi(\mathbf{x})^T)^{-1} \Phi(\mathbf{x})\mathbf{Y} \quad (4-26)$$

So far, the procedure for constructing the proposed KDE-PCE is shown in Figure 4-6.

#### 4.1.4 Uncertainty quantification with KDE-PCE

Part of the ease of use of PCE is the simplicity with which one obtains the most used statistics of the mean, variance, and Sobol's indices. The first term represents the means and the squares sum of the coefficients describes the variance.

$$\begin{aligned} E[y(\xi)] &= c_0 \\ \text{Var}[y(\xi)] &= \int \left[ \sum_{m=1, \dots, Q} c_m \phi_m(\xi) \right]^2 p(\xi) d\xi = \sum_{m=1, \dots, Q} c_m^2 \|\psi_m\|^2 \end{aligned} \quad (4-27)$$

Since the multivariate are not Gaussian or joint Gaussian distributions, the standard deviation can qualitatively describe the distribution of the results, but it cannot provide the exact confidence intervals. To obtain the PDF and CDF of the results, it is necessary to carry out the sampling statistics with the help of efficient PCE, with the variables sampled from the joint estimated PDF  $\tilde{p}(\xi)$ .

The problem is that there is no inverse function for the KDE PDF  $\tilde{p}(\xi)$  or CDF. The acceptance-rejection sampling method is introduced here to generate a set of samples from the estimated PDF. The essence is to accept samples that are sampled uniformly with target probabilities  $\tilde{p}(\xi)$ .

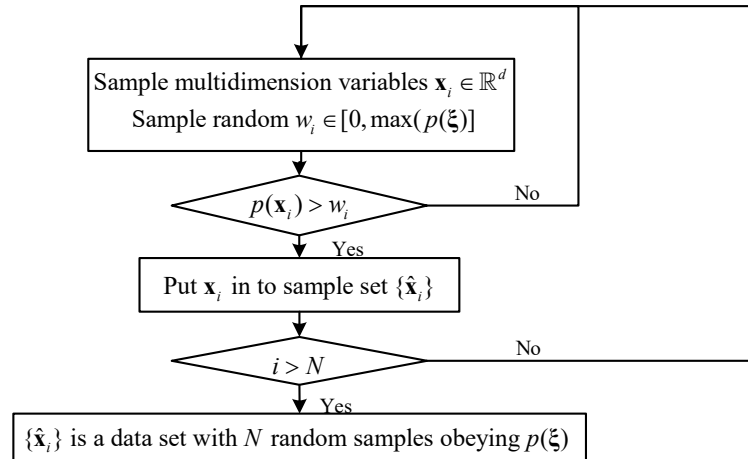


Figure 4-7 Flow chart of the acceptance-rejection sampling method

The procedure of resampling from estimated density is shown in Figure 4-7. The  $d$ -dimensional variables  $\{\mathbf{x}_k\}_{\text{resample}}$  are first sampled in the multidimensional variable space  $\mathbb{R}^d$ , while a series of reference values are sampled in the domain of values of probabilities  $\{w_k, w_k \in [0, \max(p(\xi))]\}$ . For each random variable, the probability of the sample  $p(\mathbf{x}_i)$  is compared with the reference value  $w_k$ . When the probability of one sample is higher than the

reference value, the sample is put into the sample set, otherwise, it is discarded. The occurrence probability of the accepted variable is as

$$p(\xi \leq \mathbf{x}_i | z \leq p(\xi)) = \frac{\int_{\mathbf{x}_0}^{\mathbf{x}} \int_0^{p(\mathbf{x})} \frac{1}{S} d\xi dz}{\int_{\mathbb{R}^d} \int_0^{p(\mathbf{x})} \frac{1}{S} d\xi dz} = \int_{\mathbf{x}_0}^{\mathbf{x}} p(\xi) d\xi \quad (4-28)$$

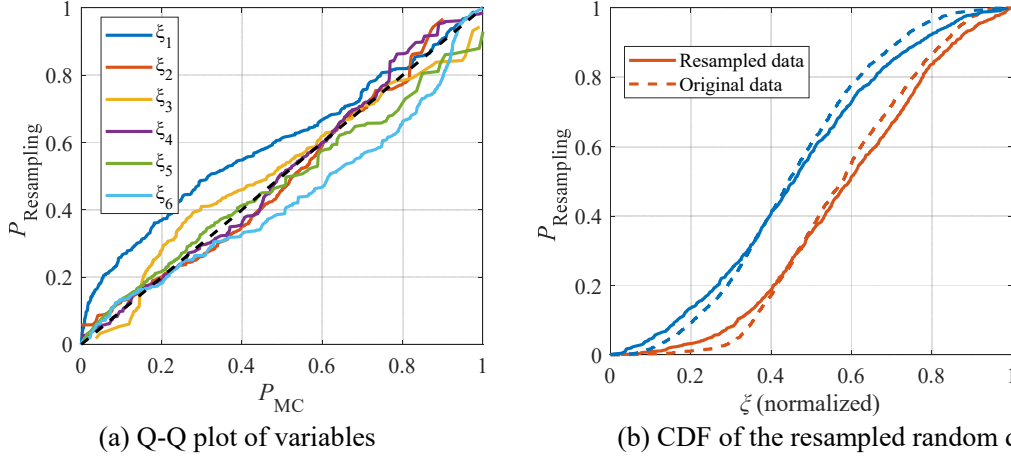


Figure 4-8 The distribution of resampled random data from estimated PDF by using the acceptance-rejection sampling method

The quantile-quantile plots in Figure 4-8 show that the marginal distributions of the six variables obtained from the resampled samples have a good agreement compared with the results directly obtained from the original data. The increase in dimensionality cause makes the high-dimensional variable space very extensive, and the finite original data samples used for KDE estimation are very sparse compared with the space. The resampled data increase the number of samples, and the CDF of the data becomes smooth and causes a slight difference between the CDFs.

Thanks to the multivariate basis functions that are constructed with the consideration of correlated multivariate, the Sobol's indices can be calculated directly from the PCE:

$$s_i = \sum_{a(i)} c_m^2, \quad s_i = \sum_{m(\dots,i,\dots)} c_m^2 \quad (4-29)$$

## 4.2 Uncertainty quantification of TED and coupling response based on the hierarchical stochastic model

### 4.2.1 Uncertainty quantification of the HEMP waveform

In order to validate and motivate the proposed PCE method with arbitrary distribution and correlated variables based on KDE. A three-dimension correlated multivariate case is used to validate the PCE method with arbitrary distribution and correlated variables. The uncertainty of the energy and waveform of the random electric field is studied, while the amplitude and 2 temporal coefficients describing the time domain QEXP waveform of the electric field are considered as random, their probability distributions are quantified by the

stochastic model of HEMP and are shown in Figure 4-9. The potential distribution of energy and waveform of the electric field, as well as the worst-case, will be given by using the proposed KDE-PCE method.

It is clear that the probability distributions of the variables are correlated, which is decided by the physical limitation.  $\alpha_E, \beta_E$  determine the rise time and FWHM of the HEMP waveform, both of the values increase with the amplitude  $E_0$  decrease. Meanwhile, the relationship is not deterministic and cannot be described analytically, because of the uncertain variables of the scenario and environment variables. When using the variables as they are independent, or ignoring the correlation in simulation, it may lead to slow convergence of the uncertainty quantification method. Sometimes even bring irrational results, the maximal energy may be calculated with the largest amplitude and the widest FWHM. However, the occurrence probability for such kind of situation is zero.

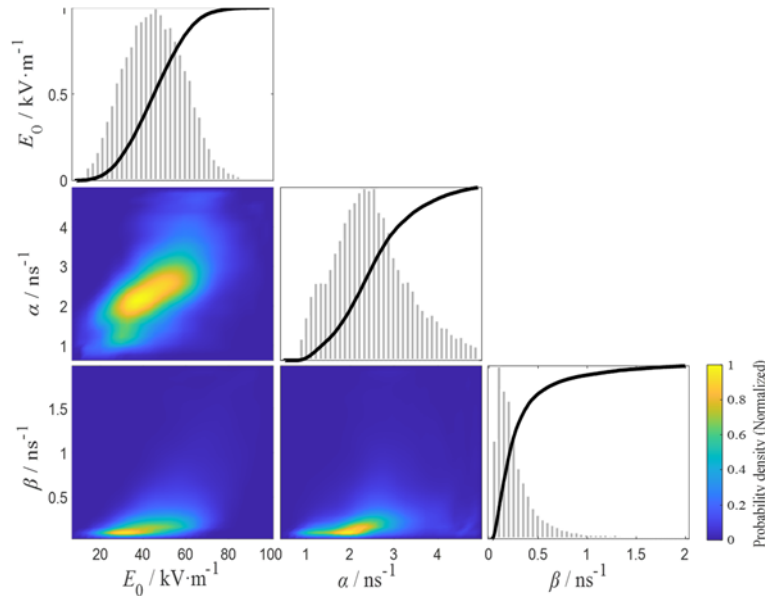
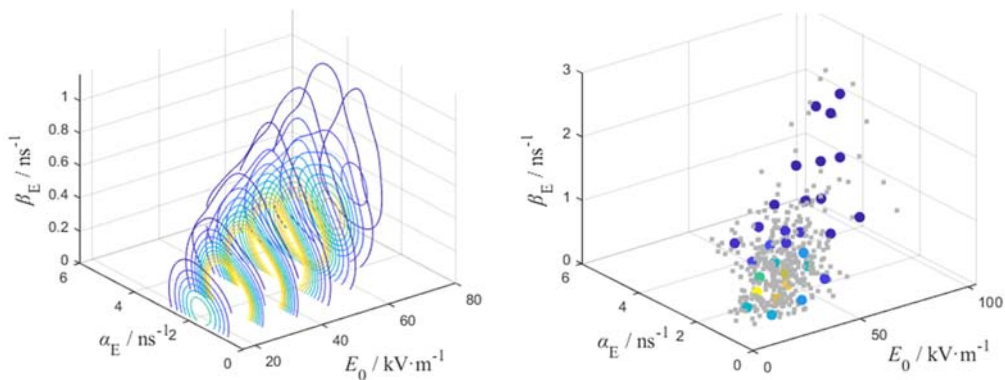


Figure 4-9 The joint and marginal distributions of  $E_0, \alpha_E, \beta_E$  obtained by the stochastic model of HEMP. The color represents the normalized joint probability density.



(a) 3-dimension joint probability density of  $E_0, \alpha_E, \beta_E$

(b) New data and optimal Gauss nodes  $E_0, \alpha_E, \beta_E$

Figure 4-10 Joint probability density and Optimal Gauss nodes of  $E_0, \alpha_E, \beta_E$  estimated by MCMC-KDE (The color represents the probability density value.)



The practice of uncertainty quantification by using the proposed correlated multivariate KDE-PCE is carried out following the flow summarized in Figure 4-6.

Firstly, the 3-dimension joint probability density of  $E_0, \alpha_E, \beta_E$  is estimated by using the data-driven MCMC-KDE. Meanwhile, new data sets and Gauss nodes are generated at the same time as shown in Figure 4-10.

Arbitrary distribution correlated multivariate  $E_0, \alpha_E, \beta_E$  are written as  $\xi_1, \xi_2, \xi_3$ . The correlated multivariate basis functions are constructed based on the strategy introduced in Section 4.1.2, using the joint probability density estimated by MCMC-KDE, the first several basic functions are listed in Table 4-4. Several basis functions are plotted in the uncertainty space as shown in Figure 4-11.

Table 4-4 Compare of correlated multivariate basis function and independent multivariate basis function for 3 correlated variables.

| $e_m(\xi)$   | Correlation multivariate basis                                 | Independent multivariate basis             |
|--------------|--|--|
| 1            | 1  | 1  |
| $\xi_3$      | $\xi_3 - 0.02$   | $\xi_3 - 0.02$                             |
| $\xi_2$      | $\xi_2 + 2.04\xi_3 - 0.11$                                     | $\xi_2 - 0.23$                             |
| $\xi_1$      | $\xi_1 + 0.49\xi_2 + 1.69\xi_3 - 0.38$                         | $\xi_1 - 0.55$                             |
| $\xi_3^2$    | $\xi_3^2 + 0.06\xi_1 + 0.01\xi_2 - 0.18\xi_3$                  | $\xi_3^2 - 0.14\xi_3 - 0.01$               |
| $\xi_2\xi_3$ | $\xi_2\xi_3 - 1.23\xi_3^2 + 0.01\xi_1 - 0.03\xi_2 - 0.13\xi_3$ | $\xi_2\xi_3 - 0.05\xi_2 - 0.23\xi_3 - 0.1$ |
| ...          | ...  | ...  |

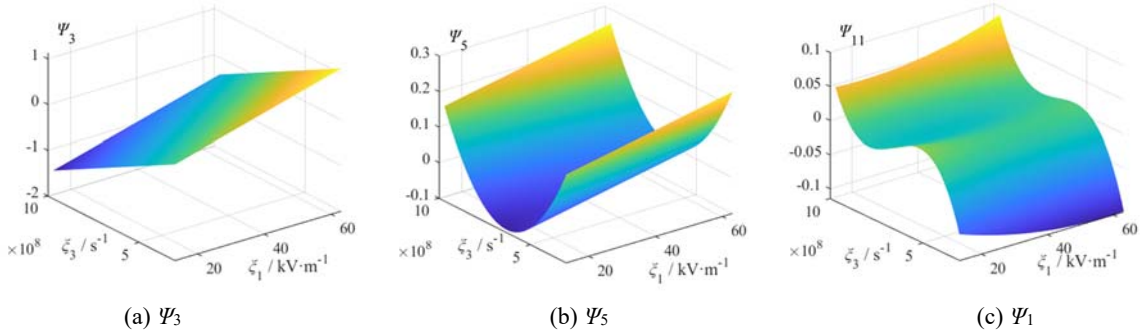


Figure 4-11 Number 3, 5, 11 basis function for three correlated multivariate

The analytic expression of cumulative energy flow density with respect to the three variables is

$$\begin{aligned}
 E_{\text{en}} &= \int_0^{\infty} \frac{2|E(\omega)|^2}{377} d\omega = \\
 &\approx \frac{2(E_{\text{max}}k)^2 \operatorname{atan} \left( \frac{1j(4 \sin(C\alpha_E)^2 - 4)}{2\sqrt{-\sin(2C\alpha_E)^2}} \right) 1j}{377(\alpha_E + \beta_E)^2 \sqrt{-\sin(2C\alpha_E)^2}}, \quad C = \frac{\pi}{(\alpha_E + \beta_E)}
 \end{aligned} \tag{4-30}$$

The PCE is established with the correlated multivariate basis functions

$$E_{\text{en}}(\xi_1, \xi_2, \xi_3) = \sum_{m=0, \dots, P} c_m^{(\text{en})} \psi_m(\xi_1, \xi_2, \xi_3) \quad (4-31)$$

The probability distributions of the cumulative energy flow density obtained by the KDE-PCE, a-PCE with independent multivariate basis functions, and MC are compared. The convergence of the result is quantified by the  $D_{\text{RMS}}$  defined in (4-9).

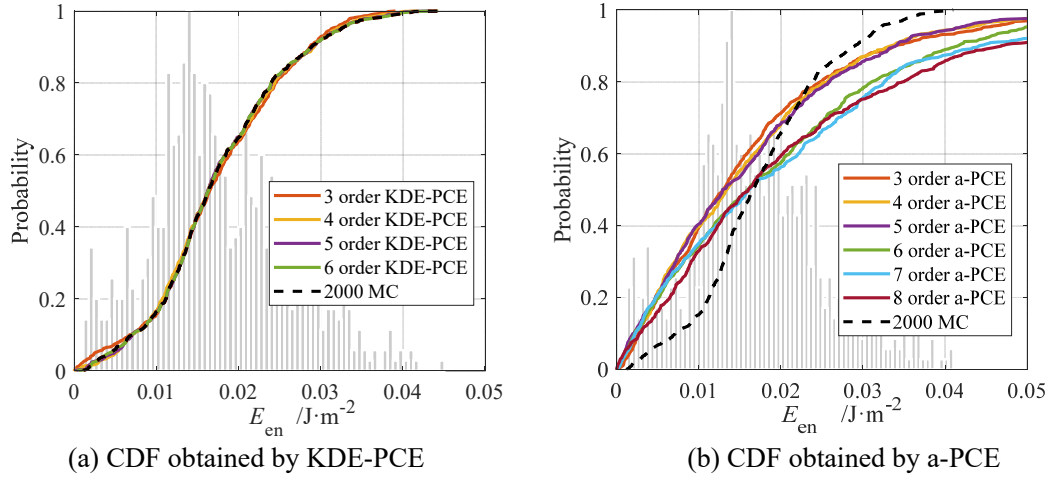


Figure 4-12 CDF of the cumulative energy flow density of the HEMP

When solving the coefficients of the PCE by numerical integration, Figure 4-12 shows that the KDE-PCE has a very fast convergence speed, while the error monotonically decreases as the term of expansion increases. The CDF obtained by the proposed method has good agreement with the 2000 times MC results. The KDE-PCE achieves good performance with a quite low order of 3. On the contrary, the a-PCE can hardly converge. The error even gets larger because the orthogonal basis functions are not independent of each other.

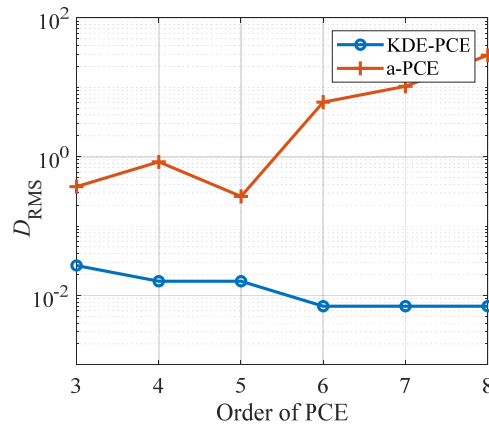


Figure 4-13 Root-mean-square deviation of KDE-PCE and a-PCE compared with 2000 times MC

On one hand, the correlated multivariate basis functions are constructed to be mutually orthogonal in the KDE-PCE. It can achieve the best convergence speed in the multivariate space. On the other hand, accurate results can be achieved with low-order PCE because the complex and multi-level field-coupling-to-line problem has been split into problems in sequence by the multiple stage uncertainty quantification, and the relationship between input

variables and output variables in each independent uncertainty quantification process is straightforward. There are usually smooth response surfaces (even analytic expressions like in this case), which is able to be approximated by low-order PCE.

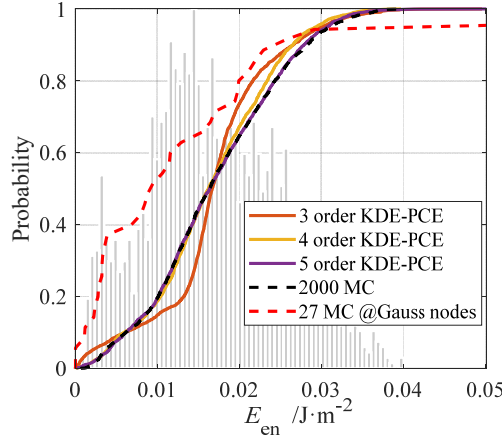


Figure 4-14 CDF of the cumulative energy flow density of the HEMP based on LS coefficient calculation

We also investigate the performance of the coefficient solved by LS. The LS matrix is established based on the information at the optimal Gauss point. The results are as good as that obtained by numerical integration for KDE-PCE.

Table 4-5 Comparison of time consumption and accuracy of MC, a-PCE, KDE-PCE

|           | MC | KDE-PCE with numerical integration |       |       | KDE-PCE with LS |       |       |
|-----------|----|------------------------------------|-------|-------|-----------------|-------|-------|
| Order     | \  | 3                                  | 4     | 5     | 3               | 4     | 5     |
| $D_{RMS}$ | \  | 0.027                              | 0.016 | 0.015 | 0.117           | 0.047 | 0.014 |
| Time / s  | 74 | 4.6                                | 6.1   | 13.4  | 2.02            | 3.15  | 5.2   |

Then we studied the uncertainty of the electric field waveform of HEMP. The PCE of the electric field waveform in the frequency domain is established with the correlated multivariate basis functions,

$$E(\xi_1, \xi_2, \xi_3, \omega) = \sum_{m=0, \dots, P} c_m^{(Ef)}(\omega) \psi_m(\xi_1, \xi_2, \xi_3, \omega) \quad (4-32)$$

The results in the time domain can be obtained from  $c_m^{(Ef)}(\omega)$  to  $c_m^{(Et)}(t)$  via inverse Fourier transform

$$E(\xi_1, \xi_2, \xi_3, t) = \sum_{m=0, \dots, P} c_m^{(Et)}(t) \psi_m(\xi_1, \xi_2, \xi_3, t) \quad (4-33)$$

Figure 4-15 shows that the mean waveform obtained by PCE is consistent with the mean of MC in both the frequency and time domain, the waveform of the upper  $3\sigma$  interval can be considered the worst-case or the bounding case for the HEMP. The worst-case waveform has an amplitude of 60.8 kV/m, a 10%-90% rise time equals 3 ns, and an FWHM equals 21 ns. The amplitude is higher than the 50 kV/m in the IEC standard. The rise time is slightly slower than 2.5 ns in the IEC standard, and the FWHM is slightly shorter than 23 ns in the IEC standard.

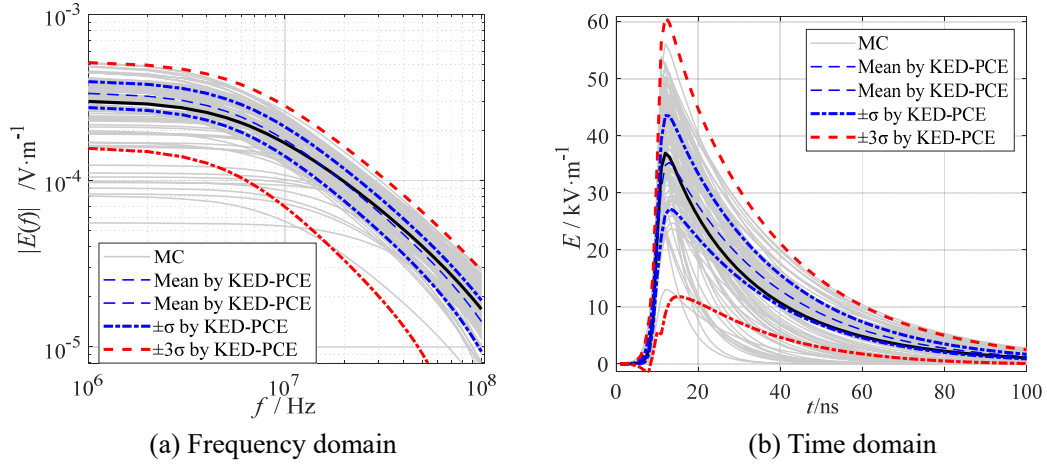


Figure 4-15 Expectation and variance interval of electric field waveform obtained based on KDE-PCE

However, there are no recognized ranges for many uncertain variables in the simulation of HEMP, which is also the motivation of the uncertainty quantification study, the absolute values of these results in this dissertation are only of reference significance. It shows that the uncertainty quantification based on the proposed stochastic models is reasonable and comparable with the published data.

#### 4.2.2 Uncertainty quantification of the HEMP-to-line coupling responses

This example is to quantify the uncertainty of TED-to-line coupling by using the proposed KDE-PCE method, comparing it with the classical single TL examples given by IEC 61000-2-10. The uncertainties that affect the coupling responses current are summarized as electromagnetic variables of the incident electric field, including the amplitude, polarization angle, elevation angle, and azimuth angle. A KDE-PCE stochastic model is constructed with 3 correlated uncertainty variables and 1 independent uncertainty variable.

In the IEC 61000-2-10 and related research, the polarization angle, elevation angle, and azimuth angle are treated as independent uncertainty variables subject to probability distributions, while the amplitude of the electric field is taken as a certain value of 50 kV/m<sup>[186][191]</sup>. In fact, the amplitude may vary due to kinds of uncertain variables. Meanwhile, the variation of the amplitude of the electric field relates to the variations of the polarization angle, elevation angle, and other variables mentioned early. Researchers acknowledged that simplifications for the electric field amplitude may lead to errors in the results. The lack of uncertainty quantification dealing with the correlated variables strengthens the motivation for this study.

Here, based on the uncertainty quantification of the fields in Chapter 2, the amplitude is an uncertainty variable as well. The amplitude, polarization angle, and elevation angle vary in the following range:  $\alpha \in [0, \pi/2]$ ,  $\psi \in [0, \pi/2]$ ,  $E_0 \in [0, 70 \text{ kV/m}]$ . Their probability distributions are shown in Figure 4-16. The azimuth angle is calculated by the relative angle of the object transmission line orientation  $\delta'$  and the direction of the incident field  $\delta$

$$\phi = \delta - \delta', \quad \delta \in [0, 2\pi], \quad \delta' \in [0, 2\pi]$$

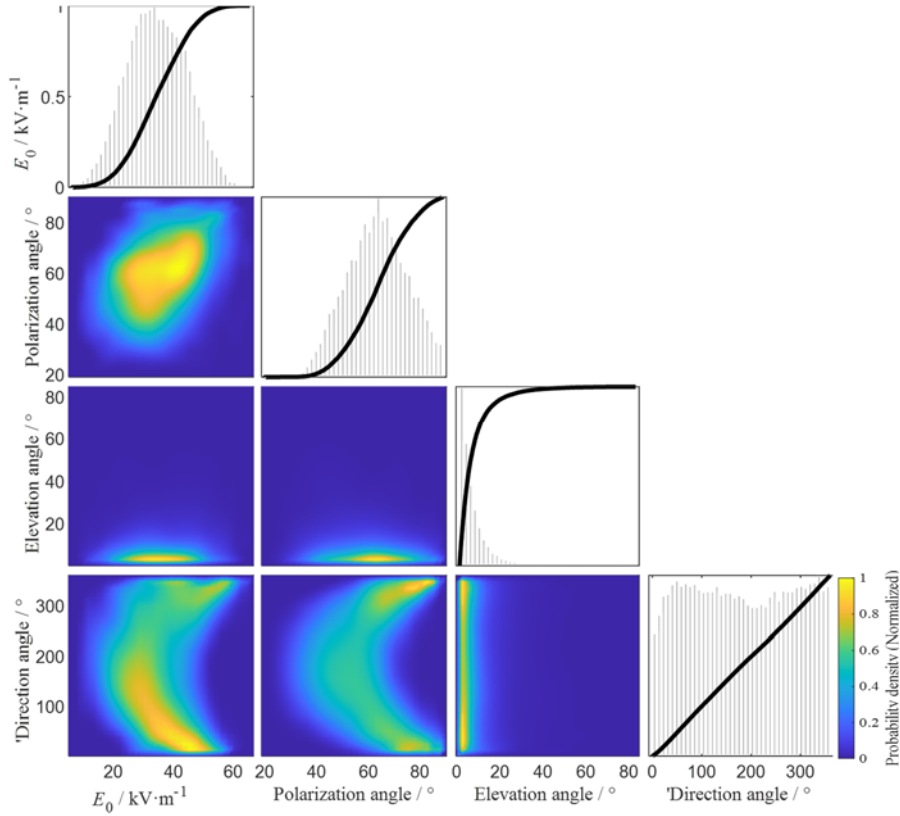


Figure 4-16 The joint and marginal distributions of amplitude, polarization angle, elevation angle, and direction angle obtained by the stochastic model of HEMP. The color represents the normalized joint probability density.

In this case, the TL coupling responses are quantified in the form of the equivalent Norton current model. So that the observed end of the conductor is short-circuited, and the terminal load at another end is matched to avoid multiple reflections. Characteristic impedance is the internal impedance for the equivalent Norton ideal source. The far-end induced current is the equivalent Norton ideal source for the TL under the incident field, calculated by the deterministic solution in (3-33) with  $\mathbf{Z}_S = \mathbf{Z}_C$ ,  $\mathbf{Z}_L = 0$ :

$$\begin{aligned}
 \mathbf{I}_{\text{eq}}(l, s) &= E_0(\omega) \frac{(A' + B')D}{\mathbf{Z}_C} \\
 A' &= \frac{\omega\mu_0 h}{377k \sin \psi} \left[ \begin{aligned} &\sin \alpha \sin \psi \sin \phi (1 - R_h) \\ &+ \cos \alpha \cos \phi (1 + R_v) \end{aligned} \right] \\
 &\quad + \left[ \cos \alpha \sin \psi \cos \phi (1 - R_v) + \sin \alpha \sin \phi (1 + R_h) \right] \\
 B' &= \frac{-\gamma h}{jk \sin \psi} \cos \alpha \cos \psi (1 + R_v) \\
 D &= \frac{e^{-j\omega l \cos \psi \cos \phi / c} - e^{-\gamma l}}{\gamma - jk \cos \psi \cos \phi}
 \end{aligned} \tag{4-34}$$

A stochastic model for the induced current equivalent Norton ideal source in frequency-domain or time-domain by PCE with three correlated variables and one independent variable

$$\begin{aligned} \mathbf{I}_{\text{eq}}(l, s, \xi) &= \sum_m^p c_m^{(I)}(s) \psi_m(\xi) \\ Z_{\text{eq}}(l, t, \xi) &= \sum_m^p c_m^{(Z)}(t) \psi_m(\xi) \end{aligned} \quad (4-35)$$

As we studied in Section 3.3.2, when the variance interval of the variables is small, especially for the azimuth angle  $\phi$ , both frequency domain and time domain PCE methods can well demonstrate the uncertainties and variance intervals of the results. However, when the value of the azimuth angle  $\phi$  varies in a large interval, such as  $\phi \sim U(0, \pi/2)$ . In this case, the Gibbs phenomenon occurs in the time domain results. The frequency-domain results are no longer smooth as well because of the abrupt changes in the waveform. Thus we study the uncertainty of induced current by the stochastic model of the induced current amplitude,

$$\|\mathbf{I}_{\text{eq}}(\xi)\|_{\infty} = \sum_a^p c_a^{(A)}(\omega) \psi_a(\xi) \quad (4-36)$$

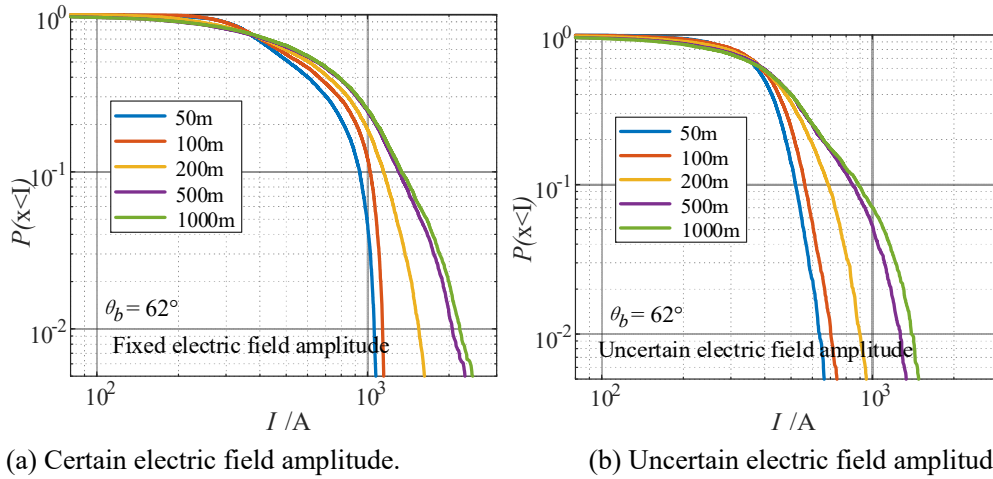
Firstly, the case with fixed field amplitude is studied by a KDE-PCE with two correlated variables  $\alpha$ ,  $\psi$ , and an independent variable  $\delta$ . The variables are referenced from Reference [191]. Soil relative permittivity:  $\varepsilon_r=10$ . Soil conductivity:  $\sigma=0.01$  S/m. Line height:  $h=10$  m. Line radius:  $a=0.01$  m. Geomagnetic inclination:  $\theta_b=62^\circ$ . Table 4-6 shows the induced current amplitude with different quantiles and reference values given in several references. The induced current increases with the increase of line length, and tends to saturate when the line is longer than 200 m. The conclusion is consistent with the results obtained by MC in the Reference [191]. The values are not exactly the same, because the MC samples used to generate the results in IEC are not random, limited by the computation efficiency. Only four burst heights (100, 200, 300, and 400 km) and 36 values of polarization angles were chosen to perform the MC simulation<sup>[186][191]</sup>.

Table 4-6 Induced current peak in ampere versus quantile and line length

| Lower quantiles | Induced current peak / A |            |          |            |          |            |          |            |      |
|-----------------|--------------------------|------------|----------|------------|----------|------------|----------|------------|------|
|                 | l=50 m                   |            | l=100 m  |            | l=200 m  |            | l=1000 m |            |      |
|                 | Proposed                 | Ref. [191] | Proposed | Ref. [191] | Proposed | Ref. [191] | Proposed | Ref. [191] |      |
| 50%             | 503                      | 586        | 555      | 563        | 604      | 544        | 655      | 464        | 500  |
| 90%             | 935                      | 1170       | 1020     | 1228       | 1145     | 1310       | 1331     | 1313       | 1500 |
| 99%             | 1378                     | 1514       | 1483     | 1764       | 1710     | 1910       | 2188     | 2205       | 4000 |

Note: Data in red are from the Reference [191] Table VI.

Then, considering the electric field amplitude as an uncertain variable as well, the distribution of induced current obtained by the KDE-PCE stochastic model is shown in Figure 4-17 (b). Compared with the conventional statistical study that regards the electric field amplitude as a fixed value, the severity of the induced responses reduces. This is because that severe coupling responses usually occur under grazing incidence fields. However, when the elevation angle is small, the amplitude of the HEMP fields is usually small.



(a) Certain electric field amplitude. (b) Uncertain electric field amplitude.  
 Figure 4-17 CDF of induced current amplitude with and without the consideration of the electric field amplitude uncertainty.

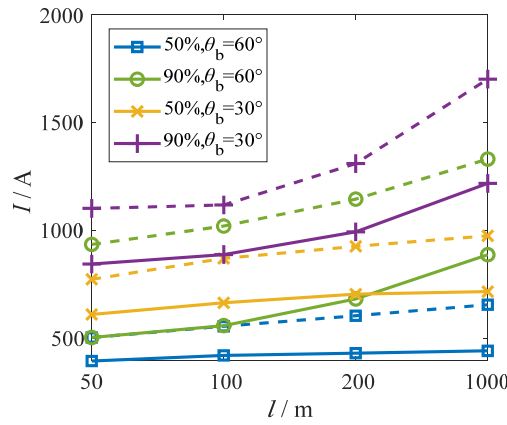


Figure 4-18 Induced current amplitude with different quantiles simulated with fixed amplitude (with dash line) and uncertainty amplitude (with solid line)

Figure 4-18 shows the quantile of induced response with different dip angles. In general, the induced responses for the same conductors are less severe in the low-altitude area. The consideration of the uncertainty of field amplitude leads to a significant reduction in the severity of induced current. The uncertainty of the field should not be ignored or used as a fixed value during the uncertainty quantification of the coupling response. Otherwise, it will cause an overestimation of the conducted environment of the lines.

#### 4.2.3 Uncertainty quantification of line coupling response with nonlinear load

This example is to validate the uncertainty of coupling responses on the TL with nonlinear loads by using the proposed KDE-PCE method. A 300 m-long 10 kV power line excited by HEMP is studied. The diameter and height of the lines are 6.6 mm and 10 m, respectively. Both sides of the line are loaded with matched resistance. In the case with the consideration of MOA, the 10-kV YH5WZ-17/45 MOA is in parallel with the loads at the far end.

The probability distributions of  $E_0$ ,  $\alpha$ ,  $\psi$  are shown in Figure 4-16. The amplitude, polarization angle, and elevation angle vary in the following range:  $E_0 \in [0, 70 \text{ kV/m}]$ ,  $\alpha \in$

$[0, \pi/2]$ ,  $\psi \in [0, \pi/2]$ . The azimuth angle  $\phi$  is considered as an independent variable. A KDE-PCE is constructed with 3 correlated uncertainty variables and 1 independent uncertainty variable based on the deterministic solution of the TLs with the nonlinear load. The simulation is carried out with both the proposed dynamic nonlinear model and the conventional static model of MOA.

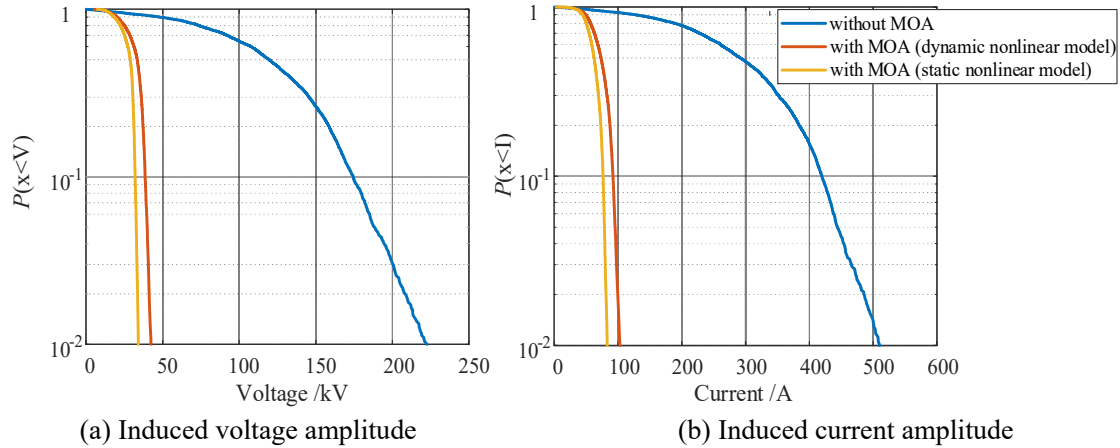


Figure 4-19 CDF of induced responses on the terminal load without and with the protection of parallel MOA

The amplitude of the induced current and voltage at the far-end load are shown in Figure 4-19. The existence of MOA can greatly reduce the induced current and voltage on the equipment under the protection of MOA. The induced voltage is slightly greater for the result with the proposed MOA model than with the conventional model. This is caused by the dynamic characteristic of MOA, that the residual voltage of the MOA will increase with the increase of the induced current. Since the induced current is less than 1kA, the MOA works in the nonlinear region, the dynamic characteristics are not obvious, so the difference between the results with different MOA models is not obvious.

### Concluding remarks

(1) The PCE method based on MCMC-KDE is proposed to address the problem of transferring arbitrary distribution correlated multidimensional variables in the hierarchical stochastic model. The KDE-PCE has the following advantages: (i) efficient and accurate description of high dimensional correlated variables, (ii) easy to be used for multi-variable polynomial basis construction, (iii) simple form that does not increase the difficulty of integration for coefficients solving, (iv) good performance with low order and high convergence speed.

(2) By using the proposed hierarchical stochastic method, statistical analysis is performed for the HEMP electric field. The upper  $3\sigma$  interval is regarded as the bounding case of the HEMP waveform with 60 kV/m amplitude, 3 ns rise time, and 21 ns FWHM, which has comparable results with the IEC standard waveform and other references. It should be noted that the results are affected by many uncertainty variables and their value ranges, the absolute values of the results are only of reference significance.



(3) The coupling responses of classical TLs are quantified by the proposed hierarchical stochastic method. Compared with the IEC standard and related studies, the consideration of the spatial distribution and uncertainty of the electric field amplitude leads to a significant reduction in the severity of induced current. Ignoring the variation of the field waveform and using the HEMP field amplitude as a fixed value will cause an overestimation of the HEMP conducted environment of the line.

## 5 Vulnerability assessment based on quantification of margins and uncertainties

For the equipment terminating at the end of long transmission lines, the only way to test their ability under the TED effect is by injecting conducted waveform. The failure probability based on experimental data has been widely adopted to evaluate the equipment under TEDs. However, due to the complex and black-box failure mechanism of the equipment under TED and small data obtained from the expensive effect test, it is difficult to determine the preset distribution of the threshold and provide estimation from the small data collection because of the sampling variability and estimation errors.

This chapter introduces a distribution-free vulnerability assessment method of equipment connected with lines under TED, with the consideration of the uncertainties of stress caused by the TED, and the inherent probability and uncertainties of the equipment strength under TED. The stress is represented by the probability distribution of the coupling responses and is obtained by the proposed stochastic model. The strength is represented by the probability distribution and tolerance interval of the threshold, and it is estimated from the estimation of test data. The proposed method could provide a reasonable evaluation with certain confidence levels.

### 5.1 Distribution-free quantification of margins and uncertainties

#### 5.1.1 Basic concept and procedure of uncertainty quantification for margins

The vulnerability assessment of electrical and electronic equipment excited by TED is supposed to be appropriate and reasonable with the consideration of the probability characteristic of the TED environment and equipment performance. The probability distribution of the amplitude and other electromagnetic norms of the possible TED have been collected based on long-term experimental data or by simulation with uncertainties<sup>[196]-[199],[40]</sup>. The failure probability based on experimental data has been widely adopted<sup>[201]-[206]</sup>. This section introduces the quantification of margins and uncertainties (QMU) method, which considers both the probability distribution and the uncertainty of the strength and stress of the electrical and electronic equipment.

QMU was proposed for the assessment of the performance of equipment in the presence of insufficient data and lacking knowledge<sup>[207]-[209]</sup>. Recently, it has been used for the effect and safety assessment of mechanical structures and electrical systems, such as the flutter analysis of wing structures and the radiation effect evaluation of satellite electric power systems<sup>[210]-[213]</sup>. The classical QMU was based on the assumption that the equipment stress and strength are values described by the best estimation and its uncertainties<sup>[214]</sup>. However, the threat and failure threshold of the equipment under TED may follow probability distributions and cannot be described by the best estimation and its uncertainties. The QMU metrics calculated by best estimation and standard deviation were no longer suitable for the

vulnerability evaluation. A new QMU approach was proposed to quantify margin and uncertainties through the computation of the chosen quantiles and the statistical bound rather than by sample standard deviation<sup>[215]</sup>.

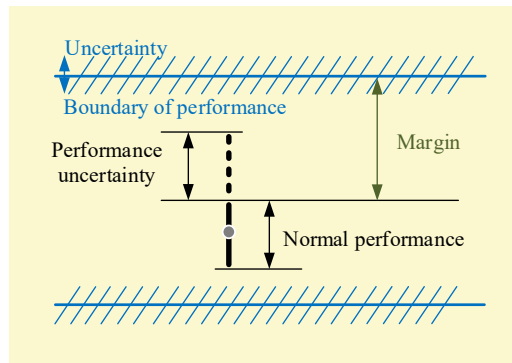


Figure 5-1 Basic principle of Quantification of Margins and Uncertainties (QMU) method<sup>[206]</sup>

The vulnerability assessment based on the QMU method can provide comprehensive evaluations including the simulation and uncertainties quantification of the margins between the “strength” and the “stress” of the equipment. The notional illustration of the QMU method is shown in Figure 5-1<sup>[206]</sup>. To apply the QMU method in the vulnerability assessment of equipment under TED, some basic concepts are redefined and explained as follows:

(a) Stress (D): the stress (or demand, threat) of the equipment is represented by the change in equipment parameters caused by external disturbances. The stress of the equipment excited by electromagnetic disturbances can be represented by the coupling responses on the conducted coupling path of the equipment.

(b) Strength (C): the strength (or capacity, performance threshold) of the equipment refers to the maximum or minimum allowable value of one or several given parameters when the equipment operates normally. The equipment strength under TED is quantified by the occurrence probabilities of the failure varying with the coupling responses.

Here, the induced current amplitude on the conducted coupling path of the equipment is chosen as the key parameter to quantify the stress and the strength.

(c) Margin (M): the margin is defined as the distance between the performance and the performance boundary in the traditional QMU method. Here, the margin is defined as the Euclidean distance between the strength and the stress of the equipment.

(d) Uncertainty (U): the uncertainties are defined as the changes in margins. The uncertainties of the margin are the result of the uncertainties in both equipment stress and strength. The uncertainties can be divided into two types<sup>[214]</sup>. The epistemic uncertainties are due to the lack of knowledge or incomplete knowledge, such as the probability distribution of stress caused by the uncertain variables in the simulations. The aleatory uncertainties include the inherent probability characteristics such as the probability of the failure, and the uncertainties caused by the sampling variability in every sampling process which can be expressed by the tolerance intervals of the probability distributions.

(e) QMU metric: QMU metric is the figure-of-merit defined by the ratio of margin and the uncertainties. With the QMU metric, the identification, likelihood, and credibility of the

equipment vulnerability can be effectively obtained. The evaluation results can answer several questions: Is the equipment vulnerable or not? What is the probability of effect occurrence for the equipment excited by TED? And what is the confidence level of the result?

The classical QMU metrics are based on the normality assumption for both strength ( $X_C \sim N(\mu_C, \sigma_C^2)$ ) and stress ( $X_D \sim N(\mu_D, \sigma_D^2)$ ) of the equipment, which has a specific name called the QMU calculator  $Q$ <sup>[214]</sup>:

$$Q = \frac{M}{U} = \frac{\mu_C - \mu_D}{\sqrt{(\alpha\sigma_C)^2 + (\alpha\sigma_D)^2}} \tag{5-1}$$

$M$  refers to the margins, it is calculated by the difference between the best estimations of equipment stress and strength.  $U$  refers to the uncertainties, it is calculated by using  $\alpha$  as the standard deviation for both normal distributions. The QMU metrics are the criterion of vulnerability. When it is larger than 1, the equipment is not vulnerable.

The procedure of vulnerability assessment based on the QMU method can be summarized as follows: firstly, due to the effect mechanism of the equipment under TED, choose the amplitude of the current on the conducted coupling path of the equipment as the parameter of interest. Then, obtain the induced current by simulation with the consideration of the uncertainties of TED, equipment, and coupling process. Take the result as the stress of the equipment. Thirdly, obtain the equipment failure threshold experimentally, and take it as the strength of the equipment. Finally, utilize the QMU method to evaluate the margins and the uncertainties of the equipment, and assess the equipment vulnerability by the QMU metrics.

Quantifying the margins and uncertainties is the key to the assessment of equipment vulnerability based on QMU. Since the margins are calculated by the distance between the stress and the strength of the equipment excited by TED, as shown in Figure 5-2, there are two significant tasks: the uncertainty quantification of the equipment stress and the equipment strength under TED. Here, we introduce the procedure of quantification of the margins and uncertainties, with HEMP as a kind of TED event.

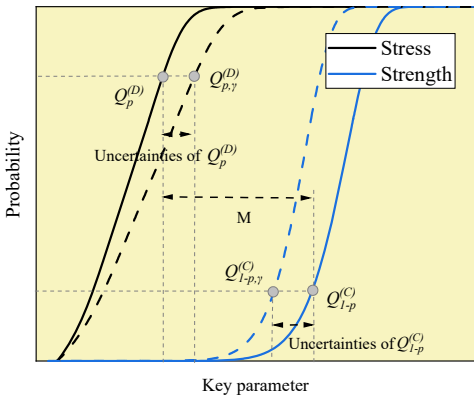


Figure 5-2 Graphical Depiction of the Quantile, statistic tolerance bound, margins and uncertainties

### 5.1.2 QMU metric based on quantiles and tolerance bounds

When evaluating the assessment of equipment excited by disturbances, the stress and strength of the equipment follow probability distributions themselves, and the distributions are

rarely Gaussian. The traditional QMU metrics calculated with the best estimation and uncertainties are not suitable. Therefore, a novel figure-of-merit is necessary.

With the consideration of the inherent probability characteristics of the strength, researchers have provided a figure-of-merit based on statistical tolerance interval methodology, called tolerance ratio (TR)<sup>[215]</sup>:

$$TR = \frac{M}{U} = \frac{Q_{1-p}^{(C)} - LPR}{Q_{1-p}^{(C)} - Q_{1-p,\gamma}^{(C)}} \quad (5-2)$$

LPR means the lower performance requirement, which can be regarded as equipment stress.  $Q_{1-p}$  denotes the lower quantile; similarly, there is an upper  $p$  quantile  $Q_p$ :

$$P(x > Q_{1-p}) = p, \quad P(x < Q_p) = p \quad (5-3)$$

$Q_{p,\gamma}$  is the one-side statistical tolerance bound, which bounds the possible range for the distribution with some confidence levels. For comparison, the widely-used confidence interval only bound the possible range for a statistical parameter such as mean or variance. The tolerance bound refers to the aleatory uncertainties caused by the process of data sampling and estimating. The tolerance bound for lower and upper  $p$  quantile are defined as follows:

$$P(P(x > Q_{1-p,\gamma}) \geq p) \geq \gamma, \quad P(P(x < Q_{p,\gamma}) \geq p) \geq \gamma \quad (5-4)$$

which means  $p \cdot 100\%$  of the values will be greater than  $Q_{1-p,\gamma}$  with  $\gamma \cdot 100\%$  confidence. The relationship between quantiles and statistical tolerance bounds is shown in Figure 5-2.

In fact, the equipment stress may be from probability distribution as well. Therefore, a novel distribution-free QMU metric based on quantiles and statistical tolerance bound is defined:

$$CF = \frac{M}{U} = \frac{Q_{1-p}^{(C)} - Q_p^{(D)}}{(Q_{1-p}^{(C)} - Q_{1-p,\gamma}^{(C)}) + (Q_{p,\gamma}^{(D)} - Q_p^{(D)})} \quad (5-5)$$

The superscript D and C mean that the quantile and statistical tolerance bound are for the stress and the strength respectively. CF is the ratio of margin and total uncertainties, which is consistent with the original definition of the QMU metric. The distance between stress and strength is calculated by the quantile of the estimated probability distribution, instead of the distance between two single best estimation values. The uncertainties are calculated by the tolerance bounds. The relationship between the values used in (5-5) is demonstrated in Figure 5-3. The curve made up of quantiles refers to the estimated probability distribution of stress and strength, and the curve made up of the tolerance bounds refers to the uncertainties of the distribution.

In the general QMU method, the strength and the stress of the equipment under test are represented as the best estimation of the values and uncertainties, which are described by normal distributions. Relative QMU metrics  $Q$  is calculated by the ratio of margin and uncertainties as in (5-1).  $\alpha$  is the number of standard deviation values that corresponds to a given confidence level of the estimation. When  $Q$  equals 1, the margin is exactly equal to the

uncertainties:

$$\mu_C - \mu_D = \alpha \sqrt{\sigma_C^2 + \sigma_D^2} \quad (5-6)$$

which means the value of  $(C-D)$  follows a new normal distribution  $N(\mu_C - \mu_D, \sigma_C^2 + \sigma_D^2)$ . The confidence level of that the strength greater than the stress can be calculated

$$\begin{aligned} P(C > D) &= P\left(C - D > \mu_C - \mu_D - \alpha \sqrt{\sigma_C^2 + \sigma_D^2}\right) \\ &= P\left(\frac{C - D - (\mu_C - \mu_D)}{\sqrt{\sigma_C^2 + \sigma_D^2}} > -\alpha\right) \\ &= \Phi(\alpha) \end{aligned} \quad (5-7)$$

where  $\Phi(\alpha)$  is the percentage of values up to  $\alpha$  in a standard normal distribution and can be checked from the standard normal distribution table of  $\Phi(\alpha)$ . When  $Q \geq 1$ , there is no less than  $\Phi(\alpha)$  confident that strength is greater than stress, and the equipment is not vulnerable under the stress.

It can be also explained from the point of view of the probability with reference to the stress-strength interference method.  $\alpha$  is the number of standard deviation values that corresponds to the probability of the values. The failure probability of the equipment can be calculated by the probability that the stress is greater than the strength.

$$R = \Pr(D > C) = \Phi(-\alpha) \quad (5-8)$$

where  $\Phi(-\alpha)$  equals to  $1 - \Phi(\alpha)$ .

When  $Q=1$ , the failure probability equals  $\Phi(-\alpha)$ . For example, when  $\alpha=1$  and 3, the confidence level is less than 15% and 0.13%, respectively. When  $Q>1$ , the failure probability  $R$  is less than  $\Phi(-\alpha)$ . If the failure probability of  $\Phi(-\alpha)$  is considered negligible, the conclusion can be given that the equipment is not vulnerable under the stress. When  $Q<1$ , the failure probability is larger than 0.13%. In other words, the equipment may be vulnerable.

In the proposed distribution-free QMU method, when the stress and strength are from distribution  $F^{(C)}$  and  $F^{(D)}$ , the failure probability can be calculated as well:

$$\begin{aligned} R &= P(D < C) \\ &= \int_{-\infty}^{\infty} f^{(C)}(\delta) \left[ \int_{\delta}^{\infty} f^{(D)}(\sigma) d\sigma \right] d\delta \\ &= \sum_{\delta=-\infty}^{\infty} [F^{(C)}(\delta + \Delta\delta) - F^{(C)}(\delta)] [1 - F^{(D)}(\delta)] \end{aligned} \quad (5-9)$$

When the strength and stress are represented by distribution  $F^{(C)}$  and  $F^{(D)}$  (or the quantiles  $\{Q_{1-p,\gamma}^{(C)}\}, \{Q_{p,\gamma}^{(D)}\}$ ) with a confidence level of  $\gamma \cdot 100\%$ , the failure probability is

$$R = \sum_{\rho=0}^1 \Delta\rho [1 - F_{\gamma}^{(D)}(Q_{1-\rho,\gamma}^{(C)})] \quad (5-10)$$

When  $CF = 1$ , we have  $Q_{1-p,\gamma}^{(C)} = Q_{p,\gamma}^{(D)}$  as shown in Figure 5-3. It is obvious that  $R < p$ .

When  $1-p$  is small,  $R$  can be approximately equal to  $(1-p)^2 \cdot 100\%$ . When  $CF > 1$ , the failure probability is less than  $R \cdot 100\%$ . If the  $R \cdot 100\%$  failure probability can be considered negligible, the equipment is not vulnerable with  $\gamma \cdot 100\%$  confidence level. Therefore, referring to traditional QMU methods, we define that: when  $CF > 1$ , it is  $\gamma \cdot 100\%$  certain that at least  $(1-R) \cdot 100\%$  of the parameters of the equipment will be in the operating region of the equipment. If  $R \cdot 100\%$  is less than the acceptable failure probability for the equipment, the equipment is not vulnerable with a confidence level of  $\gamma \cdot 100\%$ . When  $CF < 1$ , the performance requirement for equipment under TED is not satisfied, and the equipment may be vulnerable.

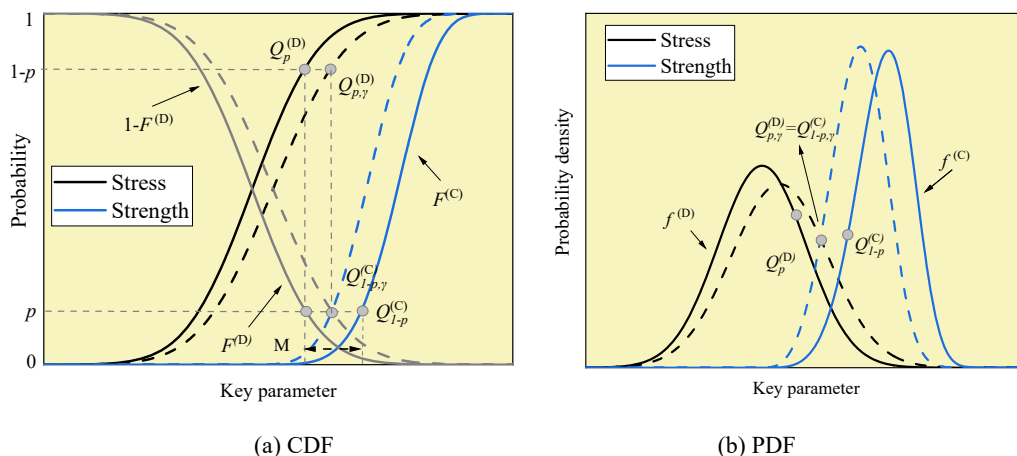


Figure 5-3 Graphical depiction of the probability distribution of equipment strength and stress in the distribution-free QMU method

Particularly, if the equipment stress is a fixed value, the calculation of CF will degenerate to Equation (5-2).

## 5.2 Uncertainty quantification for equipment strength based on experiment

### 5.2.1 Equivalence between PCI experiment and field-to-line coupling

PCI is an important approach of effect for the equipment under impulse, which refers to injecting a transient signal into the coupling conductor path outside the electromagnetic barrier of equipment under test.

PCI is recommended for the equipment connected with the conductor exposed to the electromagnetic field. When the lines are long, such as power lines or communication wires with length of kilometers, sufficient coupling responses cannot be generated through the radiation test. When the lines are in limited scales of the radiation field simulator, even though it radiation test is possible, it is difficult to change the incident angle and polarization angle with the state-of-the-art radiation field simulator platform. Sufficient situations of coupling responses cannot be generated as well. PCI can directly inject the conducted interference into the device port according to the simulated coupling response, which is feasible and efficient.

The current PCI technology is mainly used for the study of HEMP effect tests, the methods can also be extended to other TED effect tests, such as lightning electromagnetic pulse, substation electromagnetic pulse, etc.

A typical test platform for PCI is provided in MIL-STD-461G<sup>[216]</sup>, as shown in Figure 5-4.

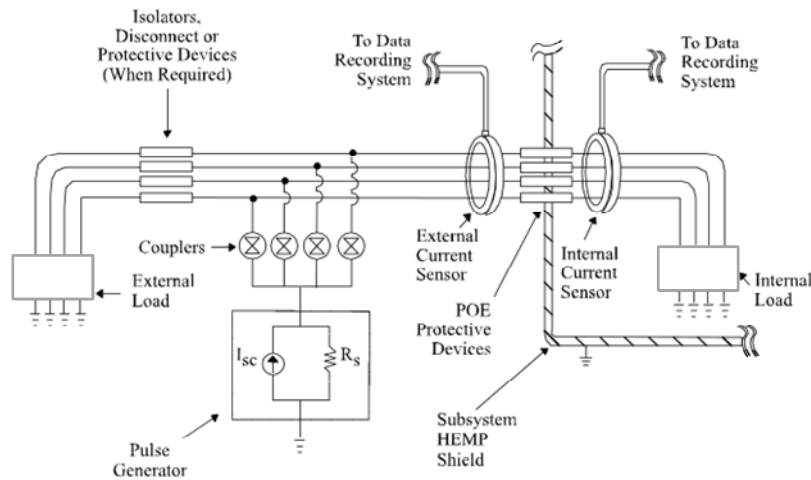


Figure 5-4 Typical PCI test platform in MIL-STD-461G<sup>[216]</sup>

The existing PCI for HEMP is mainly used for the examination and acceptance test of equipment or system. The waveforms recommended for injection pulse in standards are extracted from the “bounding case” for a specific conductor, which aims to test the viability of the equipment under the worst case. However, the “bounding case” standards are too strict for the evaluation of widely-distributed equipment in the power system. Since we could quantify the coupling responses with uncertainties by the stochastic models in Chapter 4, most of the coupling responses are smaller than those have been given by the standard. Moreover, the transient signal that is actually injected into the device port may be quite different from the measured waveform of the pulse source due to the input impedance of the EUT.

In order to cope with the various coupling response, as well as obtain the threshold of the equipment in addition to the viability under the worst case, it is necessary to establish an equivalent method of PCI and field line coupling. On the one hand, it can be used to put forward requirements for the injection waveform generated by PCI before the test. On the other hand, it can be used to evaluate the consistency between the actual injection signal and the expected coupling responses, and extract the failure threshold of the equipment under realistic TED.

PCI through inductive coupler is the most widely adopted. The inductive coupler is a current injection ring based on the principle of the transformer. The primary windings of the coupler are connected with the pulse generator, and the injected lines are regarded as the secondary winding. The electrical model of the coupler and a single line under injection is shown in Figure 5-5 (a) as an example. If the coupler and injected lines are considered electrically small structures, a classical relationship between voltage and current on the line and the voltage and current of the pulse source can be given<sup>[217]</sup>:

$$\begin{bmatrix} V_2 - V_1 \\ I_2 \end{bmatrix} = \Phi_{CP} \cdot \begin{bmatrix} V'_s - Z_s I'_s \\ I'_s \end{bmatrix} \quad (5-11)$$



where  $\Phi_{CP}$  is calculated by the stray parameters of the coupler and the coupling between the coupler and the injected wire:

$$\Phi_{CP} = \Phi_{FC} \Phi_{ST}$$

$$\Phi_{FC} = \begin{bmatrix} \frac{1}{N_{T1}} + N_{T1} \frac{L_{2L}}{L_{1S}} & -j\omega N_{T1} L_{2L} \\ -\frac{1}{j\omega} N_{T1} \frac{1}{L_{1S}} & N_{T1} \end{bmatrix} \quad (5-12)$$

$$\Phi_{ST} = \begin{bmatrix} 1 + j\omega C_{wd} R_{wd} & \omega^2 L_{wd} C_{wd} R_{wd} - j\omega L_{wd} - R_{wd} \\ -j\omega C_{wd} & 1 - \omega^2 L_{wd} C_{wd} \end{bmatrix}$$

where  $C_{wd}, R_{wd}, L_{wd}$  — the stray parameters for the coupler;  $N_{T1}$  and  $L_{1S}$  — the number of turns and self-inductance for the primary windings of the coupler;  $L_{2L}$  — the leakage inductance for the injected lines:

$$L_{1S} = \mu_r \mu_0 \frac{N_{T1}^2 l_c}{2\pi} \ln\left(\frac{r_{c2}}{r_{c1}}\right), \quad L_{2L} = \mu_0 \frac{l_c}{2\pi} \ln\left(\frac{r_{c1}}{r_L}\right) \quad (5-13)$$

$r_{c1}, r_{c2}, r_L$  — the inner and outer radius of the coupler and the radius of the injected line;  $\mu_r$  — the relative permeability of the coupler;  $l_c$  — the length of the coupler.

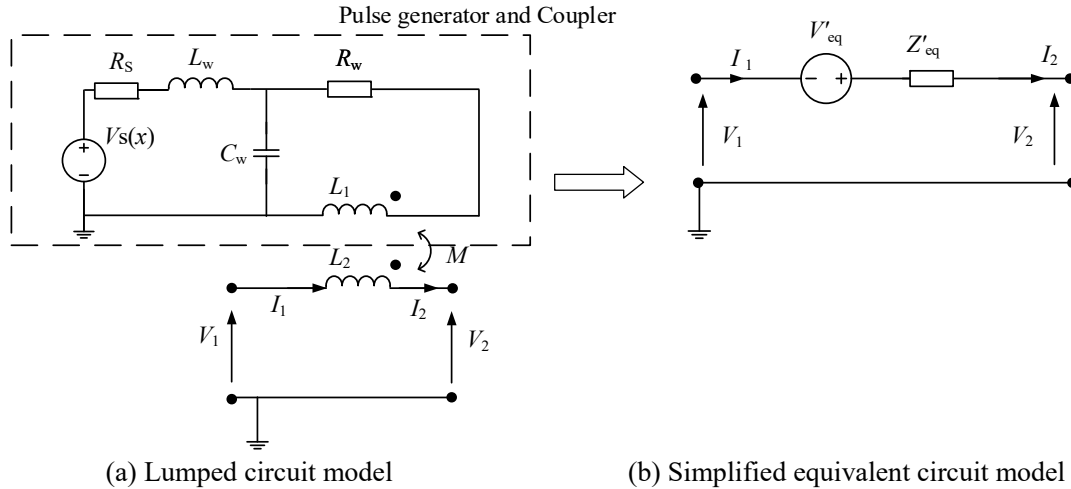


Figure 5-5 Lumped circuit models of the PCI coupler clamped onto the injected line

$\Phi_{CP}$  can be calculated by measuring every single parameter in (5-12). The model used to predict the coupler and the injected line can also be non-invasively extracted by measurement of voltages and currents in (5-11). (5-11) can be derived in a simple form that is easy for extracted:

$$\begin{bmatrix} V_2 \\ I_2 \end{bmatrix} = \begin{bmatrix} 1 & Z''_{eq} \\ 0 & 1 \end{bmatrix} \begin{bmatrix} V_1 \\ I_1 \end{bmatrix} + \begin{bmatrix} V'_{eq} \\ 0 \end{bmatrix} \quad (5-14)$$

$$V'_{eq} = \frac{\Phi_{CP,12} \Phi_{CP,21} - \Phi_{CP,11} \Phi_{CP,22}}{\Phi_{CP,21} Z_S - \Phi_{CP,22}} V'_S, \quad Z''_{eq} = \frac{\Phi_{11} Z_S - \Phi_{12}}{\Phi_{21} Z_S - \Phi_{22}}$$

The excitation caused by the PCI coupler is equivalent to a voltage source  $V_{eq}$  with internal impedance  $Z''_{eq}$  connected in series in the line as shown in Figure 5-5 (b).

However, detailed design parameters of the PCI coupler are not always available, especially when off-the-shelf commercial devices are adopted. Therefore, the four unknown frequency-dependent parameters in the matrix  $\Phi_{CP}$  are simplified into two unknown parameters, which can be extracted by at least two measurements for voltage  $V_2$ -  $V_1$  and one current  $I_2$ . The lack of information about detailed information on the internal parameters of the generator and coupler is overcome.

During the study, it is found that  $Z''_{eq}$  is small and can be ignored. This is because the leakage inductance of the injected line  $L_{21}$  is large, which means the transformer ratio of the coupler is large. The secondary side (injected line) has little influence on the primary side (pulse generator and coupler).

When the injected signal has a fast rise time and narrow wideband, the wavelength of the signal is comparable with the length of the PCI coupler and injected lines, therefore the distributed parameter model of the line needs to be considered. The whole system is composed of the coupler, injected line, EUT with input impedance  $Z_{EUT}$  (assuming on the right side end of the injected line), auxiliary equipment input impedance  $Z_A$  (assuming on the right side end of the injected line), and the system can be divided into three parts, including a part composed of line, coupler, and ground, and two transmission line parts composed of injected lines and ground, as shown in Figure 5-6.

The distribution model of the coupler part can be constructed by normalizing the excitation caused by coupling according to the coupler length:

$$\begin{bmatrix} \frac{dV}{dx} \\ \frac{dI}{dx} \end{bmatrix} = \begin{bmatrix} Z & 0 \\ 0 & Y \end{bmatrix} \begin{bmatrix} V \\ I \end{bmatrix} + \frac{1}{l_{CP}} \begin{bmatrix} V_{eq} \\ 0 \end{bmatrix} \quad (5-15)$$

where  $Z$ ,  $Y$  are the p.u.l. parameter of the TL. The shell of the coupler is metal and grounded and can be regarded as the perfect ground in the calculation of  $Z$  and  $Y$ . The calculation can be referred to (3-3) in Chapter 3. The frequency-dependent parameter caused by the imperfect earth can be discarded. The other part can be modeled as a classical TL without the external field.

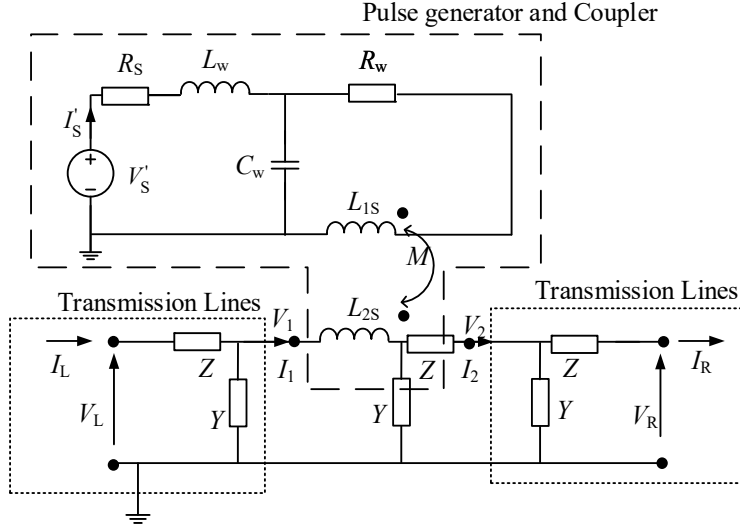
Therefore, the three parts of the system can be modeled by the chain parameters method.

$$\begin{aligned} \begin{bmatrix} V_2 \\ I_2 \end{bmatrix} &= \Phi_{TL1}(l_{CP}) \begin{bmatrix} V_1 \\ I_1 \end{bmatrix} + \begin{bmatrix} V_{eq} \\ 0 \end{bmatrix} \\ \begin{bmatrix} V_1 \\ V_1 \end{bmatrix} &= \Phi_{TL2}(l_L) \begin{bmatrix} V_L \\ I_L \end{bmatrix} \\ \begin{bmatrix} V_R \\ I_R \end{bmatrix} &= \Phi_{TL3}(l_R) \begin{bmatrix} V_2 \\ I_2 \end{bmatrix} \end{aligned} \quad (5-16)$$

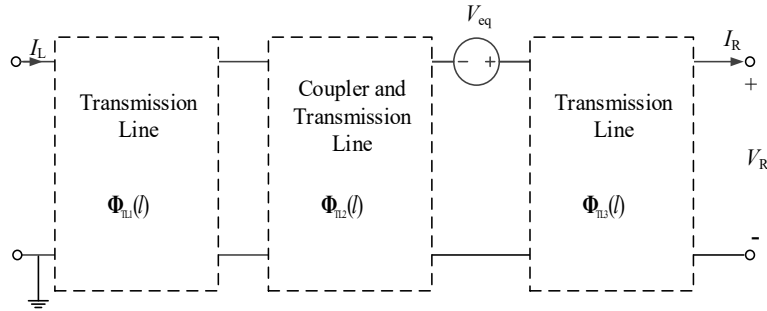
where the excitation of the coupler is equivalent to a voltage source connected in series with

the line at the right port of the line settled in the coupler. The boundary conditions for both ends of the line are

$$V_L = Z_A I_L, \quad V_R = Z_{EUT} I_R \quad (5-17)$$



(a) Distributed parameter model of the PCI coupler clamped onto the injected line



(b) Macromodel of the distributed parameter model

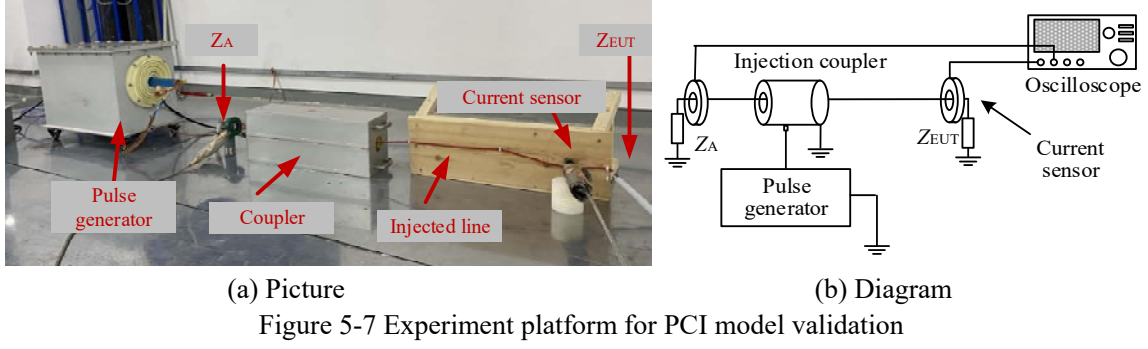
Figure 5-6 Distributed parameter model of the PCI coupler clamped onto the injected line

Due to the characteristics of chain parameters, the equation in (5-16) can be multiplied directly:

$$\begin{bmatrix} V_R \\ I_R \end{bmatrix} = \Phi_{TL1}(l_R) \Phi_{TL2}(l_{CP}) \Phi_{TL3}(l_L) \begin{bmatrix} V_L \\ I_L \end{bmatrix} + \Phi_{TL3}(l_R) \begin{bmatrix} V_{eq} \\ 0 \end{bmatrix} \quad (5-18)$$

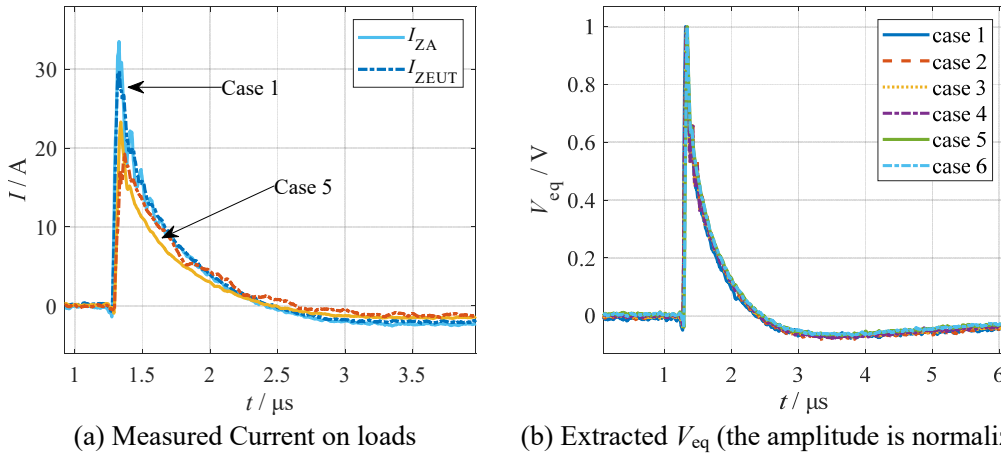
In particular, if the shell of the coupler is in direct contact with the earth, and the distance between the line and the ground is equal to the distance between the line and the metal shell of the coupler, the p.u.l parameters are the same for the three parts.

To validate the model, tests were carried out for injected lines with different lines and loads. The injected line in cases 1-3 and cases 4-6 are 1 m and 3 m respectively. The load  $Z_A$  is 300  $\Omega$ .  $Z_{EUT}$  are 0  $\Omega$ , 100  $\Omega$ , and 300  $\Omega$  in every 3 cases, respectively. The current sensors used in the experiment are Pearson 8585C with a bandwidth of 150 MHz. The oscilloscope used in the experiment is Tektronix DPO3054 with a bandwidth of 500 MHz. The test platform is shown in Figure 5-7.



(a) Picture (b) Diagram  
Figure 5-7 Experiment platform for PCI model validation

It can be observed from the measured results in Figure 5-8 (a), that the current at different positions of the injected line in the same test is different, it is necessary to consider the distributed parameters and wave process on the line. The measured current increase with the impedance of the loads decrease, which can be explained by the distribution model of the PCI test, the measured current is a combination of injection current and reflected current caused by the mismatched loads. The reflection coefficient increase when the impedance of the loads decreases.



(a) Measured Current on loads (b) Extracted  $V_{eq}$  (the amplitude is normalized to 1)  
Figure 5-8 Measured current on loads at both ends of the injected line and Extracted  $V_{eq}$  (Case 1: length of the line: 1 m.  $Z_A=300 \Omega$ .  $Z_{EUT} = 0 \Omega$ ; Case 5: length of the line: 3 m.  $Z_A=300 \Omega$ .  $Z_{EUT} = 100 \Omega$ .)

By using (5-18),  $V_{eq}$  can be extracted and shown in Figure 5-8 (b). The equivalent voltage source  $V_{eq}$  caused by the coupler is independent of load and line length. This provides us enlightenment, that for loads with unknown or complex (nonlinear) input impedance, it is incorrect to measure the current on the line to evaluate the effect during the experiment. An equivalent source independent of the load can be constructed, which has the same form as the equivalent source established for field-to-line coupling in Chapter 3.

By using the same derivation of macromodel in the field-to-line coupling problem, there is:

$$V_R - Z_C I_R = e^{\sqrt{ZY}(l_r+l_{CP}+l_L)} (V_L - Z_C I_L) + e^{\sqrt{ZY}(l_r+l_{CP}+l_L)} 2V_{eq} \quad (5-19)$$

When the auxiliary equipment  $Z_A$  equals the characteristic impedance  $Z_C$ , the PCI system can be equivalent to a Norton source, with the equivalent ideal current source and equivalent

internal impedance:

$$\begin{aligned} I'_{eq} &= e^{\sqrt{ZY}(l_R+l_{CP}+l_L)} 2V_{eq} \\ Z'_{eq} &= Z_C \end{aligned} \quad (5-20)$$

The simulated results with the proposed model and the measured results are compared for validation in Figure 5-9. The EUT is made up of a 100 Ω resistor and a 6 μH inductor, the length of the line is 3 m. It shows good agreement between measured and simulated results. It can also conclude from Figure 5-9 (b), that the measured voltage may be much different from the equivalent injected voltage  $V_{eq}$ , because of the reflection at the terminal loads. Therefore, it may cause an incorrect evaluation of the equipment strength if directly use the measured results in the estimation.

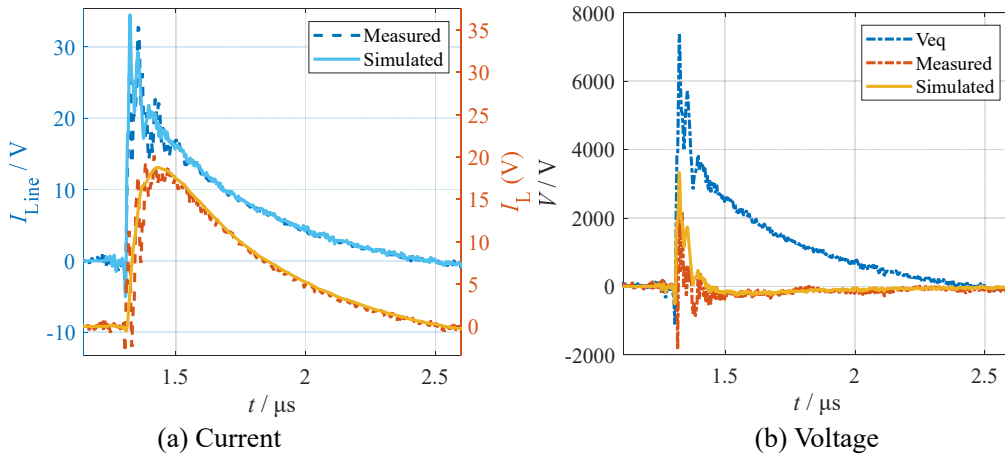


Figure 5-9 Injected current and voltage on the line and through the inductor

In order to obtain an equivalent characterization with the coupling responses on the lines excited by the external fields, the following conditions should be satisfied:  $Z'_{eq}=Z_C$ ,  $I'_{eq}=I_{eq}$ .  $I_{eq}$  is given by the uncertainty quantification of coupling responses in Chapter 4. The equivalent between the ideal current source is achieved by adjusting the signal of the pulse generator, and the target waveform of  $V_s$  can be calculated by (5-14). When the characteristic impedance of the injected line is different from that of the line under injection, the equivalent internal impedance is not the same. To achieve the purpose of equivalence, the equivalent internal impedance of the PCI system can be changed by connecting an auxiliary element  $Z'_A$  in parallel or in series with the EUT. The PCI test platform was built based on the equivalent method, as shown in Figure 5-10.

The line impedance stabilization network (LISN) avoids the back injection into city power and plays the role of auxiliary equipment with a stable impedance  $Z_C$ . The reference line should be the same as the injected line, and used to obtain the equivalent ideal Norton current source generated by the PCI system., instead of the actual current measured on injected lines connected EUT.

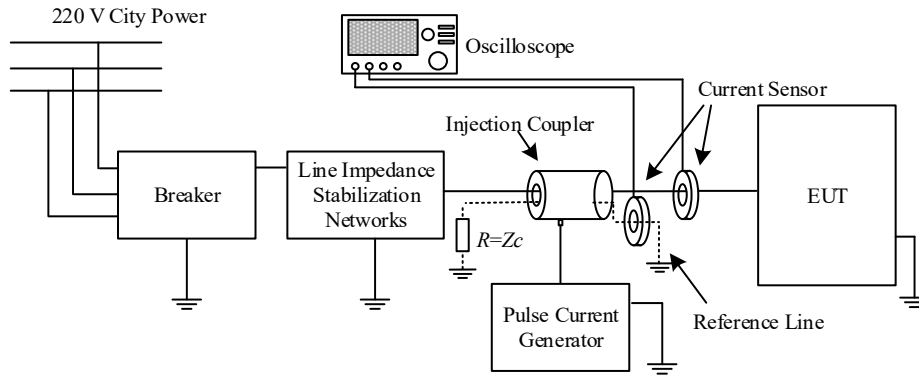


Figure 5-10 Diagram of the PCI experimental setup

The key parameters of the induced current vary in a range, including amplitude, rise time, pulse width, and energy. The equivalent experiment platform should satisfy the conditions  $I'_{eq}=I_{eq}$ , which means the equivalent Norton source should have a related adjustment range. This puts forward additional requirements for the PCI platform, especially for the pulse generator. However, the waveform parameters of PCI can be poorly adjustable limited by the state-of-the-art PCI technology. Therefore, instead of completely reproducing various waveforms for the coupling responses caused by uncertainty, the PCI test can be carried out by studying one of these norms (amplitude, rise time, pulse width, or energy of the induced current). The key parameters are chosen based on the physical analysis failure mechanism of EUT.

The author acknowledged that the failure mechanism may a combination of multiple factors. The design of adjustable PCI is beyond the scope of this dissertation, the method can be extended after further development of the PCI injection technology with accurate waveform control.

### 5.2.2 Nonparametric estimation method based on order statistics

The strength of the equipment is represented by the failure threshold and obtained by the effect test. The threshold is considered with probability distribution instead of a fixed value. The failure mechanism of equipment excited by TED is complex and is usually used as a black-box model. Without analytic expression of the failure mechanism, there is little knowledge of the probability distribution of strength. The distribution maybe not even classical distribution as well. Meanwhile, the effect experiment is expensive and the amount of data may be small, which may be not sufficient to interfere with the actual distribution of the threshold, and the estimation from insufficient data may introduce extra aleatory uncertainty. It is reasonable to provide not only the probability distribution of the threshold but also the tolerance bound with confidence information for the equipment strength, with the consideration of the uncertainty.

Assuming the EUT is sensitive to the amplitude of the injection current into the port, the threshold  $\chi$  is quantified by the injection current amplitude and is from an unknown probability distribution  $F_{\chi}$ .  $F_{\chi}(x_k)$  refers to the probability that the threshold  $\chi$  is less than  $x_k$ , and is equivalent to the probability that failure may occur when the induced current amplitude  $X$  (or equivalent induced current generated by PCI) is large than  $x_k$ :

$$F_{\chi}(x_k) = P(\chi < x_k) = P(y = 1 | X \geq x_k) = F_X^{(C)} \quad (5-21)$$

where  $P(X)$  means the probability of event  $X$ . The estimation of  $F_{\chi}$  is converted to the estimation of cumulated probability  $F_X^{(C)}$ .

To obtain  $F_X^{(C)}$ , the rising-current test strategy is recommended for the test arrangement. The test should start from a current pulse injection with low amplitude (or some other variables), the amplitude increases pulse by pulse continually until the equipment failure occurs. Then the test continues from the current pulse injection with low amplitude and the amplitude increases repeatedly. The amplitude of injection currents is recorded when the failure occurs, and the recorded current amplitudes are used to estimate the probability of threshold. After each test, it is necessary to check the function of the equipment. If there is unrecoverable damage, the damaged device or equipment should be replaced.

A group of test data is shown to illustrate the test procedure in Figure 5-11. The arrow indicates the procedure of the test. Pulse current inject carried out with current amplitude increase, empty circles represent test without effect, filled circles represent test with effect. Once the failure happened, the current amplitude is recorded as the possible threshold for the equipment, and the injection pulse amplitude decreased for the next test.

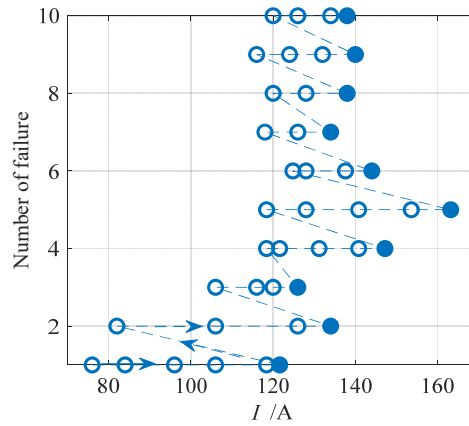


Figure 5-11 Example of test data obtained by experiment with rising-current test strategy (The filled circles represent tests with failure. The hollow circles represent tests without failure.)

Thanks to the experimental procedure, the probability of data with failure can be regarded as equal, according to the definition of the strength in (5-21), there is

$$\begin{aligned} F_X^{(C)}(x_k) &= P(y = 1 | X > x_k) \\ &= \frac{P(X > x_k | y = 1)P(y = 1)}{P(X > x_k | y = 1)P(y = 1) + P(X > x_k | y = 0)P(y = 0)} \\ &= P(X > x_k | y = 1) \end{aligned} \quad (5-22)$$

$F_X^{(C)}$  and its tolerance bound can be estimated by the probability distribution of effect data. When there is plenty of knowledge about the distribution of the threshold, the parametric estimation methods for the distribution and tolerance bound can refer to Reference [218]. However, the failure mechanism is complex and black-box, especially for the secondary equipment, which is difficult to provide an analytical expression. When the data sample is of

small size, data from any distribution can easily pass the hypothesis test of a probability distribution, such as the Kolmogorov-Smirnov test for normality test or the Weibull distribution test. It is hard to determine the kind of distribution of the data. Meanwhile, the estimation of the tolerance interval by the parametric method is sensitive to the preset distribution type<sup>[219]</sup>. It is difficult to estimate with poor knowledge of the distribution.

The nonparametric estimation (NPE) based on order statistics is a data-driven method and is not constrained by the type of preset distribution. It can provide robust estimations of quantiles and tolerance bound for the QMU assessment.

For the collection of data from the experiment, which is supposed be to from distribution  $F_X^{(C)}$ , the samples are collected as order statistics  $\mathbf{x}=\{x_1, \dots, x_k, \dots, x_n, x_k < x_{k+1}\}$ . The quantiles and tolerance bounds used in QMU assessment are estimated by the NPE based on order statistics.

Assume the one-sided statistical tolerance bound for the lower quantile of  $x$  is:

$$Q_{1-p,\gamma} = x_k \quad (5-23)$$

which is required to satisfy the condition:

$$P(P(X > Q_{1-p,\gamma}) \geq p) \geq \gamma \quad (5-24)$$

Substituting the cumulative probability density function of the variables into inequity (5-24) will result in the following transformation:

$$P(F_X(x_k) \leq 1-p) \geq \gamma \quad (5-25)$$

Since  $x$  is the sample from a continuous distribution  $F_X$ , therefore  $F_X(x)$  is the sample from a uniform distribution between 0 and 1. The probability in (5-25) can be solved as:

$$P(F_X(x_k) \leq 1-p) = P(k \leq Y | n, 1-p) \quad (5-26)$$

where,  $Y \sim \text{Bin}(n, 1-p)$ . Therefore,  $x_k$  is the desired one-sided tolerance for the lower quantile  $Q_{1-p}$ , also called the one-sided lower tolerance bound, where  $k$  is the biggest integer with the following inequality:

$$\sum_{i=0}^k \binom{n}{i} (1-p)^i (p)^{n-i} \leq 1-\gamma \quad (5-27)$$

Similarly, for the upper quantile  $Q_p$  of  $x$ , the one-sided statistical tolerance bound can be obtained as:

$$Q_{p,\gamma} = x_{n-k+1} \quad (5-28)$$

Both side tolerance bounds construct the tolerance interval for the distribution. In addition, the estimated empirical cumulative distribution is made up of the quantiles and is the same as the one-side 50% tolerance bound.

When the data set is small, the statistical tolerance bound characterized by order statistics tends to be conservative. An interpolation strategy is explored by Reference [220] to reduce conservatism. For a given confidence level  $\gamma$ ,  $x_k$  is obtained by Equation (5-26), there is:



$$P(F_X(x_{k+1}) \leq 1-p) = P(k+1 \leq Y | n, 1-p) < \gamma \quad (5-29)$$

The one-sided lower tolerance bound for the lower quantile is calculated by linear interpolation between  $x_k$  and  $x_{k+1}$ :

$$Q'_{p,\gamma} = \lambda x_k + (1-\lambda)x_{k+1}^{\text{BH}} \quad (5-30)$$

where

$$\lambda = \frac{\gamma - P(k+1 \leq Y | n, 1-p)}{P(k+1 = Y | n, 1-p)} \quad (5-31)$$

The error is proven as  $O(n^{-1})$ , which is related to the size of the data and cannot be reduced further by higher-order interpolation<sup>[218]</sup>.

Take the experimental data in Figure 5-11 as an example, the estimated  $F_X^{(C)}$  and tolerance bound estimated by the NPE is shown in Figure 5-12.

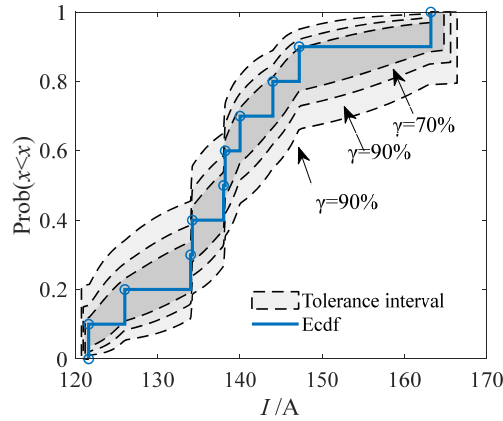


Figure 5-12 Probability distribution and the tolerance intervals made up by one-sided tolerance bound of obtained by the NPE method

To compare the proposed NPE method with the parametric method. Figure 5-13 shows the comparison of the 90% tolerance bounds estimations by NPE and parametric method. The sample data with different sizes are from a lognormal distribution and a Weibull distribution, respectively.

Both of the two distributions are skew distributions with fixed lower boundary, and cannot be distinguished in the test of distribution from few data. For the samples from the log-normal distribution, the parametric method with preset log-normal distribution has a similar performance to the NPE. For the samples from a Weibull distribution, the tolerance bounds estimated by the NPE can always contain the correct quantiles with less redundancy than the parametric method with the unmatched preset distribution. When the data size increases, the tolerance bounds tend to approach the real estimation quantile. When the data size is small, the tolerance interval is conservative, but can still cover the real quantile.

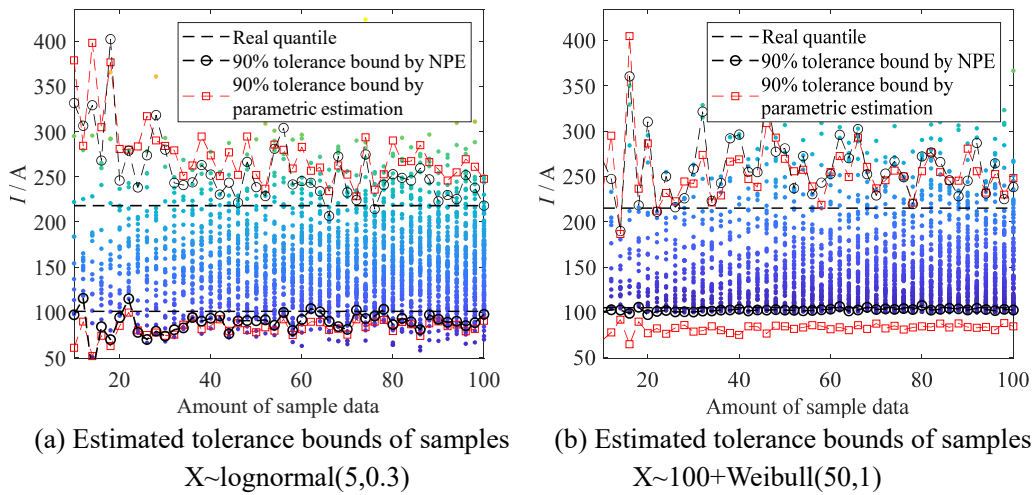


Figure 5-13 Comparison of both side tolerance bound of 90% confidence level obtained by NPE method and parametric estimation with a preset log-normal distribution

### 5.2.3 Nonparametric regression method based on MaxEnt-Bagging

The amount of data is very small. In order to make full use of information from the effect experiment, the data point without failure can be taken into consideration. The probability of the threshold can be regressed from binary state data. Logistic regression and Bayesian regression based on maximum likelihood are the most commonly used methods for binary state data regression, which are both parametric methods. The given confidence interval is the estimation of the parameters, and what we need is the interval of distribution. The disadvantages of these methods are consistent with the abovementioned parametric estimation method based on non-classified data. In addition, the parametric regression could only provide confident intervals for the parameter instead of the tolerance interval for the distribution that we are concerned about. There is no state-of-the-art for tolerance interval estimation for binary state data yet.

This section proposes a nonparametric regression (NPR) method for small sample binary state data based on the maximum entropy method (MaxEnt), and the tolerance intervals for the distribution are estimated based on the bootstrap aggregation (Bagging) method.

The MaxEnt theory is a completely data-driven method, which makes no assumptions about the probability distribution except for the existing data<sup>[221]-[223]</sup>. The model with the largest entropy is the most possible model. For event(s)  $X$  with the probability  $P$ , the entropy is defined as:

$$H(P) = - \sum_X \text{Pr}(X) \log(\text{Pr}(X)) \quad (5-32)$$

The probability for deterministic events is  $p=1$ , therefore the entropy has zero entropy. The probability for uncertainty events with uniform distribution, the entropy is maximum. Therefore, when estimating an unknown model, the know data contribute zero to the entropy, the larger the entropy is, the fewer subjective assumptions are introduced, and the more possible the estimated model is. The regression problem from binary state data can be transformed into an optimization problem of the estimated model with maximal entropy.

The distribution of the equipment strength can be written as a part of a conditional probability distribution  $P(Y|X)$  to be estimated:

$$F_X^{(C)} \approx P(y=1|X) \quad (5-33)$$

For the collection of binary state data from the experiment,  $T = \{(x_1, y_1), \dots, (x_k, y_k), \dots, (x_N, y_N)\}$ , there is empirical joint probability density distribution  $\tilde{P}(x, y)$  and empirical marginal probability density distribution  $\tilde{P}(x)$ . Characteristic function  $f$  describes the relationship between the binary state data. According to the physical meaning of the experimental data, when the data is represented as the amplitude or energy of the amplitude,  $(x_k, 1)$  means that when  $x = x_k$ , the failure occurs, therefore when  $x > x_k$ , the failure may likely occur as well. Conversely,  $(x_k, 0)$  means that when  $x = x_k$ , the equipment works normally. Therefore, when  $x < x_k$ , the failure may likely not occur as well. The characteristic function can be written as:

$$f(x_k, y_k) = \begin{cases} 1 & y=1, x > x_k \text{ or } y=0, x < x_k \\ 0 & \text{otherwise} \end{cases} \quad (5-34)$$

The expectation of the characteristic function can be calculated based on known data and estimated distribution, respectively:

$$E_{\tilde{p}}(f) = \sum_{x,y} \tilde{P}(x, y) f \quad (5-35)$$

$$E_p(f) = \sum_{x,y} \tilde{P}(x) P(y|x) f \quad (5-36)$$

The information entropy of the estimated  $\tilde{p}$  can be written as a maximum optimization problem with constrain:

$$\begin{aligned} \max H(P) &= - \sum_{x,y} P(x) P(y|x) \log(P(y|x)) \\ \text{s.t. } E_{\tilde{p}}(f) &= E_p(f), \quad \sum_y P(y|x_k) = 1 \end{aligned} \quad (5-37)$$

The constrained optimization problem can be solved by an unconstrained optimization problem. The Lagrange function is constructed as:

$$\begin{aligned} L \equiv & \sum_{x,y} \tilde{P}(x) P(y|x) \log(P(y|x)) + \sum_x \omega_0 \left( 1 - \sum_y P(y|x) \right) \\ & + \sum_T \omega_k \left( \sum_{x,y} \tilde{P}(x, y) f(x_k, y_k) - \sum_{x,y} \tilde{P}(x) P(y|x) f(x_k, y_k) \right) \end{aligned} \quad (5-38)$$

$L$  is a convex function about  $P$ , and its minimum value can be obtained by partial derivation of  $P$ :

$$\frac{\partial L}{\partial P(y|x)} = \tilde{P}(x) \left( (\log(P(y|x)) + 1) - \omega_0 / \tilde{P}(x) - \sum_T \omega_k f(x_k, y_k) \right) \quad (5-39)$$

where  $\tilde{P}(x)$  is obtained from the test data collection and does not change with the model.

$\tilde{P}(x) > 0$ . When the partial derivative is zero, the optimal solution for  $P$  is:

$$P(y|x) = \frac{\exp\left(\sum_T \omega_k f(x_k, y_k)\right)}{\sum_Y \exp\left(\sum_T \omega_k f(x_k, y_k)\right)} \quad (5-40)$$

The optimal solution for  $P(Y|X)$  depends only on weights  $\omega$ . The problem is transformed into an optimization problem about weights  $\omega$  and solved by the improved iterative scaling method (IIS). The weight is updated by iteration to maximize the information entropy of  $P(y|x)$ :

$$\begin{aligned} \omega^{(i+1)} &= \omega^{(i)} + \delta^{(i)} \\ \delta^{(i)} &= \underset{\delta}{\operatorname{argmin}} \frac{\partial L(P(y|x), \omega^{(i)})}{\partial \delta} \end{aligned} \quad (5-41)$$

Laplace equation about  $\delta$  can be written in the same form of (5-38), the best estimation of  $\delta_k$  is calculated:

$$\begin{aligned} \sum_{X,Y} \tilde{P}(x) P(y|x) f(x_k, y_k) \exp\left((\omega_k^i + \delta_k^i) - \omega_k\right)^N &= E_{\tilde{P}}(f) \\ \delta_k &= \frac{1}{N} \log \frac{E_{\tilde{P}}(f(x_k, y_k))}{E_P(f(x_k, y_k))}, \quad k = 1, 2, \dots, N \end{aligned} \quad (5-42)$$

To compare the MaxEnt method with the parametric method. Figure 5-14 shows the comparison of the MaxEnt method and classical Logistic regression by using binary state data and the NPE based on order statistics by using only the data with effect. Because the data obtained from the effect test are censored. This means only collect partial information about values is obtained. The threshold is no large than the recorded amplitude in the test with effect, but the actual values cannot be obtained. The estimation based on the censored data is always biased. The threshold will be overestimated by using only the data with effect, especially when there are few data. By contrast, the regression from binary state data reduces the impact of censored data on the estimation of the threshold. Logistic regression can provide a smooth result.

**Algorithm 1** The pseudocode of calculation of weights by IIS based on improved iterative scaling method

**Input:** Binary state data collection  $T = \{(x_1, y_1), \dots, (x_k, y_k), \dots, (x_n, y_n)\}$ , tolerance error  $\varepsilon$ , initial  $\omega = 0.5$ .

Calculated the expectation of  $E_{\bar{p}}(f)$  by using the data sample

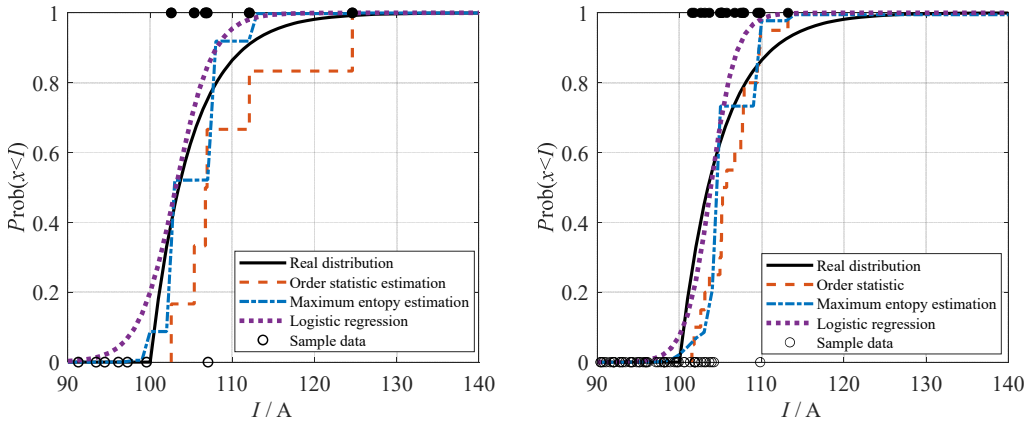
```

while  $\sum \delta_k > \varepsilon$  do
  for  $k = 1, \dots, N$  do
    Update the  $\omega_k^{(i+1)} = \omega_k^{(i)} + \delta_k^{(i)}$  via solving
    Update the  $E_p(f)$  with  $\omega = (\dots, \omega_{k-1}^{(i+1)}, \omega_k^{(i+1)}, \omega_{k+1}^{(i+1)})$  by solving
   $i = i + 1$ 

```

**Output:** Optimal weights  $\{\omega_k\}_{k=1}^N$

The MaxEnt method is totally dependent on the data, so the estimated distribution may not be smooth but can better estimate the distribution without constriction by the pre-set distribution. For the example in Figure 5-14, the real distribution is a Weibull distribution with a fixed lower boundary. The MaxEnt has a better estimation around the lower bound than Logistic regression. When the distribution becomes more complex, it is reasonable to believe that the MaxEnt method can provide a more flexible prediction without the limitation of the pre-set distribution type.



(a) Regressed probability distribution when the size of the data is 15 (b) Regressed probability distribution when the size of the data is 50

Figure 5-14 Comparison of probability distribution regressed from binary state data by using the proposed MaxEnt method, logistic regression, and from effect data only by using the NPE.

However, it can be seen from the limited examples, that even though MaxEnt is better than the parametric regression method, it is difficult to provide a perfect estimation of the actual distribution, because of the aleatory uncertainties caused by the sampling variability and estimation errors from a small sample. The tolerance interval of the probability distribution is necessary.

The tolerance bounds of the distribution regressed from binary state data are defined as

$$P(P(y=1 | x = Q_{1-p,\gamma}) < 1-p) \geq \gamma \quad (5-43)$$

where  $Q_{1-p,\gamma}$  are estimated by using Bagging combined with the MaxEnt. Bagging is a commonly used nonparametric MC method for small sample estimation<sup>[224]</sup>. Bootstrap refers to resampling with replacement from the original sample:  $T = \{(x_1, y_1), \dots, (x_k, y_k), \dots, (x_N, y_N)\}$ . The new collection of random-pair bootstrap samples is generated from the original data set  $\{(x_i, y_i), i \in 1, \dots, N\}$ .  $\hat{P}(Y|X)$  is regressed by MaxEnt method for every new sample. Aggregation refers to the statistical inference from the collection of Bootstrap. The lower  $\gamma$  quantile for the collection  $\{x_j | \hat{P}(y = 1 | x_j = X) = 1 - p\}$  is the lower  $\gamma$  tolerance bound for the threshold probability.

Take the experimental data in Figure 5-11 as an example, the estimated  $F_X^{(C)}$  and the tolerance bound estimated by the proposed MaxEnt-Bagging is shown in Figure 5-15.

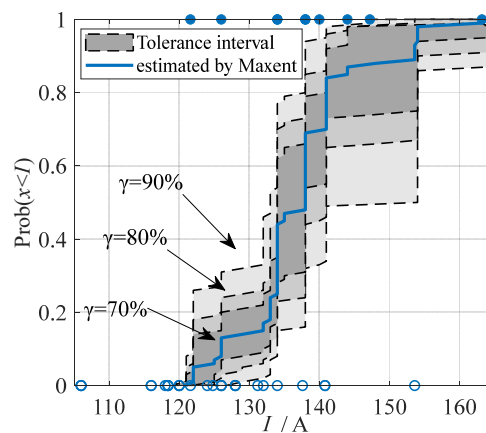
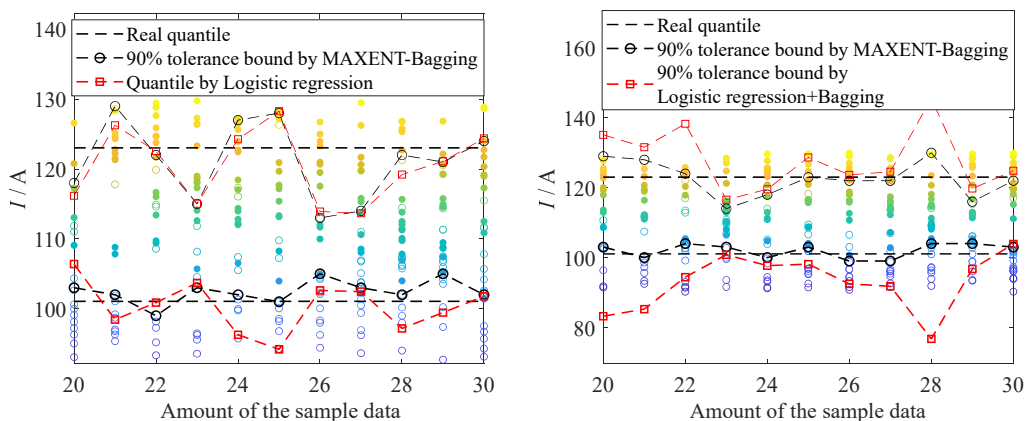


Figure 5-15 Probability distribution and tolerance intervals regressed from binary state data by using the proposed MaxEnt-Bagging NPR method (The data is from Figure 5-12.)

To compare the proposed MaxEnt-Bagging method with the parametric regression method and the parametric regression method combined with Bagging, Figure 5-16 shows the comparison of both side 90% tolerance bounds.



(a) Comparison between MaxEnt-Bagging method and Logistic regression (b) Comparison between MaxEnt-Bagging method and Logistic-Bagging method

Figure 5-16 Comparison of both side tolerance bound of 90% confidence level with data from non-Gaussian distribution  $X \sim 100 + \text{Weibull}(10,1)$

Due to the small size of the data, error is unavoidable. Proposed MaxEnt-Bagging can

provide good results for tolerance bounds of lower quantiles. Fortunately, the lower quantile of equipment strength is what we are concerned about in the vulnerability assessment based on QMU.

### 5.2.4 Validation of the distribution-free QMU method

With the equipment stress simulated by the stochastic model, and the equipment strength estimated by the NPE or NPR method, the quantile-based QMU metric can be calculated. To validate the distribution-free QMU method, a simulation validation was designed with the stress and strength following known probability distributions.

When the distributions of equipment stress and strength have no overlapping part, the minimum of the possible threshold is larger than the maximum of the possible threat, the equipment is certainly not vulnerable under the TED. So we are mainly concerned about the situation that part of the threshold is less than the possible threat. Two cases were designed to validate the proposed method. The distribution of the stress  $F_X^{(D)}$  was assumed as Weibull in both cases. The probability distribution of the equipment threshold  $F_X^{(C)}$  was assumed as normal in case 1 and the non-Gaussian distribution in case 2. The CDF and PDF are shown in Figure 5-17. The true failure probability R of two cases can be calculated analytically by Equation (5-10), equal to 0.03% and 0.7%, respectively.

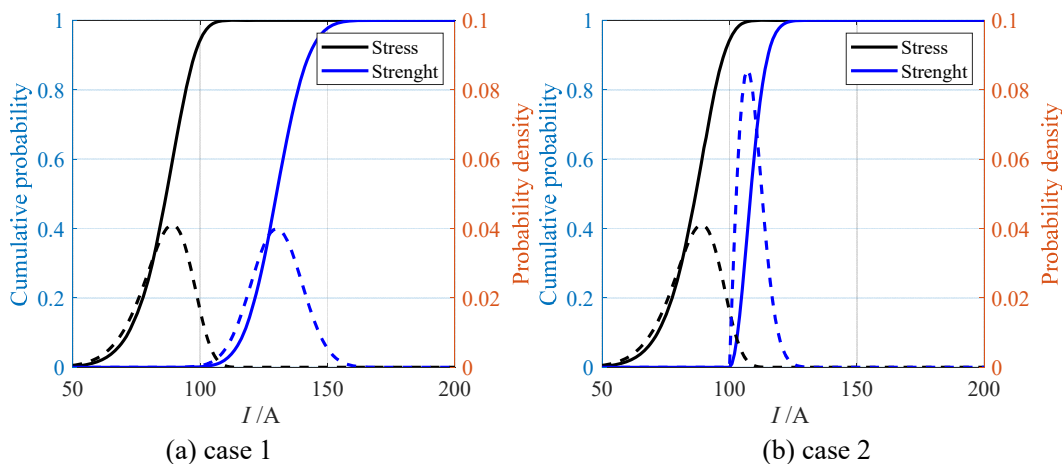


Figure 5-17 CDF and PDF of the assumed equipment stress and strength in two cases

The equipment stress was calculated by a collection of 2000 samples from  $F_X^{(D)}$ . Binary state random samples with different sizes represent the effect test data generated from the  $F_X^{(C)}$ , and the equipment strength was regressed by the NPR method. When evaluating whether the equipment is reliable with a failure probability of less than 1%, the CF with  $p=0.1$ ,  $\gamma=90\%$  was calculated by using Equation (5-5) and as shown in Figure 5-18.

The theoretical value of CF should be larger than 1 which means the equipment is reliable according to the requirement with 90% confidence. The absolute value of CF has no practical meaning.

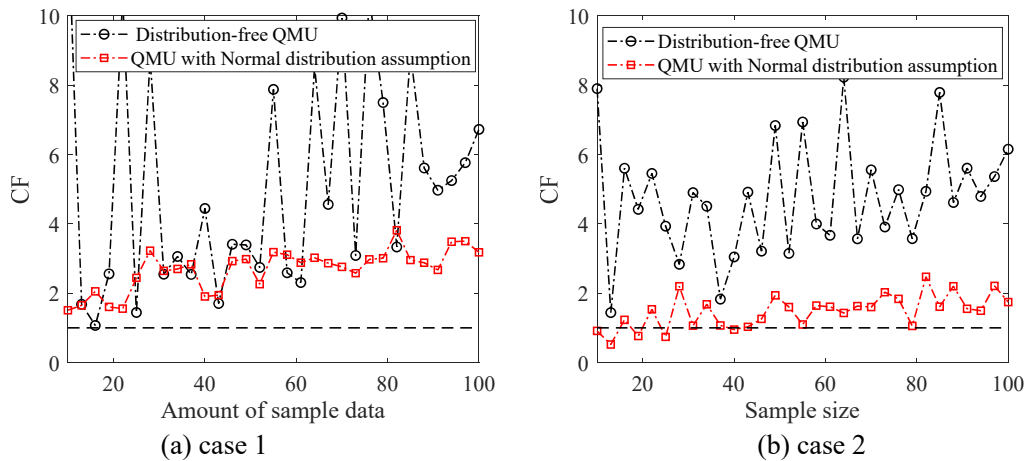


Figure 5-18 The QMU metric CF obtained by data samples with different sizes in two case

When the strength is from a normal distribution, both of the two QMU methods could provide reasonable evaluation results. When the distribution is non-Gaussian, the QMU method based on the assumption of normality can only provide reasonable results only when the data sample is large. When the amount of sample data is small, it may overestimate the vulnerability of the equipment. In contrast, the proposed distribution-free QMU based on NPR is able to provide reasonable predictions with different sizes of samples.

### 5.3 Evaluation of equipment vulnerability based on the distribution-free QMU method

The equipment under test is an instrumentation and control (I&C) unit, which is a significant equipment providing monitoring, control, and operation for the electronic system in the power plant. The I&C unit was settled in a metal cabinet and was powered by an outside power. Therefore, we assumed that the power cable was the only conducted coupling path of the I&C unit.

The vulnerability assessment based on the distribution-free QMU method was carried out in four steps.

Firstly, the common-mode induced current on the cable was selected as the observed key performance parameters of the I&C unit. Because the mechanism of field-to-wire coupling mainly acts on the common-mode response<sup>[225]</sup>. The prediction for common-mode induced current is independent of termination unbalance and can be directly used as the parameters of the PCI test. Second, the uncertainty quantification of the equipment stress under HEMP was carried out by simulation. The cable was simulated as one elevated transmission line with a height of 0.3 m and a length of 10 m. The uncertainty of HEMP parameters was similar to the above analysis in Chapter 4, the geomagnetic inclination is chosen as 30°. Third, the effect data were collected by common-mode PCI experiments and the uncertainty quantification of the equipment strength was obtained. The test platform is shown in Figure 5-10. The equivalent pulse current was injected into the power cable by the injection probe, while the I&C unit was powered by city power through the line impedance stabilization networks. A



reference line was settled in the injection probe as well. The current on the reference line was regarded as the equivalent current source for the PCI approximately. Finally, the QMU metric determined by the margins and the uncertainties was calculated.

The probability distribution of the induced current amplitude is shown in Table 5-2. The result presented the uncertainty quantification of the stress of the I&C unit under HEMP. It also provided a reference range for the determination of PCI waveform parameters. The probability distribution of stress is shown as the black line in Figure 5-19 (a).

The strength of the I&C unit was obtained based on the PCI effect experiments. The experiments were carried out as the procedure introduced in Section 5.2.2. During the test, failure of the I&C unit appeared as the operation screen went blank and shut down. With the recorded failure data, the distribution and uncertainties of the equipment threshold were quantified by the NPE method and shown as the blue lines in Figure 5-19 (a).

With the uncertainty quantification results of the stress and the strength of the I&C unit, the tolerance bound of the stress was ignored, and the metric CF could be calculated as

$$CF = \frac{M}{U} = \frac{Q_{1-p}^{(C)} - Q_p^{(D)}}{Q_{1-p}^{(C)} - Q_{1-p,\gamma}^{(C)}} \quad (5-44)$$

Figure 5-19 (b) presents the variation in CF versus  $p$  under different confidence levels. The results are interpreted in several ways. A qualitative conclusion is inferred from the intersections of the CF curve and the reference line of constant 1, that there is a possibility of equipment failure under HEMP disturbance.

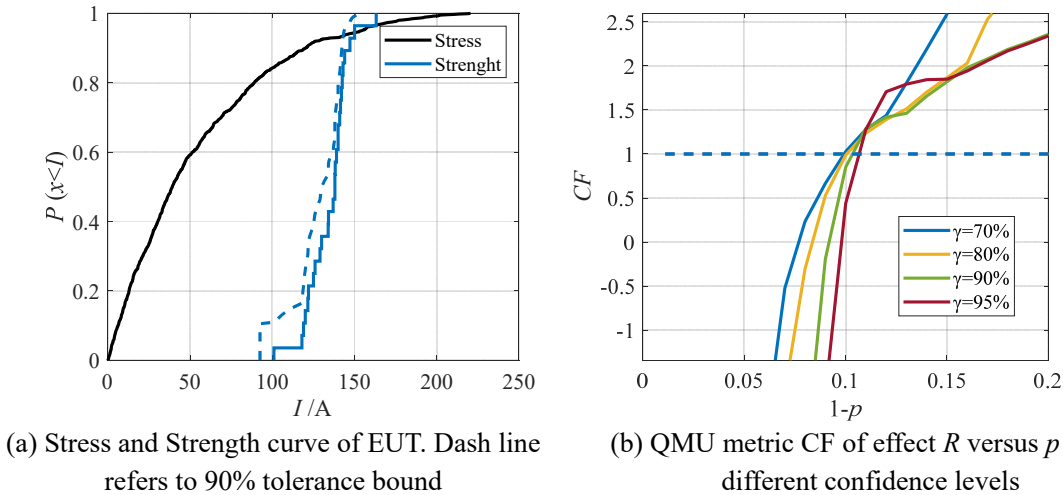


Figure 5-19 Numerical results of QMU evaluation.

When there is a requirement that the failure probability should be less than 1%. The QMU metric CF with  $p=0.9$  can be provided in Table 5-1. Table 5-1 shows that CF is greater than 1 with a confidence level of 70%. This means we have only 70% confidence in saying that the EUT is not vulnerable under HEMP. CF decreases below 1 as the confidence level increase, the equipment may be vulnerable according to the requirement. In order to achieve an evaluation with a higher confidence level, the conclusion is more conservative.

Table 5-1 Value of CF with different confidence levels ( $p=0.9$ )

| Confidence level $\gamma$ | 70%  | 80%  | 90%  | 95%  |
|---------------------------|------|------|------|------|
| CF                        | 1.02 | 0.98 | 0.85 | 0.43 |

The failure probability was calculated by Equation (5-44). The failure probability of the I&C unit is less than 6.5% with 95% confidence.

1) Influence of the conducted coupling path parameters

The evaluation was adapted to study the influence of parameters in the conducted coupling path. By using the proposed assessment approach, the change in the equipment vulnerability with the variation of conducted coupling path parameters can be quantified using existing experimental data instead of further effect tests, as long as the variation does not change the strength of EUT.

In this case, the influence of the orientation and length of the conducted coupling path was studied for the I&C unit equipment.

The orientation of the power cable was regarded as a known variable instead of a random variable. The orientation of the conducted coupling path mainly influences the azimuth angle of the incident HEMP and results in different coupling responses. Table 5-2 presents the induced current amplitudes of three quantiles for a 10 m elevated line, which was assumed to be placed randomly, along the geomagnetic West-East (W-E) orientation, and along the geomagnetic North-South (N-S) orientation.

Table 5-2 Lower quantile for the induced current peak in ampere versus line orientation ( $l=10$  m,  $h=0.3$ m)

| Lower quantile | Induced current peak / A |                 |                    |     |
|----------------|--------------------------|-----------------|--------------------|-----|
|                | W-E orientation          | N-S orientation | Random orientation | IEC |
| 50%            | 39                       | 28              | 34                 | 25  |
| 90%            | 117                      | 91              | 100                | 75  |
| 99%            | 206                      | 175             | 193                | 100 |

Note: Data in red are from recommended values for elevated conductors above 5 m in IEC 61000-2-10 Table 1a, Page 14<sup>[188]</sup>.

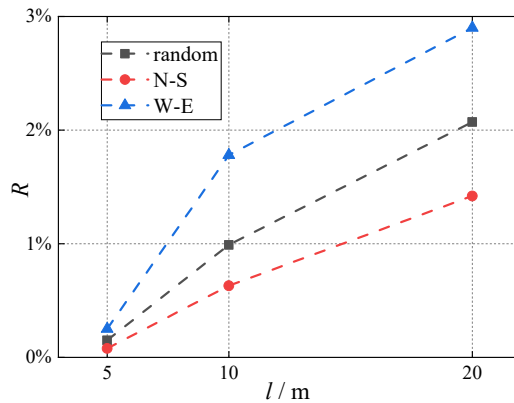


Figure 5-20 Influence of the orientation and length of the conducted coupling path on the failure probability of the EUT with 90% confidence

These quantiles in Table 5-2 were used as  $Q_p^{(D)}$  in Equation (5-44). With  $Q_p^{(D)}$  increases, CF decreases. When CF decreases below 1, the equipment is vulnerable. In addition, quantitative results can also be given as the failure probability calculated by Equation (5-10), the results are shown in Figure 5-20.

When the conductor is placed along the W-E orientation, its conducted environment was more severe. The I&C unit under HEMP is more vulnerable when the line is along the W-E.

When the conducted coupling path was less than the efficient coupling length, the severity of the conducted environment increased as the length of the conducted coupling path increased. The influence of conductor length on equipment vulnerability assessment results is shown by the variation of probability in Figure 5-20 as well.

## 5.4 Concluding remarks

(1) Distributed parameter model of the PCI platform and injected line is established, and the parameters of the model are extracted from the measured results to overcome the lack of detailed information on the internal parameters of the generator, coupler, and input impedance of the EUT. It is found that the equivalent injected voltage source into the lines is almost independent of the injected line's length and loads. A Norton equivalent source is derived and validated, which can be equivalent to the field-to-line coupling conditionally by adjusting the pulse generator and the auxiliary loads connected with the line. The equivalent injection current is used to characterize the device effect threshold instead of the actual measured current on the lines in the pulse current injection test.

(2) Small samples from the effect test provide poor knowledge and may introduce great aleatory uncertainties to the equipment strength, in order to overcome the influence of sampling variability and estimation errors, NPE based on order statistics is proposed for estimation of the quantile of the distribution and their tolerance bounds. However, due to the censored characteristic of the effect data, when the data is very few, the biased estimation will overestimate the threshold of the equipment. The problem can be overcome if the binary state data is retained and used for the estimation. The MaxEnt-Bagging method can give a reasonable regression of the probability distribution and the confident boundary, especially for the lower quantiles and tolerance bounds, which is what we are concerned about for the equipment strength.

(3) The vulnerability assessment method based on distribution-free QMU can comprehensively consider the uncertainty of stress and strength. By using the QMU metric based on quantile and tolerance bounds, it can provide both quantitative and qualitative conclusions about equipment vulnerability with confidence levels. Compared with the evaluation which uses the "bounding case" stress and the traditional stress-strength method, it avoids the overestimation of the stress and the underestimation of the equipment strength, and can provide more reasonable results for the vulnerability evaluation of the equipment in the power system.

## 6 Conclusions and perspectives

### 6.1 Conclusions

For the purpose of quantification of the potential coupling responses on the TLs excited by TED, taking the HEMP as an example of TED, this dissertation proposed deterministic models of the HEMP and field-to-line coupling, respectively. Two construction method of the stochastic model is proposed for the problem with and without analytic expressions, respectively. A hierarchical uncertainty quantification framework is proposed as well to combine these stochastic models. The statistical results of the coupling responses can be used to guide risk prediction, vulnerability tests, and protection of the power system under HEMP. The uncertainty quantification method has the potential to be extended to the uncertainty quantification of coupling responses on the TL excited by other kinds of TED. The main research achievements are as follows:

(1) To overcome the difficulty in constructing the non-invasive surrogate model for uncertain quantification, a physical-based stochastic surrogate model is proposed based on a simplified Compton electron model. It can describe the spatial distribution characteristics and stochastic characteristics of the HEMP incident to the ground surface. The physical-based stochastic surrogate model has better results than the stochastic model based on the conventional non-intrusive surrogate model with similar time-consuming. The time-consuming is reduced to several hours from several days of the conventional MC method.

According to the uncertainty quantification of the HEMP, there is an upper limit for the electric field amplitude caused by the self-consistent effect and saturation effect; the increase in the amplitude is often accompanied by a decrease in the pulse width; the horizontal polarization is the dominant component when the electric field is large. The uncertainty quantification of key parameters of HEMP such as amplitude, rise time, and polarization angle is carried out and will be used in subsequent uncertainty quantification of field-to-line coupling.

(2) To simulate the coupling responses of TLs with nonlinear loads when the coupling response may vary in a large range, an equation-based dynamic nonlinear model for the MOA was proposed based on analog behavior modeling. Once the model is established for a certain MOA, it is capable to predict the responses of the MOA under different surges with front time ranging from 20 ns to 30  $\mu$ s. Two different types of MOA used in the power distribution systems were tested for validation. The proposed model was validated from measured results, the error of simulated peak voltage and absorbed energy is less than 6%.

(3) When the parameters of the incident fields and lines are assumed as mutually independent variables, a stochastic model is constructed by expanding the telegraph equations through the PCE, and solved by the macromodel of the augmented TLs.

When the uncertainty quantification results of the HEMP are used as the inputs, the variables are no longer mutually independent, and the marginal and joint distributions of the variables are unknown and may be complex. To solve the problem of transferring arbitrary

distribution correlated multidimensional variables in the hierarchical stochastic models, this dissertation proposes a PCE based on kernel density estimation (KDE), which can accurately estimate the joint probability distribution and construct orthogonal polynomial basic functions for the arbitrary distribution correlated variables. The hierarchical stochastic models have the advantage of high efficiency and fast convergence speed, which is suitable for the uncertainty quantification of the problem that can be divided into several independent physical processes.

By using the proposed hierarchical stochastic method, uncertainty quantification is performed for the HEMP electric field. The upper  $3\sigma$  interval is regarded as the bounding case of the HEMP waveform with 60 kV/m amplitude, 3 ns rise time, and 21 ns FWHM, which has comparable results with the IEC standard waveform and other references. It should be noted that the results are affected by many uncertainty variables and their value ranges, the absolute values of the results are only of reference significance. Uncertainty quantification is performed for the TLs coupling responses as well. Compared with the IEC standard 61000-2-10 and related studies, the consideration of the spatial distribution and uncertainty of the electric field amplitude leads to a significant reduction in the severity of induced current.

(4) Distributed parameter model of the PCI platform and injected line is established, the parameters of the model are extracted from the measured results to overcome the lack of detailed information about the internal parameters of the generator and coupler. When the input impedance of the equipment under test is unknown, an equivalent Norton source model is established based on the distributed parameter model for the PCI platform. The equivalent injection current is used to characterize the device effect threshold instead of the actual measured current on the lines in the pulse current injection test.

In order to evaluate the equipment connected with the TLs with the consideration of response uncertainties, the distribution-free method is proposed in the framework of the QMU method. By using the QMU metric based on quantile and tolerance bounds, the vulnerability assessment can be provided with confidence levels. Compared with the evaluation that uses “bounding case” stress and the traditional stress-strength method, it avoids the overestimation of the stress and the underestimation of the equipment strength, and can provide more reasonable results for the vulnerability evaluation of equipment based on the power system.

## 6.2 Future work

In this dissertation, the research results of the uncertainty quantification method for TLs excited by TED have been obtained. However, due to the limited time, there are still some problems to be solved. Further research can be carried out from the following aspects

(1) This dissertation developed the stochastic models for TLs excited by TED based on the classical TL model. For TED with higher frequency spectra, such as IEMI and HPM, it is necessary to study the high-frequency TLs method for deterministic simulation and to develop the corresponding stochastic model

(2) The stochastic models developed in this dissertation could provide the statistical results for amplitude, rise time, and pulse width of the induced current. However, limited by the effect test platform, this work only investigated the vulnerability evaluation with only one

key parameter. In fact, the failure mechanism may be a combination of multiple factors. For one thing, the development of an adjustable PCI platform is required, especially the adjustable pulse generator with adjustable amplitude, rise time, and pulse width. For another, future work is needed to develop the vulnerability evaluation method with the consideration of multiple parameters, in particular, the multivariate estimation method for the probability and the tolerance bounds.

## Acknowledgments

This is the conclusion of an adventure full of challenges and gains. To all who have helped and supported me to go through all the difficulties and complete this dissertation, I am deeply grateful.

Firstly, I would like to express my most sincere gratitude to my supervisors for their knowledge, support, and kindness. I would like to thank my Xi'an Jiaotong University supervisor, Prof. Yan-zhao Xie, for offering me this great opportunity to join the HPEMC Group and undertake the co-tutelle PhD project. His attentive guidance, broad knowledge, strict requirement, optimism and kind encouragement have always helped me in all the time from selecting the topic to writing this dissertation. I would like to thank my Politecnico di Torino supervisor, Prof. Flavio Canavero, for accepting me as his student and continuing to teach me even when I was unable to return to Torino due to the pandemic. His patient guidance and professional suggestions have helped me in an immeasurable way.

I also would like to give my great thanks to Dr. Yinhui Cheng, Professor Jun Guo, Dr. Shaoyin He, Dr. Shaofei Wang, Dr. Tao Liang, Dr. Yuhao Chen, and Dr. Yi Zhou from Xi'an Jiaotong University, Professor Qing Liu from Xi'an University of Science and Technology, Dr. Kejie Li from Hefei University of Technology, Prof. Igor Simone Stievano, Prof. Riccardo Trincherio and Prof. Paolo Manfredi from Politecnico di Torino, for many useful discussions on my research. Their ideas, comments, and suggestions were always appreciated.

I would like to thank all professors, staffs, and students in HPEMC group in XJTU and EMC group in PoliTo for making the work environment enjoyable. Thanks for the financial support from school of electrical engineering of XJTU during my exchange study in Italy. Thanks go to the following colleagues, Dr. Ziweihua Du, Dr. Xiaoyu Ge, Dr. Yanpeng Ge, Dr. Qi Li, Minzhou Liu, Yangxin Qiu, YuYing Wu, Zeqi Lv, Mingyue Gou, Daozhong Zhang, Zongyang Wang, Yuhao Gu, Siqi Wang, Zetong Li, Yifan Yang, Zhihao Xi, Weichen Xie, Haizhao Rong, Yizhe Shang, Ziqian Yin, Enrico Vaccariello, Zain Anwer Memon, et al, the common experiences of doing experiments, deriving formulas and debugging codes are unforgettable.

Next, I wish to thank Prof. Shuhong Wang, Prof. Wei Bing and Prof. Hongjie Li, for taking time from their busy jobs to review my dissertation very carefully.

My final thought is with my parents. Without their endless encouragement and terrific support, I would not persist during the journey full of ups and downs and have opportunity to complete this dissertation's research. Special thanks to my beloved father, he inspired me with his words and deeds, to stay brave and strong and never give in to fate. Memories of the past happiness are the source of strength to confront all the difficulties in my study and life. To him I dedicate this dissertation.

## References

- [1] Rachidi F. A review of field-to-transmission line coupling models with special emphasis to lightning-induced voltages on overhead lines[J]. *IEEE Transactions on Electromagnetic Compatibility*, 2012, 54(4):898-911.
- [2] Li BZ, He JL, Zhou H, et al. Electromagnetic interference of transmission line in HEMP environment[J]. 2009, 35(11):2753-2758.
- [3] Wu HT, Jiao CQ, Cui X, et al. Transient electromagnetic disturbance induced on the ports of intelligent component of electronic instrument transformer due to switching operations in 500 kV GIS substations[J]. *IEEE Access*, 2017,5:5104-5112.
- [4] Shetye K, Overbye T. Modeling and analysis of gmd effects on power systems: an overview of the impact on large-scale power systems[J]. *IEEE Electrification Magazine*, 2015, 3(4):13-21.
- [5] Gold S H, Nusinovich G S. Review of high-power microwave source research[J]. *Review of Scientific Instruments*, 1997, 68(11):3945-3974.
- [6] Radasky W A, Baum C E, Wik M W. Introduction to the special issue on high-power electromagnetics (HPEM) and intentional electromagnetic interference (IEMI)[J]. *IEEE Transactions on Electromagnetic Compatibility*, 2004, 46(3):314-321.
- [7] Zhou L, Zhang S, Yin WY, et al. Investigating a thermal breakdown model and experiments on a silicon-based low-noise amplifier under high-power microwave pulses[J]. *IEEE Transactions on Electromagnetic Compatibility*, 2015, 58(2):487-493.
- [8] Wang H, Li J, Zhou Y, et al. Theoretical and experimental study of complementary metal oxide semiconductor inverters under high-power microwave interferences[J]. *Electromagnetics*, 2009, 29(5):393-405.
- [9] Fang J Y, Shen J A, Yang ZQ, et al. Experimental study on microwave vulnerability effect of integrated circuit[J]. *High Power Laser & Particle Beams*, 2003, 15(6):591-594.
- [10] Tianle P, Changjun L, Liping Y. Experimental study on microwave radiation effects on personal computer[J]. *High Power Laser and Particle Beams*. 2006, 18(9):1549.
- [11] Zhai A, Xie Y, Han J, et al. Effect of high altitude nuclear electromagnetic pulse upon phone call[J]. *High Power Laser and Particle Beams*. 2009, 21(10):1529-1533.
- [12] Cang C, Bo Z. The effect of HPM to electric equipment[J]. *Aerospace Electronic Warfare*, 2007,23(5):26-28.
- [13] Baum, C E. EMP radiation and protective techniques[J]. *Proceedings of the IEEE*, 1978, 66(2):269-270.
- [14] Rakov V A and Uman M A. Review and evaluation of lightning return stroke models including some aspects of their application[J]. *IEEE Transactions on Electromagnetic Compatibility*, 1998, 40(4):403-426.
- [15] Zhou B H, Chen B, Shi L H. Electromagnetic pulse and its engineering protection[M]. National Defense Industry Press, 2003.
- [16] China Electricity Council. Code for design of overvoltage protection and insulation coordination of AC electrical installations: GB/T 50064-2014[S]. 2014.
- [17] IEEE guide for improving the lightning performance of electric power overhead distribution lines: IEEE Std 1410-2010[S]. 2010.
- [18] IEEE guide for improving the lightning performance of electric power overhead distribution lines: IEEE Std 1410TM[S]. 2004.
- [19] De la Rosa F. Assessing the operation of distribution lines in a lightning environment[J]. *High*



- Technology in the Power Industry, 1986, 20: 316-319.
- [20] Electromagnetic pulse handbook for missiles and aircraft in flight[M]. EMP Interaction 1-1, 1972.
  - [21] Ghose R N. EMP environment and system hardness design[M]. Virginia: Don White Consultants, 1984.
  - [22] Segro J R, Abi-Samra N C, Crouse J C, et al. Study to assess the effects of high-altitude electromagnetic pulse on electric power systems. Phase I, final report[R]. Virginia: Oak Ridge national laboratory 1986.
  - [23] High-altitude electromagnetic pulse and the bulk power system: potential impacts and mitigation strategies[R]. California: Electric power research institute, 2019.
  - [24] Modeling framework for bulk electric grid impacts from hemp E1 and E3 effects EMP-resilient grid grand challenge: Task 3.1 Final Report[R]. New Mexico: Sandia National Laboratory, 2021.
  - [25] Karzas W J, Latter R. Air conductivity produced by nuclear explosions[R]. Santa Monica: Rand Corporation, 1963.
  - [26] Karzas W J, Latter R. Detection of the electromagnetic radiation from nuclear explosions in space[J]. Physical Review, 1965, 137(5B): 1369-1378.
  - [27] Karzas W J, Latter R. Detection of the electromagnetic radiation from nuclear explosions in space[R]. Santa Monica: Rand Corporation, 1964.
  - [28] Karzas W J, Latter R. Electromagnetic radiation from a nuclear explosion in space[J]. Physical Review, 1962, 126(6):1919-1926.
  - [29] Karzas W J, Latter R. Satellite-based detection of the electromagnetic signal from low and intermediate altitude nuclear explosions[R]. Santa Monica: Rand Corporation, 1965.
  - [30] Karzas W J, Latter R. The electromagnetic signal due to the exclusion of the earth's magnetic field by nuclear explosions[R]. Santa Monica: Rand Corporation, 1961.
  - [31] Karzas W J, Latter R. The electromagnetic signal due to the interaction of nuclear explosions with the earth's magnetic field[J]. Journal of Geophysical Research, 1962, 67(12): 4635-4640.
  - [32] Karzas W J, Latter R. Detection of the Electromagnetic Radiation from Nuclear Explosions in Space[J]. Physical Review, 1965, 137(5B):43.
  - [33] Longmire C L. Close in E. M. effects lectures X and XI[R]. New Mexico: Los Alamos Scientific Lab, 1964.
  - [34] Longmire C L. Justification and verification of high-altitude EMP theory Part I[R]. California: Lawrence Livermore National Laboratory, 1987.
  - [35] Longmire C L. On the electromagnetic pulse produced by nuclear explosions[J]. IEEE Transactions on Antennas and Propagation, 1978. 20(1): 3-13.
  - [36] Longmire C L. Improvements in the treatment of compton current and air conductivity in EMP problems[R]. California: Lawrence Livermore National Laboratory, 1974.
  - [37] Longmire C L, Longley H J. Development of CHAP-A high altitude EMP code[R]. California: Lawrence Livermore National Laboratory, 1974.
  - [38] Leuthäuser K D. A complete EMP environment generated by high-altitude nuclear bursts[R]. Euskirchen: Franhofer-Institut für Naturwissenschaftlich-Technische Trendanalysen, 1992.
  - [39] Brau E, Canavan H, Wittwer A. CHEMP: A Code for calculation of high-altitude EMP[R]. New Mexico: Air Force Weapon Laboratory, 1974,
  - [40] Longmire C L, Hamilton R M, Hahn J M. A nominal set of high-altitude EMP environments[R]. Santa Barbara: Mission Research Corporation, 1987.
  - [41] Leuthäuser K D. Distribution functions of the HEMP environment[R]. Euskirchen: Franhofer-Institut für Naturwissenschaftlich-Technische Trendanalysen, 1992.
  - [42] Wang J. Simulation of high-altitude nuclear electromagnetic pulse using a modified model of scattered gamma[J]. IEEE Transactions on Nuclear Science, 2020, 67(12):2474-2480.

- [43] Eng C D. Development of the time dependence of the nuclear (E1) HEMP electric field[J]. IEEE Transactions on Electromagnetic Compatibility, 2011, 53(3):737-748.
- [44] Zhang J, Zhang YR. Study of high-altitude nuclear emp by using an integral equation method[J]. IEEE Transactions on Electromagnetic Compatibility, IEEE, 2018, 60(3): 665-673.
- [45] Zhang J, Zhang YR. Using a second-order integral equation method to study the high-altitude nuclear EMP[J]. IEEE Transactions on Electromagnetic Compatibility, IEEE, 2018, 61(5): 1483-1481.
- [46] EMP engineering and design principles[R]. Whippany: Bell Laboratory, 1975.
- [47] Giri D V, Prather W D. High-altitude electromagnetic pulse (HEMP) risetime evolution of technology and standards exclusively for e1 environment[J]. IEEE Transactions on Electromagnetic Compatibility, 2013, 55(3): 484-491.
- [48] Giri D V, Prather W D. Risetime evolution in HEMP (High-altitude electromagnetic pulse) E1 waveforms-technology and standards[J]. IEEE Transactions on Electromagnetic Compatibility, 2013, 55(3): 484-491.
- [49] Tesche F M, et al. Development of a new high altitude electromagnetic pulse (hemp) environment and resulting overhead line responses[J]. Electromagnetics, 1988, 8(2-4): 213-239.
- [50] Taylor C, Satterwhite R, Harrison C. The response of a terminated two-wire transmission line excited by a nonuniform electromagnetic field[J]. IEEE Transactions on Antennas & Propagation, 2003, 13(6):987-989.
- [51] Agrawal A K, Price H J, Gurbaxani S H. Transient response of multiconductor transmission lines excited by a nonuniform electromagnetic field[J]. IEEE Transactions on Electromagnetic Compatibility, 2007, 22(2):119-129.
- [52] Vance E F. Coupling to Shielded Cables[M]. New York: John Wiley & Sons Press, 1978.
- [53] Rachidi F. Formulation of the field-to-transmission line coupling equations in terms of magnetic excitation field[J]. IEEE Transactions on Electromagnetic Compatibility, 1993, 35(3): 404-407.
- [54] Chowdhuri P, Gross E. Voltage surges induced on overhead lines by lightning strokes[J]. Electrical Engineers Proceedings of the Institution of, 1972, 114(12):1899-1907.
- [55] Nucci C A, Rachidi F, Ianoz M and Mazzetti C. Comparison of two coupling models for lightning-induced overvoltage calculations[J]. IEEE Transactions on Power Delivery, 1995, 10(1): 330-339.
- [56] Xie YZ, Wang ZJ, Wang QS, et al. Comparison of Agrawal and Taylor models for response calculations of aboveground cable excited by HEMP[J]. High Power Laser & Particle Beams, 2005, 17(004):575-580.
- [57] Qiu RQ. Research on distribution characteristics and suppression of induced current on field-to-line coupling[D]. Chengdu: Southwest Jiaotong University, 2018.
- [58] Ianoz M, Orzan D, Rachidi F. Validation of field-to-transmission line coupling models[C]. International Symposium on Electromagnetic Compatibility, Beijing, 1997: 231-234.
- [59] Burke G J, Poggio A J, Logan, J C, et al. Numerical electromagnetic code (NEC)-method of moments[J]. 1979 IEEE International Symposium on Electromagnetic Compatibility, 1979, pp:1-3.
- [60] Guerrieri S, Nucci C A, Rachidi F. Influence of the ground resistivity on the polarity and intensity of lightning induced voltages[C]. 10th International Symposium on High Voltage Engineering, Montreal, 1997.
- [61] Sunde E D. Earth conduction effects in transmission systems[J]. Students Quarterly Journal. 1949, 20(78):92.
- [62] Rachidi F, Nucci C A, Ianoz M. Transient analysis of multiconductor lines above a lossy ground[J]. IEEE Transactions on Power Delivery. 1999, 14(1):294-302.
- [63] Li D, Cheng W, Liu X. Investigation of lightning-induced overvoltages affected by the sag of the overhead transmission line[C]. 2011 IEEE Power Engineering and Automation Conference, Wuhan, 2011: 335-338.

- [64] Nucci C A, Guerrieri S. Influence of corona on the voltages induced by nearby lightning on overhead distribution lines[J]. *IEEE Transactions on Power Delivery*, 2000, 15(4):1265-1273.
- [65] Nucci C A, Rachidi F, Rubinstein M. Electromagnetic field interaction with transmission lines: derivation of telegrapher's equations and field-to-transmission line interaction[M]. Southampton: WIT Press, 2008.
- [66] Nakhla N, Nakhla M, Achar R. Simplified delay extraction-based passive transmission line macromodeling algorithm[J]. *IEEE Transactions on Advanced Packaging*. 2010, 33(2):0-509.
- [67] Yinghui Z, Lihua S, Cheng G. A time-domain method to calculate EMP coupling of buried cables based on transmission line model[J]. *High Power Laser and Particle Beams*. 2006, 18(7):1166.
- [68] Guo J, Xie YZ, Canavero F G. Gauss-Seidel iterative solution of electromagnetic pulse coupling to three-conductor transmission lines[J]. *IEEE Transactions on Electromagnetic Compatibility*. 2014, 57(2):292-298.
- [69] Tesche F M, Ianoz M, Karlsson T. EMC analysis methods and computational models [M]: John Wiley and Sons, 1996.
- [70] Grivet-Talocia S, Huang H M, Ruehli A E, et al. Transient analysis of lossy transmission lines: an efficient approach based on the method of characteristics[J]. *IEEE Transactions on Advanced Packaging*. 2004, 27(1):45-56.
- [71] Dounavis A, Achar R, Nakhla M S. Efficient passive circuit models for distributed networks with frequency-dependent parameters[J]. *IEEE Transactions on Advanced Packaging*. 2000, 23(3):382-392.
- [72] Paul C R. A Spice model for multiconductor transmission lines excited by an incident electromagnetic field[J]. *IEEE Transactions on Electromagnetic Compatibility*. 1994, 36(4):342-354.
- [73] Liu X, Cui X, Qi L. Calculation of lightning-induced overvoltages on overhead lines based on deapctmacromodel using circuit simulation software[J]. *IEEE Transactions on Electromagnetic Compatibility*. 2011, 54(4):837-849.
- [74] Du Z, Xie YZ, Canavero F G. A Spice-compatible macromodel for field coupling to multiconductor transmission lines based on the analog behavioral modeling[J]. *IEEE Transactions on Electromagnetic Compatibility*, 2019,62(5): 2045 - 2054.
- [75] Liu X. Di Y. An easy-to-implement macro-model for evaluation of lightning induced voltages on overhead lines and its interface with PSCAD[J]. *IEEE Transactions on Electromagnetic Compatibility*, 2021, 64(2): 472 - 481.
- [76] Dounavis A, Li X. Passive closed-form transmission-line model for general-purpose circuit simulators[J]. *IEEE Transactions on Microwave Theory and Techniques*. 1999, 47(12):2450-2459.
- [77] Xie HY. Transient electromagnetic topology theory and its application in electromagnetic pulse effect of electronic system[D]. Beijing: Tsinghua University, 2011.
- [78] Guo J. Du X. Sensitivity Analysis with mixture of epistemic and aleatory uncertainties[J]. *Aiaa Journal*, 2007, 45(9):2337-2349.
- [79] Hoffman F O, Hammonds J S. Propagation of uncertainty in risk assessments: the need to distinguish between uncertainty due to lack of knowledge and uncertainty due to variability[J]. *Risk Analysis*, 1994, 14: 707-712.
- [80] Urbina A, Mahadevan S, Paez T L. Quantification of margins and uncertainties of complex systems in the presence of aleatory and epistemic uncertainty[J]. *Reliability Engineering & System Safety*, 2011, 96(9):1114-1125.
- [81] Eyke H K, et al. Reliable classification: learning classifiers that distinguish aleatory and epistemic uncertainty[J]. *Information Sciences An International Journal*, 2014,255:16-29.
- [82] Paul C R. Analysis of multiconductor transmission lines[M]. Kentucky: Wiley, 1994:45 - 54.
- [83] Ianoz M, Nicoara B, Radasky W A. Modeling of an EMP conducted environment[J]. *IEEE*

- Transactions on Electromagnetic Compatibility, 2002, 38(3):400-413.
- [84] Spadacini G, Pignari S A. A bulk current injection test conforming to statistical properties of radiation-induced effects[J]. IEEE Transactions on Electromagnetic Compatibility, 2004, 46(3):446-458.
  - [85] Fei Z, Huang Y, Zhou JF, et al. Numerical analysis of a transmission line illuminated by a random plane-wave field using stochastic reduced order models[J]. IEEE Access, 2017, 5(99):8741-8751.
  - [86] Fei ZX, Huang Y, Zhou JF, et al. Uncertainty quantification of crosstalk using stochastic reduced order models[J]. IEEE Transactions on Electromagnetic Compatibility, 2017, 59(1):228-239.
  - [87] Lallechere S, Carobbi C F M, Arnaut L R, Review of uncertainty quantification of measurement and computational modeling in EMC Part II: computational uncertainty[J]. IEEE Transactions on Electromagnetic Compatibility, 2019, 61(6): 1699-1706.
  - [88] Manfredi P, Canavero F G. Stochastic analysis of multiconductor cables and interconnects[J]. IEEE Transactions on Electromagnetic Compatibility, 2011, 53(2):501-507.
  - [89] Stievano I S, Manfredi P, Canavero F G. Parameters variability effects on multiconductor interconnects via Hermite polynomial chaos[J]. IEEE Transactions on Components Packaging and Manufacturing Technology, 2011, 1(8):1234-1239.
  - [90] Manfredi P, Canavero F G. Polynomial chaos representation of transmission-line response to random plane waves[C]. International Symposium on Electromagnetic Compatibility - EMC EUROPE, Torino, 2012:1-6.
  - [91] Manfredi P, Canavero F G. Polynomial chaos for random field coupling to transmission lines[J]. IEEE Transactions on Electromagnetic Compatibility 2012, 54(3):677-680.
  - [92] Biondi A, Ginste D V, De Zutter D, Manfredi P, et al. Variability analysis of interconnects terminated by general nonlinear loads[J]. IEEE Transactions on Components Packaging and Manufacturing Technology, 2013, 3(7):1244-1251.
  - [93] Manfredi P, Vande Ginste D, De Zutter D, et al. On the passivity of polynomial chaos-based augmented models for stochastic circuits[J]. IEEE Transactions on Circuits and System I, Regular Papers, 2013, 60(11):2998-3007.
  - [94] Manfredi P. High-speed interconnect models with stochastic parameter variability[D]. Piemonte: Politecnico di Torino, 2013:81-88.
  - [95] Manfredi P, Canavero F G. Statistical analysis of multiconductor cables and interconnects with internal variability and field coupling.[C] 42nd European Microwave Conference, Amsterdam, 2012:348-351.
  - [96] Zhang Z, El-Moselhy T A, Elfadel I M, et al. Stochastic testing method for transistor-level uncertainty quantification based on generalized polynomial chaos[J]. IEEE Transactions on Computer-Aided Design of Integrated Circuits and Systems, 2014, 32(10):1533-1545.
  - [97] Manfredi P, Ginste D V, Stievano I S, et al. Stochastic transmission line analysis via polynomial chaos methods: an overview[J]. IEEE Electromagnetic Compatibility Magazine, 2017, 6(3):77-84.
  - [98] Larbi M, Stievano I S, Canavero F G, et al. Analysis of a printed circuit board with many uncertain variables by sparse polynomial chaos[C]. IEEE International Conference on numerical electromagnetic and multiphysics modeling and optimization for radio frequency, microwave, and terahertz applications, Seville, Spain, 2017:323-325.
  - [99] Larbi M, Stievano I S, Canavero F G, et al. Variability impact of many design parameters: the case of a realistic electronic link[J]. IEEE Transactions on Electromagnetic Compatibility, 2017, 60(1):34-41.
  - [100] Li ZY, Ning D, Feng J, et al. Uncertainty quantification analysis of random field coupling to transmission lines based on polynomial chaos expansion method[J]. High Power Laser and Particle Beams, 2017, 29(11):1-7.
  - [101] Hao JP, Dong N, Guo F, et al. Multivariable uncertainty quantification of transmission line field-to-

- line coupling based on stochastic collocation method[C]. 2017 IEEE Conference on Energy Internet and Energy System Integration, 2017, Beijing:650-654.
- [102] Zhang Z, Weng TW, Daniel L. Big-data tensor recovery for high-dimensional uncertainty quantification of process variations[J]. IEEE Transactions on Components Packaging & Manufacturing Technology, 2016, 7(5):687-697.
- [103] Zhang Z, Batselier K, Liu H, et al. Tensor computation: a new framework for high-dimensional problems in EDA[J]. IEEE Transactions on Computer-Aided Design of Integrated Circuits and Systems, 2016, 36(4):521-536.
- [104] Trincherò R, Manfredi P, Stievano I S, et al. Machine learning for the performance assessment of high-speed links[J]. IEEE Transactions on Electromagnetic Compatibility, 60(6):1627-1634.
- [105] Shiran S, Reiser B, Cory H. A probabilistic method for the evaluation of coupling between transmission lines[J]. IEEE Transactions on Electromagnetic Compatibility, 1993, 35(3):387-393.
- [106] Pignari S, Bellan D. Statistical characterization of multiconductor transmission lines illuminated by a random plane-wave field[C]. IEEE International Symposium on Electromagnetic Compatibility, Washington DC, 2000:605-609.
- [107] Bellan D, Pignari S. A probabilistic model for the response of an electrically short two-conductor transmission line driven by a random plane wave field[J]. IEEE Transactions on Electromagnetic Compatibility, 2001, 43(2):130-139.
- [108] Pignari S, Bellan D, Rienzo L D. Statistical estimates of crosstalk in three-conductor transmission lines[C]. IEEE International Symposium on Electromagnetic Compatibility, Sorrento, Italy, 2002: 877-882.
- [109] Barmada S, Musolino A, Raugi M, et al. Efficient method to treat parameters' uncertainties in complex circuits[C]. 2006 Biennial IEEE Conference on Electromagnetic Field Computation, Miami, 2006:294-294.
- [110] Wu M, Beetner D, Hubing T, et al. Estimation of the statistical variation of crosstalk in wiring harnesses[C]. IEEE International Symposium on Electromagnetic Compatibility, Florida, 2010:1-7.
- [111] Xie H, Wang J, Yong L, et al. Efficient evaluation of multiconductor transmission lines with random translation over ground under a plane wave[J]. IEEE Transactions on Electromagnetic Compatibility, 2014, 56(6):1623-1629.
- [112] Xia J, Yin J, Zhao J, et al. Sensitivity analysis for time domain response of nonuniform coupled transmission lines with nonlinear loads[C]. International Conference on Biomedical Engineering and Informatics, Las Vegas, 2016:867-871.
- [113] Zhang Z, Elfadel I M, Daniel L. Uncertainty quantification for integrated circuits: Stochastic spectral methods[C]. IEEE/ACM International Conference on Computer-Aided Design, San Jose, 2014:803-810.
- [114] Pusateri E N, Improving high-altitude EMP modeling capabilities by using a non-equilibrium electron swarm model to monitor conduction electron evolution[D]. Rensselaer Polytechnic Institute, New York, 2016.
- [115] Farmer W A, Friedman A. Effect of multiple scattering on the Compton recoil current generated in an EMP, Revisited[J]. IEEE Transactions on Nuclear Science, 2015, 62(4):1695-1706.
- [116] Jones C W. Electron-ion ion-ion recombination coefficients for use in EMP prediction codes[R]. New Mexico: Air Force Weapon Laboratory, 1977.
- [117] Gilbert J L, Radasky W A, Savage E B. Study of nonequilibrium air chemistry[J]. IEEE Transactions on Electromagnetic Compatibility, 2013, 55(3):446-450.
- [118] Farmer W A, Cohen B I, Eng C D. On the Validity of certain approximations used in the modeling of nuclear EMP[J]. IEEE Transactions on Nuclear Science, 2016, 63(2):1259-1267.
- [119] Longmire C L. Effect of multiple scattering on the Compton recoil current[R]. Santa Barbara: Mission

- Research Corporation, 1978.
- [120] Ouyang JM, Ma YY, Shao FQ, et al. Ionization effect of atmosphere by prompt rays from high-altitude nuclear explosions[J]. *IEEE Transactions on Nuclear Science*, 2014, 61(3):1433-1438.
  - [121] Jones C W. Electron-ion ion-ion recombination coefficients for use in EMP prediction codes[R]. New Mexico: Air Force Weapon Laboratory, 1977.
  - [122] Nelson E M, et al. Determination of equilibrium electron temperature and times using an electron swarm model with BOLSIG+ calculated collision frequencies and rate coefficients[J]. *Journal of Geophysical Research, D. Atmospheres: JGR*, 2015, 120(15):7300-7315.
  - [123] Morris E M, et al. Comparison of equilibrium ohmic and nonequilibrium swarm models for monitoring conduction electron evolution in high-altitude EMP calculations[J]. *Journal of Geophysical Research, D. Atmospheres: JGR*, 2016, 121(20):11884-11899.
  - [124] Wei HC, Kiang JF. simulation of high-altitude electromagnetic pulse (hemp) above sea surface[J]. *Progress In Electromagnetics Research M*, 2016, 50:195-204.
  - [125] Zhou YF, Cheng YH, Zhu ZZ, et al. Simulation study of air effects on SGEMP based on swarm model[J]. *IEEE Transactions on Nuclear Science*, 2022, 69(1): 26-34.
  - [126] Wittwer A. High altitude conductivity models for electromagnetic pulse calculations[R]: New Mexico: Air Force Weapon Laboratory, 1975.
  - [127] Baum C E. Electron thermalization and mobility in air[R]. New Mexico: Air Force Weapon Laboratory, 1965.
  - [128] Baum C E. Some considerations concerning analytic EMP criteria waveforms[R]. New Mexico: Air Force Weapon Laboratory, 1976.
  - [129] Giri D V, Prather W D. High-altitude electromagnetic pulse (HEMP) risetime evolution of technology and standards exclusively for E1 environment[J]. *IEEE Transactions on Electromagnetic Compatibility*, 2013, 55(3):484-491.
  - [130] Fu MY, Zhang MY. Self-consistent particle simulation of early-time high altitude electromagnetic pulse[J]. *Modern Applied Physics*, 2018,9(2): Art. no. 020502.
  - [131] Wang J, Zhang D, Liu C, et al. UNIPIC code for simulations of high power microwave devices[J]. *Physics of Plasmas*, 2009, 16(3), Art. no. 033108.
  - [132] Friedman A, Cohen B I, Farmer W A, et al., EMPulse, a new 3-D simulation code for EMP formation and propagation[R]. California: Lawrence Livermore National Laboratory, 2015.
  - [133] Taylor C, Satterwhite R, Harrison C. The response of a terminated two-wire transmission line excited by a nonuniform electromagnetic field[J]. *IEEE Transactions on Antennas & Propagation*, 1965, 13(6):987-989.
  - [134] Agrawal A K, Price H J, Gurbaxani S H. Transient response of multiconductor transmission lines excited by a nonuniform electromagnetic field[J]. *IEEE Transactions on Electromagnetic Compatibility*, 1980, 22(2):119-129.
  - [135] Rachidi F, Nucci C A, Ianoz M, et al. Response of multiconductor power lines to nearby lightning return stroke electromagnetic fields[J]. *IEEE Transactions on Power Delivery*, 1997, 12(3):1404-1411.
  - [136] Luenberger D. State space analysis of control systems[J]. *IEEE Transactions on Automatic Control*, 1967, 12(6):805-805.
  - [137] Xie H, Li Y, Qiao H, et al. Empirical formula of effective coupling length for transmission lines illuminated by E1 HEMP[J]. *IEEE Transactions on Electromagnetic Compatibility*, 2016, 58(2):581-587.
  - [138] Gupta T K. Application of zinc oxide varistors[J]. *Journal of the American Ceramic Society*, 2010, 73(7):1817-1840.
  - [139] Lundquist J, Stenstrom L, Schei A, et al. New method for measurement of the resistive leakage

- currents of metal-oxide surge arresters in service[J]. *IEEE Transactions on Power Delivery*, 2002, 5(4):1811-1822.
- [140] Nigol O. Methods for analyzing the performance of gapless metal oxide surge arresters[J]. *IEEE Transactions on Power Delivery*, 1992, 7(3):1256-1264.
- [141] Brito V S, Lira G, Costa E G, et al. A wide-range model for metal-oxide surge arrester[J]. *IEEE Transactions on Power Delivery*, 2017,30(1):102-109.
- [142] Bowman T, Halligan M, Llanes R. High-frequency metal-oxide varistor modeling response to early-time electromagnetic pulses[C]. 2020 IEEE International Symposium on Electromagnetic Compatibility & Signal/Power Integrity (EMCSI), Reno, NV, 2020:466-471.
- [143] ABB Application Guide. Overvoltage protection metal oxide surge arresters in medium voltage systems 5th edition[R]. Wetzlar: ABB, 2011.
- [144] Schmidt W, Meppelink J. Behaviour of MO-surge-arrester blocks to fast transients[J]. *IEEE Transactions on Power Delivery*, 1989, 4(1):292-300.
- [145] Zhou Y, Xie YZ, Zhang DZ, et al. Response of 10-kV metal-oxide surge arresters excited by nanosecond-level transient electromagnetic disturbances[J]. *IEEE Transactions on Electromagnetic Compatibility*, 2020, 63(2): 614 - 621.
- [146] Qin F, Chen W, Wang X, et al. Transient response characteristics of metal oxide arrester under high-altitude electromagnetic pulse[J]. *Energies*, 2022, 15(9):1-10.
- [147] IEEE Working Group 3.4.11. Modeling of metal oxide surge arresters[J]. *IEEE Transactions on Power Delivery*, 1992, 7(1):302-309.
- [148] Kim I, Funabashi T. Study of ZnO arrester model for steep front wave[J]. *IEEE Transactions on Power Delivery*, 1996, 11(2):834-841.
- [149] Pinceti P, Giannettoni M. A simplified model for zinc oxide surge arresters[J]. *IEEE Transactions on Power Delivery*, 1999, 14(2):393-398.
- [150] Fernández R D. Metal oxide surge arrester model for fast transient simulations[C]. 144th International conference on power system transients, Rio de Janeiro, Brazil, 2001.
- [151] Vita V, Mitropoulou A D, Ekonomou L, et al. Comparison of metal-oxide surge arresters circuit models and implementation on high-voltage transmission lines of the Hellenic network[J]. *IET Generation, Transmission & Distribution*, 2010, 4(7): 846-853.
- [152] Hileman R, Roguin J, and Weck K. Metal-oxide surge arresters in ac systems-part v: Protection performance of metal oxide surge arresters[J]. *Electra*, 1990, 133: 132-144.
- [153] Hong Y, Yue Y, Yang L, et al. SPICE Behavioral model of the tunneling field-effect transistor for circuit simulation[J]. *IEEE Transactions on Circuits & Systems II Express Briefs*, 2009, 56(12):946-950.
- [154] Christodoulou C A, Gonos I F, Stathopoulos I A. Estimation of the parameters of metal oxide gapless surge arrester equivalent circuit models using genetic algorithm[J]. *Electric Power Systems Research*, 2011, 81(10):1881-1886.
- [155] Christodoulou C A, Vita V, et al. Adjusting the parameters of metal oxide gapless surge arresters' equivalent circuits using the harmony search method[J]. *Energies*, 2017, 10: Art.no.2168.
- [156] Yuan Z, Li T, He J, et al. New mathematical descriptions of ESD current waveform based on the polynomial of pulse function[J]. *IEEE Transactions on Electromagnetic Compatibility*, 2006, 48(3):589-591.
- [157] Strunz K, Su QL. Stochastic formulation of SPICE-type electronic circuit simulation with polynomial chaos[J]. *Acm Transactions on Modeling & Computer Simulation*, 2008, 18(4):1-23.
- [158] Manfredi P, Stievano I S, Canavero F G. Stochastic analysis of switching power converters via deterministic SPICE equivalents[J]. *IEEE Transactions on Power Electronics*, 2014, 29(9):4475-4478.
- [159] Manfredi P, Ginste D V, Zutter D D, et al. Stochastic modeling of nonlinear circuits via spice-

- compatible spectral equivalents[J]. *IEEE Transactions on Circuits & Systems I Regular Papers*, 2014, 61(7):2057-2065.
- [160] Xin L, Le J, Gopalakrishnan P, et al. Asymptotic probability extraction for non-normal distributions of circuit performance[J]. *IEEE/ACM International Conference on Computer Aided Design (ICCAD-2004)*, San Jose, 2004, pp. 2-9,
- [161] Xin L, Le J, Gopalakrishnan P, et al. Asymptotic probability extraction for nonnormal performance distributions[J]. *IEEE Transactions on Computer-Aided Design of Integrated Circuits and Systems*, 2007, 26(1):16-37.
- [162] Fritsch F N, Carlson R E. Monotone piecewise cubic interpolation[J]. *Siam Journal on Numerical Analysis*, 1980, 17(2):238-246.
- [163] Hyman J M. Accurate monotonicity-preserving cubic interpolation[J]. *Siam Journal on Scientific & Statistical Computing*, 1983, 4(4):645-654.
- [164] Delbourgo R, Gregory J A. Shape preserving piecewise rational interpolation[J]. *Siam Journal on Scientific & Statistical Computing*, 1984, 6(4):967-976.
- [165] Gregory J A, Delbourgo R. Piecewise rational quadratic interpolation to monotonic data[J]. *IMA Journal of Numerical Analysis*, 1982, 2(2): 123–130.
- [166] Navarro M, Witteveen J, Blom J. Polynomial chaos expansion for general multivariate distributions with correlated variables[J]. *Eprint Arxiv*, 2014.
- [167] Schoutens W. *Stochastic processes and orthogonal polynomials*[M]. New York: Springer-Verlag, 2000.
- [168] Xiu D, Karniadakis G E. The Wiener-Askey polynomial chaos for stochastic differential equations[J]. *SIAM Journal on Scientific Computing*, 2002, 24(2): 619-644.
- [169] Oladyshkin S, Nowak W. Data-driven uncertainty quantification using the arbitrary polynomial chaos expansion[J]. *Reliability Engineering & System Safety*, 2012, 106:179-190.
- [170] Zheng Z, El-Moselhy T A, Elfadel I M, et al. Calculation of generalized polynomial-chaos basis functions and gauss quadrature rules in hierarchical uncertainty quantification[J]. *IEEE Transactions on Computer-Aided Design of Integrated Circuits and Systems*, 2014, 33(5):728-740.
- [171] Zheng Z, Yang X, Oseledets I V, et al. Enabling high-dimensional hierarchical uncertainty quantification by anova and tensor-train decomposition[J]. *IEEE Transactions on Computer-Aided Design of Integrated Circuits and Systems*, 2014,34(1):63-76.
- [172] Arnaut L R. *Uncertainty reduction and decorrelation of mode-stirred reverberation chamber data using transformation and expansion techniques* [M]. Texas: University of Texas Press, 1983.
- [173] Rosenblatt M. Remarks on a multivariate transformation[J]. *Annals of Mathematical Statistics*, 1952, 23(3):470-472.
- [174] Liu PL, Kiureghian A D. Multivariate distribution models with prescribed marginals and covariances[J]. *Probabilistic Engineering Mechanics*, 1986, 1(2):105-112.
- [175] Arnaut L R. Copulas, outliers, and rogue states of nonelliptic fields and energy in electromagnetic reverberation[J]. *IEEE Transactions on Electromagnetic Compatibility*, 2016, 58(2):1-12.
- [176] Torre E, Marelli S, Embrechts P, et al. A general framework for data-driven uncertainty quantification under complex input dependencies using vine copulas[J]. *Probabil Engineering Mechanics*, 2019,55:1-16.
- [177] Torre E, Marelli S, Sudret B. *UQLab user manual–Statistical inference*[R]. Zurich: ETH Chair of Risk, Safety and Uncertainty Quantification, 2022.
- [178] Marelli S, Lüthen N, Sudret B. *UQLab user manual–Polynomial chaos expansions*[R]. Zurich: ETH Chair of Risk, Safety and Uncertainty Quantification, 2022.
- [179] Oladyshkin S, Nowak W. Data-driven uncertainty quantification using the arbitrary polynomial chaos expansion[J]. *Reliability Engineering & System Safety*, 2012, 106:179-190.



- [180] Izenman A J. Recent developments in nonparametric density estimation[J]. *Journal of the American Statistical Association*, 1991, 86(413):205-224.
- [181] Scott D W. *Multivariate density estimation, Theory, Practice and Visualization*[M]. New York: John Wiley, 1994.
- [182] Simonoff J S. *Smoothing methods in statistics (springer series in statistics)*[M]. Springer, New York, 1996.
- [183] Golub G H, Welsch J H. Calculation of Gauss quadrature rules[J]. *Mathematics of Computation*, 1969, 23(106):221-221.
- [184] Trefethen L N. Is Gauss quadrature better than Clenshaw-Curtis?[J]. *Siam Review*, 2008, 50(1):67-87.
- [185] Cui CF, Zhang Z, High-dimensional uncertainty quantification of electronic and photonic ic with non-gaussian correlated process variations[J]. *IEEE Transactions on Computer-Aided Design of Integrated Circuits and Systems*, 2020.39(8):1649-1661.
- [186] Ianoz M, Nicoara B. Modeling of an EMP conducted environment[J]. *IEEE Transactions on Electromagnetic Compatibility*, 1996, 38(3):400-413.
- [187] *Electromagnetic Compatibility (EMC)-Part 2-9: Description of HEMP environment-radiation disturbance, IEC Standard 61000-2-9*[S]. 1998.
- [188] *Electromagnetic Compatibility (EMC)-Part 2-10: Environment description of emp environment conducted disturbance, IEC Standard 61000-2-10*[S]. 1998.
- [189] Baum C E. From the electromagnetic pulse to high-power electromagnetics[J]. *Proceedings of the IEEE*, 1992, 80(6):789-817.
- [190] Leuthäuser K D. *A complete EMP environment generated by high-altitude nuclear bursts and standardization*[R]. Euskirchen: Franhofer-Institut für Naturwissenschaftlich-Technische Trendanalysen, 1992.
- [191] Mora N, Lugrin G, Becerra J, et al. Revisiting the calculation of the early-time hemp conducted environment[J]. *IEEE transactions on electromagnetic compatibility*, 2020,63(1):111-124.
- [192] Sobol I M. Global sensitivity indices for nonlinear mathematical models and their Monte Carlo estimates[J]. *Mathematics and Computers in Simulation*, 2001,55(1):271-280.
- [193] Trincherro R, Larbi M, Torun H M, et al. Machine learning and uncertainty quantification for surrogate models of integrated devices with a large number of parameters[J]. *IEEE Access*, 2018, 7:4026-4066.
- [194] LS-SVMlab version 1.8[R]. Department of electrical engineering, Katholieke Universiteit Leuven, Leuven, Belgium.
- [195] Mandea M, Macmillan S, Lowes F J. *Geomagnetic field modelling and IGRF 2000 - Preface*[J]. *Earth Planets and Space*, 2000, 52(12):1117-1117.
- [196] Rakov V A, Borghetti A, Bouquegneau C, et al. *Lightning parameters for engineering applications*[C]. 2013 International Symposium on Lightning Protection (XII SIPDA), Belo Horizontem, 2013: 373-377.
- [197] Romero C, Paolone M, Rachidi F, et al. A statistical analysis on the risetime of lightning current pulses in negative upward flashes measured at Sântis tower[C]. *International Conference on Lightning Protection*, Vienna, 2012.
- [198] Popolansky F. Frequency distribution of amplitudes of lightning currents[J]. *CIGRE Electra*, 1972, 20:139-147.
- [199] Borghetti A, Nucci C A, Paolone M. Estimation of the statistical distributions of lightning current parameters at ground level from the data recorded by instrumented towers[J]. *IEEE Transactions on Power Delivery*, 2004, 19(3): 1400-1409.
- [200] *High-altitude electromagnetic pulse (EMP) Protection for ground-based C4I facilities performing critical, time-urgent missions, MILSTD-188-125-1/2*[S]. 1998.

- [201] Fichte L O, Knoth S, Potthast S, et al. Application of generalized linear models to evaluate nuclear EMP tests[J]. *IEEE Transactions on Electromagnetic Compatibility*, 2016: 748-753.
- [202] Houret T, Besnier P, Vauchamp S, et al. Inferring the probability distribution of the electromagnetic susceptibility of equipment from a limited set of data[C]. *2018 International Symposium on Electromagnetic Compatibility (EMC EUROPE)*, Amsterdam, 2018: 527-532.
- [203] Camp M, Gerth H, Garbe H, et al. Predicting the breakdown behavior of microcontrollers under EMP/UWB impact using a statistical analysis[J]. *IEEE Transactions on Electromagnetic Compatibility*, 2004, 46(3):368-379.
- [204] Chen YH, Xie YZ, Ge XY, et al. Vulnerability assessment of equipment excited by disturbances based on support vector machine and gaussian process regression[J]. *IEEE Transactions on Electromagnetic Compatibility*, 2020,63(1):103-110.
- [205] Li KJ, Xie YZ, Zhang F, et al. Statistical inference of serial communication errors caused by repetitive electromagnetic disturbances[J]. *IEEE Transactions on Electromagnetic Compatibility*, 2019, 62(4): 1160-1168.
- [206] Li K J, Xie YZ, Chen YH, et al. Bayesian inference for susceptibility of electronics to transient electromagnetic disturbances with failure mechanism consideration[J]. *IEEE Transactions on Electromagnetic Compatibility*, 2019, 62(4):1160-1168.
- [207] Sharp D H, Wood-Schultz M M. QMU and nuclear weapons certification[R]. California: Lawrence Livermore National Laboratory, 2003.
- [208] Pilch M, et al. Ideas underlying quantification of margins and uncertainties (QMU): a white paper[R]. New Mexico: Sandia National Laboratory, 2006.
- [209] Pilch M, Trucano T G, Helton J C. Ideas underlying the quantification of margins and uncertainties[J]. *Reliability Engineering & System Safety*, 2011, 96(9):965-975.
- [210] Xie CY, Huang HZ, Wei FY. Application of QMU to structural analysis considering uncertainty[C]. *2012 International Conference on Quality, Reliability, Risk, Maintenance, and Safety Engineering*, Chengdu, 2012: 1152-1155.
- [211] Ding F, Sheng L, Sun X, et al. Reliability assessment for traction power supply system based on Quantification of Margins and Uncertainties[J]. *Microelectronics Reliability*, 2018, 88-90:1195-1200.
- [212] Liu Z. Radiation effects evaluation of satellite electric power system based on quantifications of margins and uncertainties[D]. Changsha: National University of Defense Technology, 2013.
- [213] Yang Q. Uncertainty propagation and QMU application for flutter analysis of wing Structures[D]. Xiamen: Xiamen University, 2017.
- [214] Jason E, et al. Defining a practical QMU metric[C]. *49th AIAA/ASME/ASCE/AHS/ASC Structures, Structural Dynamics, and Materials Conference*, Illinois, 2008.
- [215] Newcomer J T. A new approach to quantification of margins and uncertainties for physical simulation data[R]. New Mexico: Sandia National Laboratory, 2012.
- [216] Requirements for the control of electromagnetic interference characteristics of subsystems and equipment, MIL-STD-461G[S]. 2015.
- [217] Zhou Y, Xie YZ, Zhang DZ, et al. Modeling and performance evaluation of inductive couplers for pulsed current injection[J]. *IEEE Transactions on Electromagnetic Compatibility*, 2020, 63(3):710-719.
- [218] Krishnamoorthy K, Mathew T. *Statistical tolerance regions: theory, applications, and computation: nonparametric tolerance intervals*[M], New Jersey: Wiley. 2009.
- [219] Fernholz L T, Gillespie J A. Content-corrected tolerance limits based on the Bootstrap[J]. *Technometrics*, 2001, 43(2): 147-155.
- [220] Beran R, Hall P. Interpolated nonparametric prediction intervals and confidence intervals[J]. *Journal of the Royal Statistical Society. Series B, Methodological*, 1993, 55(3) :643-652, 1993.

- [221] Cyranski J F. Maximum entropy and bayesian methods: Maxent applied to linear regression[M]. Netherlands: Springer. 1990.
- [222] Li H. Statistical learning method[M]. Beijing: Tsinghua University Press, 2019.
- [223] Elith J, Phillips S J, Hastie T, et al. A statistical explanation of MaxEnt for ecologists[J]. Diversity & Distributions, 2010:1-15.
- [224] Anderson M G, Ning Z, Pierre J W, et al. Bootstrap-based confidence interval estimates for electromechanical modes from multiple output analysis of measured ambient data[J]. IEEE Transactions on Power Systems, 2005, 20(2):943-950.
- [225] Grassi F, Pignari S A. Bulk current injection in twisted wire pairs with not perfectly balanced terminations[J]. IEEE Transactions on Electromagnetic Compatibility, 2013, 55(6): 1293–1301.

## Achievements

- [1] **Dong N**, Xie YZ. On the Self-Consistent Simulation of High-altitude Electromagnetic Pulse[J]. IEEE Transactions on Nuclear Science, 2022, 69(9):2074-2082. (DOI: 10.1109/TNS.2022.3193586)
- [2] **Dong N**, Xie YZ, Wang ZY. Vulnerability Assessment of Equipment Excited by Transient Electromagnetic Disturbances Based on Distribution-free QMU Method[J]. IEEE Transactions on Electromagnetic Compatibility.2023,65(1). (DOI: 10.1109/TEMC.2022.3220685)
- [3] **Dong N**, Xie YZ. An Efficient Iterative Scheme for HEMP Simulation with Consideration of Self-consistency[C]. 2022 3rd URSI Atlantic and Asia Pacific Radio Science Meeting (AT-AP-RASC), Gran Canaria, Spain, 2022. (DOI: 10.23919/AT-AP-RASC54737.2022.9814248)
- [4] **董宁**, 孙颖力, 王宗扬等. 基于 QMU 的高空电磁脉冲下电气电子设备易损性评估方法[J]. 强激光与粒子束, 2021, 33(12): Art.no.123011. (DOI:10.11884/HPLPB202133.210386)
- [5] **董宁**, 谢彦召. 考虑参数不确定性的高空电磁脉冲 E1分量环境计算及分析[J]. 强激光与粒子束, 2019, 31(7): Art.no.070002. (DOI: 10.11884/HPLPB201931.190140)
- [6] Du ZWH, Xie YZ, **Dong N**, Canavero F G. A Spice-Compatible Macromodel for Field Coupling to Underground Transmission Lines Based on the Analog Behavioral Modeling[J]. IEEE Transactions on Electromagnetic Compatibility, 2020, 62(5):2045-2054. (DOI: 10.1109/TEMC.2019.2954358)
- [7] Liu Q, Xie YZ, **Dong N**, et al. Uncertainty Quantification of Geo-Magnetically Induced Currents in UHV Power Grid[J]. IEEE Transactions on Electromagnetic Compatibility, 2020, 62(1):258-265. (DOI: 10.1109/TEMC.2019.2894945)
- [8] Liu MZ, Xie YZ, **Dong N**, et al. Numerical Analysis of Nonuniform Geoelectric Field Impacts on Geomagnetic Induction in Pipeline Networks[J]. IEEE Transactions on Electromagnetic Compatibility, 2022, 64(4):999-1009. (DOI: 10.1109/TEMC.2022.3158885)

